Search for T violation and CP violation in the Weak Semileptonic Λ0b and Λ+c Decays with the LHCb Detector

Mohamad Kozeiha

HAL Id: tel-01980282
https://theses.hal.science/tel-01980282

Submitted on 14 Jan 2019

Université Clermont Auvergne
U.F.R Sciences et technologies

École Doctorale des Sciences Fondamentales

Thèse

en vue de l'obtention du grade de

Docteur en Physique
Spécialité: Constituants élémentaires

Présentée par

Mohamad KOZEIHA

Search for T violation and CP violation in the Weak Semileptonic Λ_b^0 and Λ_c^+ Decays with the LHCb Detector

Soutenue publiquement le 30 Novembre 2017 devant la commission d'examen constituée de :

Président :	M. Pascal PERRET
Rapporteurs :	M. Olivier LEROY
	M. Patrick OWEN
Examinateurs :	Mrs. Marina ARTUSO
Directeur de thèse :	M. Ziad Jean AJALTOUNI

Résumé

Trois symétries discrètes: C, P, T sont importantes en Physique Subatomique; leur produit combiné étant supposé être une symétrie exacte. La symètrie CPT est considérée comme la pierre angulaire de la Physique des Particules. Étant donné que C et P sont violées, il est important de tester la violation de la symétrie T. L'objet de cette thèse, y compris l'ensemble des thèmes étudiés, est de proposer d'une manière directe une nouvelle stratégie pour tester la symétrie de renversement du temps (T). Le collisioneur LHC nous donne l'opportunité de le faire grâce à l'énorme production de baryons beaux. La désintégration $\Lambda_b^0 \to (\Lambda_c^+ \to \Lambda\pi)(W^* \to \mu^-\nu_\mu)$, qui est considérée comme une source d'observables impaires par la symétrie T est utilisée. Une étude exhaustive de la Polarisation du Λ_b^0 et des résonances issues du baryon beau est effectuée. En premier lieu, le cadre théorique, concernant les symétries et leur rôle, est présenté. Des progrès significatifs ont été réalisés dans le développement d'un modèle cinématique à partir duquel sont calculées les distributions angulaires des particules issues des différentes désintegrations. Une étude détaillée de la reconstruction et de la sélection des événements est exposée ainsi que la méthodologie suivie pour extraire les polarisations à partir des différentes distributions angulaires.

Cette étude est réalisée en utilisant les données 2011-2012 enregistrées par le détecteur LHCb lors de la première phase du LHC.

Mots-Clés: Cinématique de désintégration. LHCb. Violation de T. Violation de CP. Polarisation, Désintégrations en cascade.

Abstract

Three discrete symmetries: C,P,T are important in subatomic Physics, their combination (CPT) is considered as the corner stone of investigation in Particle Physics and many other fields. Since C and P are violated, it is important to investigate the direct violation of the T symmetry. This thesis, with all the discussed topics, aims to propose in a direct way a new strategy to test the symmetry of time reversal (T). The Collider LHC gives us the opportunity to do that throughout the enormous production of the beauty baryons. Here, the emphasis will be put on the decay $\Lambda_b^0 \to (\Lambda_c^+ \to \Lambda\pi)(W^* \to \mu^-\nu_\mu)$, that is considered as a source of observables that are odd under T symmetry. A special attention is paid to the polarization of Λ_b^0 and the resonating particles coming from it. First, the theoretical framework concerning the symmetries and their role in physics are presented. Significant progress has been achieved in the development of a kinematic framework from which the angular distributions of the particles involved in the decays are calculated. A detailed study of the reconstruction and selection of the events have been exposed as well as the methodology used to extract the different polarizations from the angular distribution fits.

This study is performed using the 2011-2012 data recorded by the LHCb detector during the first run of the LHC.

Key Words : Decay Kinematics. LHCb. T violation. CP violation. Polarization. Cascade Decays.

Remerciements

No matter what one writes or how he writes, the words will be always unable to describe the feelings or even deliver the thanks to people who deserve.

My acknowledgments go to everyone who has contributed in some way to the development of this work. I start by thanking the former director of the LPC, Alain Falvard, for granting me the chance to prepare my thesis in good conditions. I also would thank the director Dominique Pallin for facilitating my stay in the LPC also.

I am so happy to make my PhD with LHCb team in the LPC. I would like to bring thanks to all the members of the team especially Ziad Ajaltouni who have worked hard with me so as to elaborate this work and make it in a good condition. In the past three years I have experienced the most beautiful moments, memories that I will never forget.

Also I am so happy to know and work with the Semileptonic group, so I would like to thank all the members of those groups especially Patrick Owen, Basem Khanji for their continuous support and help.

My friends in the LPC, Moustafa, Ibrahim, Marouen, Jan, Christus, Maxime, Boris, Giulio, Gabriella, Sara.. I want to thank you for your help and the time you have spent with me.

My friends in Le Mans, Fatima, Zainab, Alaa, Natalia, Rim, Haidar, and Amal, thank you for you support and help (for cooking also). Every now and then, a series of beautiful moments that I lived with you flash in my mind, reminding me how I was so lucky to have you in my life.

Giulio and Boris, I will never forget all the times we spent in the office eating and joking, those moments were the best moments of a so called working day.

Rima, even I lack the words, I would like to thank you for your continuous, very well appreciated support. I wish you all the best in your life.

My friends in Clermont, Noura, Wassim, Moujtaba, and Ali, thank you for you support. Every now and then, a series of beautiful moments that I lived with you flash in my mind, reminding me how I was so lucky to have you during the journey of my PhD and in my life.

Also, I am very grateful to Pascal Perret, Patrick Owen, Marina Artuso and Olivier Leroy for having accepted to be a part of my thesis jury.

I am to mention my brothers: Ahmad, Mahmoud, Hussein, and my sisters: Fatima, Zainab and Iman, since their presence has made me realize more and more their importance in my life. I can not just pass by such situation without

realizing how much my parents cared about me and how much they have sacrificed. Thanking them is not enough to express the enormous amount of gratitude that I have towards them. I feel how much they are happy to see that I has achieved something in this life.

So with all my greeting and kind regards....
Thank you all...

Contents

Introduction

Three discrete symmetries: Charge Conjugation **C**, Parity **P**, and the Time Reversal **T** have played an important role in particle physics and especially in the Standard Model. After the violation of both **C** and **P** symmetries, the scientists were shocked and started searching for new observable that restore the broken symmetry, they come to the famous **CP** symmetry (which is the product of **C** and **P**). In particle physics, **CP**-symmetry states that the laws of physics should be the same if a particle is interchanged with its antiparticle (**C** symmetry), and then its spatial coordinates are inverted ("mirror" or **P** symmetry). However, their happiness didn't last long, since in 1964, the **CP** violation has been discovered in the decays of neutral kaons and resulted in the Nobel Prize in Physics in 1980 for its discoverers James Cronin and Val Fitch.

It plays an important role both in the attempts in cosmology to explain the dominance of matter over antimatter in the present Universe, and in the study of weak interactions in particle physics.

CPT symmetry is a fundamental symmetry of physical laws under the simultaneous transformations of charge conjugation **C**, parity transformation **P**, and time reversal **T**. **CPT** is the only combination of **C**, **P**, and **T** that's observed to be an exact symmetry of nature at the fundamental level. The **CPT** theorem says that **CPT** symmetry holds for all physical phenomena, or more precisely, that any Lorentz invariant local quantum field theory with a Hermitian Hamiltonian must have **CPT** symmetry.

The **CPT** theorem for the first time appeared ,implicitly, in the Julian Schwinger's work in 1951 to prove the connection between spin and statistics [1]. In 1954, more explicit proofs were derived by Gerhart Luders and Wolfgang Pauli, so this theorem is sometimes known as the Luders–Pauli theorem [2][3]. During the same time, but independently, this theorem was also proved by John Stewart Bell[4]. All these proofs are based on the principle of Lorentz invariance and the principle of locality in the interaction of quantum fields.

The implication of **CPT** symmetry is that a "mirror-image" of the universe — with all objects having their positions reflected by an imaginary plane (corresponding to a parity inversion), all spin reversed (corresponding to a time inversion) and with all matter replaced by antimatter (corresponding to a charge inversion)— would evolve under exactly the same physical laws. The **CPT** transformation turns our universe into its "mirror image" and vice versa. **CPT** symmetry is recognized to be a fundamental property of physical laws. The main consequence is that X and $\bar{X}$ have the same mass.

N.B: $|X, \vec{r}, \vec{p}, \vec{s}, q > \longrightarrow$ **CPT** $|\bar{X}, -\vec{r}, \vec{p}, -\vec{s}, -q >$, where $\vec{r}, \vec{p}, \vec{s}, q$ are the position, momentum, spin vectors and the charge of the particles respectively.

In order to preserve this symmetry, every violation of the combined symmetry of two of its components (such as **CP**) must have a corresponding violation in the third component (such as **T**); in fact, mathematically, these are the same thing. Thus violations in **T** symmetry are often referred to as **CP** violations.

In 2002 Oscar Greenberg proved that **CPT** violation could implies the breaking of Lorentz symmetry [5]. This implies that any study of **CPT** violation includes also

Lorentz violation. The overwhelming majority of experimental searches for Lorentz violation have yielded negative results. However, the experiments in the **CERN** (CPLEAR) ([6] [7] [8]) and FERMILAB, in 1990, have given a clear evidence on the possibility to test the direct **T** independently away from the **CP**.

We are going in this thesis to test the discrete Time Reversal Symmetry **T** violation in the production of the beauty and charmed baryons, especially the $\Lambda_b^0 \to \Lambda_c^+ \mu^- \nu$ by searching for the **T** ODD observables. If the value of the observable is different from zero, this could reveal a sign for the time reversal violation.

This study is done with the help of the LHCb experiment at the CERN. We make benefit of the data taken in 2011 (7 TeV) and 2012 (8 TeV) during the first run in order to test the T violation. The first chapter gives a general ideas on the discrete symmetries (C, P, T) , how observables behave with each symmetry and the current status for each one. The last lines in this chapter are dedicated for the Time Reversal Symmetry, and the experiments that shed light on the violation of this symmetry.

The second chapter is reserved for the LHCb detector in which we scan into its different parts showing the importance and the advantages of choosing this detector in our study. Moreover, an overview of the LHCb software, data taking and their flow is also presented. The chapter 3 describes the kinematical studies performed, and a detailed presentation for the phenomenology of the $\Lambda_b^0 \to \Lambda_c^+ \mu^- \nu$ decay. The polarization formalism is presented and the angular distributions are stated allowing the introduction of the T-odd observables. Chapters 4 and 5 includes reconstruction of the events, special selections, comparison between Monte-Carlo and data, unfolding and finally correcting by the global efficiency of the LHCb detector.

The last part is dedicated for final fit to the data and interpretation of the results in which we extract the polarization vector of the different particles studied that are directly related to the Time Reversal Violation.

Finally, a general conclusion and our perspectives are stated.

Chapter 1

Theoretical Overview

Contents

In physics, a system is said to be invariant (or preserves symmetry) if its physical features are preserved or remains unchanged under some transformations.

A family of particular transformations could be continuous or discrete, and thus give rise to two types of symmetries: Continuous symmetries and discrete symmetries. With the development of quantum mechanics, in the 1920, symmetry principles came to play an even more fundamental role. In the latter half of the 20th century symmetry has been the most dominant concept in the exploration and formulation of the fundamental laws of physics. Today it serves as a guiding principle in the search for further unification and progress of the physical fields.

In this chapter, we are going to define symmetries in both classical and quantum mechanics.After that, we will present the different types of the discrete symmetries, their usage and finally the search for the discrete time reversal violation.

1.1 Symmetries in Classical Mechanics

A symmetry of a classical system is a transformation of the dynamical variable $\vec{x}(t)$, $\vec{x}(t) \Rightarrow \mathcal{R}[\ \vec{x}\ (t)]$, that leaves the action -denoted by $S = \int L dt$- unchanged. If follows that the classical equations of motion are invariant under the symmetry transformation.The symmetry can then be used to derive new solutions. Thus, if the laws of motion are invariant under spatial rotations, and if $\vec{x}(t)$ is a solution of the equations of motion, say an orbit of the earth around the sun, then the spatially rotated $\vec{x'}(t) = \mathcal{R}[\ \vec{x}\ (t)]$, is also a solution. This is interesting and useful.

Noether Theorem

Associated with each continuous symmetry is a conserved quantity, i.e. there is a physical quantity associated with the system which does not change if the system is symmetric under a certain transformation. This result is known as Noether's Theorem and is named after the German Physicist who discovered it, Emmy Noether. In other words one can list Noether Theorem as follows:

- Invariance under time reversal ⇔ Conservation of energy.

- Invariance under space translation ⇔ Conservation of Linear momentum.

- Invariance under space rotation ⇔ Conservation of the angular momentum.

1.2 Symmetries in Quantum Mechanics

In quantum theory, invariance principles permit even further reaching conclusions than in classical mechanics. In quantum mechanics the state of a physical system is described by a ray in a Hilbert space, $|\Psi\rangle$. A symmetry transformation gives rise to a linear operator, R, that acts on these states and transforms them to new states. Just as in classical physics the symmetry can be used to generate new allowed states of the system. However, in quantum mechanics there is a new and powerful twist due to the linearity of the symmetry transformation and the superposition principle. Thus if $|\Psi\rangle$ is an allowed state then so is R$|\Psi\rangle$, where R is the operator in the Hilbert space corresponding to the symmetry transformation R. So far this is similar to classical mechanics. However, we can now superpose these states, i.e., construct a new allowed state: $|\Psi\rangle + R|\Psi\rangle$, which is not the case in the classical mechanics.

Consider a transformation operator R ,being independent of time and linear (R$|\alpha\Psi\rangle = \alpha|\Psi\rangle$),applied on the state vector $|\psi\rangle$, the new vector state is :

$$|\tilde{\Psi}(t)\rangle = R|\Psi(t)\rangle$$

The evolution of the state $|\tilde{\Psi}(t)\rangle$ in time is given by the Schrödinger equation:

$$
\begin{aligned}
HR|\Psi(t)\rangle &= H|\tilde{\Psi}(t)\rangle \\
&= i\hbar\frac{\partial|\tilde{\Psi}(t)\rangle}{\partial t} \\
&= i\hbar\frac{\partial R|\Psi(t)\rangle}{\partial t} \\
&= Ri\hbar\frac{\partial|\Psi(t)\rangle}{\partial t} \\
&= RH|\Psi(t)\rangle \tag{1.1}
\end{aligned}
$$

The last equation shows that the operator R commutes with H : $HR = RH$ but never forget that R doesn't need to be hermitian, but on the contrary it must be unitary $R^\dagger R = 1$. This could be achieved by imposing the following condition:

$$
\langle\tilde{\Psi}|\tilde{\Psi}\rangle = \langle\Psi|\Psi\rangle
$$

1.3 Discrete Symmetries

In this section we are going to study three types of discrete symmetries: the parity, the charge conjugation and the time reversal.

1.3.1 Charge Conjugation

Definition

In physics, the C parity or charge parity is a multiplicative quantum number of some particles that describes their behavior under the symmetry operation of charge conjugation.
Charge conjugation changes the sign of all quantum charges (that is, additive quantum numbers), including the electrical charge, baryon number and lepton number, and the flavor charges like: strangeness, charm, beauty, topness and Isospin (I3). In contrast, it doesn't affect the mass, linear momentum or spin of a particle.

Formalism

Consider an operation C that transforms a particle into its antiparticle:

$$
C|\psi\rangle = |\bar{\psi}\rangle \tag{1.2}
$$

The projection of the states on it self (it is supposed that C doesn't change the mass), is given by:

$$
1 = \langle\psi|\psi\rangle = \langle\bar{\psi}|\bar{\psi}\rangle = \langle\psi|C^\dagger C|\psi\rangle \tag{1.3}
$$

From Dirac equation, C is an unitary operator and also hermitian, because its eigenvalues are ± 1,

$$
CC^\dagger = 1 \tag{1.4}
$$

By applying the C operator twice on the state $|\psi\rangle$:

$$
C^2|\psi\rangle = C|\bar{\psi}\rangle = |\psi\rangle \tag{1.5}
$$

we see that $C^2=1$ and $C=C^{-1}$. Putting all this together, we see that

$$
C = C^\dagger = C^{-1}
$$

which means that the charge conjugation operator is Hermitian and therefore a physically observable quantity.

Eigenvalues

For the eigenstates of charge conjugation,

$$C|\psi\rangle = \eta_C|\psi\rangle \tag{1.6}$$

As with parity transformations, applying C twice must leave the particle's state unchanged,

$$C^2|\psi\rangle = \eta_C C|\psi\rangle = \eta_C^2|\psi\rangle = |\psi\rangle \tag{1.7}$$

this means that the eigenvalues of the charge operator are $\eta_C = \pm 1$, the so-called C-parity or charge parity of the particle.

Multiparticle Systems

For a system of free particles, the C parity is the product of the C parties for each particle-antiparticle system. we have two cases:

- Bosons : There is an additional component due to the orbital angular momentum. Due to the angular part of the spatial wave function there will be a contribution by a phase factor of $(-1)^L$, where L is the angular momentum quantum number associated with $\mathbf{L}$.

$$C|\pi^+\pi^-\rangle = (-1)^L|\pi^+\pi^-\rangle \tag{1.8}$$

- Fermions: Two extra factors appears one comes from the spin part of the wave function, and the second from the exchange of a fermion by its antifermion.

$$C|f\bar{f}\rangle = (-1)^L(-1)^{S+1}(-1)|f\bar{f}\rangle = (-1)^{L+S}|f\bar{f}\rangle \tag{1.9}$$

1.3.2   Parity

Definition

In quantum physics, a parity transformation is the flip in the sign of one spatial coordinate $(\vec{r} \longrightarrow -\vec{r})$. In three dimensions, it is also commonly described by the simultaneous flip in the sign of all three spatial coordinates:

$$P : \begin{pmatrix} x \\ y \\ z \end{pmatrix} \Longrightarrow \begin{pmatrix} -x \\ -y \\ -z \end{pmatrix}$$

It can also be thought of as a test for chirality of a physical phenomenon, in that performing a parity inversion transforms a chiral phenomenon into its mirror image. A parity transformation on something achiral, on the other hand, can be viewed as an identity transformation. All fundamental interactions of elementary particles are symmetric under parity, except for the weak interaction, which is sensitive to chirality and thus provides a handle for probing it, elusive as it is in the midst of stronger interactions. In interactions which are symmetric under parity, such as electromagnetism in atomic and molecular physics, parity serves as a powerful controlling principle underlying quantum transitions.

Possible Eigenvalues

In quantum mechanics, space-time transformations act on quantum states (Wigner theorem). The parity transformation P is a unitary operator acting on states $|\psi(\vec{r}, t)\rangle$ as follows:

$$P|\psi(\vec{r}, t)\rangle = e^{i\frac{\phi}{2}}|\psi(-\vec{r}, t)\rangle$$

One must then have $P^2\psi(\vec{r},t)\rangle = e^{i\phi}|\psi(-\vec{r},t)\rangle$, since an overall phase is un-observable (ϕ is an arbitrary phase). The operator P^2, which reverses the parity of a state twice, leaves the space-time invariant, and so is an internal symmetry which rotates its eigenstates by phases $e^{i\phi}$. If P^2 is an element $e^{i\phi}$ of a continuous U(1) symmetry group of phase rotations, then $e^{-i\frac{\phi}{2}}$ is part of this U(1) and so is also a symmetry. In particular, we can define $P' = P\, e^{-i\frac{\phi}{2}}$, which is also a symmetry, and so we can choose to call P' our parity operator, instead of P. Note that $P'^2 = 1$ and so P' has eigenvalues ± 1.

Effect of Parity Transformation on some Observables

Here are some quantities that are affected by the parity operator Tab.(1.1):

observable	P(observable)
t	t
$\vec{r}$	-$\vec{r}$
$\vec{p}$	-$\vec{p}$
$\vec{L}$	$\vec{L}$
$\vec{s}$	$\vec{s}$

Table 1.1: Effect of Parity Transformation on some Observables.

Orbital Parity

The spherical harmonics have well defined parity in the sense that they are either even or odd with respect to reflection about the origin. Reflection about the origin is represented by the operator $P|\psi(\vec{r},t)\rangle = |\psi(-\vec{r},t)\rangle$. For the spherical angles, $\{\theta, \phi\}$ this corresponds to the replacement $\{\pi - \theta, \pi + \phi\}$. The associated Legendre polynomials gives $(-1)^{l+m}$, and from the exponential function we have $(-1)^m$, giving -together for the spherical harmonics- a parity of $(-1)^l$:

$$Y_\ell^m(\theta, \phi) \rightarrow Y_\ell^m(\pi - \theta, \pi + \phi) = (-1)^\ell Y_\ell^m(\theta, \phi)$$

This remains true for spherical harmonics in higher dimensions: applying a point reflection to a spherical harmonic of degree (l) changes the sign by a factor of $(-1)^l$.
This means that the orbital angular momentum determines the orbital parity . We can classify them into two categories:

- Even parity : l = 0,2,4,....etc

- Odd parity : l = 1,3,5,.....etc

Intrensic Parity of Particles

We can assign an intrinsic parity to each particle as long as nature preserves parity. Weak interactions don't conserve parity, but one can still assign a parity to any hadron by examining the strong interaction reaction that produces it, or through strong decays.

1.3.3   Time Symmetry

In theoretical physics, T-symmetry is a symmetry of physical laws under the time reversal transformation.

$$T : t \rightarrow -t$$

Lets start from Schrödinger equation and let us apply the time reversal operator T on the state $|\psi(\vec{r},t)\rangle$:
$$T|\psi(\vec{r},t)\rangle = |\psi'(\vec{r},-t)\rangle$$

$$TH|\psi(\vec{r},t)\rangle = i\hbar\frac{\partial|\psi(\vec{r},-t)\rangle}{\partial(-t)} = -i\hbar\frac{\partial|\psi(\vec{r},-t)\rangle}{\partial t} \qquad (1.10)$$

Note the negative sign, which means that the Schrödinger equation is not invariant under this transformation. In order to recover the quantum mechanics under time reversal, we should do a transformation to the wave function as well, namely:

$$T|\psi(\vec{r},t) = \psi^*(\vec{r},-t)$$

In this case we are going to divide the time operator into two parts: one for complex conjugation K (being anti-unitary) and another unitary U

$$T = KU$$

N.B: Indeed, T is Anti-linear and unitary(weinberg, Ch 1). It is

$$TH|\psi(\vec{r},t)\rangle = -i\hbar\frac{\partial|\psi^*(\vec{r},-t)\rangle}{\partial(-t)} = +i\hbar\frac{\partial|\psi^*(\vec{r},-t)\rangle}{\partial t} \qquad (1.11)$$

and by setting the $|\psi^*(\vec{r},-t)\rangle = T|\psi(\vec{r},t)\rangle$ one can see that the Schrödinger equation will restore its broken symmetry.

Remark:

- T is not linear operator : $|\psi(t)\rangle = c_1|\psi(t)\rangle_1 + c_2|\psi(t)\rangle_2 \rightarrow T|\psi(t)\rangle = c_1^*|\psi^*(t)\rangle_1 + c_2^*|\psi^*(t)\rangle_2 \neq c_1|\psi(t)\rangle_1 + c_2|\psi(t)\rangle_2$

- T ,being not hermitian,is not an observable, this means that it is not measured directly.

Here are some observables under the time reversal transformation Tab.1.2:

observable	T(observable)
t	-t
$\vec{r}$	$\vec{r}$
$\vec{p}$	$-\vec{p}$
$\vec{L}$	$-\vec{L}$
$\vec{E}$	$\vec{E}$
$\vec{B}$	$-\vec{B}$
$\vec{s}$	$-\vec{s}$

Table 1.2: Some observables under the time reversal transformation.

1.3.4   CPT Theorem

The CPT theorem says, roughly, that every relativistic quantum field theory has a symmetry that simultaneously reverses charge (C), reverses the orientation of space (or 'parity,' P), and reverses the direction of time (T).

The CPT is well-defined only under the following assumptions:

- The theory is Lorentz invariant.

- The vacuum is Lorentz invariant.

- The energy is bounded below.

A consequence of this derivation is that a violation of CPT automatically indicates a Lorentz violation.

When the above hold, quantum theory can be extended to a Euclidean theory, defined by translating all the operators to imaginary time using the Hamiltonian formalism.

1.4 Violation of the Discrete Symmetries

1.4.1 Parity Violation

For charged strange mesons we have find two different decays:

$$\theta^+ \rightarrow \pi^+ + \pi^0$$

$$\tau^+ \rightarrow \pi^+ + \pi^+ + \pi^-$$

The intrinsic parity of a meson is $P = -1$ (Pseudo-scalar), and parity is a multiplicative quantum number. Therefore, the two final states have different parity ($P = +1$ and $P = -1$, respectively). It was thought that the initial states should also have different parities, and hence be two distinct particles. However, with increasingly precise measurements, no difference was found between the masses and lifetimes of each, respectively, indicating that they are the same particle. This was known as the $\theta - \tau$ puzzle. It was resolved only by the discovery of parity violation in weak interactions. Since the mesons decay through weak interactions, parity is not conserved, and the two decays are actually decays of the same particle, now called the K^+.

Neutrinos Violate P-Symmetry
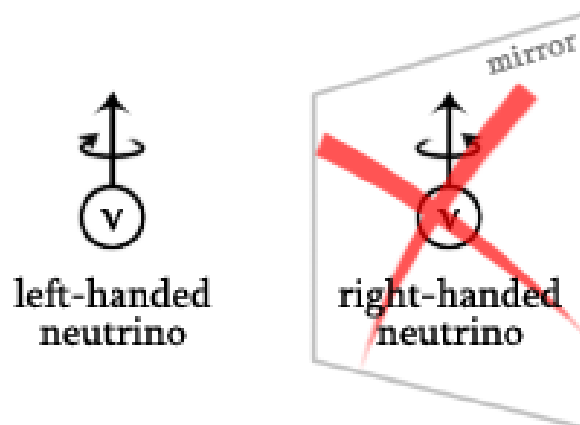
Figure 1.1: parity-violation.

As we have known before that P-symmetry is parity symmetry: this means that it transforms every object into its mirror image, so left becomes right and vice versa,that is the helicity of any particle will change sign ($\chi = \frac{\vec{s} \cdot \vec{p}}{|\vec{p}|}$). Now lets come to the neutrinos: if you flip a left-handed neutrino, we will have a right-handed neutrino. But the problem is that till now no right handed neutrinos have been observed, but in the same time we have seen plenty of the left handed neutrinos. In this case, mirroring causes the laws of physics to change: this violates the parity-symmetry(Fig.1.1).
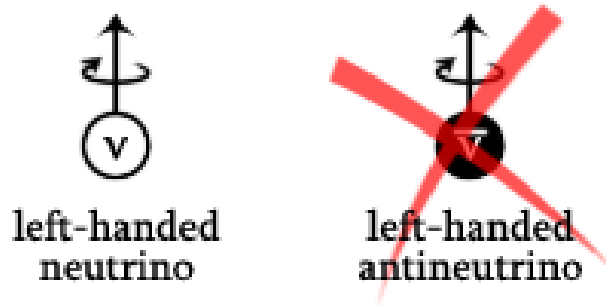
Figure 1.2: charge-violation.

1.4.2 C-Violation

Neutrinos Violate C-symmetry

By taking the charge conjugation of the left handed neutrino ν, we surely will get a left handed anti-neutrino $\bar{\nu}$. But again the problem is that there is no observation for a left handed anti-neutrino: this means the C-symmetry is also violated(Fig. 1.2).

1.5 CP-Symmetry

After the discovery of the C and P symmetry violations, the physics community was so excited and anxious (Wigner, 1960 "Symmetry Principles"). After that, a new thought comes to the minds of the physics that time: the CP- symmetry, a combination of both C and P symmetry (Landau,A.Salom, Lee-Yang). They say that maybe the right way for defining the symmetry is not C and P separately , but their combination CP. For a while, CP seemed to fix the more-symmetrical world of neutrinos (and the weak force): N.B: $\vec{j} = \rho \cdot \vec{v} \Rightarrow CP(\vec{j}) = -(-\rho) \cdot (-\vec{v}) = +\rho \cdot \vec{v} = \vec{(j)}$
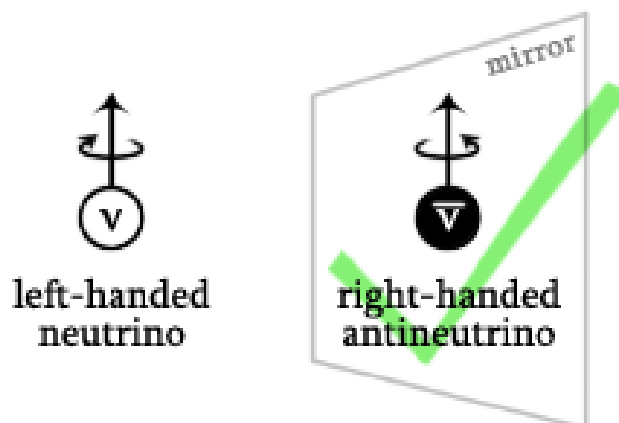
Figure 1.3: CP-symmetry.

If you take both the mirror and charge conjugation of a left-handed neutrino, you get a right-handed anti-neutrino, which does exist(Fig.1.3)!

CP symmetry have restored the broken C and P symmetries. Particles behaved according to CP symmetry combined together. All seemed right and symmetrical again. There were no surprises until the violation of CP symmetry was discovered.
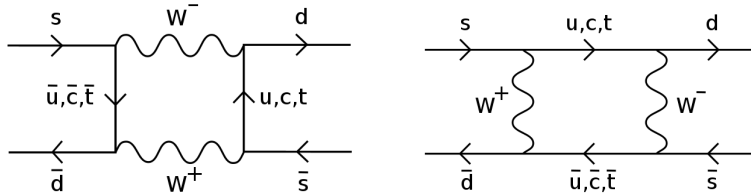
Figure 1.4: The two box diagrams above are the Feynman diagrams providing the leading contributions to the amplitude of $k^0 - \bar{k}^0$ oscillation.

1.6   CP Violation in Neutral Kaons

Direct CP Violation

CP violation is the violation for the standard CP-symmetry which was first discovered in 1964. It is linked to the fact that the neutral kaons transform to their anti-particles (each quark transform into its anti quark) and vise versa. But such transformation don't occur with exactly the same probability in both directions: this was called a CP violation(Fig.1.4).

$$K^0_{L(2)} \longrightarrow \pi^+\pi^- \tag{1.12}$$

The K^0 and $\bar{K}^0$ states have strangeness equal to -1 and 1 respectively, as their quark content is $\bar{s}d$ and $\bar{d}s$. These states have no a definite value of the CP parity, but they transform one into another under the action of this transformation in the next way

$$CP|K^0\rangle = +|\bar{K}^0\rangle$$

We can construct eigenstates with a definite CP transformation by combining K^0 and $\bar{K}^0$

$$K_1 = \frac{1}{\sqrt{2}}(K^0 + \bar{K}^0), K_2 = \frac{1}{\sqrt{2}}(K^0 - \bar{K}^0)$$

with $CP|K_1\rangle = +|\bar{K}_1\rangle, CP|K_2\rangle = -|\bar{K}_2\rangle$.

The strange particles can decay only via weak interactions as strong and electromagnetic interactions preserve the strangeness quantum numbers. If we assume that weak interactions are symmetric under CP violation as strong and electromagnetic interactions are, then the $K_{1(2)}$ states must decay into an state with even(odd) CP parity. Taking into account that the main decay mode of K^0 -like states is $\pi\pi$ and the fact that a two pion state with charge zero and orbital angular momentum zero is always CP even, the decay $K_1 \to \pi\pi$ is possible (as well as $K_2 \to \pi\pi\pi$) but $K_2 \to \pi\pi$ is impossible. However, in 1964 it was observed the decay of K_L mesons, that were identified with K_2, in states of two pions [9]. This meant that these transitions directly violated CP since an odd state decayed into an even state.

However, K_L and K_S are not the K_1 and the K_2 themselves, in fact they are similar to them but up to a factor ([10]) :

$$|K_S\rangle = \frac{1}{\sqrt{1 + |\epsilon|^2}}(|K_1 - \epsilon\bar{K}_2), |K_L\rangle = \frac{1}{\sqrt{1 + |\epsilon|^2}}(|K_2 - \epsilon\bar{K}_1), \epsilon \approx 2.2 \times 10^{-3} \tag{1.13}$$

CP Violation in the Standard Model

"Direct" CP violation is allowed in the Standard Model if a complex phase appears in the (CKM) matrix describing quark mixing, or the (PMNS) matrix describing neutrino mixing. A necessary condition for the appearance of the complex phase is the presence of at least three generations of quarks (if fewer

generations are present, the complex phase parameter can be absorbed into the redefinition of the quark fields).

Consider any given particles a and b, and their antiparticles $\bar{a}$ and $\bar{b}$. Now consider the processes $a \rightarrow b$ and the corresponding antiparticle process $\bar{a} \rightarrow \bar{b}$, and denote their amplitudes M and $\bar{M}$ respectively. Before CP violation, these terms must be the same complex number. We can separate the magnitude and phase by writing $M = |M|e^{i\theta}$. Note that $\bar{M}$ contains the conjugate matrix to M, so it picks up a phase term $e^{-i\phi}$. Now we have:

$$M = |M|e^{i\theta}e^{i\phi} \tag{1.14}$$

$$\bar{M} = |M|e^{i\theta}e^{-i\phi} \tag{1.15}$$

However, physically measurable reaction rates are proportional to $|M|^2$, so far nothing is different. However, consider that there are two different routes (e.g. intermediate states) for $a \rightarrow b$. Now we have:

$$M = |M_1|e^{i\theta_1}e^{i\phi_1} + |M_2|e^{i\theta_2}e^{i\phi_2} \tag{1.16}$$

$$\bar{M} = |M_1|e^{i\theta_1}e^{-i\phi_1} + |M_2|e^{i\theta_2}e^{-i\phi_2} \tag{1.17}$$

Some further calculation gives:

$$|M|^2 - |\bar{M}|^2 = 4|M_1||M_2|\sin(\theta_1 - \theta_2)\sin(\phi_1 - \phi_2) \tag{1.18}$$

Thus, we see that a complex phase gives rise to processes that proceed at different rates for particles and antiparticles, and CP is violated.

1.7 Searching For Discrete Time Reversal Violation

Why search for T violation? It is the counterpart of the CP, because of the invariance of the CPT theorem. CPT is invariant, but CP is violated, hence T should be violated.

1.7.1 Electric Dipole Moment of the Neutron

To date, every measurement of the neutron electric dipole moment (EDM) has given a value of zero, but there is a good reason to believe it is actually a very small, but non zero, value 2.9×10^{-26} ecm.
A non-zero electric dipole moment of the neutron (or any fundamental particle) would be a violation of parity (P) and time-reversal (T) symmetry [11]. This can be explained by the following picture: if the neutron has a finite EDM, the charge distribution is reversed under P; it is unchanged under T, but the orientation of a particle is specified by its spin, which is unchanged under P, but reverses under T (Fig.1.5). Therefore, if the EDM is not zero, then P and T are not conserved.

Assuming the combined operation CPT is invariant, then a measurement of T violation implies CP is also violated. This has significant consequences for cosmology. Present theories of particle physics and cosmology predict that our Universe was formed with equal parts matter and antimatter, which should by now have annihilated into radiation. To explain the dominance of matter, CP violation must exist.
CP violation has been observed in accelerator experiments studying the decays of K and B mesons, but not at a level which can explain the matter-antimatter asymmetry of the Universe. Therefore, in order to explain why the Universe exists,

we need to study other CP violating systems such as the neutron EDM. This also provides a way to test theories of New Physics, as super symmetry (for example) predicts a neutron EDM at a level of 10^{-28} ecm, above the standard model prediction. Theories such as additional Higgs fields, and left-right symmetric models also predict a neutron EDM at a level which will be probed by new experiments.
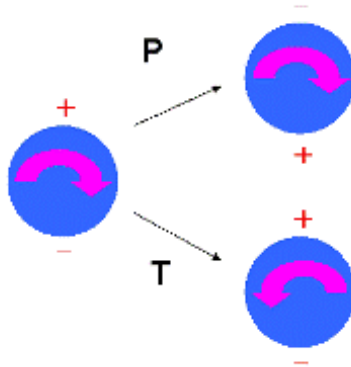
Figure 1.5: The neutron EDM is reversed by the parity operation. It is unchanged by time-reversal, but this reverses the spin, which specifies the orientation, so a non zero EDM would be a violation of both T and P symmetry.

Neutron EDM measurements have also shown that CP is conserved to a remarkable degree by the strong interaction. This would appear to require significant fine tuning of the relevant QCD parameter; but it can also be explained by a hypothetical particle, the axion, which would effectively cancel the CP violating term in the QCD Lagrangian. Axions are also a possible dark matter candidate.

1.7.2 Experimental situation of the nEDM

The current limit on the neutron EDM is $d < 2.9 \times 10^{-26}$ecm ([12]-[13]-[14]), set by the nEDM experiment. This was measured at the Institute Laue-Langevin using room temperature apparatus, by storing a large number of ultra-cold neutrons in a storage cell in an electric and magnetic field. The Larmor spin precession frequency was measured to a high precision for parallel and anti-parallel fields. A shift in the precession frequency between these two measurements, would be a sign of the neutron EDM.

A significant systematic error is caused by any drift in the magnetic field between measurements; as the neutron has a non-zero magnetic dipole moment, this also produces a shift in the precession frequency. The nEDM group used atomic mercury spectrometer to monitor the magnetic field to nano-Tesla precision.

By 1999 the experiment had reached the best sensitivity which could be achieved with the apparatus, and the collaboration started design and construction of the cryoEDM project (Fig.1.6).

The cryoEDM experiment was formed to further improve the neutron EDM limit set by nEDM, and maybe measure a non-zero value. The improvement in sensitivity will be achieved by producing, storing and detecting ultra-cold neutrons (UCN) inside super fluid helium. This allows a greater number of UCN to be produced by down-scattering a cold neutron beam. A further improvement comes from operating at a higher electric field which can be achieved in the super-fluid.

Figure 1.6: The cryoEDM apparatus at the ILL, Grenoble. The neutron beam enters on the right, and the storage cell is at the center of the cylinder on the left, surrounded by several layers of magnetic shielding.
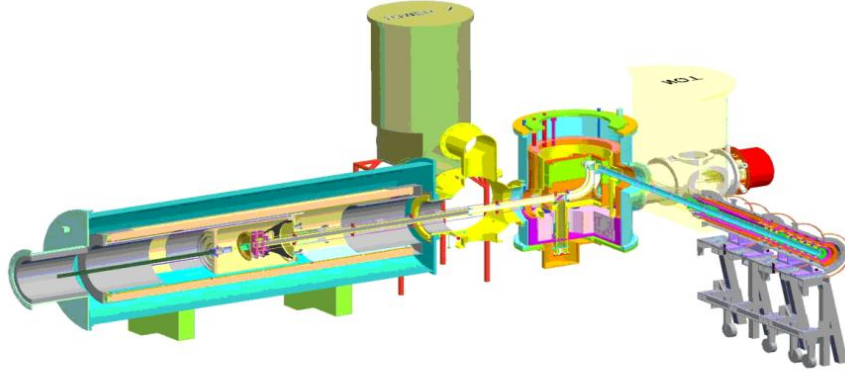
1.7.3   Neutron's β Decays

In 1957, Jackson, Treiman, Wyrld have studied the violation of the Time Reversal symmetry in the neutron β decay. They have parametrized the angular correlations between the different products of the β decay.
The differential cross section is given by:

$$d\sigma \approx \vec{s_n} \cdot (A\vec{p_\nu} + B\vec{p_e} + D\vec{p_e} \times \vec{p_\nu}) \tag{1.19}$$

where $\vec{p_e}$ and $\vec{p_\nu}$ are the momenta of the electron and the neutrino respectively, $\vec{s_n}$ is the neutron spin.
The correlation $D\vec{s_n} \cdot \vec{p_e} \times \vec{p_\nu}$ is odd by time reversal, and hence could be used as a method for searching for time reversal violation, taking into account the final state interactions.
Any non zero value of the coefficient D is an indication for time reversal violation. Until this moment, there is no prove or report that find out a non zero value for the D coefficient. The prediction of the Standard Model is D$< 10^{-12}$. All the values above the final state interaction effects (for neutrons $D_{FS} = 10^{-5}$) are a sign of new physics.

1.7.4   Kabir Parameter [15]

Since the CP symmetry is violated in the weak interactions, T should also be violated due to the CPT invariance. In 1998, CPLEAR experiment located at CERN [6] reported the first direct observation of the time reversal violation in the neutral kaon system. In fact this observation relies on comparing decay rates of neutral kaons that were produced as $\bar{K}_0$ and K_0, and are decaying into the charge conjugate final states $\bar{f}$ and f.
By definition, time reversal violation is directly related to Kabir asymmetry factor which is time dependent and given by:

$$A_T = \frac{|\langle K_0^{out}(t_f)|\bar{K}_0^{in}(t_i)\rangle|^2 - |\langle \bar{K}_0^{out}(t_f)|K_0^{in}(t_i)\rangle|^2}{|\langle K_0^{out}(t_f)|\bar{K}_0^{in}(t_i)\rangle|^2 + |\langle \bar{K}_0^{out}(t_f)|K_0^{in}(t_i)\rangle|^2} \tag{1.20}$$

Each non zero value of A_T represents a sign for the violation of Time symmetry. CPLEAR produces the system of neutral kaons from proton-anti proton annihilation process via the following reactions :

$$p\bar{p} \longrightarrow K^-\pi^+K^0 p\bar{p} \longrightarrow K^+\pi^-\bar{K}^0 \tag{1.21}$$
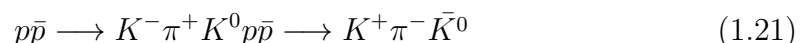
The strangeness of the neutral kaon is tagged by the accompanying charged kaon. In the case of semileptonic decays, the strangeness of the neutral kaons may also be tagged at the decay time ($\Delta S = \Delta Q$ rule). The semi-semileptonic decays, $K^0 \to e^+\pi^-\nu$, and the $\bar{K}^0 \to e^-\pi^+\bar{\nu}_e$ are characterized by $\Delta S = \Delta Q$ whereas $K^0 \to e^-\pi^+\bar{\nu}_e$, and the $\bar{K}^0 \to e^+\pi^-\bar{\nu}_e$ are characterized by $\Delta S = -\Delta Q$, which means either (i) there is an explicit violation of the $\Delta S = \Delta Q$ or (ii) the oscillations between K^0 and $\bar{K}^0$ produce a final state that violates $\Delta S = \Delta Q$. The CPLEAR experimental asymmetry is given by:

$$A_T^{exp} = \frac{\bar{R}_+(\delta t) - R_-(\delta t)}{\bar{R}_+(\delta t) + R_-(\delta t)} \tag{1.22}$$

where $\bar{R}_+(\delta t)$ and $R_-(\delta t)$ are the transition probabilities of K^0 to $\bar{K}^0$ and vice versa. The mean value of the of A_T^{exp} is found to be $(6.6 \pm 1.6) \cdot 10^{-3}$ which is a clear indication for time violation.

1.7.5 $K_L \to \pi^+\pi^- e^+ e^-$ decay at KTeV

The first observation of the CP violation in the decay $K_L \to \pi^+\pi^- e^+ e^-$ was announced by the collaboration KTeV [16]. Another important asymmetry was observed in the distribution of the product $\cos\phi\sin\phi$, where ϕ is the angle between the planes formed by $\pi^+\pi^-$ and e^+e^- in the K_L rest frame. This observable is odd by time reversal symmetry.
After the acceptance corrections, the global asymmetry was found to be $13.6 \pm 2.5(stat) \pm 1.2(sys)\%$ [17] which is compatible with the theoretical predictions (14% [18]). This asymmetry implies a violation of the time reversal symmetry.
Since the electromagnetic interactions can modify the ϕ distribution and thus can simulate a T-odd asymmetry, the KTeV collaboration examine if this asymmetry is due to the final state interaction but this claim proved controversial.

1.8 BaBar and Time Reversal Violation

The BaBar collaboration has made the first direct observation of time-reversal (T) violation in $B^0 - \bar{B}^0$ oscillation process. The results are in agreement with the basic tenets of quantum field theory, and reveal differences in the rates at which the quantum states of the $B^0 - \bar{B}^0$ mesons transform into one another [19]. BaBar reported the direct observation of the T violation in the B meson system, through the exchange of the initial and final sates in transitions that can only be connected by a T-symmetry transformation. The method is described in Ref.[20], based on the concepts proposed in Ref.[21] and further discussed in Refs. ([22],[23]).

1.9 Search for Time Reversal Violation in the Weak Semileptonic $\Lambda_b^0 \to \Lambda_c^+ \mu^- \nu_\mu$ Decays

The first channel used to test the Time Reversal Symmetry, (T) in LHCb experiment, is the $\Lambda_b^0 \longrightarrow \Lambda J/\Psi$ decay channel. We used the Jacob-Wick helicity formalism [24] which defines the decay amplitudes involving the spin of the particles. In this study we extend the same formalism to the semi-semileptonic decays of the heavy baryons,$\Lambda_b^0 \to (\Lambda_c^+ \to \Lambda\pi)(W^* \to \mu^-\nu_\mu)$ and a quasi two body approach is used, due to the presence of a virtual W^*-boson.
Stressing on these decays comes from the fact that semileptonic decays are abundant B-decays and so could be used to measure both the life-time and the polarization of the Λ_b^0 with high statistics.
These decays allow a direct test of T, by testing the polarization vector of the

hyperon and the resonating particles.

Our study is organized as follows: recalling the basics of the helicity formalism, then the proposed decays are respectively detailed, emphasizing the angular distributions of their decay products, enabling a direct testing of TR symmetry.

In this chapter we have presented the theoretical part of this PhD. We introduced the different discrete symmetries; charge conjugation C, parity P, time reversal T, and also their combination CP and T in both classical and quantum mechanics. Since T is an anti-unitary operator, it is impossible to associate a physical observable to T (on contrary to C and P). So we are going to search for time reversal violation through out its effects on physical observables; especially the T-odd ones. On the upcoming chapters, we are going to discus how to construct T-odd observables, that could give an evidence for a possible T violation. In the next chapter we will talk about the Large Hadron Collider and the LHCb detector.

Chapter 2

The Collider and The Detector

Contents

LHCb is an experiment designed to study CP violation and other rare phenomena in B meson decays with high precision [25]. The goal of LHCb is to check the theoretical predictions made in the Standard Model about quark mixing and to search for hints of new physics.

2.1   Large Hadron Collider

The European Organization for Nuclear Research (CERN) has done a great attempt and a giant step in building the world's largest and most powerful particle Collider from 1998 to 2008, known by the Large Hadron Collider (LHC). It lies in a tunnel 27 kilometers (17 mi) in circumference, at a depth ranging from 50 to 175 meters (164 to 574 ft) beneath the Franco-Swiss border near Geneva, Switzerland (Fig.2.1). This machine has been designed for proton-proton (p-p) collision. The collisions take place in four main points called the interaction points, where the detectors are located. There are four main experiments at the LHC:

- i) The ATLAS (A Toroidal LHC ApparatuS) and CMS (Compact Muon Solenoid) detectors are general purpose experiments, mainly designed to search for the Higgs boson and to shed light on new theories by searching for direct evidence of physics beyond the Standard Model.

- ii) ALICE (A Large Ion Collider Experiment) is optimized to study heavy-ion (Pb-Pb nuclei) collisions at a center of mass energy of 2.76 TeV per nucleon. ALICE is focusing on the physics of strongly interacting matter at extreme energy densities and searching for Quark Gluon Plasma (QGP).

- iii) LHCb (Large Hadron Collider beauty) to check the theoretical predictions made in the standard model about quark mixing and to search for hints of new physics. It is a specialized b-physics experiment measuring the parameters of CP violation in the decays of b-hadrons, also in charm physics , electroweak and heavy ions physics.

On November 20, 2009 proton beams were successfully circulated with the first recorded proton-proton collisions occurring three days later at the injection energy of 450 GeV per beam. On March 30, 2010, the first collisions took place between two 3.5 TeV beams, setting a world record for the highest-energy man-made particle collisions, and the LHC began its planned research program.
When running at 6.5 TeV (full design 7 TeV) per beam in early 2015, the protons are accelerated from 450 GeV to 6.5 TeV, giving a total collision energy of 13 TeV. Rather than continuous beams, the protons are bunched together, into up to 2,808 bunches, with 115 billion protons in each bunch, so that interactions between the two beams will take place at discrete intervals never shorter than 25 nanoseconds (ns) apart, providing a bunch collision rate of 40 MHz. However it was operated with fewer bunches when it is first commissioned, giving it a bunch crossing interval of 50 ns(2.1).
The design luminosity of the LHC is $10^{34} cm^{-2} s^{-1}$. Before being injected into the main accelerator, the particles are accelerated by a series of systems that successively increase their energy. The first one is the linear particle accelerator (LINAC 2) that generates 50-MeV protons, feeding the Proton Synchrotron Booster (PSB). There, the protons after that are accelerated to 1.4 GeV and injected into the Proton Synchrotron (PS), where they are again accelerated to 26 GeV. Finally, the Super Proton Synchrotron (SPS) is used to further increase their energy to 450 GeV before they are at last injected (over a period of several minutes) into the main ring. Here the proton bunches are accumulated, accelerated (over a period of 20 minutes) to their peak energy, and finally circulated for few hours while collisions occur at the four intersection points.
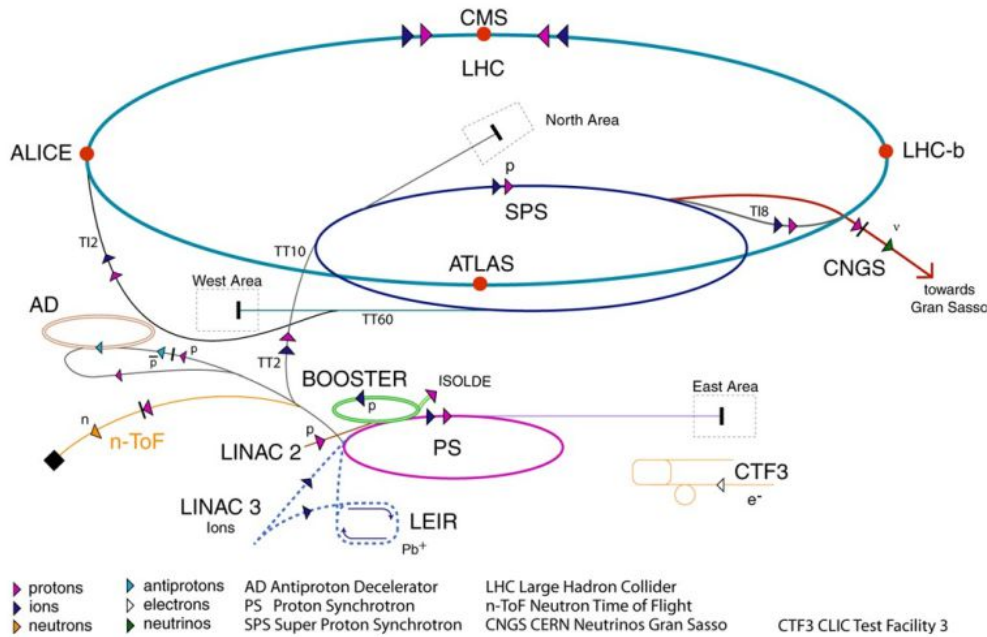
Figure 2.1: CERN Complex Accelerator (CERN web page).

2.1.1 Production of B-mesons

The analysis of B meson decays is interesting for the study of CP violation. In high energy pp-interactions the production mechanisms for heavy quarks are processes involving gluons and partons [26]. The relatively high mass of the b-quark allows for perturbative (and non-perturbative) QCD calculations to make predictions about $B\bar{B}$ production and decay at LHC conditions.

From first order calculations it is already clear that LHC will be by far the most copious source of B mesons. The leading order Feynman diagrams of heavy-flavor production are typically categorized in three different types [27]. One of them, pair production, is shown in (Fig.2.2). The others are flavor excitation, with one gluon and one quark in the initial and final state ($Qg \rightarrow Qg$) and gluon splitting ($gg \rightarrow gg$, creating an additional $Q\bar{Q}$ pair in the parton shower).
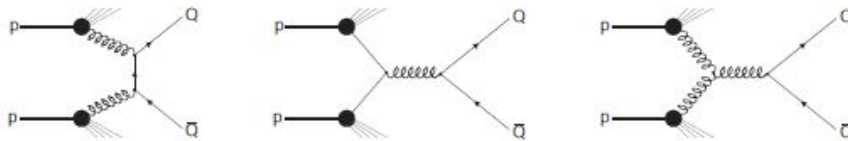
Figure 2.2: Feynman diagrams of the first order pair production mechanisms of heavy quarks at the LHC.

The production cross sections of these leading order processes are calculated by PYTHIA using the CTEQ4 particle distribution functions [28] (i.e. the proton structure functions as determined at HERA). This program includes elastic and diffractive proton interactions in order to obtain a realistic estimate of the background processes. The accuracy of these calculations is limited due to higher order corrections and non-perturbative hadronization effects. Both the b and the $\bar{b}$ recombine with other quarks during the hadronization process, which means that a variety of b hadron species will be produced. The broad longitudinal momentum distribution of the gluons in the protons combined with their relatively low transverse momentum, results in the production of boosted b and $\bar{b}$ hadrons (each carrying one quark from the produced $b\bar{b}$ pair) along the beam axis in either the forward or the backward cone. This is demonstrated in (Fig.2.3) where the polar

angles of the b and $\bar{b}$ hadrons calculated with the PYTHIA event generator are shown.

Figure 2.3: Polar angles of the b and $\bar{b}$ hadrons, calculated with the PYTHIA event generator.

2.2 LHCb : Beauty Detector

The goal of LHCb is to check the theoretical predictions made in the standard model about quark mixing CP violations and to search for hints of new physics. LHCb is a specialized b-physics experiment, that is measuring the parameters of CP violation 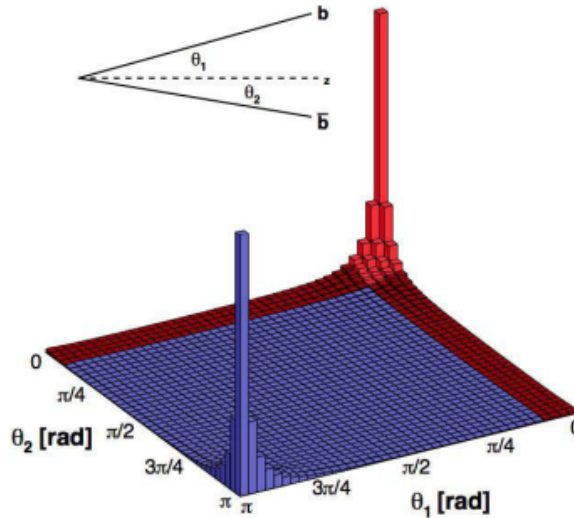in the decays of b-hadrons (heavy particles containing a bottom quark). Such studies can help to explain the Matter-Antimatter asymmetry of the Universe. The detector (Fig.2.4) is also able to perform measurements of production cross sections and electroweak physics in the forward region. Approximately 1160 people from 72 scientific institutes, representing 16 countries, form the collaboration who built and operate the detector. The experiment is located at point 8 on the LHC tunnel close to Ferney-Voltaire, (France) just over the border from Geneva. In this chapter, the LHCb experiment will be described detailing how the decay vertices are reconstructed, how the momentum/energy of the final particles and their tracks are measured and how those particles are identified. Also, in this chapter the LHCb sub-detectors will be explained as well as the hardware and the software triggers. Last but not least, the LHCb performance during the 2011-2012 run period will be discussed.

The fact that the two b-hadrons are predominantly produced in the same forward cone is exploited in the layout of the LHCb detector. The LHCb detector is a single arm forward spectrometer with a polar angular coverage from 10 to 300 milliradians (mrad) in the horizontal and 250 mrad in the vertical plane (Fig.2.4). The $b\bar{b}$ cross-section, $75.3 \pm 5.4 \pm 13.0\,\mu$b at 7 TeV, is dominated by configurations in which one of the partons has energy more than other.

2.2.1 Data taking periods and operating conditions

LHCb recorded its first pp collisions at $\sqrt{s} = 0.9$ TeV injection energy with the end of 2009. These data were used to finalize the commissioning of the sub-detector systems and the reconstruction software and to perform a first alignment and calibration of the tracking, the calorimeter and the particle identification (PID) systems. In this period, the VErtex LOcator (VELO) was left in the open
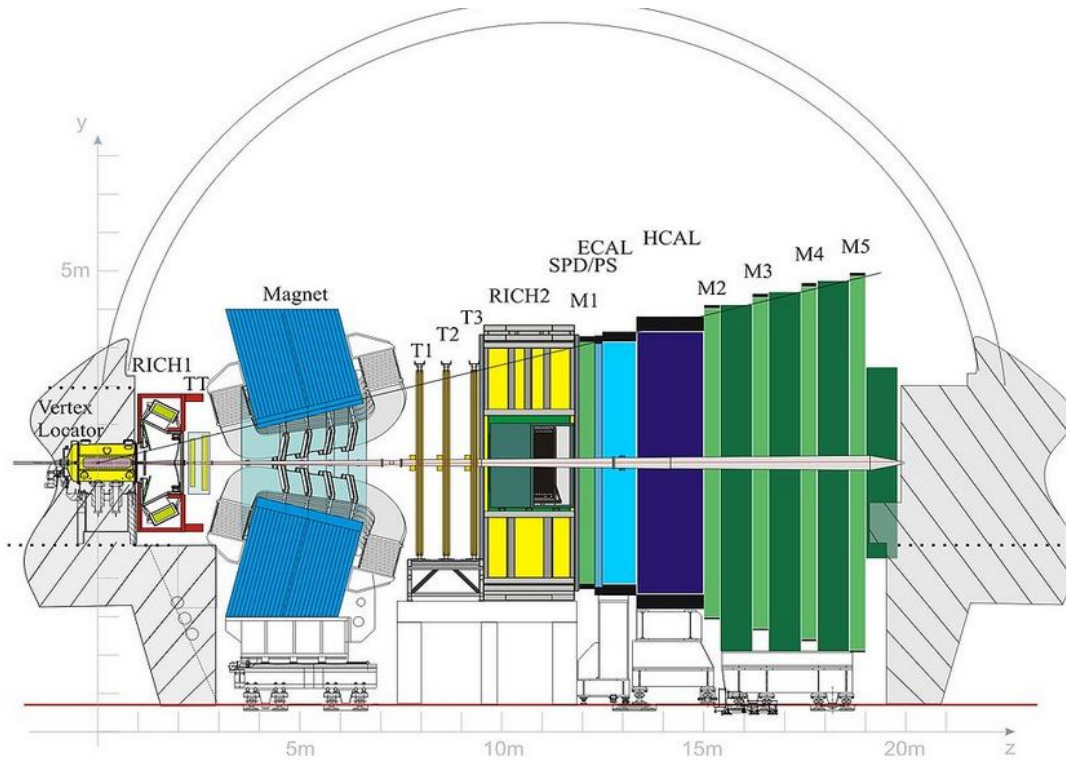
Figure 2.4: LHCb detector(LHCb web page).

position, due to the larger aperture required at lower beam energies. The operating conditions changed rapidly due to the ramp-up of the LHC luminosity. A critical parameter for LHCb performance is the pile-up, defined as the average number of visible interactions per beam-beam crossing. While the highest luminosity in 2010 was already 75 percent of the LHCb design luminosity, the pile-up was much larger than the design value due to the low number of bunches in the machine. It was demonstrated that the trigger and reconstruction work efficiently under such harsh conditions with increased detector occupancy due to pile-up, and that the physics output was not compromised. The LHC beam energy was 3.5 TeV during 2010 and 2011. In 2012 the LHC beam energy was increased to 4 TeV. LHCb took data at a luminosity of $4 \times 10^{32} cm^{-2} s^{-1}$, twice the LHCb design luminosity. The LHC delivered stable beams for about 30 percent of the operational year (Fig.2.5). The integrated luminosity recorded by LHCb was 38 pb^{-1} in 2010, 1.11 fb^{-1} in 2011 and 2.08 fb^{-1} in 2012. The analysis presented in this thesis uses the data collected in 2011 and 2012.

2.2.2 LHCb luminosity

The number of selected events of a given process per unit of time, denoted as $\frac{dn}{dt}$, is given by:

$$\frac{dn}{dt} = \sigma L \epsilon$$

where σ is the process cross section, L is the instantaneous luminosity and ϵ is the total efficiency accounting for : detector acceptance, track reconstruction and selection efficiency. Hence, the determination of the luminosity is an essential cornerstone for the measurement of any cross section. The average instantaneous luminosity of two colliding bunches can be expressed as:

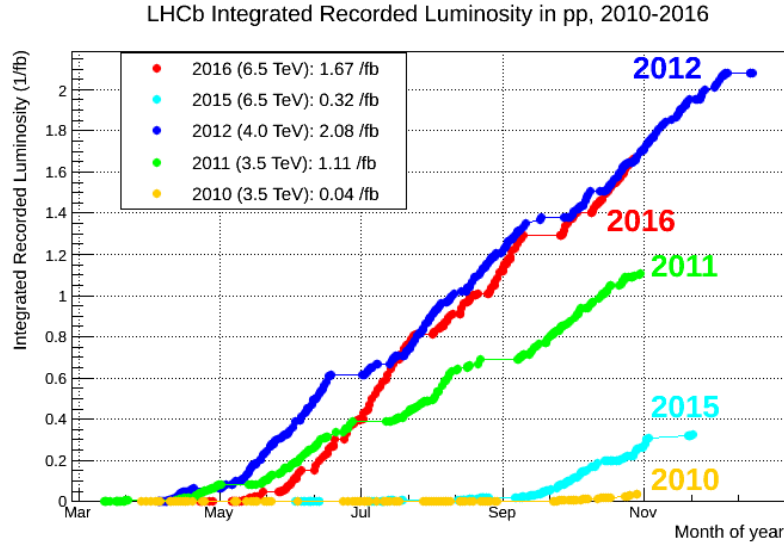$$L = \frac{f N_1 N_2}{4\pi \sigma_x \sigma_y}$$

Figure 2.5: The LHCb integrated luminosity recorded over the run periods(LHCb web page).

where f is the revolution frequency (11245 Hz at the LHC), N1 and N2 are the number of protons in the two bunches, σ_x and σ_y are the transverse sizes of the bunch at the interaction point along the x and y axis respectively.

At LHCb there are two methods used to determine the absolute luminosity [29]:

- i) The Van der Meer scan: The beams are moved in transverse directions in order to investigate the beam transverse profiles counting the interaction rate as a function of the beam offsets.

- ii) The beam-imaging gas method: The high acceptance of the VELO around the interaction point is used to reconstruct beam-gas vertices produced by the collision of protons. The positions of the beam-gas interactions are used to determine beam angles and profiles [30].

Combining the two methods, the absolute luminosity can be determined with a relative precision of 3.5%, this allows to calculate a reference cross section of visible interactions.

2.2.3   Vertex LOcator: The VELO

The VErtex LOcator (VELO) is the sub detector closest to the interaction point. It consists of a series of 21 stations made of silicon modules arranged along the beam direction spreading from $z = [-18, 88]$ cm. The stations are circular in shape and of 300 μm thick each. Each station of the VELO is divided in two completely independent halves. The VELO provides a precise measurement of the track coordinates, r and ϕ (each station has its own z coordinate), which are used to reconstruct the displaced secondary vertices generated by the lifetimes of b- and c-hadron decays. The use of cylindrical geometry (z,r,ϕ coordinates),and not Cartesian scheme, is required by the LHCb trigger performance, for which 2D (rz) tracking has been demonstrated to yield a faster reconstruction with enough impact parameter resolution (IP, distance of closest approach of a track to a vertex). The VELO is designed to reconstruct primary and secondary vertices providing measurements of flight distances and of IP. It is able to detect particles within a pseudo rapidity range $1.6 < \eta < 4.9$, pseudo rapidity being defined as $\eta = -ln(tan(\theta/2))$ with θ being the angle between the momentum of the particle and the beam axis.

Fig.2.6 and Fig 2.7 show a cross section of the LHCb vertex detector. A complete description of this device is given in [31]. The design of the vertex detector

could be simplified in the following lines. The silicon sensor configuration is optimized to accurately identify particle trajectories with small polar angles. The innermost radius of these sensors should be as small as possible, since a short track extrapolation distance leads to a more precise impact parameter reconstruction. These sensors are very close to the interaction point, this means that the hardness of sensors and read out electronics require special attention because they will be exposed to radiation damage [32].
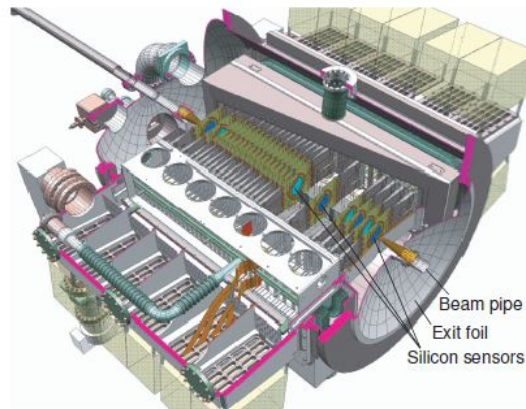
Figure 2.6: Cross section of the vertex detector. The beam pipe, silicon sensors and exit foil are indicated(LHCb web page).
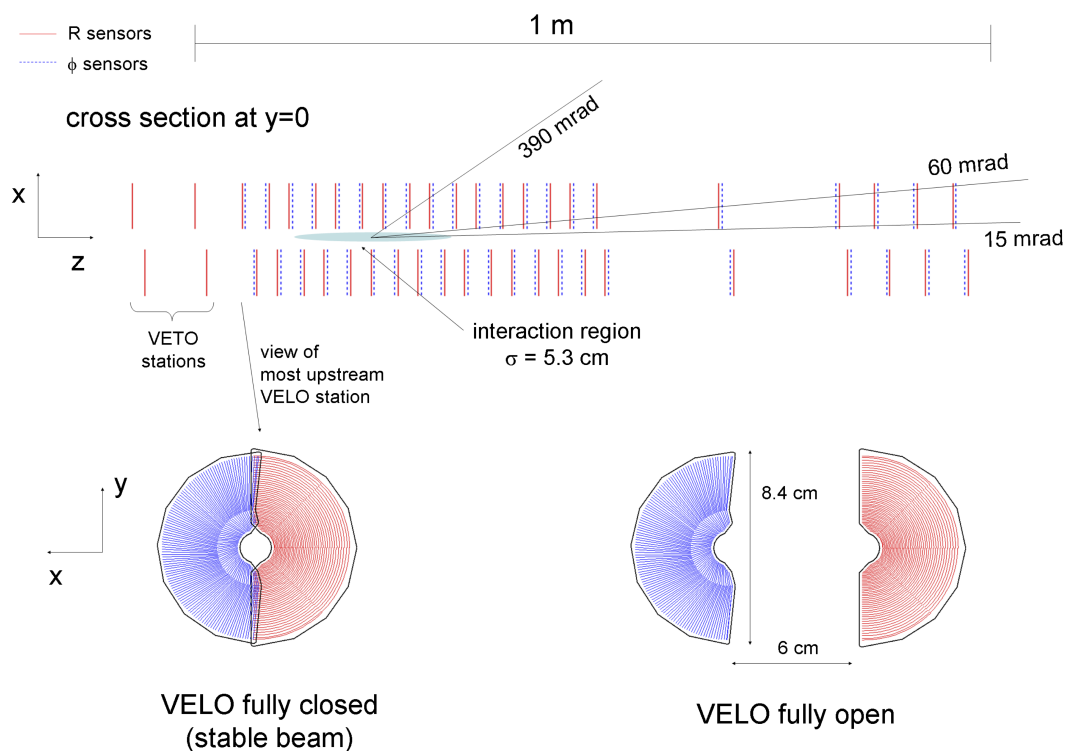
Figure 2.7: Cross section in the (x,z) plane of the VELO silicon sensors at y = 0, with the detector in the fully closed position. The front face of the first modules is also illustrated in both closed and open positions.

2.2.4 RICH detectors

The RICH (Ring-Imaging CHerenkov detector) system is used to identify charged particles with momentum range [1-150] GeV/c, and within an angular acceptance

of [10-300] milliradians (mrad). Particle identification is so important in order to reduce background in desired final states (see graphs below Fig.2.8). It is also used to provide an efficient tag of the b-quark flavour.
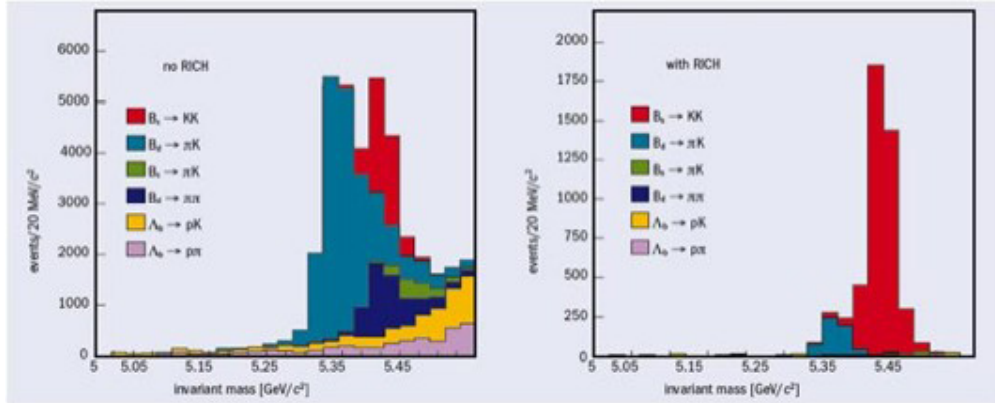
Figure 2.8: Effectiveness of the RICH system(LHCb web page).

The system consists of an upstream detector (RICH-1), positioned directly behind the VELO, and a downstream detector (RICH-2) located behind the magnet and the tracking system.

2.2.5 Mirrors and radiators

Silica aerogel is a colloidal form of solid quartz, but with an extremely low density and a high refractive index (1.01-1.10), which makes it perfect for the lowest-momentum particles (order of a few GeV/c). To cover the regions of medium and high momentum, LHCb uses a combination of C_4F_{10} and CF_4 radiators for momenta in range $[10, 65]$ GeV/c, and $[15, 100]$ GeV/c, respectively (Fig.2.9).

The RICH-1 detector is set up to detect low-momentum particles, while RICH-2 has an acceptance that is limited to the low-angle region where there are mostly high-momentum particles.
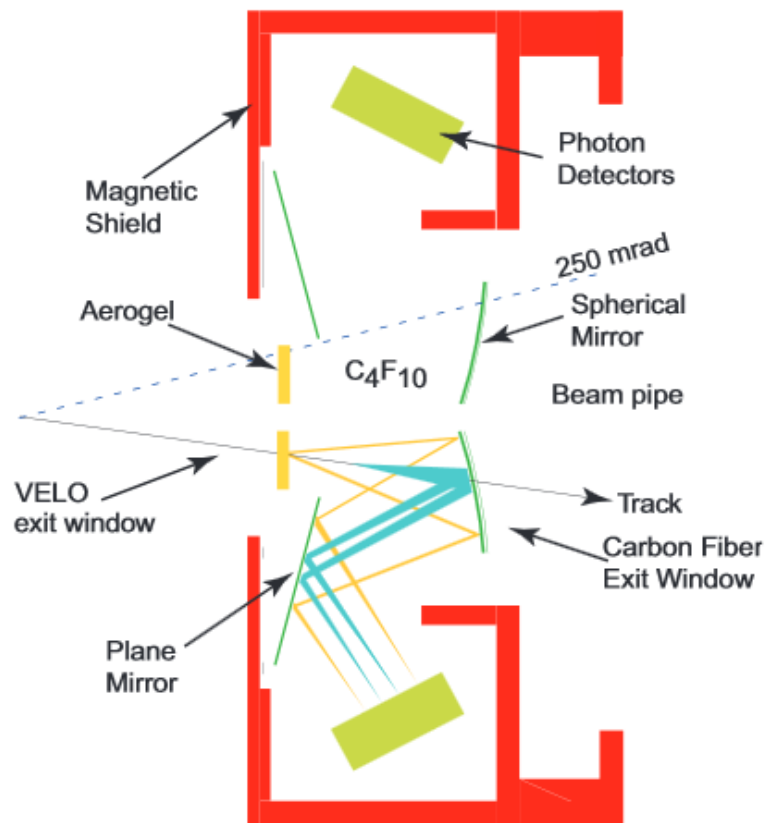
Figure 2.9: RICH1diagram(LHCb web page).

2.2.6 Seeing the light

Both RICH detectors use hybrid photon detectors (HPDs) to amplify the light signal of the emitted Cherenkov photons. The HPD is a vacuum photon detector in which a photo electron, released when an incident photon converts within a photo cathode, is accelerated by a high voltage of typically 10-20 kV onto a reverse-biased silicon detector.

The LHCb collaboration has developed a novel dedicated pixel-HPD (Fig.2.10)for the RICH detectors, working in close co-operation with industry. Here, the silicon detector is segmented into 1024 "super" pixels, each $500\mu m \times 500\mu m$ in area and arranged as a matrix of 32 rows and 32 columns.
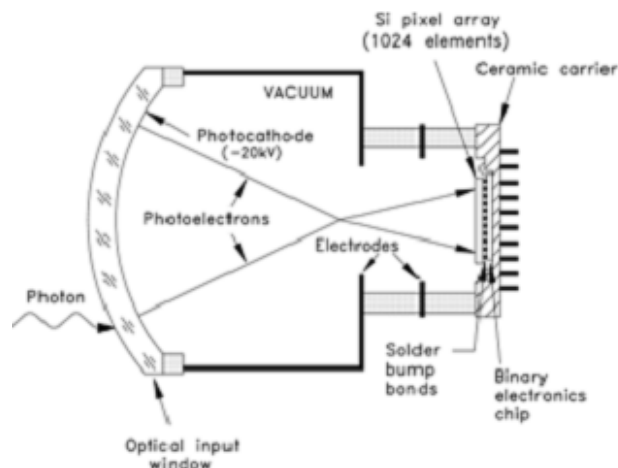
Figure 2.10: HPD-diagram(LHCb web page).

When a photo electron loses energy in silicon, it creates electron-hole pairs at an average yield of one for every 3.6 eV of deposited energy. The nominal operating voltage of LHCb HPDs is -20 kV, corresponding to around 5000 electron-hole pairs released in the silicon. Careful design of read-out electronics and interconnects to the silicon detector results in a high efficiency for detecting single photo electrons.

2.2.7   The Dipole Magnet

Figure 2.11: MagnetBanner2(LHCb web page)

Particle detectors typically include a powerful magnet [33] used to reconstruct the tracks of the particles produced after the collision. The LHCb experiment's enormous magnet (Fig.2.11) consists of two coils, weighing 27 tonnes, mounted inside a 1,450 tonne steel frame. LHCb exploits the forward region of proton collisions with a dipole field with a free aperture of ± 300 mrad horizontally and ± 250 mrad vertically.

The precision of the tracking detectors for charged particles momenta (up to 200 GeV/c) is about 0.4%, by the help of an integrated field of 4 Tm for tracks originating near the primary interaction point.

A good field uniformity along the transverse co-ordinate is required by the muon trigger. The lateral aperture of the magnet is defined by the longitudinal extension of the detectors, placed upstream of the magnet.

2.2.8   Tracking system

The principle task of the tracking system is to provide efficient reconstruction of charged-particle tracks (Fig.2.12). These are used to determine the momenta of charged particles. The main tracking system comprises four tracking stations: one station ("TT") is located between RICH-1 and the LHCb dipole magnet, while the other three stations ("T1-T3") are located over 3 meters between the magnet and RICH-2(Fig.2.13).

Two detector technologies are employed:

  1) The Outer Tracker.

  2) The Silicon Tracker.
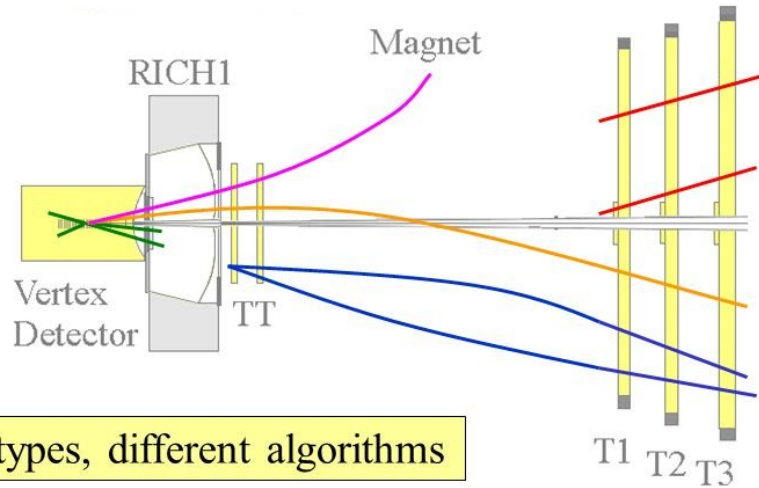
Figure 2.12: A schematic illustration of the various track types: long, upstream, downstream, VELO and T tracks.
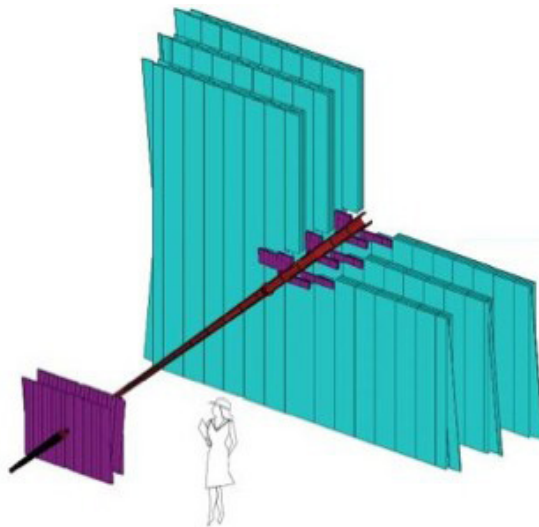
Figure 2.13: Tracking-system-diagram-2(LHCb web page).

The Silicon Tracker

The silicon tracker comprises two detectors - the Trigger Tracker (TT) and the Inner Tracker (IT) [34], both of which use silicon micro strip detectors.

The TT (Fig.2.14)is a 150 cm wide and 130 cm high planar tracking station that is located upstream of the LHCb dipole magnet and covers the full acceptance of the experiment.
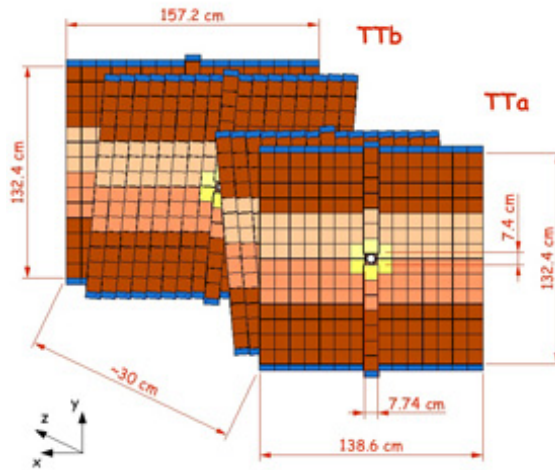
Figure 2.14: TT-layout(LHCb web page).

The IT (Fig.2.15) covers a roughly 120 cm wide and 40 cm high cross-shaped region in the center of three large planar tracking stations downstream of the magnet. Each of the four Silicon Tracker stations consists of four detection layers with specific angles between them.
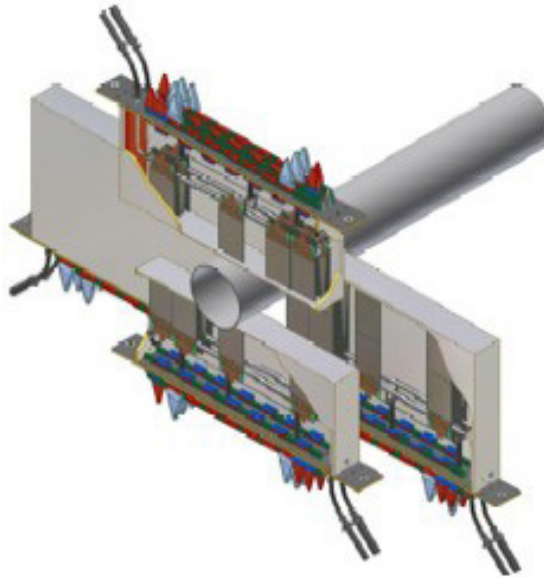
Figure 2.15: IT-boxes-diagram(LHCb web page).

The Outer Tracker: Spark Chambers

The design of the three Outer Tracker stations is modular(Fig.2.16). Each is built from 72 separate modules supported on four independently moving aluminium frames (18 modules per frame).
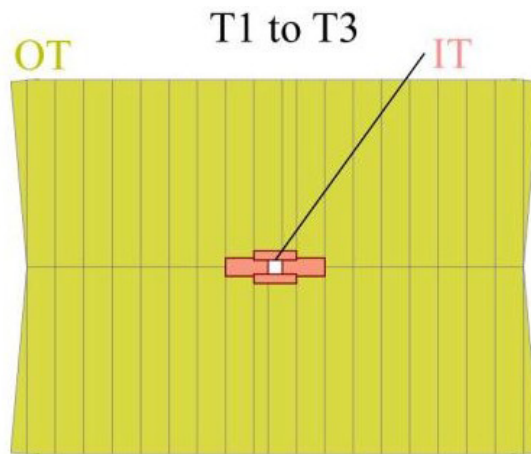
Figure 2.16: OT-Module-design(LHCb web page).

2.2.9 Calorimeter system
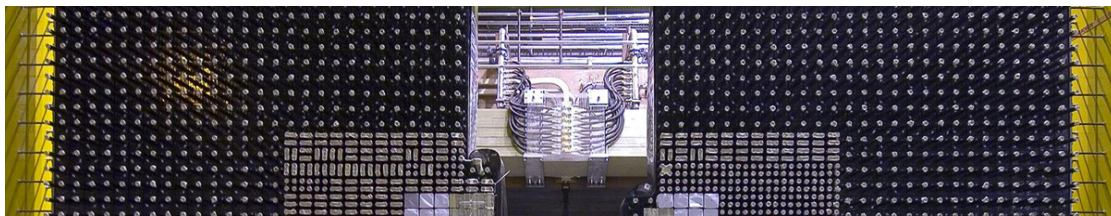
Figure 2.17: CalorimeterBanner1(LHCb web page).

LHCb calorimeter system (Fig.2.17) is used to identify electrons, photons and hadrons. It also determines the energy and position of the particles produced in their angular acceptance, which are used in offline event analysis. The photons will be identified by the EM calorimeter, and the hadrons are identified by the hadronic calorimeter.
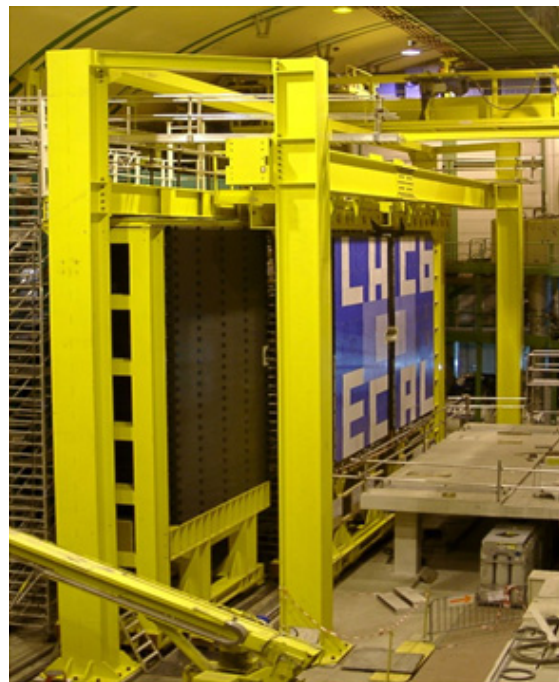
Figure 2.18: Calorimeters(LHCb web page).

The calorimeter system (Fig.2.18) consists of several layers:

- The Scintillating Pad Detector (SPD): The SPD determines the nature of the particles hitting the calorimeter system: charged or neutral particles.

- The Pre-Shower Detector (PS): The PS checks the electromagnetic character of the particle (i.e. whether it is an electron, if charged, or a photon, if neutral).

- Electromagnetic Calorimeter (ECAL): The ECAL (Fig.2.19) employs "shash-lik" technology of alternating scintillating tiles and lead plates. The cell size varies from 4 x 4 cm in the inner part of the detector, to 6 x 6 cm and 12 x 12 cm in the middle and outer parts. The cell granularity corresponds to that of the SPD/PS, aiming at a combined use in γ/e separation. The overall detector dimensions are 7.76 x 6.30 m, covering an acceptance of 25 mrad $< \theta_x <$ 300 mrad in the horizontal plane and 25 mrad $< \theta_y <$ 250 mrad in the vertical one. Light is detected by 10-stage photo-multipliers (Hamamatsu R7899-20) with an individually regulated high voltage base of Cock-croft-Walton type.

Figure 2.19: ECAL-modules(LHCb web page).

- Hadron Calorimeter (HCAL): The HCAL (Fig.2.20) is positioned behind the ECAL. Its internal structure consists of thin iron plates inter-spaced with scintillating tiles arranged parallel to the beam pipe. The inner and outer parts of the calorimeter have different cell dimensions. The HCAL features can be described as follows: in the lateral direction, tiles are inter-spaced with 1 cm of iron (matching with the radiation length X0); while in the longitudinal direction the length of tiles and iron spacers corresponds to the hadron interaction length λ_I in iron. The total weight of the HCAL is about 500 tonnes.
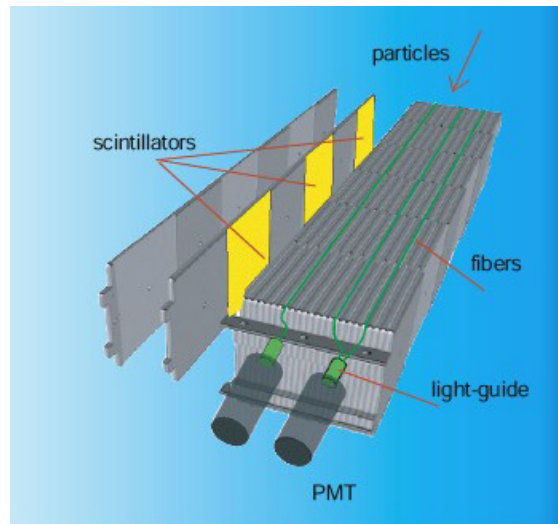
Figure 2.20: HCAL-tiles(LHCb web page).

2.2.10 Muon system

Figure 2.21: Muon-banner.

Muon triggering and offline muon identification are fundamental requirements of the LHCb experiment. Muons are present in the final states of many CP-sensitive B decays and play a major role in CP asymmetry and oscillation measurements, as muons from semi-semileptonic b decays provide a tag of the initial state flavour of the accompanying neutral B mesons.

The muon system provides fast information for the high-P_T muon trigger at the earliest level (Level-0) and muon identification for the high-level trigger (HLT) and offline analysis.
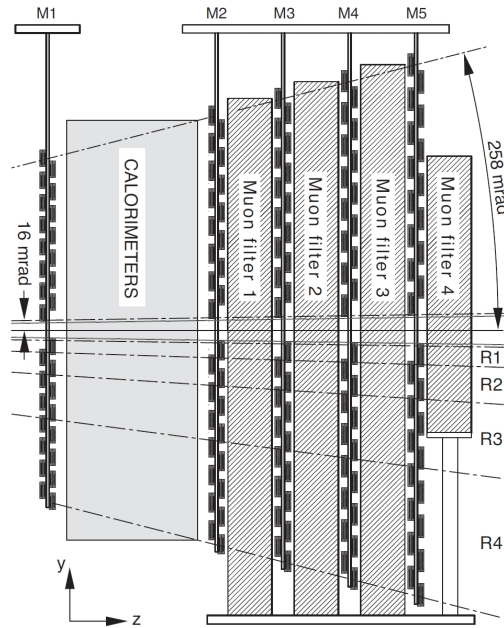
Figure 2.22: Muon-diagram(LHCb web page).

The system (Fig.2.21 and Fig.2.22) is composed of five stations (M1-M5) of rectangular shape, covering an acceptance of $\pm 300(\pm 250)$ mrad horizontally (vertically). M1 is placed in front of the scintillating pad detector/pre-shower. M2-M5 follow the hadron calorimeter (HCAL) and are separated by iron filters. The stations cover an area of 435 m^2.

Each station is divided into four regions, R1 to R4, with increasing distance from the beam axis. All the regions have approximately the same acceptance, and their granularity is shaped according to the particle density in that region in order to keep occupancy roughly constant over the detector. The granularity of the readout is higher in the horizontal plane, in order to give an accurate measurement of the track momentum and P_T.

Information must be gathered within 20 nanoseconds, so the detectors are optimized for speed. The system is therefore equipped with Multi Wire Proportional Chambers (MWPC) with 2 mm wire spacing and a small gas gap (5 mm). Triple-GEM detectors are used in the innermost region (R1) of Station M1, where the rate is highest. This choice was dictated by the better ageing properties of this type of detector.

2.3   Particle Identification

The reconstructed tracks for each event are given a particle identification(PID) based on the information provided from the different sub-detectors. The PID is given by the RICH counters (π, K, p), the ECAL, the HCAL (hadrons) and finally the muon system (μ).

The PID information is used in the offline selection through the likelihood hypothesis by combining information from all the sub-detectors. A track is supposed to be a muon or a hadron according to the likelihood hypothesis is given by the following relation:

$$L(\mu) = L^{RICH}(\mu) L^{CALO}(non\mu) L^{MUON}(\mu)$$

$$L(h) = L^{RICH}(h) L^{CALO}(none) L^{MUON}(non\mu)$$

where h, e, μ stands for hadron, electron, and muon respectively. Each function computes the probability of being of the given type of the particle.

Therefore, particles are selected according to the ratio of the likelihood between different hypothesis. To do that, particle identification procedure has been designed based on a log-likelihood difference (DLL) and it is defined by:

$$\Delta lnL_{AB} = lnL_A - lnL_B = ln\left(\frac{L_A}{L_B}\right]$$

where A,B stands for the hypothesis to have A, B. The ratio tends to be positive for correctly A-type identified A-particles and negative for correctly B-type identified B-particles.

2.4 The LHCb trigger system

There are two levels for the trigger system [35]: the Level-0 Trigger (L0) and the High Level Trigger (HLT). The trigger (Fig.2.23) purpose is mainly to select the interesting B-mesons decays, giving the final rate of visible interactions a value $\approx$ 5kHz.
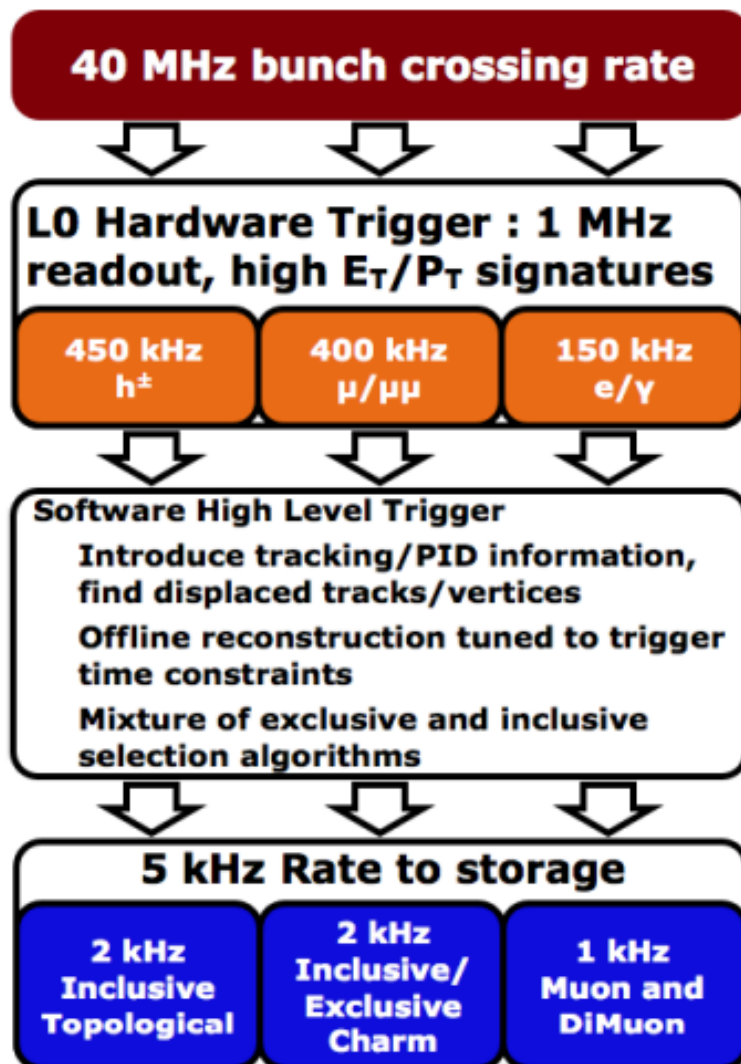

Figure 2.23: How the event flow in the LHCb trigger system(LHCb web page).

2.4.1   The Level-0 trigger

The Level-0 trigger (L0) reduces the visible event rate from 40MHz to the 1MHz at which the whole detector can be read out. It is implemented using custom made hardware. The L0 uses electronics operating synchronously (with the LHC clock) with the 40 MHz bunch crossing frequency. The L0 information is coming from the Pile-Up (PU) sensors of the VELO, the calorimeter and the muon system. It is sent to the L0 Decision Unit (L0DU) where the L0 selection algorithms are run. **The PU system** rejects events with several primary vertices, by the help of the information coming from the PU sensors of the VELO. It is used to trigger on beam-gas events providing the number of hits in the PU stations, which are the only detector elements upstream of the interaction point.

The L0 calorimeter trigger system uses information coming from calorimeter system, SPD, PS, ECAL and HCAL. It computes the transverse energy deposited in 2×2 calorimeter cells clusters. From these clusters, three types of candidates are built:

- 1) L0Hadron is the highest E_T HCAL cluster added with the energy of the associated ECAL cluster.

- 2) L0Photon is the highest E_T ECAL cluster with an energy threshold of 5 MIP in the PS and no hit in the SPD cells corresponding to the PS cells.

- 3) L0Electron has the same requirements as L0Photon, with the additional condition of at least one SPD cell hit in front of the PS cells.

The candidate's E_T is compared to a fixed threshold, causing the L0 trigger to fire if there is at least one candidate's event above threshold. The total number of hits in the SPD is used to veto events that would take a disproportionately large fraction of the available processing time in the HLT.

The muon chambers are responsible for muon reconstruction with a P_T resolution of $\sim 25\%$. To reconstruct the tracks, the pad data from the five muon stations pointing towards the interaction region are selected. The muon stations are divided in independent quadrants where in each quadrant, the two muon candidates with the highest p_T are selected (p > 3 GeV/c).

2.4.2   The High Level Trigger

The High Level Trigger (HLT) filters events using a software application. HLT is executed asynchronously on a processor farm, the Event Filter Farm. It uses the Online Event Filter Farm (EFF), containing more than 20,000 CPU cores, to reduce down the rate events to 3-5.5 kHz. The HLT is divided into: HLT1 that is responsible for partial reconstruction, and the HLT2 that performs full event reconstruction to further discriminate signal events.

HLT1

The HLT1 is designed to reduce the rate till 50kHz. It is a single track trigger, searching for a single track with high momentum, a large impact parameter (IP, shortest distance between a track and the primary vertex), and a good track quality [36]. The track should have an IP larger than 125 μm with respect to any PV, $p_T > 1.8$ GeV/c and $p > 12.5$ GeV/c. The Level-0 photon and electron lines require the p_T to be relaxed to 0.8 GeV/c for triggering the events.

Hlt1TrackMuon exists if the track is matched with hits in the muon chambers. This single muon trigger line selects good quality muon candidates with a

$p_T > 1$ GeV that are not coming from the primary vertex. Single muon candidates which satisfy a p_T requirement of $p_T > 4.8$ GeV are selected by the line **Hlt1SingleMuonHighPT** without any vertex separation requirements.

HLT2

The HLT2 reconstructs tracks with $p_T > 500$ MeV/c and $p > 5000$ MeV/c due to its low input rate and it is used to perform full offline reconstruction. Moreover, Global Event Cuts (GEC), such as the reconstructed track multiplicity, are used to reject complex events which require a big amount of processing time. The HLT2 runs exclusive and inclusive selections. The inclusive ones search for generic B decay features such as displaced vertices or dilepton pairs whereas the exclusive lines select specific decays using similar selections to those used offline. Special inclusive lines (topological lines: based on displaced vertices with 2, 3 or 4 associated tracks) have been developed to trigger on partially reconstructed b-hadron decays. Moreover, to improve the performances, additional lines using a multivariate approach were then added [37], [38].

2.5 LHCb Software

The LHCb software development strategy follows an architecture-centric approach as a way of creating a resilient software framework that can withstand changes in requirements and technology over the expected long lifetime of the experiment. The software architecture, called GAUDI, supports event data processing applications that run in different processing environments ranging from the real-time high-level triggers in the online system to the final physics analysis performed by more than 100 physicists. The major architectural design choices and the arguments that lead to these choices will be outlined. Object oriented technologies have been used throughout. Initially developed for the LHCb experiment, GAUDI has been adopted and extended by other experiments. Several iterations of the GAUDI software framework have been released and are now being used routinely by the physicists of the LHCb collaboration to facilitate their development of data selection algorithms. The LHCb reconstruction (Brunel), the digitization (Boole) and analysis (DaVinci) applications together with the simulation application (Gauss), also based on Geant4, and event and detector visualization program (Panoramix) are all based on the GAUDI framework. All these applications are now in production.

The LHCb software environment is based upon the GAUDI framework [39]. GAUDI is a full Object Oriented frame work used for all the software packages and applications of the LHCb experiment. The full Monte Carlo stimulation, reconstruction and data analysis are developed in the same common environment. The main LHCb software tools are:

- GAUSS: Simulation of the LHCb events is handled by GAUSS application [40] . GAUSS incorporates both event generation and full detector simulation tasks. pp primary interactions are generated with a tuned version of PYTHIA, while the decays of the intermediate particles are handled with the EVENTGEN package. After generation, the interaction of the particles in the detector is described with GEANT4. Acceptance cuts can be applied at the generator level to increase the production efficiency.

- BOOLE: The simulation of each sub detector response to the output of GAUSS is performed with a separate application: the BOOLE package [41]. BOOLE simulates the digitization of the energy deposited in the LHCb detector active material. The L0 hardware trigger is emulated at this stage as

well. The simulation of the detector electronics takes into account possible overlap between different pp events, the so-called spillover. The output format of BOOLE is exactly that used in real raw data files, therefore simulated and real data files can be reconstructed with the same software chain.

- MOORE: The MOORE package [42] is used to run the HLT1 and HLT2 triggers in both the online system and the offline simulated events. The trigger settings are defined via a unique Trigger Configuration Key. Each TCK must be processed with a specific version of the MOORE software (the same that was running in the online event filter far at the time data was taken) to ensure a correct reproduction of the trigger performance.

- BRUNEL: The raw hits are read by BRUNEL[43] in order to reconstruct basic physics objects, e.g charged tracks, calorimeter clusters and Cherenkov rings. BRUNEL accesses the LHCb conditions database in order to retrieve the experimental condition of the detector at the time each event was taken. Physical objects are saved into .DST files for data analysis.

- DAVINCI: DAVINCI [44] represents the last stage of the reconstruction. It is used to create composed objects, e.g. the composed particles in the decay chain, and perform candidate selections. Several tools are available to construct and save useful quantities for offline analysis. Once candidates are selected, they can be stored in different file formats, ready for further analysis and visualization.

2.6   Data flow in LHCb

First of all, events coming from the experiment are selected by the trigger system and then transferred to the CERN Tier-0 for further processing and archiving.They are called the raw data of the events. The next reconstruction process is performed in the Tier-1s. Combining the information from the tracks and particle identification, with the help oh the raw information (such as the hits or the calorimeter cluster energies) the physical particles are reconstructed. Reconstructed events are saved in a Stripping Data Summary Tape (SDST) file, which contains the necessary information for further event filtering without including the raw data. After that, the SDST files undergoes the Stripping stage: analyzing these files in order to further filter events for physical analysis by using the full reconstructed information. Finally, the raw data event information is attached to a Data Summary Tape (DST) file. DSTs are the files accessible to scientists for physics analysis.

2.7   Stripping:

What is stripping?
Stripping is the art of selecting the interesting events to be used after the reconstruction. Stripped DSTs, stripped events, and stripping selections are the only selections which are run centrally, and therefore the only events and selections which are available for the entire LHCb data-set.

What is a stripping Line?
A line is the sequence of selections and cuts used to create candidates and select the events.

The LHCb experiment has been presented in this chapter, We have presented the detector context, its different parts and their performance obtained from the data taken by the software of the LHCb detector.

The detector benefits from two trigger systems that allow to select online the events we are interested in. For our studies we are going to use MC11 and MC12 to be discussed is the next chapters.

In the next chapter, the decay $\Lambda_b^0 \to \Lambda_c^+ l \nu_l$ is being discussed.

Chapter 3

Phenomenology of the $\Lambda_b^0 \to \Lambda_c^+ \mu^- \bar{\nu}_\mu)$ Decay

Contents

In this chapter we are going to study the physics of the Λ_b^0, especially the decay channel $\Lambda_b^0 \to (\Lambda_c^+ \to \Lambda\pi^+)(W^- \to \mu^- \bar{\nu}_\mu)$ in an attempt from us to achieve the following aims:

- Measuring the Λ_b^0 polarization

- Testing the CP symmetry in the system $\Lambda_c^+ - \bar{\Lambda_c^-}$.

- Testing the time reversal symmetry (T).

3.1 Polarization Formalism

3.1.1 Polarization and Density Matrix

The spin is an intrinsic property of a particle, it is one of the two types of angular momentum in quantum mechanics. After the experimental discovery of the Spin by Sterm and Gerlach, the spin observable was deduced in 1927 when P. Dirac derived his relativistic quantum mechanics. In some ways, spin is like a vector quantity; it has a magnitude and a direction. In quantum mechanics the spin is represented by an operator $\hat{s}$. The projection of the spin on the quantization axis results in $(2S+1)$ possible values between -S and +S.

In fact, and from a physical point of view, we can only measure the mean value of the spin (in a given direction) and not the spin itself. In order to do that we will introduce the Polarization Density Matrix (Annex A)[45].
A density matrix is a matrix that describes a quantum system in a mixed state, a statistical ensemble of several quantum states.
Explicitly, suppose a quantum system may be found in state $|\psi_1\rangle$ with probability p_1, or it may be found in state $|\psi_2\rangle$ with probability p_2, and so on. The density operator for this system is:

$$\hat{\rho} = \sum_i p_i |\psi_i\rangle\langle\psi_i|$$

For an operator $\hat{A}$ (which describes an observable A of the system), the expectation value $\langle A \rangle$ is given by [46]:

$$\langle A \rangle = \sum_i p_i \langle\psi_i|\hat{A}|\psi_i\rangle = \sum_{mn} \langle u_m|\hat{\rho}|u_n\rangle\langle u_n|\hat{A}|u_m\rangle = \sum_{mn} \rho_{mn} A_{nm} = Tr(\rho A)$$

In other words, the expectation value of A for the mixed state is the sum of the expectation values of A for each of the pure states $|\psi_i\rangle$ weighted by the probabilities p_i and can be computed as the trace of the product of the density matrix with observable $\hat{A}$.
Remarks:

- ρ is hermitian: $\rho = \rho^\dagger$, therefore it can be diagonalized having positive or zero eigenvalues simply because they are probabilities.

- $Tr(\rho) = 1$

- $|\rho_{ij}|^2 \leq \sum \rho_{ii}\rho_{jj}$ (Schwartz Inequality)

3.1.2 Polarization

Let ρ be a (2×2) density matrix describing a spin 1/2 system. Because the unit matrix I and the three Pauli spin matrices form a complete set of (2×2) matrices, we may write the density matrix ρ as :

$$\rho = \frac{1}{2}(I + \vec{\sigma}.\vec{P})$$

where we have introduced the polarization vector $\vec{P}$. Polarization of a particle of spin S is the expectation value of the spin operator normalized to 1:

$$\vec{P} = \frac{\langle \vec{s} \rangle}{s}$$

The polarization vector in the Cartesian coordinates of the initial frame (X,Y,Z) can be written as :

$$\vec{P} = P_X \vec{X} + P_Y \vec{Y} + P_Z \vec{Z}$$

where $|\vec{P}| = \sqrt{P_X^2 + P_Y^2 + P_Z^2}$ is the polarization degree. Making use of the explicit representation of the Pauli matrices, we may also write :

$$\rho = \frac{1}{2} \begin{pmatrix} 1 + P_z & P_x - iP_y \\ P_x + iP_y & 1 - P_z \end{pmatrix}$$

• Choosing a z-axis to be the quantization axis, one can deduce the components of the polarization vector as a function of the polarization density matrix elements :

$$P_z = (\rho_{++} - \rho_{--}) \quad , \quad P_x = 2Re(\rho_{+-}) \quad , \quad P_y = -2Im(\rho_{+-})$$

where $\rho_{++}(\rho_{--})$ is the probability of finding the particle with spin projection $+1/2(-1/2)$ along the quantization axis ($o\vec{z}$ in this case).

There are three particular cases the polarization can take:

- non polarized state: it takes the value 0, this means that $\rho_{++} = \rho_{--} = 1/2$.

- totally polarized state: takes the value 1,$\rho_{ii} = 1$ and $\rho_{jj} = 0 (j \neq i)$.

- partially polarized state: it takes a value between 0 and 1.

The projection of $\vec{P}$ on an axis (Δ) defines the degree of polarization according to that axis. In the case of spin S=1/2, the polarization of the system is equal to the probability of finding the system in the state $|+1/2\rangle$ minus that of finding it in the state $|-1/2\rangle$ and is given by :

$$P_\Delta = \frac{N(+1/2) - N(-1/2)}{N(+1/2) + N(-1/2)}$$

where $\frac{N(\pm 1/2)}{N(+1/2) + N(-1/2)}$ are respectively the probability of finding in the mixture the pure states with 'spin up' along Δ.

The basic principles of quantum mechanics allow us to deduce the Spin Density Matrix (SDM) for any final state coming from a decay, which is considered an essential parameter for the calculation of the polarization vector of a resonance state. The SDM of the final system is given by the relation: $\rho^f = T^\dagger \rho^R T$. T is the transition matrix defined by the S matrix through out the following relation: S= 1+iT. The normalization factor of the matrix ρ^f is given by:

$$Tr(\rho^f) = \frac{d\sigma}{d\Omega} = F(\theta_1, \phi_1)$$

where θ_1 and ϕ_1 are the polar and the azimuthal angles of the daughter in the mother rest frame.

For instance, the polarization vector of a resonance state R_i of a final state is defined by :

$$\vec{P}_i = \langle \vec{S}_i \rangle = \frac{Tr(\rho_i^f \vec{S}_i)}{Tr(\rho_i^f)}$$

where ρ_i^f is the spin density matrix of the resonance R_i deduced from the total one, ρ^f. The elements of the polarization density matrix are not free of constraints, and those are:

- $Tr(\rho^{\Lambda_b}) = \rho_{++} + \rho_{--} = 1$.

- $(\rho_{+-})^* = \rho_{-+}$.

3.2   Angular Distributions of the Λ_b^0 Decay

Λ_b^0-baryons are formed in high-energy particle collisions produced by particle accelerators. The general method to find them is to detect their decay products, identify what particles they are, and measure their momenta. If all the decay products are found and measured correctly, then the mass of the parent particle may be calculated.

As an example, a favored decay of the Λ_b^0 is into a Λ_c^+ and a W. The momenta of these particles are measured by the detector and using conservation of four-momentum ($M^2 = (P_1 + P_2)^2$) gives a measure of the mass of the parent particle.

Figure (3.1) represents the Λ_b^0 baryon and its quark constituents (udb). Via weak interaction Λ_b^0 decays to Λ_c^+ of quark constituents (udc) and W^-.
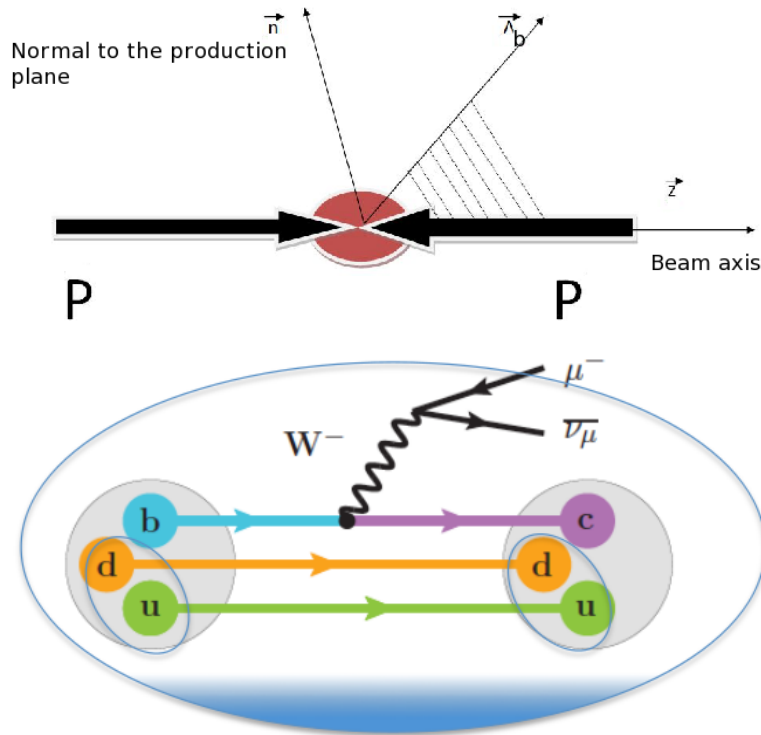
Figure 3.1: Up: p-p collision producing Λ_b^0. Bottom: Feynman diagram for the channel $\Lambda_b^0 \to \Lambda_c^+ W^-$.

The general formalism for this decay is based on the Jacob-Wick helicity formalism, and the formalism of Jackson [24].

3.2.1   Definition of the Frames and their Axis

First of all, we are going to define the production plane which is the plane that contains momentum of the Λ_b^0 and that of the incident protons. The normal to this plane is defined as :

$$\vec{n} = \frac{\vec{p}_p \times \vec{p}_{\Lambda_b}}{|\vec{p}_p \times \vec{p}_{\Lambda_b}|}$$

where $\vec{p}_p$ and $\overrightarrow{p_{\Lambda_b}}$ are respectively the momentum of the incident proton and the Λ_b^0 in the LHCb standard frame of reference (Oxyz).

We define the axis $\overrightarrow{Ox'}$ parallel to the momentum $\vec{p}_p$ of the colliding protons (LHC z-axis), this means : $\overrightarrow{Ox'} = \overrightarrow{Oz} \rightarrow \vec{e}_{x'} = \frac{\vec{p}_p}{|\vec{p}_p|} = \hat{p}_p$.

We define the axis $\overrightarrow{Oz'}$ orthogonal to the Λ_b^0 production plane and parallel to the vector $\vec{n} \rightarrow \overrightarrow{e}_{z'} = \vec{n}$.

We define the axis $\overrightarrow{Oy'} = \overrightarrow{Oz'} \times \overrightarrow{Ox'} \rightarrow \vec{e}_{y'} = \vec{e}_{z'} \times \vec{e}_{x'}$.
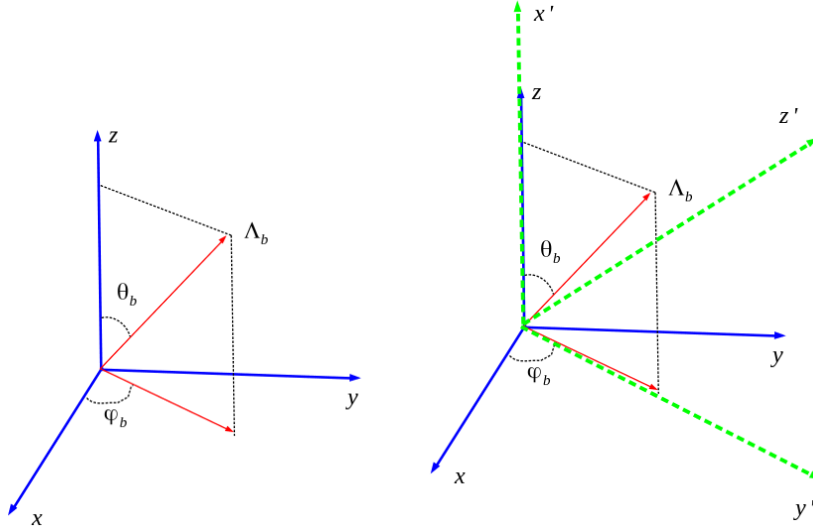

Figure 3.2: left: Λ_b^0 in LHCb frame, right: Λ_b^0 transverse frame.

The new right frame in (Fig.3.2) will be denoted as the "Λ_b^0 Transversity frame", and the axis $(\overrightarrow{Oz'})$ which is orthogonal to the production plane will be taken as the quantization axis, The components of the Λ_b^0 momentum in the new frame are $\overrightarrow{p'_{\Lambda_b^0}} = (p_{\Lambda_b^0}cos\theta_{\Lambda_b^0}, p_{\Lambda_b^0}sin\theta_{\Lambda_b^0}, 0)$

$\theta_{\Lambda_b^0}$ is the angle between the Λ_b momentum and the collision axis $(\overrightarrow{Oz})$ in the LHCb standard frame (Oxyz) and $p_{\Lambda_b} = |\overrightarrow{p_{\Lambda_b}}|$.

In order to study the angular distribution of the Λ_b decay products, the rest frame of the Λ_b ($\Lambda_b XYZ$) is constructed by:

- applying a Lorentz Transformation according to $\overrightarrow{P_{\Lambda_b}}$ axis with $\vec{\beta} = (\overrightarrow{p'}_{\Lambda_b})/(E_{\Lambda_b})$.

The quantization axis of the new frame ($\Lambda_b XYZ$) is identical to that of (Ox'y'z'), this means that $\overrightarrow{\Lambda_b Z}||\overrightarrow{Oz'}||\vec{n}$ as seen in (Fig.3.3).

Consider the following quasi two-body decay process: $\Lambda_b^0 \rightarrow \Lambda_c^+(\Lambda\pi^+)W^{(*)-}(\mu^-\bar{\nu}_\mu)$

3.2.2 Initial Resonance Decay: $\Lambda_b^0(M_i) \rightarrow \Lambda_c^+(\lambda_1)W^-(\lambda_2)$

By applying the Wigner-Eckart theorem to the S-matrix element in the framework of the Jacob-Wick helicity formalism, the analytic form of the decay amplitude is expressed as [47], [48], [49]-[57]:

$$A_0(M_i) = M_{\Lambda_b^0}(\lambda_1, \lambda_2)D_{M_i,M_f}^{1/2*}(\phi, \theta, 0)$$

where:
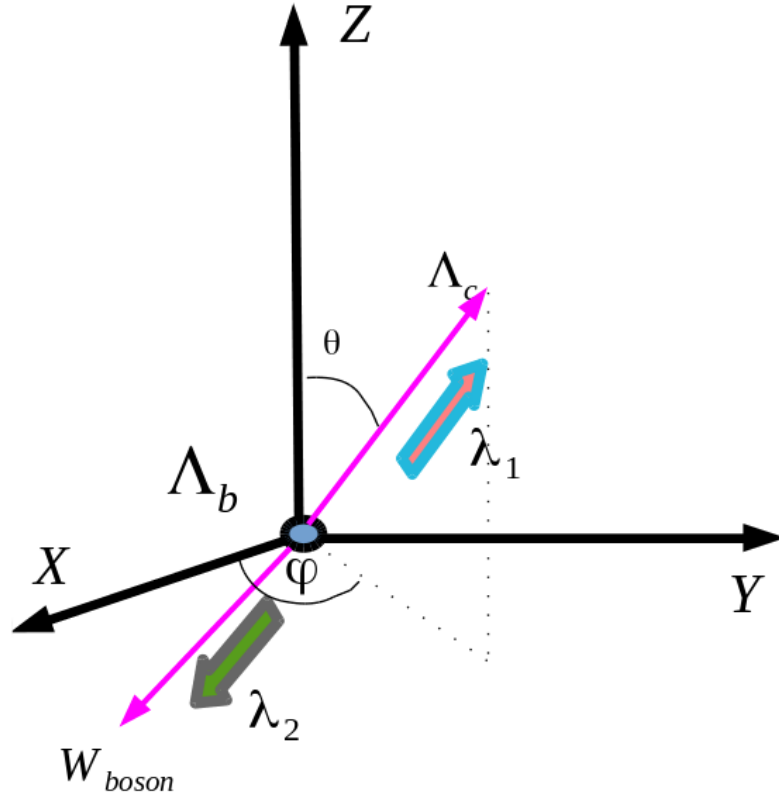
Figure 3.3: Λ_b^0 rest frame.

- $M_i = \pm 1/2$ represents the projection of the initial spin of Λ_b^0 along the quantization axis $\overrightarrow{\Lambda_b^0 Z}$.

- $\lambda_1 = \pm 1/2$ and $\lambda_2 = +1, 0, -1$ are the possible helicities of the Λ_c^+ and of the W^- respectively.

- $M_f = \lambda_1 - \lambda_2 = \pm 1/2$. It is the projection of the total angular momentum along the (Δ) axis (parallel to $\vec{p_\Lambda}$). It constrains those of λ_1 and λ_2 since, among 6 combination's, only 4 are physical: (1/2,1), (-1/2,0), (1/2,0), (-1/2,-1).

- $M_{\Lambda_b^0}(\lambda_1, \lambda_2)$: Hadronic Matrix element which contains all the decay dynamics.

- $D_{M_i,M_f}^j(\phi, \theta, 0)$: Wigner Matrix related to the kinematics. It is expressed according to the Jackson convention as:

$$D_{M_i,M_f}^j(\phi, \theta, 0) = d_{M_i,M_f}^j(\theta) \exp(-iM_i\phi)$$

This decay amplitude must include all the possible intermediate states, thus a sum over the helicity states (λ_1, λ_2) must be performed. We define:

$$A_I = \sum_{\lambda_1,\lambda_2} A_0(M_i) = \sum_{\lambda_1,\lambda_2} M_{\Lambda_b^0}(\lambda_1, \lambda_2) d_{M_i,M_f}^{1/2}(\theta) \exp(iM_i\phi)$$

Since the initial spin component of Λ_b baryon is unknown, we must introduce the polarization density matrix $\rho^{\Lambda_b^0}$ in the following form:

$$d\sigma(\theta, \phi) \propto \sum_{M_i,M_i'} \rho_{M_i,M_i'}^{\Lambda_b^0} A_I A_I^*$$

After the summation over the possible helicity couples (λ_1, λ_2): (1/2,1) (-1/2,0) (1/2,0) (-1/2,-1) and the summation over M_i, M_i' we get:

$$
\begin{aligned}
d\sigma(\theta,\phi) \quad \propto \quad & |M_{\Lambda_b^0}(1/2)|^2\big(\rho_{++}^{\Lambda_b}\cos^2(\theta/2) + \rho_{--}^{\Lambda_b}\sin^2(\theta/2) + Re(\rho_{+-}^{\Lambda_b^0}exp(-i\phi)\sin\theta)\big) \\
+ \quad & |M_{\Lambda_b^0}(-1/2)|^2\big(\rho_{++}^{\Lambda_b^0}\cos^2(\theta/2) + \rho_{--}^{\Lambda_b^0}\sin^2(\theta/2) + Re(\rho_{+-}^{\Lambda_b^0}exp(-i\phi)\sin\theta)\big)
\end{aligned}
$$

where

$$
|M_{\Lambda_b^0}(1/2)|^2 = |M_{\Lambda_b^0}(1/2,0)|^2 + |M_{\Lambda_b^0}(-1/2,-1)|^2
$$

$$
|M_{\Lambda_b^0}(-1/2)|^2 = |M_{\Lambda_b^0}(-1/2,0)|^2 + |M_{\Lambda_b^0}(1/2,1)|^2
$$

Noticing that $\rho_{++}^{\Lambda_b^0} + \rho_{--}^{\Lambda_b^0} = 1$ and $\rho_{++}^{\Lambda_b^0} - \rho_{--}^{\Lambda_b^0} = P_Z^{\Lambda_b^0}$ and $\cos^2(\theta/2) = \frac{1}{2}(1+\cos\theta)$, $\sin^2(\theta/2) = \frac{1}{2}(1-\cos\theta)$, the above relation will become:

$$
\begin{aligned}
d\sigma(\theta,\phi) \quad \propto \quad & |M_{\Lambda_b^0}(1/2)|^2\big(1 + P_Z^{\Lambda_b^0}\cos\theta + Re(\rho_{+-}^{\Lambda_b^0}exp(-i\phi)\sin\theta)\big) \qquad (3.1) \\
+ \quad & |M_{\Lambda_b^0}(-1/2)|^2\big(1 - P_Z^{\Lambda_b^0}\cos\theta - Re(\rho_{+-}^{\Lambda_b^0}exp(-i\phi)\sin\theta)\big)
\end{aligned}
$$

Because of parity violation, $|M_{\Lambda_b^0}(1/2)|^2 \neq |M_{\Lambda_b^0}(-1/2)|^2$, it is clearly seen that $d\sigma(\theta,\phi) \neq d\sigma(\pi-\theta,\pi+\phi)$. This property is put into evidence by introducing the asymmetry parameter $\alpha_{AS}^{\Lambda_b}$ defined by:

$$
\alpha_{AS}^{\Lambda_b} = \frac{|M_{\Lambda_b^0}(1/2)|^2 - |M_{\Lambda_b^0}(-1/2)|^2}{|M_{\Lambda_b^0}(1/2)|^2 + |M_{\Lambda_b^0}(-1/2)|^2}
$$

Therefore, the angular distribution of Λ_c^+ in the Λ_b rest frame will be expressed as:

$$
\begin{aligned}
\frac{d\sigma}{d\Omega} \quad &\propto \quad 1 + \alpha_{AS}^{\Lambda_b}P_Z^{\Lambda_b}\cos\theta_{\Lambda_c^+} + 2\alpha_{AS}^{\Lambda_b}Re[\rho_{+-}^{\Lambda_b}\exp(i\phi_{\Lambda_c^+})]\sin\theta_{\Lambda_c^+} \\
&\propto \quad 1 + \alpha_{AS}^{\Lambda_b}\mathbf{P}^{\Lambda_b^0}.\hat{\mathbf{p}}_{\Lambda_c^+} \qquad\qquad (3.2)
\end{aligned}
$$

- The polar distribution according to $\cos\theta$ of Λ_c^+ :

$$
\frac{d\sigma}{d\cos\theta_{\Lambda_c^+}} \propto 1 + \alpha_{AS}^{\Lambda_b}P_Z^{\Lambda_b}\cos\theta_{\Lambda_c^+}
$$

- The azimuthal distribution according to ϕ of Λ_c^+ :

$$
\frac{d\sigma}{d\phi_{\Lambda_c^+}} \propto 1 + \frac{\pi}{2}\alpha_{AS}^{\Lambda_b}Re[\rho_{+-}^{\Lambda_b}exp(i\phi_{\Lambda_c^+})] \equiv 1 + (P_X^{\Lambda_b}\cos\phi + P_Y^{\Lambda_b}\sin\phi)\alpha_{AS}^{\Lambda_b}
$$

3.2.3 Decay 1: $w^{(*)-}(\lambda_2) \to \mu^-(\lambda_5)\bar{\nu}_\mu(\lambda_6)$

However, moving forward to the decay of the virtual W^*-boson to study its final particles is not easy. The angular distributions of the final states μ^- and $\bar{\nu}_\mu$ are analyzed in the W^*-boson helicity frame. To do so, there are two steps to be performed in order to move from the Λ_b transverse frame to the W^*-boson helicity frame $(W_{boson}X_2Y_2Z_2)$, see (Fig.3.4).

- Two successive rotations $R_y(\theta)$ and $R_z(\phi)$: the new $\overrightarrow{WZ_2}$ is parallel to the direction of the momentum of the W^*-boson , $\overrightarrow{p_W}$, in the transverse frame.

- Lorentz boost $\beta_W = \frac{|\overrightarrow{p_W}|}{E_W}$.
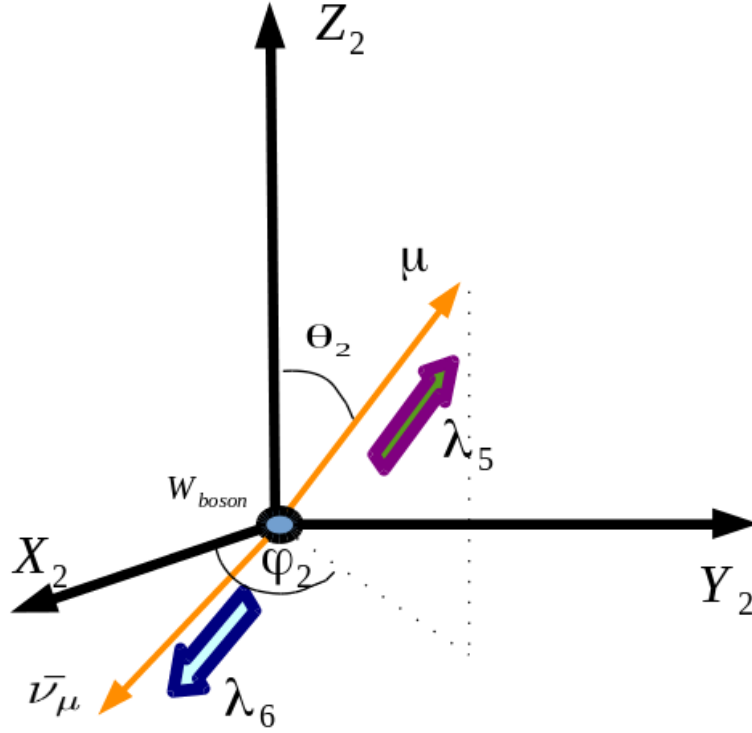
Figure 3.4: W^- rest frame.

By this method the quantization axis coincides with the helicity axis.

The general formula of the lepton angular distribution in the W^- rest frame (3.4) is [47, 48]:

$$d\sigma(\theta_2, \phi_2) \propto \sum_{\lambda_2, \lambda_2'} \rho_{\lambda_2, \lambda_2'}^W A_I A_I^*$$

where $\rho_{\lambda_2, \lambda_2'}^W$ is a (3×3) density matrix for a **spin 1** particle defined as follows:

$$\rho = \begin{pmatrix} \rho_{11} & \rho_{10} & \rho_{1-1} \\ \rho_{01} & \rho_{00} & \rho_{0-1} \\ \rho_{-11} & \rho_{-10} & \rho_{-1-1} \end{pmatrix}$$

Here we need 8 real parameters $(n^2 - 1)$ in order to define ρ. Let's define A_I:

$$A_I = \sum_{\lambda_5} A_1(\lambda_2) = \sum_{\lambda_5} M_W(\lambda_5, -1/2) d_{\lambda_2, M_f}^1(\theta_2) \exp(i\lambda_2 \phi_2)$$

such that $M_f = \lambda_5 - \lambda_6 = \lambda_5 - (\pm 1/2) = 0, -1$.

$\lambda_6 = +1/2$, since anti-neutrinos are right-handed particles. By following the same mathematical technique as above; after the summation over the possible

helicity couples and over λ_2, λ_2' we get:

$$\frac{d\sigma}{d\Omega_2} \propto \rho_{11}^W \left(|M_W(+-)|^2 \frac{(1+\cos\theta_2)^2}{4} + |M_W(--)|^2 \frac{\sin^2\theta_2}{2} \right) \tag{3.3}$$

$$+2Re\left(\rho_{10}^W exp(i\phi_2)\right) \left(|M_W(+-)|^2 \frac{\cos^2\theta_2}{2} - |M_W(--)|^2 \cos\theta_2 \right) \frac{\sin\theta_2}{\sqrt{2}}$$

$$+2Re\left(\rho_{1-1}^W exp(i2\phi_2)\right) \left(\frac{|M_W(+-)|^2}{4} - \frac{|M_W(--)|^2}{2} \right) \sin^2\theta_2$$

$$+\rho_{00}^W \left(\frac{|M_W(+-)|^2}{2} \sin^2\theta_2 + |M_W(--)|^2 \cos^2\theta_2 \right)$$

$$+2Re\left(\rho_{0-1}^W exp(i\phi_2)\right) \left(|M_W(+-)|^2 \frac{(1-\cos\theta_2)^2}{2} + |M_W(--)|^2 \cos\theta_2 \right) \frac{\sin\theta_2}{\sqrt{2}}$$

$$+\rho_{-1-1}^W \left(|M_W(+-)|^2 \frac{(1-\cos\theta_2)^2}{4} + |M_W(--)|^2 \frac{\sin^2\theta_2}{2} \right)$$

These angular distributions are in agreement with the results obtained by C.QUIGG [58] for specific polarization of the W^-; particularly, for $P_Z^W = +1, 0, -1$ where:

- For helicity $= 0$ (completely longitudinally polarized);

$$\frac{d\sigma}{d\Omega} = \frac{G_F M_W^3}{6\pi\sqrt{2}} \sin^2\theta_2$$

- For helicity $= +1$ (completely transversely polarized according to the w momentum direction) ;

$$\frac{d\sigma}{d\Omega} = \frac{G_F M_W^3}{32\pi^2\sqrt{2}} (1 + \cos\theta_2)^2$$

- For helicity $= -1$ (completely transversely polarized opposite to the w momentum direction) ;

$$\frac{d\sigma}{d\Omega} = \frac{G_F M_W^3}{32\pi^2\sqrt{2}} (1 - \cos\theta_2)^2$$

Again from Λ_b^0 decay amplitude, we can deduce the PDM of the W^-:

- $\rho_{11}^W = \dfrac{|M_{\Lambda_b^0}(1/2,1)|^2}{|M_{\Lambda_b^0}(1/2,0)|^2+|M_{\Lambda_b^0}(1/2,1)|^2+|M_{\Lambda_b^0}(-1/2,0)|^2++|M_{\Lambda_b^0}(-1/2,-1)|^2}$

- $\rho_{00}^W = \dfrac{|M_{\Lambda_b^0}(1/2,0)|^2+|M_{\Lambda_b^0}(-1/2,0)|^2}{|M_{\Lambda_b^0}(1/2,0)|^2+|M_{\Lambda_b^0}(1/2,1)|^2+|M_{\Lambda_b^0}(-1/2,0)|^2++|M_{\Lambda_b^0}(-1/2,-1)|^2}$

- $\rho_{-1-1}^W = \dfrac{|M_{\Lambda_b^0}(-1/2,-1)|^2}{|M_{\Lambda_b^0}(1/2,0)|^2+|M_{\Lambda_b^0}(1/2,1)|^2+|M_{\Lambda_b^0}(-1/2,0)|^2++|M_{\Lambda_b^0}(-1/2,-1)|^2}$

- $\rho_{10}^W = -\dfrac{\pi}{4} \dfrac{|M_{\Lambda_b^0}(1/2,1)|^2 \, |M_{\Lambda_b^0}(1/2,0)|^2}{|M_{\Lambda_b^0}(1/2,0)|^2+|M_{\Lambda_b^0}(1/2,1)|^2+|M_{\Lambda_b^0}(-1/2,0)|^2++|M_{\Lambda_b^0}(-1/2,-1)|^2} P_Z^{\Lambda_c}$

- $\rho_{1-1}^W = 0$ because of the angular momentum conservation.

- $\rho_{0-1}^W = -\dfrac{\pi}{4} \dfrac{|M_{\Lambda_b^0}(-1/2,0)|^2 \, |M_{\Lambda_b^0}(-1/2,-1)|^2}{|M_{\Lambda_b^0}(1/2,0)|^2+|M_{\Lambda_b^0}(1/2,1)|^2+|M_{\Lambda_b^0}(-1/2,0)|^2++|M_{\Lambda_b^0}(-1/2,-1)|^2} P_Z^{\Lambda_c}$

It is worthy noticing that:

$$\rho_{01}^W = \rho_{10}^{*W} \qquad \rho_{-11}^W = \rho_{-11}^{*W} \qquad \rho_{-10}^W = \rho_{0-1}^{*W}$$

We notice again that the initial polarization of Λ_b^0 appears in the non-diagonal ρ_{10}^W and ρ_{0-1}^W elements. The density matrix elements can be estimated by the aide of specific models of form factors [59].

3.2.4   Decay 2: $\Lambda_c^+(\lambda_1) \to \Lambda(\lambda_3)\pi^+(\lambda_4)$

The same method used to move to the virtual W^*-boson helicity frame is used here upon moving to the Λ_c^+ one. To do so, we perform two steps to be done in order to move to the Λ_c^+ helicity frame $(\Lambda_c^+ X_1 Y_1 Z_1)$, see Figure (3.5).

- Two successive rotations $R_y(\pi - \theta)$ and $R_z(\pi + \phi)$: the new $\overrightarrow{\Lambda_c^+ Z_1}$ is parallel to the direction of the momentum of $\overrightarrow{p_{\Lambda_c^+}}$, in the transverse frame.

- Lorentz boost $\beta_{\Lambda_c^+} = \frac{|\overrightarrow{p_{\Lambda_c^+}}|}{E_{\Lambda_c^+}}$.

By this method the quantization axis coincides with the helicity axis.
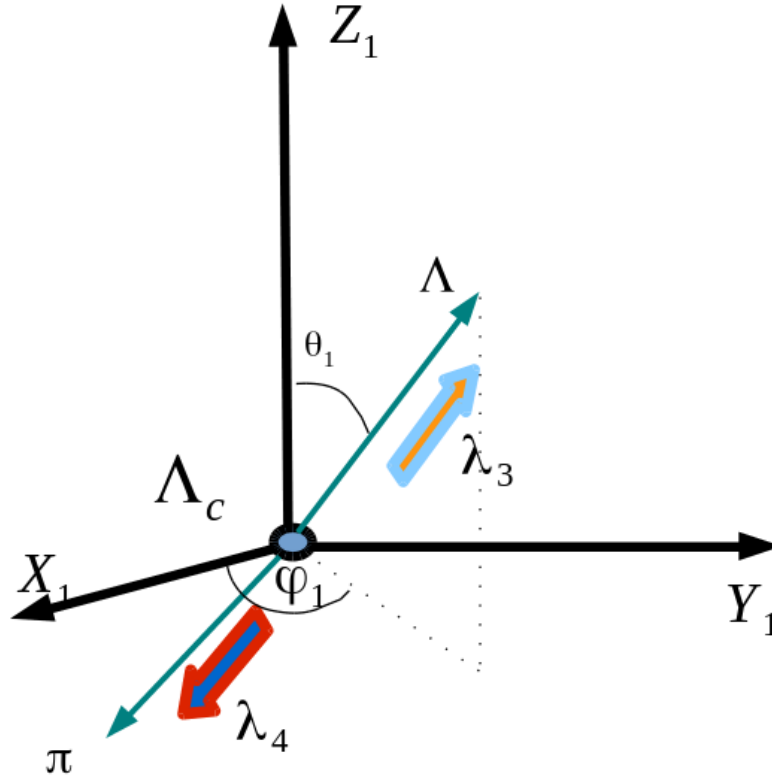

Figure 3.5: Λ_c^+ rest frame.

The general formula of the Λ angular distribution in the Λ_c^+ rest frame is [47, 48]:

$$d\sigma(\theta_1, \phi_1) \propto \sum_{\lambda_1, \lambda_1'} \rho_{\lambda_1, \lambda_1'}^{\Lambda_c^+} A_I A_I^*$$

where

$$A_I = \sum_{\lambda_3} A_1(\lambda_1) = \sum_{\lambda_3} M_{\Lambda_c^+}(\lambda_3, 0) d_{\lambda_1, M_f}^{1/2}(\theta_1) \exp(i\lambda_1 \phi_1)$$

such that $M_f = \lambda_3 - \lambda_4 = \pm 1/2$, $\lambda_4 = 0$ since the spin of the pion is zero. By following the same mathematical technique as above; after the summation over the possible helicity couples $(\lambda_3, 0)$: (1/2,0) (-1/2,0) and the summation over λ_1, λ_1' we get:

$$\frac{d\sigma}{d\Omega_1} \propto 1 + \alpha_{AS}^{\Lambda_c^+} P_Z^{\Lambda_c^+} \cos\theta_\Lambda + 2\alpha_{AS}^{\Lambda_c^+} \mathcal{R}[\rho_{+-}^{\Lambda_c^+} \exp(i\phi_\Lambda)] \sin\theta_\Lambda$$

$$\propto 1 + \alpha_{AS}^{\Lambda_c^+} \mathbf{P}^{\Lambda_c^+} \cdot \hat{\mathbf{p}}_\Lambda \qquad (3.4)$$

where

$$\alpha_{AS}^{\Lambda_c^+} = \frac{|M_{\Lambda_c^+}(1/2)|^2 - |M_{\Lambda_c^+}(-1/2)|^2}{|M_{\Lambda_c^+}(1/2)|^2 + |M_{\Lambda_c^+}(-1/2)|^2}$$

$$and$$

$$P_Z^{\Lambda_c^+} = \rho_{++}^{\Lambda_c^+} - \rho_{--}^{\Lambda_c^+}$$

Studying $\Lambda_c^+ \to \Lambda \pi^+$ coming from Λ_b^0 decays give us the opportunity to deduce the PDM of the Λ_c^+ since its production mechanism is known. We obtain:

- $\rho_{++}^{\Lambda_c^+} = \frac{|M_{\Lambda_b^0}(1/2,0)|^2 + |M_{\Lambda_b^0}(1/2,1)|^2}{|M_{\Lambda_b^0}(1/2,0)|^2 + |M_{\Lambda_b^0}(1/2,1)|^2 + |M_{\Lambda_b^0}(-1/2,0)|^2 + |M_{\Lambda_b^0}(-1/2,-1)|^2}$

- $\rho_{--}^{\Lambda_c^+} = \frac{|M_{\Lambda_b^0}(-1/2,0)|^2 + |M_{\Lambda_b^0}(-1/2,-1)|^2}{|M_{\Lambda_b^0}(1/2,0)|^2 + |M_{\Lambda_b^0}(1/2,1)|^2 + |M_{\Lambda_b^0}(-1/2,0)|^2 + |M_{\Lambda_b^0}(-1/2,-1)|^2}$

- $\rho_{+-}^{\Lambda_c^+} = -\frac{\pi}{4} \frac{M_{\Lambda_b^0}(1/2,0) M_{\Lambda_b^0}(-1/2,0)^*}{|M_{\Lambda_b^0}(1/2,0)|^2 + |M_{\Lambda_b^0}(1/2,1)|^2 + |M_{\Lambda_b^0}(-1/2,0)|^2 + |M_{\Lambda_b^0}(-1/2,-1)|^2} P_Z^{\Lambda_b}$

- $\rho_{-+}^{\Lambda_c^+} = \rho_{+-}^{\Lambda_c^+ *}$

We notice that the initial polarization of Λ_b^0 along the $\overrightarrow{OZ}$ axis appears in the non-diagonal $\rho_{+-}^{\Lambda_c^+}$ element. Thus it is confirmed that the Λ_b^0 decay mechanism is reflected in the polarization density matrix of Λ_c^+. The density matrix elements can be calculated by the aid of form factors related to a specific dynamics model [59].

3.3   Angular Distribution of the Λ_c Decay Products

Charmed baryons are formed in high-energy particle collisions, such as those produced by particle accelerators. The general method to find them is to detect their decay products, identify what particles they are, and measure their momenta. If all the decay products are found and measured correctly, then the mass of the parent particle may be calculated.

(Fig.3.6) represents the charmed baryon (Λ_c^+) and its quark constituents (udc). Via weak interaction Λ_c^+ decays to Λ of quark constituents (uds) and π ($u\bar{d}$).
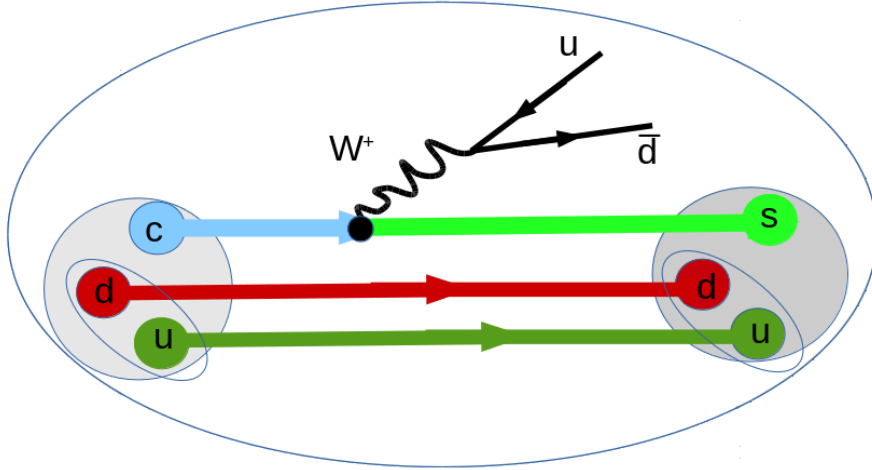

Figure 3.6: Feynman diagram for the channel $\Lambda_c^+ \to \Lambda \pi$.

The general formalism for the $\Lambda_c^+ \to \Lambda \pi$ decay is again based on the Jacob-Wick helicity formalism, and the formalism of Jackson [24].

In order to study the angular distribution of the products of the Λ_c^+ decay products, the helicity frame of the Λ_c^+ $(\Lambda_c^+ X_1 Y_1 Z_1)$ from the $(\Lambda_b XYZ)$ frame as shown above.

$d\sigma$, being the decay probability for the $\Lambda_c^+ \to \Lambda(p\pi^-)\pi^+$, is given by the general expression (Appendix A):

$$d\sigma = \sum_{M,M'} \sum_{\lambda_1,\lambda_2} \rho_{M,M'}^{\Lambda_c^+} |A_{(\lambda_1,\lambda_2)}(\Lambda_c^+ \to \Lambda\pi^+)|^2 d_{M'\lambda}^{1/2} d_{M\lambda}^{1/2} \exp i(M'-M)\phi \qquad (3.5)$$

where we denote by M, M' the projections of the Λ_c^+ spin on the $\overrightarrow{\Lambda_c^+ Z}$, $\lambda_1 = \pm 1/2$ and $\lambda_2 = 0$ are the helicities of Λ and the pion respectively, and finally $\lambda = \lambda_1 - \lambda_2$

We have 2 possibilities for the couple (λ_1, λ_2) due to the conservation of the total angular momentum : (-1/2,0) ; (+1/2,0).

We define here the asymmetry parameter $\alpha_{AS}^{\Lambda_c^+}$ depending on the final helicity of the products:

$$\alpha_{AS}^{\Lambda_c^+} = \frac{|M_{\Lambda_c^+}(1/2,0)|^2 - |M_{\Lambda_c^+}(-1/2,0)|^2}{|M_{\Lambda_c^+}(1/2,0)|^2 + |M_{\Lambda_c^+}(-1/2,0)|^2}$$

The angular distribution of Λ in the Λ_c^+ rest frame, starting from eq.(3.5), is given by the following expression:

$$\frac{d\sigma}{d\Omega} \propto 1 + \alpha_{AS}^{\Lambda_c^+} P^{\Lambda_c^+} \cos\theta_\Lambda + 2\alpha_{AS}^{\Lambda_c^+} \mathcal{R}[\rho_{+-}^{\Lambda_c^+} \exp(i\phi_\Lambda)] \sin\theta_\Lambda \qquad (3.6)$$

where $P^{\Lambda_c^+} = \rho_{++}^{\Lambda_c^+} - \rho_{--}^{\Lambda_c^+}$ is the Λ_c^+ polarization along the quantization axis $\overrightarrow{\Lambda_c^+ Z}$.

- The polar angular distribution of the Λ is :

$$\frac{d\sigma}{d\cos\theta_\Lambda} \propto 1 + \alpha_{AS}^{\Lambda_c^+} P_Z^{\Lambda_c^+} \cos\theta_\Lambda \qquad (3.7)$$

- The azimuthal distribution of the Λ is:

$$\frac{d\sigma}{d\phi_\Lambda} \propto 1 + \alpha_{AS}^{\Lambda_c^+} [P_X^{\Lambda_c^+} \cos(\phi_\Lambda) + P_Y^{\Lambda_c^+} \sin(\phi_\Lambda)] \qquad (3.8)$$

Lambda Decay to Proton and Pion

However, moving forward to the decay of the intermediate resonance $\Lambda \to p\pi^-$, and studying the angular distribution of the final states is not that easy way, we should move to the helicity frame of the Λ particle. To do so, there are two steps to be done in order to move from the Λ_c^+ transverse frame to the Λ helicity frame $(\Lambda X_3 Y_3 Z_3)$, as shown in Fig.3.7.

- Two successive rotations $R_y(\theta_3)$ and $R_z(\phi_3)$: the new $\overrightarrow{\Lambda Z}$ is parallel to the direction of the momentum of the Λ, $\overrightarrow{p_\Lambda}$, in the Λ_c helicity frame frame.
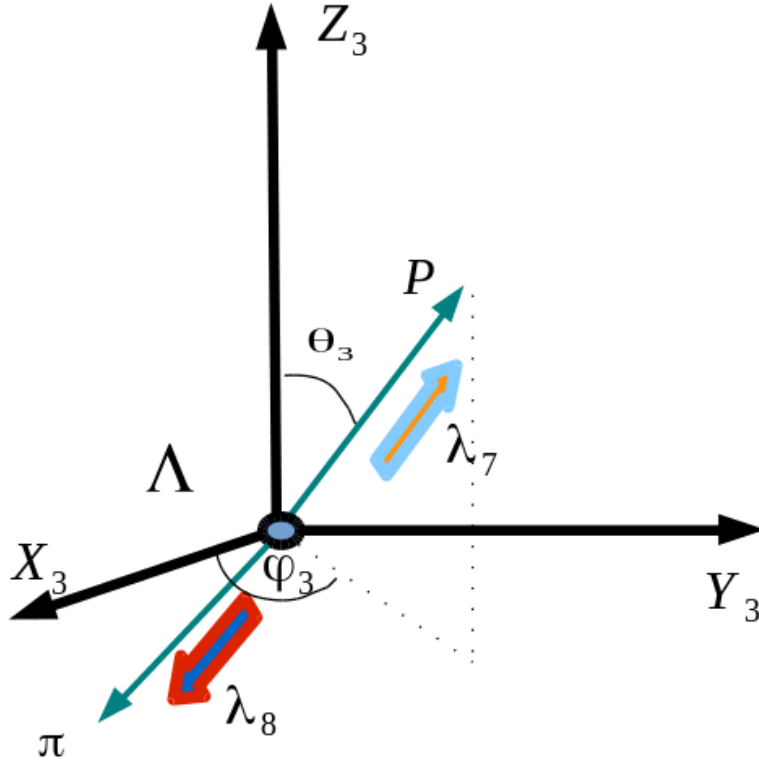- Lorentz boost $\beta_\Lambda = \frac{|\overrightarrow{p_\Lambda}|}{E_\Lambda}$.

The angular distribution of the proton in the Λ helicity frame is given by the following expression:

$$\frac{d\sigma}{d\Omega_3} = \{1 + \alpha_{AS}^\Lambda \alpha_{AS}^{\Lambda_c^+} \cos(\theta_3) - \frac{\pi}{4} \alpha_{AS}^\Lambda P_Z^{\Lambda_c^+} 2\mathcal{R}\langle \frac{M_{\Lambda_c^+}(1/2,0) M_{\Lambda_c^+}^*(-1/2,0)}{|M_{\Lambda_c^+}(1/2,0)|^2 + |M_{\Lambda_c^+}(-1/2,0)|^2} \exp(i\phi_3)\rangle \sin\theta_3\}$$

$$(3.9)$$

We define here the asymmetry parameter α_{AS}^Λ depending on the final helicity of the products:

$$\alpha_{AS}^\Lambda = \frac{|M_\Lambda(1/2,0)|^2 - |M_\Lambda(-1/2,0)|^2}{|M_\Lambda(1/2,0)|^2 + |M_\Lambda(-1/2,0)|^2}$$

Figure 3.7: Λ helicity frame.

- θ_3 is the angle between the $\overrightarrow{p_p}$ and the $\overrightarrow{\Lambda Z_3}$ axis.

- ϕ_3 is the azimuthal angle

Integrating the above equation over the variable ϕ_3 allows us to deduce the $\cos\theta_3$ angular distribution of the proton :

$$\frac{d\sigma}{d\cos\theta_3} \propto 1 + \alpha_{AS}^{\Lambda_c^+}\alpha_{AS}^{\Lambda}\cos\theta_3 \qquad (3.10)$$

Integrating the above equation over the variable $\cos\theta_3$ allows us to deduce the ϕ_3 angular distribution of the proton :

$$\frac{d\sigma}{d\phi_3} \propto 1 - \frac{\pi}{4}\alpha_{AS}^{\Lambda}P_Z^{\Lambda_c^+}2\mathcal{R}\{\frac{M_{\Lambda_c^+}(1/2,0)M_{\Lambda_c^+}^*(-1/2,0)}{|M_{\Lambda_c^+}(1/2,0)|^2 + |M_{\Lambda_c^+}(-1/2,0)|^2}\exp(i\phi_3)\} \qquad (3.11)$$

Note the presence of two asymmetry parameters next to each other in the $\cos\theta_3$ angular distribution of the proton and the absence of the polarization vector P_Z^{Λ}.

$$\frac{d\sigma}{d\cos\theta_3} \propto 1 + \alpha_{AS}^{\Lambda_c^+}\alpha_{AS}^{\Lambda}\cos\theta_3 \qquad (3.12)$$

This allows us to calculate the product $\alpha_{AS}^{\Lambda_c^+}\alpha_{AS}^{\Lambda}$ independent of the cascade polarization.

The general form of the angular distribution is the following:

$$\frac{d\sigma(p)}{d\Omega}|_\Lambda \propto 1 + \alpha_{AS}^{\Lambda} < \vec{\sigma_\Lambda} > \cdot\hat{p}_p \qquad (3.13)$$

where $\hat{p}_p = (\sin\theta_3\cos\phi_3, \sin\theta_3\sin\phi_3, \cos\theta_3)$
and $< \vec{\sigma_\Lambda} >= (P_x^\Lambda, P_y^\Lambda, P_z^\Lambda)$

After simple expansion for the above expression, the angular distribution of the proton in the Λ helicity frame is given by : $\frac{d\sigma(p)}{d\Omega}|_\Lambda$ becomes:

$$\frac{d\sigma(p)}{d\Omega}\Big|_\Lambda \propto 1 + \alpha_{AS}^\Lambda \{p_{x3}^\Lambda \sin\theta_3 \cos\phi_3 + p_{y3}^\Lambda \sin\theta_3 \sin\phi_3 + p_{z3}^\Lambda \cos\theta_3\} \qquad (3.14)$$

Now we can compare the equation (3.9) to the equation (3.14), and the result will be the different components of the Λ vector polarization.

- $|p_{x3}^\Lambda| = \dfrac{\pi}{4} \dfrac{M_{\Lambda_c^+}(1/2,0)M_{\Lambda_c^+}^*(-1/2,0) + M_{\Lambda_c^+}(-1/2,0)M_{\Lambda_c^+}^*(1/2,0)}{|M_{\Lambda_c^+}(1/2,0)|^2 + |M_{\Lambda_c^+}(-1/2,0)|^2} P_Z^{\Lambda_c^+}$

- $|p_{y3}^\Lambda| = \dfrac{\pi}{4} \dfrac{M_{\Lambda_c^+}(1/2,0)M_{\Lambda_c^+}^*(-1/2,0) - M_{\Lambda_c^+}(-1/2,0)M_{\Lambda_c^+}^*(1/2,0)}{|M_{\Lambda_c^+}(1/2,0)|^2 + |M_{\Lambda_c^+}(-1/2,0)|^2} P_Z^{\Lambda_c^+}$

- $|p_{z3}^\Lambda| = \alpha_{AS}^{\Lambda_c^+} = \dfrac{|M_{\Lambda_c^+}(1/2,0)|^2 - |M_{\Lambda_c^+}(-1/2,0)|^2}{|M_{\Lambda_c^+}(1/2,0)|^2 + |M_{\Lambda_c^+}(-1/2,0)|^2}$

Consequence: the longitudinal polarization component of the Λ is the asymmetry α_c^+ parameter.

3.4   Study of the T odd observables

In order to test the Time Reversal Symmetry, we are going to search for T odd observables. Two types of observables are suggested to show such evidence : The special angles, and the polarization of the Λ_c^+, the virtual W^*-boson and the Λ particle. In this study only the polarization will be presented.

3.4.1   The Special Angles

Definition of the Observable

We are going to build a T odd observable in the Λ_b^0 Transversity frame. This construction was inspired from the T odd and the CP observables developed by Sehgal for the decay $K_L^0 \Longrightarrow \pi^+\pi^- e^+ e^-$. As illustrated in (Fig.3.8), consider the normal vectors to the production plane of Λ_c^+ and the W^*-boson :
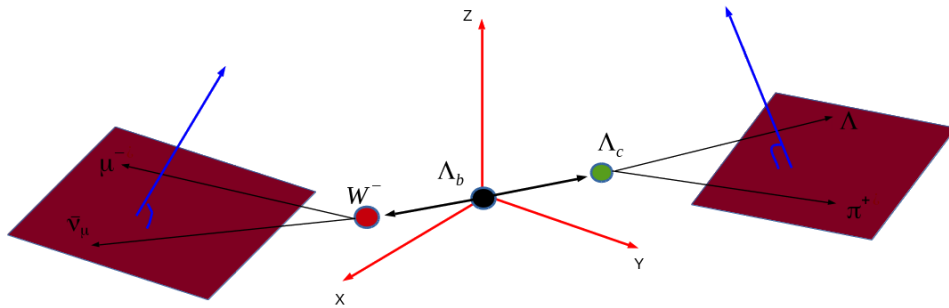

Figure 3.8: The production plane of the Λ_c^+ is determined by the momenta of Λ and π, whereas that of the W^*-boson is constructed by the momenta of the μ^- and ν (both represented in the brown colored plane). The normal vectors to the those production planes are denoted in blue and are given in eq. 3.15.

$$\overrightarrow{n_{\Lambda_c^+}} = \frac{\overrightarrow{p_\Lambda} \times \overrightarrow{p_{\pi^+}}}{|\overrightarrow{p_\Lambda} \times \overrightarrow{p_{\pi^+}}|}, \quad \overrightarrow{n_{W^-}} = \frac{\overrightarrow{p_{\mu^-}} \times \overrightarrow{p_{\nu_\mu}}}{|\overrightarrow{p_{\mu^-}} \times \overrightarrow{p_{\nu_\mu}}|} \qquad (3.15)$$

The two vectors formed above eq.(3.15) are even by T symmetry but the cosine and the sine of their azimuthal angles are odd by T. In order to prove this result, it is sufficient to write these quantities as a mixed product of the polar vectors. For the Λ_c^+ resonance, we obtain the following expressions:

$$\cos\phi_{(n_{\Lambda_c^+})} = \vec{e_Y} \cdot \frac{\vec{e_Z} \times \vec{n_{\Lambda_c^+}}}{|\vec{e_Z} \times \vec{n_{\Lambda_c^+}}|}, \quad \sin\phi_{(n_{\Lambda_c^+})} = \vec{e_Z} \cdot \frac{\vec{e_X} \times \vec{n_{\Lambda_c^+}}}{|\vec{e_Z} \times \vec{n_{\Lambda_c^+}}|} \qquad (3.16)$$

These two quantities will be denoted as the Special angles. The relation 3.17 recalls the transformation by T of the vector base of the Transversity frame used in this decay.

$$\vec{e_Z} = \frac{\vec{e_{p1}} \times \vec{p_{\Lambda_c^+}}}{|\vec{e_{p1}} \times \vec{p_{\Lambda_c^+}}|} \quad \xrightarrow{T} \quad +\vec{e_Z}, \quad \vec{e_X} = \frac{\vec{p_{p1}}}{|\vec{p_{p1}}|} \quad \xrightarrow{T} \quad -\vec{e_X}, \quad \vec{e_Y} = \vec{e_z} \times \vec{e_x} \quad \xrightarrow{T} \quad -\vec{e_Y}$$
$$(3.17)$$

Remark: the quantities $\cos\phi_{(n_{\Lambda_c^+})}$ and $\sin\phi_{(n_{\Lambda_c^+})}$ are constructed from the momenta. Since the momenta are odd by T and P, the special angles therefore change sign under these two symmetries.

3.4.2 Polarization of the Intermediate Resonances and Odd Observables under Time Reversal

The Λ_b^0 essentially is produced from strong interaction, its polarization can't be considered as a signature of Time Reversal Violation. On contrary, the components of the polarization vectors of the Λ_c^+ and the W^*-boson seem to be more relevant. In order to decompose the polarization vector of these resonances,we are going to construct the helicity frame of each of the resonances: $(\Lambda_c^+, \vec{e_{L1}}, \vec{e_{T1}}, \vec{e_{N1}})$ and $(W^-_{virtual}, \vec{e_{L2}}, \vec{e_{T2}}, \vec{e_{N2}})$, (where $\vec{e_L}$ = Longitudinal, $\vec{e_T}$ =Transverse, and $\vec{e_N}$) =Normal). Represented by figure (3.9), the two new frames are constructed starting from the Λ_b^0 Transversity frame. Their vector bases are defined as follows:
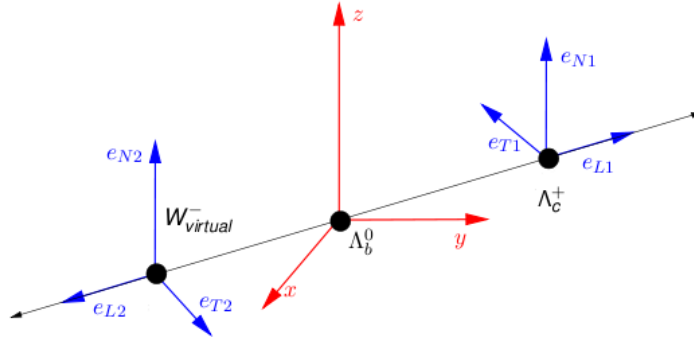

Figure 3.9: The helicity frame of each of the resonances

$$\vec{e_{L1}} = \frac{\vec{p_{\Lambda_c^+}}}{|\vec{p_{\Lambda_c^+}}|}, \quad \vec{e_{N1}} = \frac{\vec{e_Z} \times \vec{e_{L1}}}{|\vec{e_Z} \times \vec{e_{L1}}|}, \quad \vec{e_{T1}} = \vec{e_{N1}} \times \vec{e_{L1}} \qquad (3.18)$$

$$\vec{e_{L2}} = \frac{\vec{p_{\Lambda_c^+}}}{|\vec{p_{\Lambda_c^+}}|}, \quad \vec{e_{N2}} = \frac{\vec{e_Z} \times \vec{e_{L2}}}{|\vec{e_Z} \times \vec{e_{L2}}|}, \quad \vec{e_{T2}} = \vec{e_{N2}} \times \vec{e_{L2}} \qquad (3.19)$$

In order to have a clear idea on how the polarization vector of the resonance particles $R^{(i)}$ ($\Lambda_c, \Lambda^0, W^{(*)-}$) behave under discrete symmetries, the following vectors are being defined in the helicity frame of each $R^{(i)}$:

- $\vec{e_L} = \frac{\vec{p}}{p}$ with $\vec{p} = R^{\vec{(i)}}$

- $\vec{e_T} = \frac{\vec{e_Z} \times \vec{e_L}}{\vec{e_Z} \times \vec{e_L}}$, $\vec{e_Z}$ being the quantization axis in the previous frame.

- $\vec{e_N} = \vec{e_T} \times \vec{e_L}$

The general formula of the polarization vector of the resonance can be given by:

$$\vec{P^R} = P_L^R \vec{e_L} + P_N^R \vec{e_N} + P_T^R \vec{e_T} \tag{3.20}$$

Since the polarization vector is an axial one, it is important to know how its components behave under Parity and Time reversal symmetries. Tab.5.1 summarizes the transformation on the components P_L, P_N, P_T by P and T.

Observable	P	T
$\vec{e_L}$	-	-
$\vec{e_T}$	-	-
$\vec{e_N}$	+	+
$\vec{P}$	+	-
P_L	-	+
P_T	-	+
P_N	+	−

Table 3.1: Effect of Parity and Time Reversal Transformation on the components of the polarization vector.

It is clear that the normal component is odd by T. If this value is different from zero or if its distribution is not symmetric around ϕ, this means that there is a possibility for Time Reversal violation. It is important to say that the choice of the frame plays an essential role in expressing the different components of the polarization vector and hence on their transformation by T and P.

3.5   Transformation of the 4-Vector Polarization

The Lorentz transformation used to pass from one frame to another has been given. At this point, one still need to see how the spin is transformed from one frame to another.
A simple approach is to define an axial vector in Minkowski space having only three independent components and is reduced to the spin s in the proper frame of the particle. Let (S) be the 4-vector spin components of the particle in the initial frame. The co-variant extension of the spin operator is the Pauli-Lubanski quadri-vector, S^α, which is defined in the particle proper frame as : $S \equiv (S^0 = 0, \vec{S} = \vec{s})$. This quadri-vector should verify the Invariant relation $p_\mu S^\mu = 0$, where $p_\mu \equiv (m, \vec{0})$ is the momentum-energy quadri-vector in the particle rest frame.

Hence, S^α is transformed from one frame to another just like any other quadri-vector. So if $(S^\mu) = (S^0, \vec{S})$ is given in a frame (R), the Lorentz transformation of this spin as a function of $\vec{\beta}$ is given by the following relation:

$$S^0 = \gamma \vec{\beta} \cdot \vec{s}, \quad \vec{S} = \vec{s} + \frac{\gamma^2}{1+\gamma}(\vec{\beta} \cdot \vec{s}), \quad \gamma = \frac{1}{\sqrt{1-\beta^2}} \tag{3.21}$$

This relation helps in deducing the Lorentz transformation of the spin vector to any other frame, if one know the spin vector of the particle in its rest frame(generalized to polarization).

3.6 Final State Interactions

In our calculations (essentially kinematical), we do not take into account the final state interactions(PSI), which play an important role in all hadron interactions. When hadrons are produced in any process, the strong interactions between them modify their final wave-function; Which causes the modification of some physical observables.

Upon passing from a forward to backward reaction(Time Reversal), the initial and final states will be changed where as the momentum and the spin vectors will be reversed. However, supposing that T is an exact symmetry, forces the total amplitude of the decay to be unchanged. Or in other words,

$$|A(\vec{p_i}, \vec{s_i} \to \vec{p_f}, \vec{s_f})| = |A(-\vec{p_f}, -\vec{s_f} \to -\vec{p_i}, -\vec{s_i})|$$

Where $(\vec{p_i}, \vec{s_i})$ and $(\vec{p_f}, \vec{s_f})$ represents the initial and final states momentum and spin vectors. If the above equation is not verified, this could be a sign of violation of T. In the process that involve final state Interactions (FSI), there are differences between the physical process and its T-transformation.

So FSI could simulate a TR violation, even if the latter is assumed to be accurate. In the case where FSI are negligible, the inequality between the amplitudes (forward and backward) would be a sign of violation of the symmetry T (Theorem of Wolfenstein,1999)[60].

In a brief summary for this chapter, the phenomenological study of the Semileptonic decays has been performed. It has also been discussed the method of calculating the polarization of the Λ_b^0 and the resonant particles. This method is based on the Jacob-Wick and Jackson helicity formalism.

The angular distribution relations have been established, which directly permit to extract the Λ_b^0 polarization and many other important parameters.

It has been also seen that, usually, the normal component of the polarization vector of the intermediate resonance is odd by T. If this value is different from zero, this means a direct test for Time Reversal Violation.

The next chapter is dedicated to the experimental study of the Λ_b^0 decay and the analysis of the data recorded by the LHCb experiment.

Chapter 4

Reconstruction and Selection of the Events

Contents

In both p-p and p-A collisions at low and intermediate energies, hyperons $(\Lambda, \Sigma, ...)$ are produced with an important transverse polarization. Extrapolating these results to much higher energies (like at LHC), we expect that heavy hyperons like $\Lambda_b^0, \Sigma_b, ...$ are also polarized with a non vanishing transverse one. The polarization value (P_b) could be as large as 20%. The polarization of Λ_b^0 produced in hadronic environments has been measured [61]. However, Λ_b^0 produced in $e^+e^- \to Z^0 \to b\bar{b}$ are found to be substantially polarized, in agreement with the $Z^0 b\bar{b}$ coupling of the Standard Model (SM). This was studied at LEP by the ALEPH, OPAL and DELPHI collaborations ([62]-[64]) in $\Lambda_b^0 \to \Lambda_c^+ l \nu_l$ decays. For such semileptonic decay, the momentum distribution of the lepton is sensitive to the polarization. The measurement however suffers from large uncertainty from form-factor models used to predict the lepton distribution.

Semileptonics are the most abundant b-decays and so could be used to measure the life-time and the polarization of the Λ_b^0 with high statistics; however in the decay, a neutrino is emitted which cannot be detected by LHCb. This leads to the momentum of the Λ_b^0 being incorrectly reconstructed, which in turn affects the measurement of its life-time. Compensating for the additional momentum is required in any time-dependent analysis. It is a prior more difficult to select the correct primary vertex (PV) in partially reconstructed decays, since the momentum vector of the reconstructed part may not point to the correct PV; as shown in the cartoon (Fig.4.1) . Since the running conditions for 2010 and 2011 at the LHC are expected with a much higher PV multiplicity than all previous Monte Carlo studies, an investigation of the time-dependent effects of high pileup was performed.
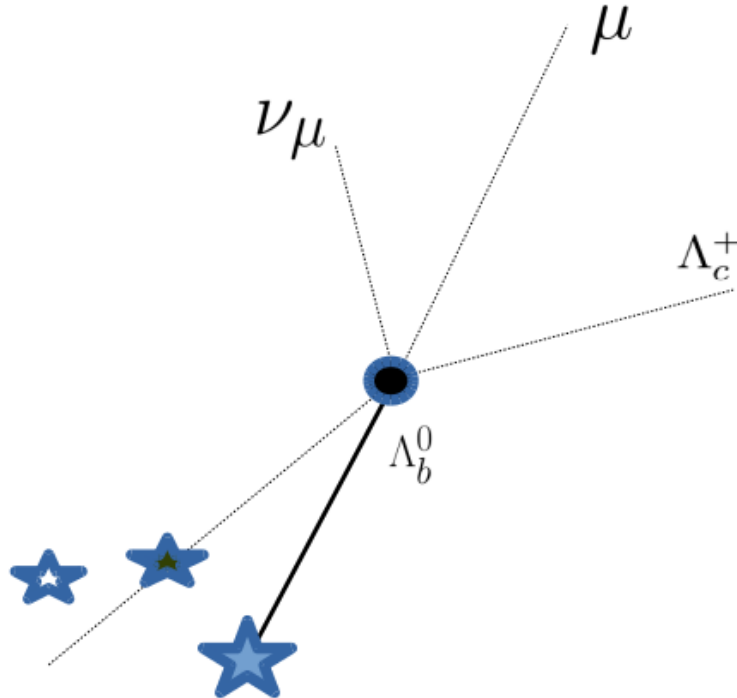

Figure 4.1: This cartoon shows a typical $\Lambda_b^0 \to \Lambda_c^+ \mu \nu_\mu$ decay. There are a neutrino, a Λ_c^+ and a muon emitted in this Λ_b^0 decay. The three stars show the multiple primary vertices in the event. The dotted line shows the reconstructed $\Lambda_c^+ \mu$ momentum pointing back to one primary vertex, however the solid line shows the true momentum which includes the neutrino momentum as well, which points back to another primary vertex.

4.1 Corrections for the missing final state particle

There are multiple methods used to correct the Λ_b^0-momentum for possible missing neutrino energy. Each method has both advantages and disadvantages that will be discussed in the sections below. In section 5.1.1, we present a method that depends on the kinematics of the decay, called " Neutrino Reconstruction ".It is a data-based method that aims to calculate the momentum of the neutrino and thus that of the Λ_b^0. In section 5.12, we present a MC method based on a statistical correction, and it is called "k-factor". In section 5.1.3 an attempt to combine these two methods is presented.

Figure 2.12 shows the different track types used in the LHCb detector. Since the study involves the presence of the Λ particles, emphasis are set on two types of tracks:

- particles decaying in the Vertex Locator (VELO) are reconstructed as Long Tracks and will be denoted by LL.

- particles decaying between the VELO and the Trigger Tracker (TT) are reconstructed as Downstream tracks and will be denoted by DD.

4.1.1 Neutrino Reconstruction

The missing momentum vector can be calculated using the kinematic information from the decay. However, to correct the Λ_b^0-momentum a few assumptions are necessary to be taken into consideration. The invariant mass of the missing state vector must be assumed. This is straight-forward if we assume there is only one missing particle, and it is a mass-less neutrino. If there are multiple neutrinos, the invariant mass of that system cannot be simply calculated and this assumption is invalid, but we ignore that for now. The flight direction of the Λ_b^0 baryon is reconstructed using the primary vertex and Λ_b^0 decay vertex positions. The momentum of the $\Lambda_c^+\mu$ can then be broken down into components parallel and perpendicular $(\vec{P}^{\parallel}_{\Lambda_c^+\mu}, \vec{P}^{\perp}_{\Lambda_c^+\mu})$ to the Λ_b^0 flight direction $\hat{F} = \frac{\vec{F}}{|\vec{F}|}$. $\vec{F}$ is given by the following relation $\overrightarrow{F} = \overrightarrow{EV} - \overrightarrow{PV}$ where $\overrightarrow{EV}$ is the Λ_b^0 end vertex position (where the Λ_b^0 decays) and $\overrightarrow{PV}$ is the position of the primary vertex.

$$\overrightarrow{P^{\parallel}_{\Lambda_c^+\mu}} = \hat{F}.\overrightarrow{P_{\Lambda_c^+\mu}} \tag{4.1}$$

$$\overrightarrow{P^{\perp}_{\Lambda_c^+\mu}} = \overrightarrow{P_{\Lambda_c^+\mu}} - (\hat{F}.\overrightarrow{P_{\Lambda_c^+\mu}})\hat{F} \tag{4.2}$$

Now we use the conservation of the momentum and energy,

$$\overrightarrow{P^{\perp}_{\Lambda_c^+\mu}} = -\overrightarrow{P^{\perp}_{\nu}} \tag{4.3}$$

$$\overrightarrow{P_{\Lambda_b^0}} = \overrightarrow{P^{\parallel}_{\Lambda_c^+\mu}} + \overrightarrow{P^{\parallel}_{\nu}} \tag{4.4}$$

$$E_{\Lambda_b^0} = E_{\Lambda_c^+\mu} + E_{\nu} \tag{4.5}$$

we make use of the $E^2 = m^2 + P^2$ (c=1) and equation 4.5 can be written in terms of equations 4.4 and 4.3 to obtain a quadratic equation of the form:

$$0 = aP_\nu^{\parallel 2} + bP_\nu^\parallel + c \tag{4.6}$$

and here we define a, b, and c as the following:

$$a = 4(P_{\Lambda_c^+\mu}^{\perp 2} + m_{\Lambda_c^+\mu}^2) \tag{4.7}$$

$$b = 4P_{\Lambda_c^+\mu}^\parallel(2P_{\Lambda_c^+\mu}^{\perp 2} - (m_{\Lambda_b^0}^2 - m_{\Lambda_c^+\mu}^2)) \tag{4.8}$$

$$c = 4P_{\Lambda_c^+\mu}^{\perp 2}(P_{\Lambda_c^+\mu}^{\parallel 2} + m_{\Lambda_b^0}^2) - (m_{\Lambda_b^0}^2 - m_{\Lambda_c^+\mu}^2)^2 \tag{4.9}$$

where we have $m_{\Lambda_b^0}$ is the Particle Data Group(PDG) mass of the Λ_b^0 and $m_{\Lambda_c^+\mu}$ is the reconstructed mass of the $\Lambda_c^+\mu$ combination. The last equation thus can be solved using the following formula:

$$P_\nu^\parallel = \frac{-b \pm \sqrt{b^2 - 4ac}}{2a} \tag{4.10}$$

However, this gives two possible solutions. It was shown that neither is more likely to be correct, and they are mostly completely ambiguous [65]. Choosing a solution at random is as good as any other method, giving half correct and half incorrect answers. For this study we choose the smallest solution. Since the smallest solution is the minimum correction from this method, and, when it is correct, it logically has a smaller associated error, since less momentum was taken by the neutrino in this case. Studies on Monte-Carlo are done and it shows that there is no bias in choosing the smallest value [66].

4.1.2   k-factor

In MC simulations, we are able to estimate the momentum of the missing particles and correct it using some statistical methods. There is correlation between the missing mass of the system and the momenta carried by the missing state, and therefore any correction to be done is parametrized in terms of the remaining mass of the $\Lambda_c^+\mu$-state which was reconstructed.
By means of the MC simulations, the correction factor can be estimated. It is the ratio of the reconstructed $\Lambda_c^+\mu$ momentum to the true $\Lambda_c^+\mu$ one and it is denoted by the k-factor.

The Slices are taken as seen in figure 4.2 through this plot in the reconstructed Λ_b^0-mass to average the k-factor per bin of reconstructed mass. The mean of each slice is then taken and fitted with a second order polynomial. By calculating the correction factor on an event-by-event from the fit function, the missing momentum in the system is being corrected.
Each slice has a its significant width, and therefore there seems to be a very large uncertainty in the k-factor, which gets worse at lower reconstructed masses.
The k-factor is calculated on the whole Monte Carlo sample then applied to the same sample, which introduces a small statistical bias in this study.
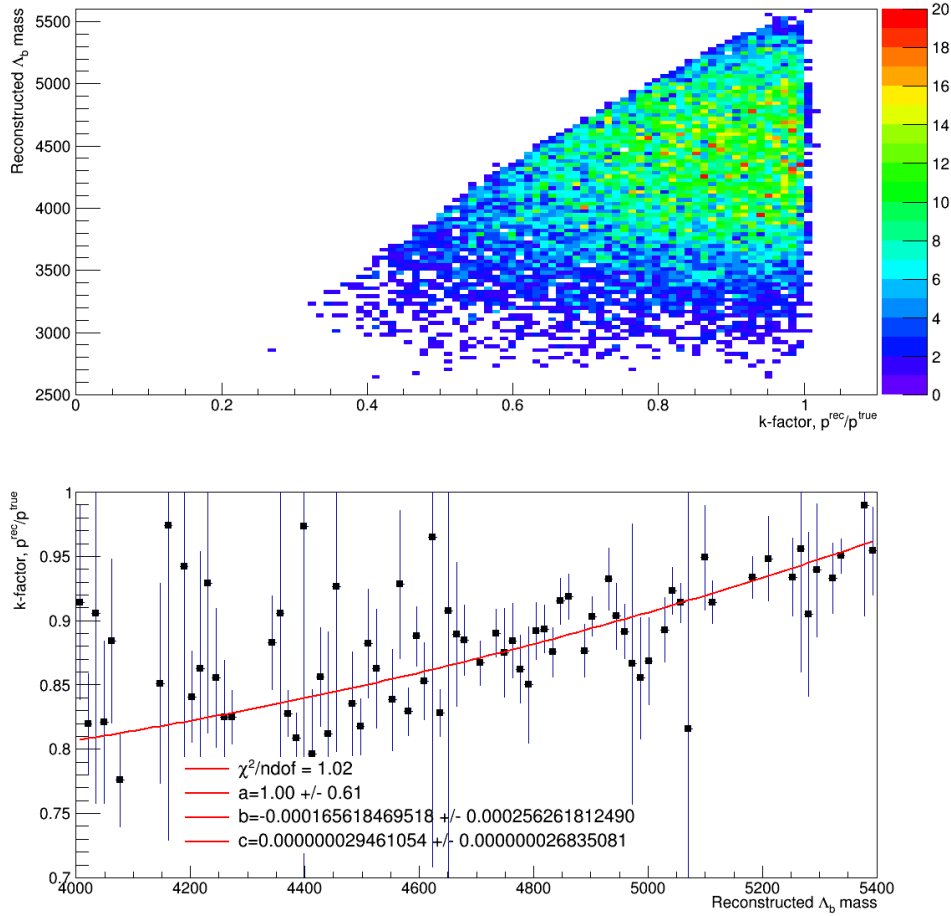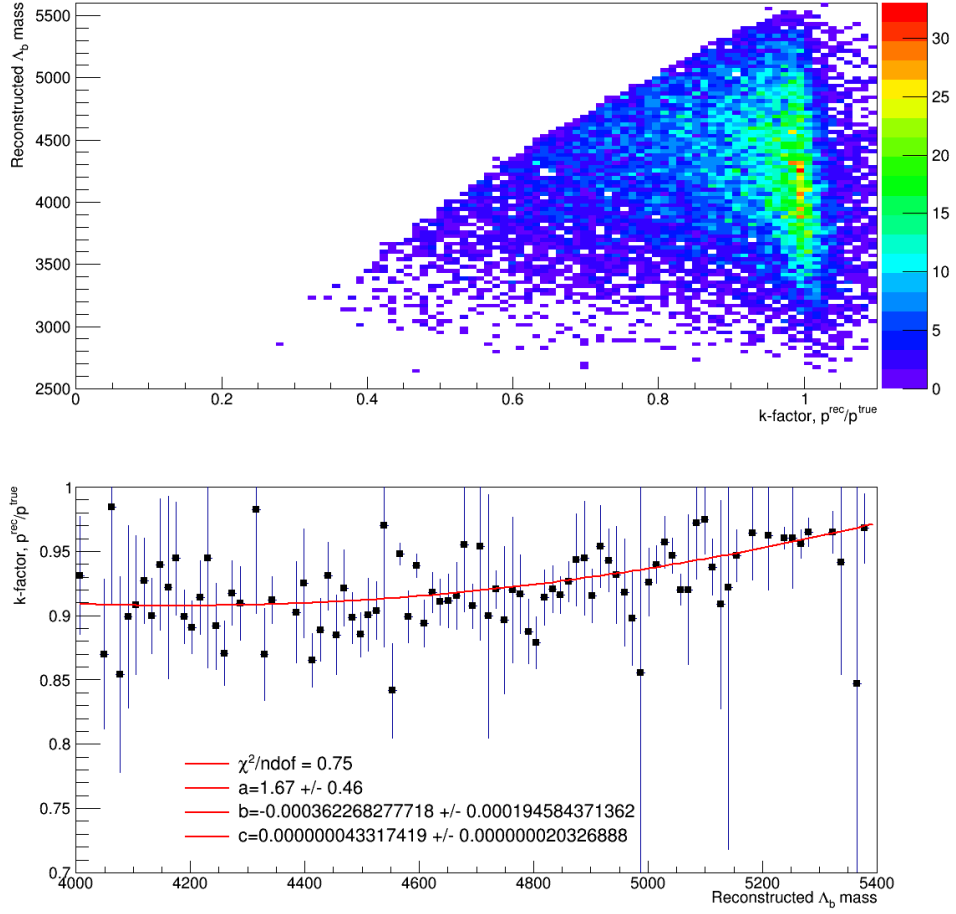
Figure 4.2: The k-factor in MC11 data. The magnitude of the reconstructed Λ_b^0-momentum, $P^{\vec{rec}}$, divided by the magnitude of the true Λ_b^0-momentum, $P^{\vec{true}}$, is plotted against the reconstructed mass of the Λ_b^0. In the bottom picture, slices are taken through the distribution along the $m_{\Lambda_c^+ \mu}$ axis to calculate the average correction factor, and a second order polynomial fit is made.

4.1.3 Neutrino Reconstruction plus k-factor

In the neutrino reconstruction method,the smallest solution is being taken, to make sure that there is less propagation of the error.

In the MC, after the neutrino reconstruction method had already been applied, again the k-factor distribution was fitted as a function of the reconstructed mass. The new k-factor is calculated on the whole Monte Carlo sample then applied to the same sample as seen in figures 4.3.

Figure 4.3: The k-factor in MC11 data after the neutrino reconstruction -starting from up- for DD(particle, anti-particle). The magnitude of the reconstructed Λ_b^0-momentum, $\vec{P^{rec}}$, divided by the magnitude of the true Λ_b^0-momentum, $\vec{P^{true}}$, is plotted against the reconstructed mass of the Λ_b^0. In the bottom, slices are taken through the distribution along the $m_{\Lambda_c^+ \mu}$ axis to calculate the average correction factor, and a second order polynomial fit is made.

4.2 Data and Monte Carlo samples

The results described in this thesis are obtained using the full Run I data collected by LHCb at the LHC at a center-of-mass energy of $\sqrt{s} = 7$ TeV for the year 2011 and $\sqrt{s} = 8$ TeV for the year 2012. The 2011 data corresponds to an integrated luminosity of $L = 1 fb^{-1}$, while 2012 data corresponds to $L = 2 fb^{-1}$.

Monte Carlo (MC) generated samples are produced using Gauss. They are used to study the behavior of the signal and background events in order to model the invariant mass line-shapes of signals, signal cross-feeds and backgrounds.

The simulation conditions have the same value of the pile-up factor ($\nu = 2.5$) for both 2011 and 2012 in order to resemble the data taking conditions. The trigger conditions however, are different for 2011 and 2012, and hence the MC samples are simulated using TCKs (Trigger configuration key: The HLT is configured via a unique key, that defines the sequence of algorithms, and the cuts (we refer to them as filters of a selection)) that are representative of the two data taking periods. The number of MC events produced for the signal decay mode for each year is summarized in Tab.4.1. About 50% of these events are produced with Mag-down detector configuration, and the other 50% are produced with Mag-up detector configuration using Pythia8 event generators. As far as signal events are concerned, we have chosen to simulate a mixture of resonating (phase space) and quasi-2-body decays involving either a Λ_c^+ and Λ baryon associated with a low-mass meson.

Decay mode	Event type	Year	Yield	Resonant
$\Lambda_b^0 \to \Lambda_c^+ \mu^- \bar{\nu}_\mu$	15574133	2012(2011)	93982(62174)	$\Lambda_c^+ \to \Lambda(p\pi^-)\pi^+$

Table 4.1: Summary of the simulation samples generated for this analysis in official Sim09b with 2011 conditions (1/3 of total events) and 2012 conditions (2/3 of total events).

4.3 Stripping Event Selection Criteria

4.3.1 Available data sample

In this analysis we use the full run 1 data set($\int L = 3 fb^{-1}$) proceeded with the stripping conditions as shown in Tab.4.2. MC simulated data samples are generated for each Λ_b^0 exclusive semileptonic decay mode with a HQET inspired form factor model [67], with the final states shown in Tab.4.1. These samples are processed using the DaVinci v36r1p1 package.

Sample	Stripping	luminosity	Stripping
2011	Charm/Phys/b2LcMuXL0PiCharmFromBSemiLine/Particles	$1.0 fb^{-1}$	21r1
2012	Charm/Phys/b2LcMuXL0PiCharmFromBSemiLine/Particles	$2.0 fb^{-1}$	21

Table 4.2: List of 2011 (Stripping 21r1) and 2012 (Stripping 21) data samples used.

4.3.2 Reconstruction of $\Lambda_b^0 \to \Lambda_c^+ \mu^- \bar{\nu}_\mu$ decay

In an LHCb event, one detects such a process by looking for a Λ_c^+ resonance. The event is kept only if the invariant mass of the detected ($\Lambda\pi$) system is within ± 77 MeV of the PDG mass value of the Λ_c^+ particle ($m_{\Lambda_c^+} = 2287$ MeV), and that the two daughter particles point at the same vertex in space.

Λ_c^+ candidates are formed combining Λ and a π^+, where the Λ is formed by combining a proton and a pion, according to the selection criteria shown in Tab.4.4. It

is also asked that a detected muon points to the same vertex as the reconstructed Λ_c^+ momentum (so that they probably come from the same Λ_b^0). LHCb does not cover a 4π solid angle, so no missing energy is measured and the neutrino in $\Lambda_b^0 \to \Lambda_c^+ \mu^- \bar{\nu}_\mu$ is not reconstructed. Therefore, the Λ_b^0 mass spectrum does not clearly peak at mPDG(Λ_b^0) =5624 MeV, so there is only a broad cut in Λ_b^0 reconstructed mass. After that, Λ_c^+ and the identified muon μ^- are kept if the vertex quality criteria is well satisfied.

The Λ_c^+ may be a ground state, or in excited state of higher mass that decays into ground state and other particles that will not be reconstructed and are considered missing particles as the neutrino.

Variable definition	Symbol
Momentum	P
Transverse momentum	P_T
χ^2 over degrees of freedom	$\chi^2/NDOF$
Track's probability of being a ghost track	$GhostProb$
Track's probability of being a muon	$ProbNNmu$
Track's probability of being a proton	$ProbNNp$
Particle identified as muon	ISMUON
Delta-log-likelihood for the given hypothesis (wrt the pion): $\Delta logL = \frac{L_x}{L_\pi}$	$DLL_{x\pi}$
Clone killer	$CloneDist <= 0$
Proper time	τ
Impact parameter	IP
Angle between particle momentum and beam-axis	$\cos\theta$
Angle between particle momentum and direction of flight from PV to DV.	DIRA
Primary vertex and Decay vertex	PV and DV
pseudo rapidity	η

Table 4.3: Definition of the variables

Variable definition	Selection requirements
Muon selections	
Muon momentum	$P > 3000$
Muon transverse momentum	$P_T > 1200$
Muon track's χ^2 over degrees of freedom	$\chi^2/NDOF < 4$
Muon track's probability of being a ghost track	$GhostProb < 0.3$
Muon track's probability of being a muon	$ProbNNmu > 0.4$
Muon track's probability of being a proton	$ProbNNp < 0.2$
ISMUON (particle identified as muon)	OK
Daughter selections	
Pion momentum	$P > 1500$
Pion transverse momentum	$P_T > 250$
Pion track's χ^2 over degrees of freedom	$\chi^2/NDOF < 4$
Pion track's probability of being a ghost track	$GhostProb < 0.3$
Particle Identification for Pions	$DLL_{K\pi} < 10$
Particle Identification for Protons	$DLL_{p\pi} < 10$ and $DLL_{p\pi} - DLL_{K\pi} > 0$
Clone killer	$CloneDist <= 0$
Λ_c^+ selections	
Sum of transverse momenta (p_T) of daughters	$p_T > 1800$
Vertex fit quality	$\chi^2/NDOF < 6$
Proper time	$\tau > 0$
Angle between Λ_c^+ momentum and beam-axis	$\cos\theta > 0.99$
Λ_b^0 selections	
Sum of transverse momenta (p_T) of daughters	$p_T > 1800$
Vertex fit quality	$\chi^2/NDOF < 6$
Λ_b^0 vertex	$Z(\Lambda_c^+) - Z(\Lambda_b^0) > 0$
DIRA: Direction angle	$\cos\theta > 0.999$
η pseudo rapidity	$2 < \eta < 5$
Invariant Mass $\Lambda_c^+\mu$	$[2500, 6000]$MeV
Other selections	
Trigger selections	Hlt2TopoMu2,3,4Body TOS on $(p\pi\pi, \mu)$
Global event multiplicity	long tracks$<= 250$

Table 4.4: Selection criteria of $\Lambda_b^0 \to \Lambda_c^+ (\to \Lambda(p\pi^-)\pi^+)\mu^-\bar{\nu}_\mu$

4.4   Identification of backgrounds

There are at least three types of backgrounds to be studied in this analysis. These are (1) the peaking backgrounds coming from decays with the same final state particles as the signal decay mode, (2) the partially reconstructed backgrounds, (3) the random combinatorial of one or several tracks unrelated to the signal decay, and (4) finally the backgrounds coming from excited states $\Lambda_b^0 \to \Lambda_c^*\mu^-\bar{\nu}_\mu$.

4.4.1   Peaking backgrounds

The analysis procedure presented here also takes into account the peaking backgrounds. These backgrounds, unlike the smooth backgrounds, cannot reliably be modeled as fit components whose parameters floats due to the fact that they resemble the shape of the signal. The alternative is to calculate from the Monte Carlo there parameters and fix them in the mass spectrum, extract their yields and then subtract their contributions.

We have one observation about the final state coming from Λ_c^+ , which is $p\pi^-\pi^+$. The $BR(\Lambda_c^+ \to \Lambda\pi) \times BR(\Lambda \to p\pi^-) = 0.0146 \times 0.63 = 0.009$. We also have another decay with the same final state, $\Lambda_c^+ \to p\pi\pi$, with a branching ratio of about 0.005. This is a significant fraction relative to the decay via hyperon. This decay is potentially tricky for us as it peaks directly at the Λ_c^+ mass with a similar width. Such contribution could be reduced by constraining the Λ life-time (τ_Λ) and its flying distance (FD_Λ).

However, the stripping also requires that the reconstructed lambda mass must be within 30 MeV of the nominal PDG mass, so this will suppress the $p\pi\pi$ contribution greatly. Another way to effectively reject random combination of tracks when forming reconstruction particles, a criteria widely used in particle physics is the quality of the vertex fit, χ^2. This criteria determines how tracks (Λ, π^+) can be fitted to form a common vertex (Λ_c^+). The smaller χ^2, the more probable the tracks are originating from the same vertex. The χ^2 requirement for the reconstruction of the Λ_c^+ is illustrated in Fig.4.4

(a) lose χ^2 (b) tight χ^2
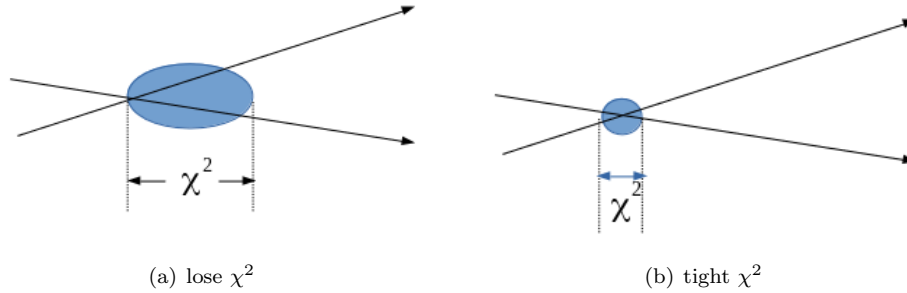
Figure 4.4: Fit of two tracks to a common vertex. The shaded blue region illustrate the vertex fit quality. (a) shows a lose vertex fit corresponding to a high vertex χ^2, (b) shows a tight vertex fit corresponding to a low vertex χ^2.

4.4.2   Partially reconstructed backgrounds

A missing particle in any decay could result in shifting the mass spectrum of the particle studied (Λ_c^+) or, in some cases, can lead to populating the events in the left side of the mass spectrum. This case is known as the partially reconstructed decay. For the decay, $\Lambda_b^0 \to \Lambda_c^+(\to \Lambda(p\pi^-)\pi^+)\mu^-\bar{\nu}_\mu$, we are concerned in the Λ_c^+ mass spectrum. We can neglect all the decays that contain the π^0 particles due to the fact that the Λ_c^+ mass spectrum lays between [2210,2370]. This mass window is slightly above the mass threshold chosen when modeling this background. In other words, to have a partially reconstructed backgrounds with a missing π^0, the mass spectrum should begin from $m_{\Lambda_c^+} - m_{\pi^0} = 2287 - 134.9 = 2152.0 < 2210$ which is the beginning of the Λ_c^+ mass spectrum.

The dominant contributor of the partially reconstructed backgrounds are the events with a missing γ coming from the $\Lambda_c^+ \to \Sigma^0(\Lambda\gamma)\pi^+$. Because of the vanishing mass of the photon, the end-point of these partially reconstructed decays sits just at the beginning of the signal peak (2260 MeV). The fit of this background is obtained from the Monte-Carlo as a Gaussian function whose mean and sigma are fixed (from the Monte-Carlo) while the yield remains floating.

4.4.3   Combinatorial Background

The last type -aside from the physical backgrounds- is the combinatorial background that comes from the combination of tracks unrelated to the signal decay. The topology and kinematics of these background events are different from those of the signal. To reduce the contribution of these backgrounds, it is possible to use a multivariate-based cuts. It is worth to say that eliminating the different above-mentioned sources of backgrounds (not easy for sure) depends on suppressing as much as we can of the combinatorial background. Therefore, a new special tool has been designed to fight against the combinatorial background. It is a BDT-based MVA method that is trained using **non-linearly correlated** variables for background and signal events in order to reduce these as much as possible from

these backgrounds. After the BDT training, those combinatorial backgrounds are modeled using an exponential function and extrapolated over the whole mass spectrum. The slope is fixed while the yield is kept free to float. By that one will be able to eliminate the combinatorial that lay under the signal and in the partially reconstructed region.

4.4.4 $\Lambda_b^0 \to \Lambda_c^* \mu^- \bar{\nu}_\mu$ Excited States

The contribution of Λ_c^+ coming from an excited state Λ_c^* and not directly from the Λ_b^0 is huge. However, constraining some kinematical variables such as the Λ_b^0-momenta, z-position of Λ_c^+ decay vertex and the Λ_c^+-momenta will reduce this contribution a lot. It is clear that the kinematics of a Λ_c^+ from Λ_c^* are not like those coming from Λ_b^0, and this gives the opportunity to reduce such backgrounds depending on the kinematics. The study of these excited states is not finished yet, but once it is done the results will be so promising.

4.5 Selections

To reduce the backgrounds for the reconstructed particles which are saved after the stripping line selections (while keeping the signal events), further offline selection cuts are applied. We have used the following strategy in the offline cuts : start with some topological and kinematical cuts to reduce great percentage of the backgrounds having distributions different from those of the signals. This allows to have a pure combinatorial backgrounds in the Right Hand Side Band (RHSB). After that, multivariate analysis is being used to subtract the contribution of those combinatorial backgrounds laying under the signal region. Last but not least, the optimization of the PID cut values are also presented.

4.5.1 Offline Selections

Further offline selection and trigger requirements cuts are applied to the stripped data before the passage to particle identification (PID) optimization and multivariate (MVA) selection.
In the stripping selection, the candidate events are reconstructed as $\Lambda_b^0 \to (\Lambda_c^+ \to \Lambda(p\pi^-)\pi^+)\mu^- \bar{\nu}_\mu$ with some PID requirement applied on the final charged particles. However, in the final tupling of the data, each candidate is reconstructed using the appropriate mass hypotheses of the daughter particles corresponding to the different possible final states. The mass range cut on the Λ_b^0 is required to be in a wide range [2500,6000]MeV. We also set the range of the $Q_{\mu\nu}^2 = [0,20]GeV^2$ which corresponds to the momentum transfer between the final and the initial particles ($(P_{\Lambda_b^0} - P_{\Lambda_c^+})^2$).

4.5.2 Trigger Selections

There are specific trigger requirements used to select the desired candidates. Such selections are applied in both reconstruction and offline selections. Some useful definitions are introduced here (for efficiencies see Tab.(4.9):

- **Trigger On Signal (TOS)**: Λ_b^0 candidates are defined TOS if they have already triggered a particular trigger line. In other words, the signal tracks are sufficient to select the event via the particular line in question.

- **Trigger Independent of Signal (TIS)**: A candidate is defined TIS if the event has been triggered by the particular trigger line independent of the candidate itself. TIS events are able to provide unbiased samples because the Λ_b^0 candidate did not play a role in triggering the line.

In order to provide a good background rejection and a high signal efficiency, HLT2 n-body lines are used. The HLT2 n-body are topological lines designed to trigger on decays B⟶ anything with at least two charged particles, exploiting all the common decay properties of the b-hadrons.

The trigger is requested to be on as show in Tab.(4.5).

Variable definition	Selection requirements
L0 Trigger selections	
Λ_b^0 L0Global TOS	OK
Λ_b^0 L0MuonDecision TOS OR μ^- L0 MuonDecisionTOS	OK
HLT2 Trigger selections	
Λ_b^0 Hlt2Global TOS	OK
Λ_b^0 Hlt2TopoMu(2,3,4)BodyBBDTDecision TOS	OK

Table 4.5: Trigger offline selections of $\Lambda_b^0 \to \Lambda_c^+ (\to \Lambda(p\pi^-)\pi^+)\mu^- \bar{\nu_\mu}$.

4.5.3 PID Selections

The PID selections for the final charged particles has been chosen to be so tight in order to reject forward mis-identification of the particles. There was a big risk in the choice of these selection, because of losing some of the signal events. However, this was necessary for the analysis. The absence of the kaon in the final particles and the presence of the muon helps in optimizing the PID selections, hence there was no need for using PIDCalibration to chose the PID cuts. It was sufficient to use straight cuts on the final charged particle

Definition	Variable
Charged Tracks selections	
Probability of the proton to be a pion	$pplus\_ProbNNpi < 0.2$
Probability of the pion to be a pion	$piplus\_ProbNNpi > 0.8$
Probability of the proton to be a proton	$pplus\_ProbNNp > 0.2$

Table 4.6: PID selection criteria.

(Fig.4.5) shows the effect of the PID cuts on the Λ_c^+ mass spectrum. The blue curve represent the raw data before applying the PID cuts, whereas the red curve represents the number of events remaining after performing the cuts shown in Tab.4.6.Here it appears clearly the power of the PID cuts chosen in reducing the backgrounds (for efficiencies see Tab.(4.9). This step was done before the TMVA Training in order to maximize the last.
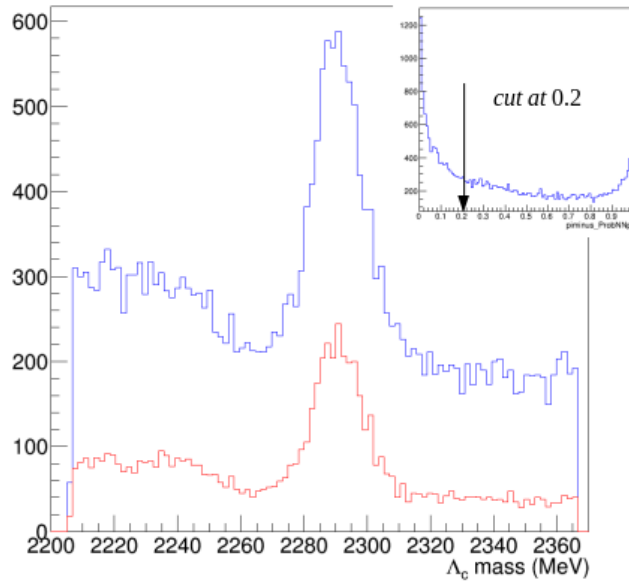
Figure 4.5: PID cuts efficiency in reducing BKG.

4.5.4 Multivariate Analysis

In order to determine the masses of the Λ_c^+ baryons, it is crucial to find an accurate description of the signal and the background underneath the signal peak. This process can be simplified by reducing the combinatorial background in this region and thereby minimizing its impact. A good handle to do so is reducing the combinatorial background caused by wrongly combined $(p\pi^-\pi^+)$ candidates. We use the technique of multivariate analysis to fuse different, less effective selection parameters into one powerful selector.

TMVA (Toolkit for Multivariate Analysis [68]) is used for discriminating the signal from the backgrounds, and defining the optimal cut point used to reject the last [69]. It is based on processing, parallel evaluation and application of multivariate classification and multivariate regression techniques. TMVA makes use of training events, to determine the mapping function that either describes a decision boundary (classification) or an approximation of the underlying functional behavior defining the target value (regression). The mapping function can contain various degrees of approximations and may be a single global function, or a set of local models. Most of the high energy analysis uses MVA training as a tool for eliminating backgrounds (especially combinatorial ones).

Boosted Decision Tree
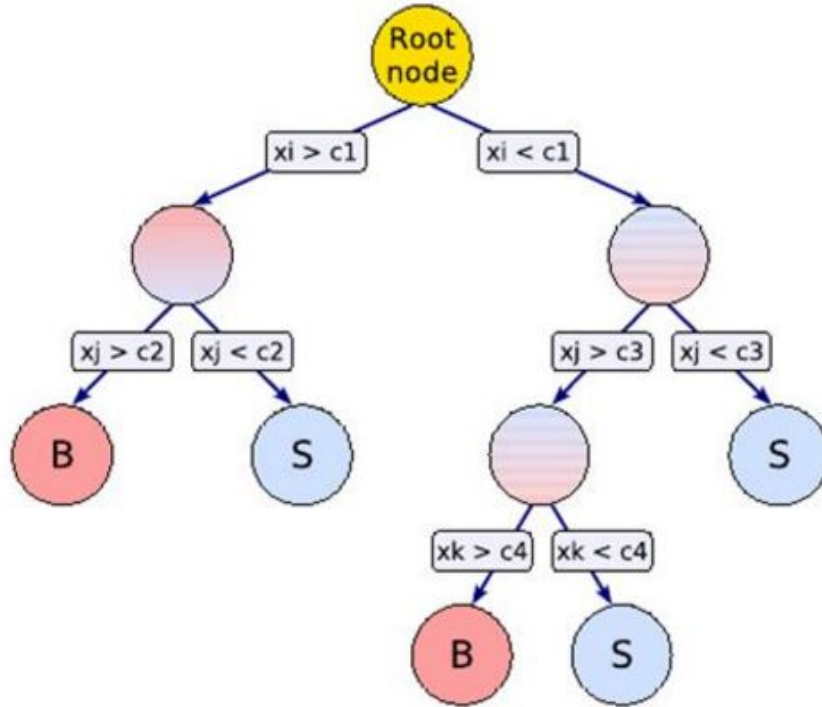
Figure 4.6: Schematic view for Boosted Decision Tree, where "x" is the variable , "c" represents the cut on this variable, "S" stands for the signal events and "B" for the backgrounds events.

The Boosted Decision Tree (BDT Fig.4.6) is found to be the most effective method to separate signal and background. A BDT is the conjunction of many decision trees which form a forest. Boosting stabilizes the response and enhances the performance with respect to a single tree method. More details about the implementation of the used BDT can be found in Ref. ([70], [71]).

We have chosen twelve discriminating variables for the training of the BDTs. These are the topological and pointing variables of the candidate baryon $\Lambda_b^0 : \chi_{IP}^2, \theta_{DIRA}^{\Lambda_b^0}$ in a cone around the direction of the Λ_b^0 candidate. The last category of variables is

Definition	Variable
Λ_b^0 Variables	
Λ_b^0 Track's minimum impact parameter χ^2 to the PV	$\chi_{IP}^2(\Lambda_b^0)$
Λ_b^0 direction angle	$\theta_{DIRA}^{\Lambda_b^0}$
Λ_b^0 X component of the momentum	$\Lambda_{b\,PX}^0$
Λ_b^0 Y component of the momentum	$\Lambda_{b\,PY}^0$
Λ Variables	
Λ Direction angle	θ_{DIRA}^{Λ}
Charged Tracks selections	
μ^- Track's χ^2 over NDF	$\chi_{TRACK}^2(\mu^-)/NDF$
π^+ Track's χ^2 over NDF	$\chi_{TRACK}^2(\pi^+)/NDF$
π^- Track's χ^2 over NDF	$\chi_{TRACK}^2(\pi^-)/NDF$
p^+ Track's χ^2 over NDF	$\chi_{TRACK}^2(p^+)/NDF$
π^- Transverse momentum	π_{PT}^-
π^+ Transverse momentum	π_{PT}^+
p^+ X component of the momentum	p_{PX}^+

Table 4.7: List of variables used in the BDT training.

the quality of the tracks of the final particles : χ_{Track}^2 and the P_T of the candidates π^-, π^+. Furthermore, samples of both magnet polarities have been merged but split our data-set for the years 2011/2012 and evaluate them separately. In addition, we bisect the samples into a training and a test sample (50 : 50). The training sample is used to adjust the parameters of the BDT and the test sample to evaluate its efficiency and to test for over training. For better TMVA training, a spontaneous sPlot [72] has been done, extract the signal yields and after that a comparison between this extracted signal and the Monte Carlo has been performed. This step permits to separate the good variables from the bad ones used in the TMVA training (Fig.4.7).

These input variables, described in Tab.4.7, are feed within a signal and a background sample into the BDT method. In order to train the BDT, the signal samples are obtained from a MC sample of the Λ_b^0 decay. The pure combinatorial background is chosen to be from the right-hand sideband (RHSB) of the Λ_c^+ mass spectrum ($\Lambda_c^+ > 2300 MeV$). The distribution of these variables are shown in Tab.B.4, (for the rest see appendix B, section: Signal background distribution figures).

One of the important remarks to be added here is the difference in the BDT response between long long tracks and the down down ones.
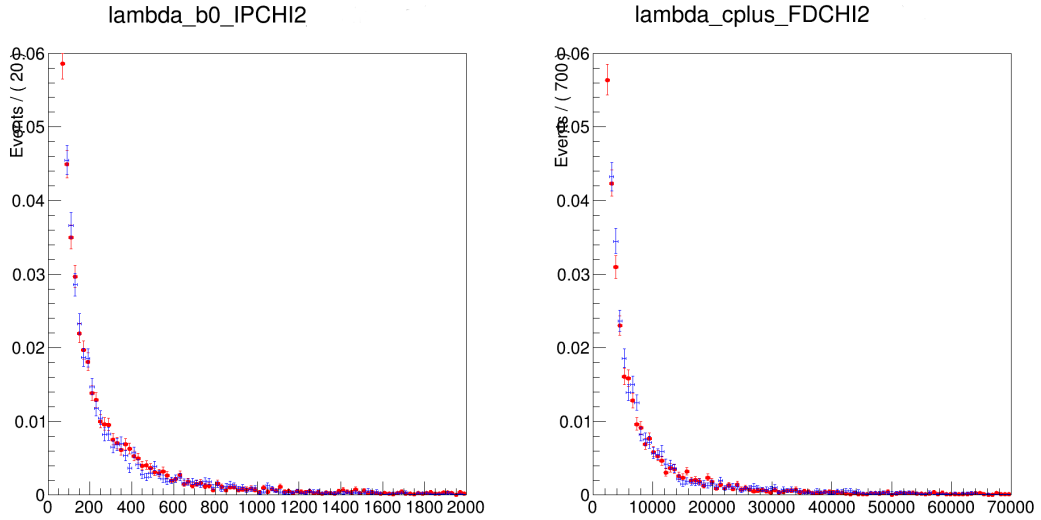
(a) Good Variables: $\chi^2_{IP}(\Lambda^0_b)$ and $\chi^2_{FD}(\Lambda^+_c)$
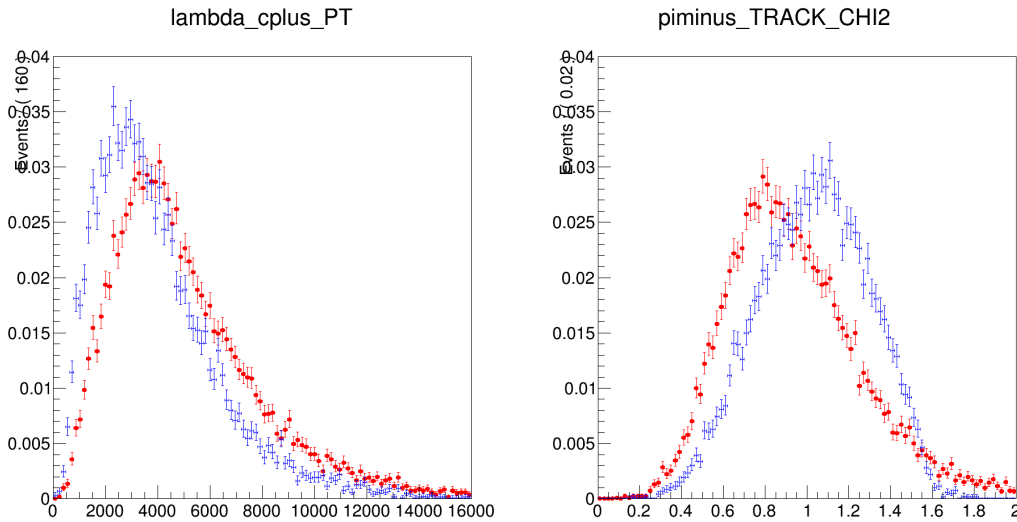
(b) Bad Variables : $P_T(\Lambda^+_c)$ and π^- track χ^2

Figure 4.7: A fit that shows the super-position between the signal (MC) and the extracted one (spontaneous sPlot) where we have: (a) a clear compatibility between the two plots whereas (b) shows a great difference between the two. We denote by the first one the "good variables" and the second to be the bad one. I the TMVA we used the good one.

4.5.5   Correlation matrix

Many multivariate analysis methods can distinguish between signal and background by comparing their correlations. Hence, even if two variables are distributed equally but differ within their correlations, they can improve the filtering process. The correlation factor ρ for two random variables x and y is defined by

$$C(x,y) = \frac{1}{N} \sum_{i=1}^{N} (x_i - \bar{x})(y_i - \bar{y}) \qquad (4.11)$$

with $C(x,y)$ being the co-variance matrix element of x and y, and σ_x, σ_y their
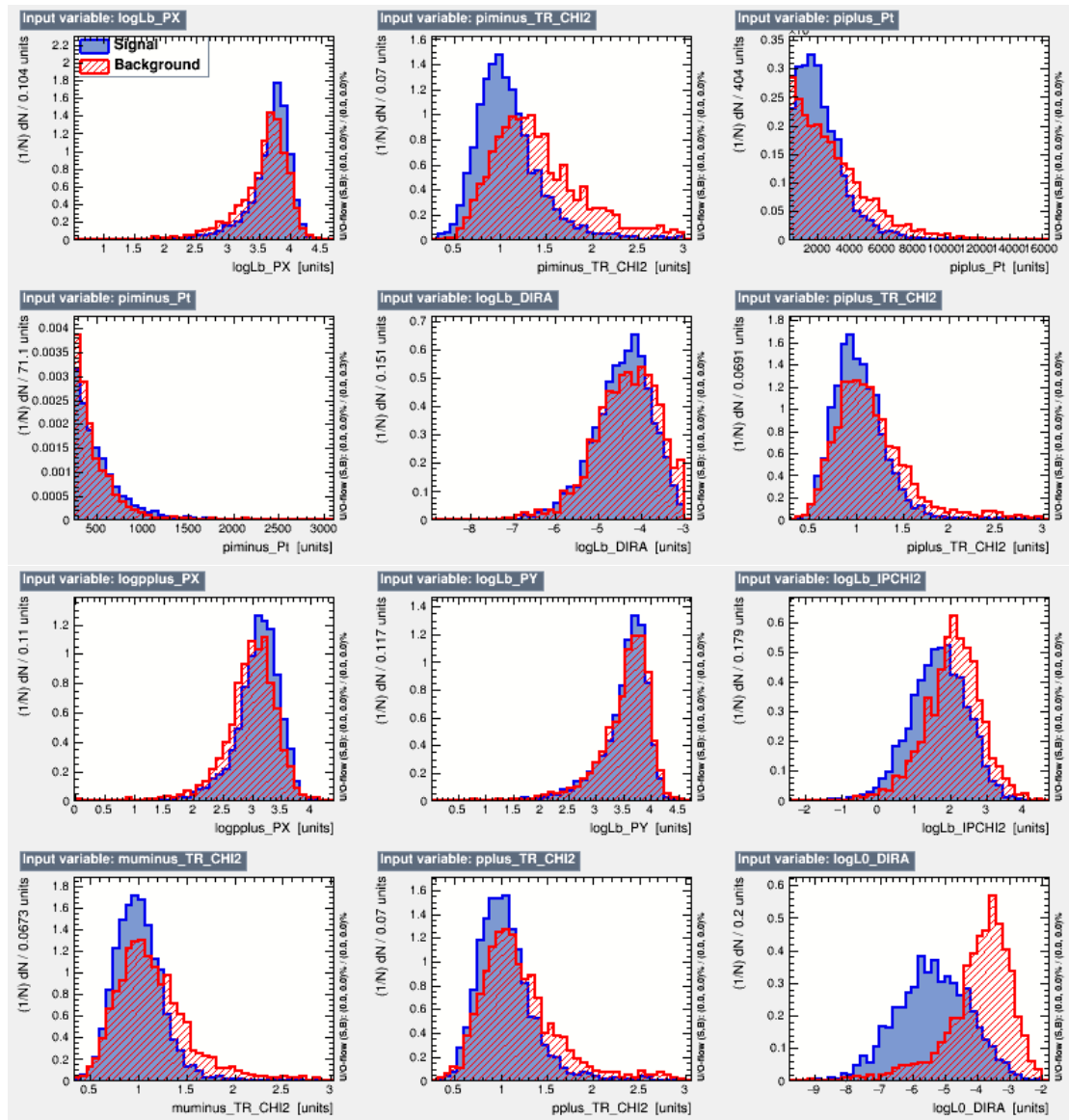
Figure 4.8: Distribution of variables used in the training of BDT for 2011 (LL, Λ_c^+ tracks) , superimposing RHSB background events (in Red) and MC-generated signal events (in Blue).

respective standard deviation.

In Figs.B.8-B.11, we show the correlation map of the variables used to train the BDT for 2011 and 2012 for different data samples. Most of the variables as seen here have weak linear correlation(Fig.4.9). Although the linear correlations are high for some pairs of variables, the correlations are not the same for signal and background events. Aside from that, for the same pair of variables, the correlations of these variables to the other variables are not the same for signal and background events, (for the rest see appendix B, section: Signal Correlation Matrices Figs. B.8-B.11).
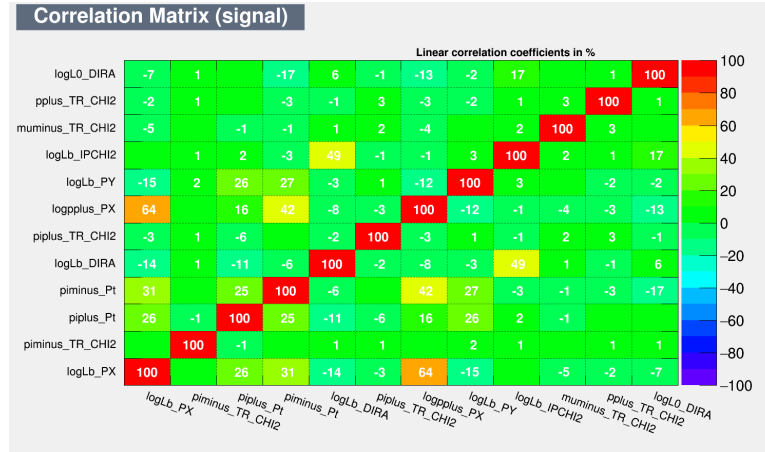
(a) DD Λ_c^+ signal correlation matrix
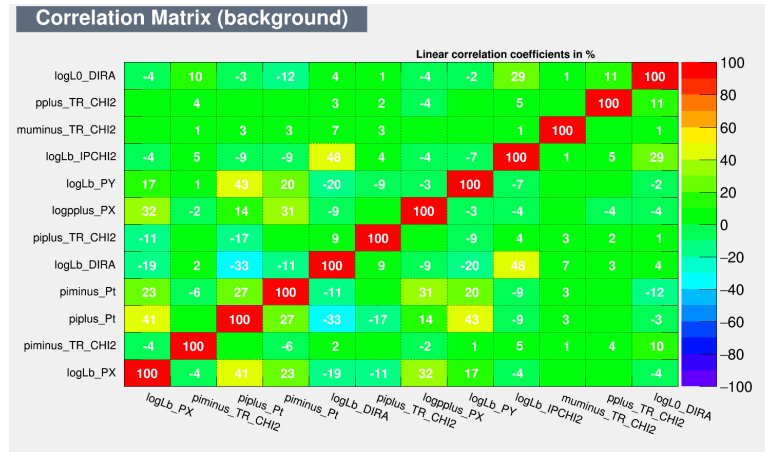
(b) DD Λ_c^+ BKG correlation matrix

Figure 4.9: Linear correlation for DD track samples , signal and background (BKG) for 2011 data sample: Λ_c^+.

4.5.6 Training and validation of the BDT

The discriminant response histograms for the different samples are presented in Fig.4.10. Kolmogorov-Smirnov tests have been computed in each case and it didn't indicate that there is clear sign of over-training.

Receiver Operation Characteristics: ROC-Curve

MLP (Multi-Layer Perceptron which is an Artificial Neural Networks (ANNs) implementation for TMVA), RuleFit and many other methods have been compared with the BDT. Shown in Figs.4.13(4.14) are the background-rejection efficiency versus signal selection efficiency curves (ROC-curve: defined as Receiver Operation Characteristics (Fig.4.12)) for 2011(2012) BDTs respectively.

The ROC-curve integrals of all the tested methods are expectedly smaller than the

(a) BDT response for Λ_c^+, DD, 2011 samples

(b) BDT response for $\bar{\Lambda}_c$ DD, 2011 samples

(c) BDT response for Λ_c^+, LL, 2011 samples

(d) BDT response for $\bar{\Lambda}_c$ LL, 2011 samples
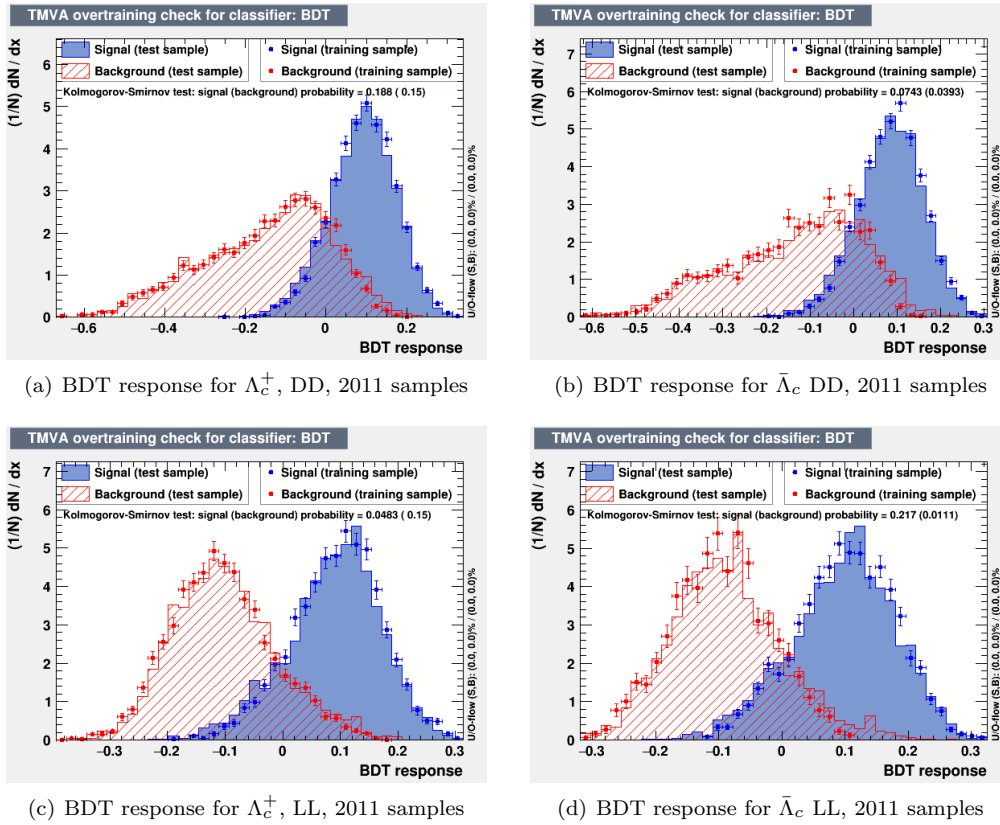
Figure 4.10: BDT response for 2011.

(a) BDT response for Λ_c^+, DD, 2012 samples

(b) BDT response for $\bar{\Lambda}_c$ DD, 2012 samples

(c) BDT response for Λ_c^+, LL, 2012 samples

(d) BDT response for $\bar{\Lambda}_c$ LL, 2012 samples
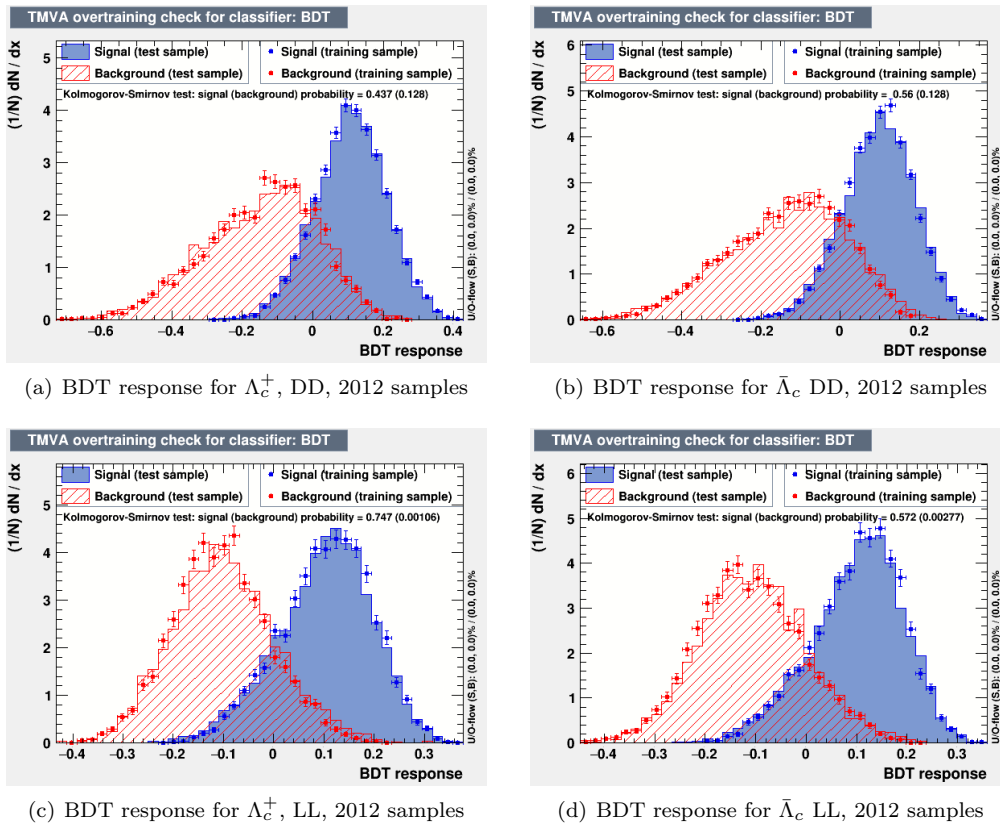
Figure 4.11: BDT response for 2012 for the different samples.

BDT, indicating that the non-linear correlations between variables are at work in the discriminating power of the BDT. As a result, the BDT is decided to be used in this analysis.
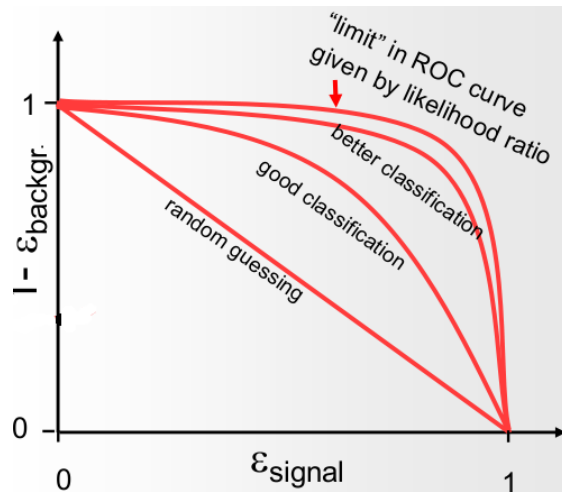
Figure 4.12: Example of the ROC-curve.

(a) Λ_c^+ DD tracks samples

(b) $\bar{\Lambda}_c$ for DD tracks samples

(c) Λ_c^+ LL tracks samples

(d) $\bar{\Lambda}_c$ for LL tracks samples
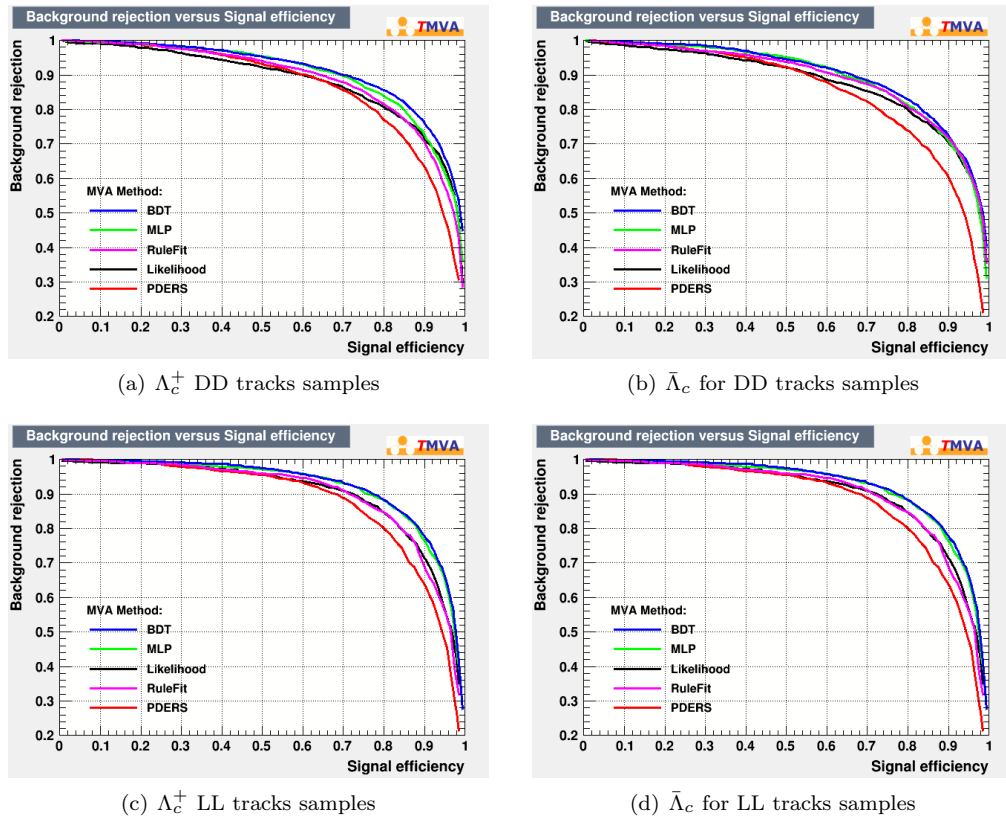
Figure 4.13: BDT ROC-curve for 2011.

The same BDT methodology is applied for all the data samples(DD,LL 2011 and 2012).

(a) Λ_c^+ DD tracks samples

(b) $\bar{\Lambda}_c$ for DD tracks samples

(c) Λ_c^+ LL tracks samples

(d) $\bar{\Lambda}_c$ for LL tracks samples
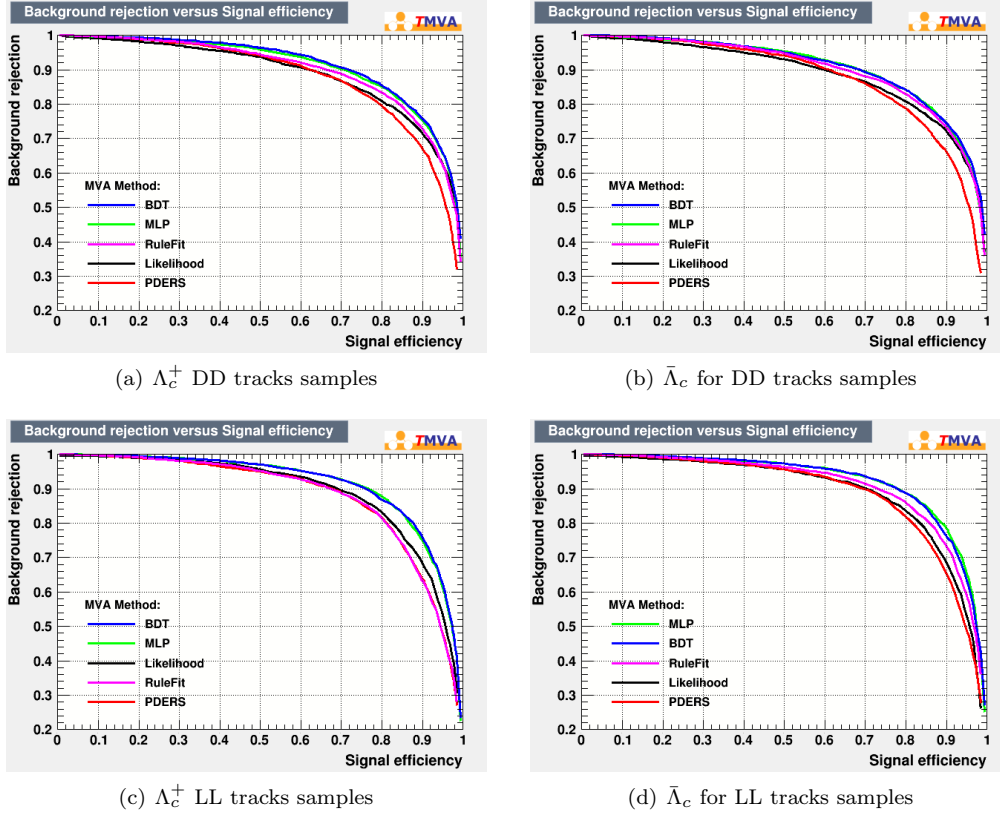
Figure 4.14: BDT ROC-curve for 2012.

4.5.7 Optimization of the BDT Cuts

The next step was to calculate the optimal BDT cut for each data sample.The choice of the optimal cut on the BDT response can be defined using several Figures of Merit. For example in our study we chose the maximal significance of the signal(S) with respect to background (B) :

$$FoM(BDT_{cut}) = \frac{N_{sig}}{\sqrt{N_{sig} + N_{bkg}}} \tag{4.12}$$

Where N_{sig} is the number of signal events that passed a BDT cut, while, N_{bkg} is the number of combinatorial backgrounds under the signal peak which is approximated using the RHSB region. Before making any BDT cut, the real data in the RHSB $(M_{\Lambda_c^+} > 2300 MeV/c^2)$ is modeled using an exponential function. This exponential function is then projected to the signal mass region, which is within $\pm 3\sigma$ from the nominal mass of Λ_c^+. And hence, the extrapolated number of combinatorial backgrounds under the signal peak, before any BDT cut, is estimated using the projected exponential function. So one can say that the number of combinatorial events under the signal peak linearly scales with the number of combinatorial events in the RHSB. The Figures of Merit for all the samples are displayed in Fig.4.15 and 4.16.

(a) Λ_c^+ DD tracks samples

(b) $\bar{\Lambda}_c$ DD tracks samples

(c) Λ_c^+ LL tracks samples

(d) $\bar{\Lambda}_c$ LL tracks samples
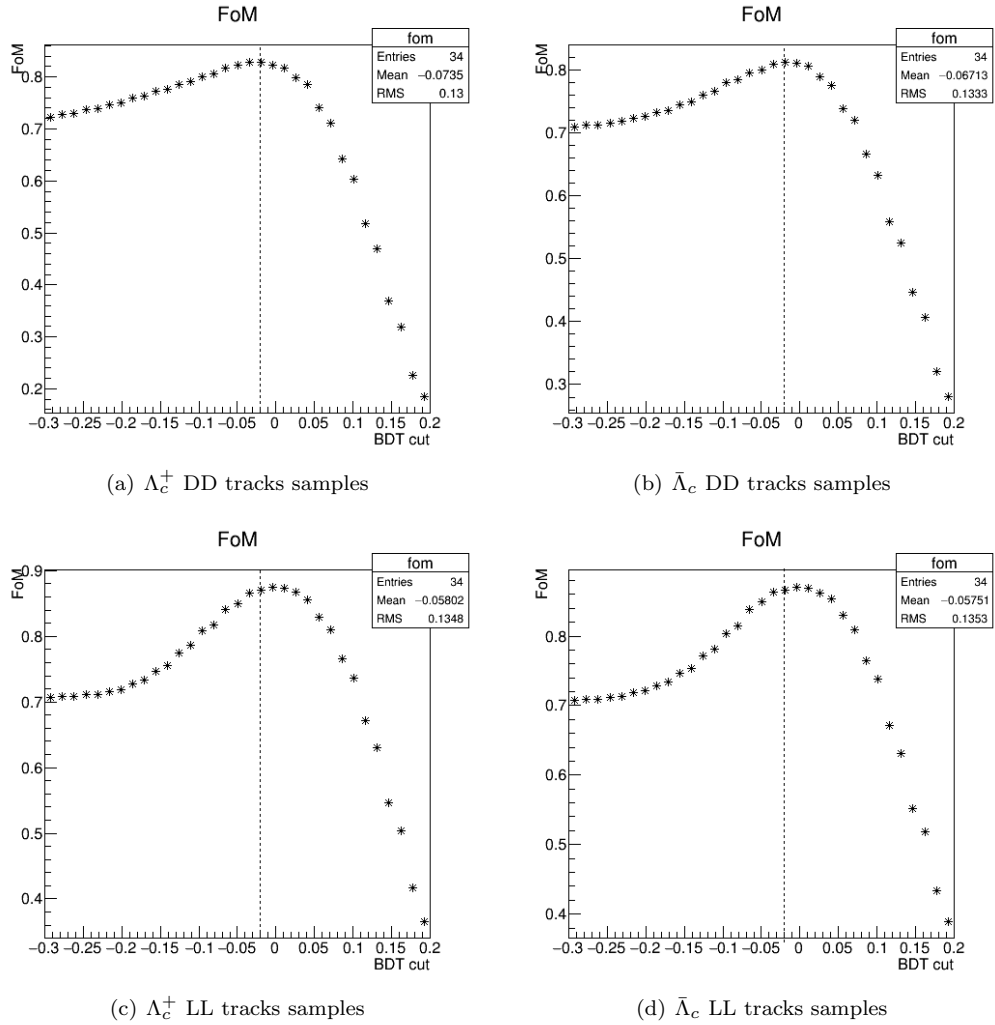
Figure 4.15: This figure represents the signal efficiency defined in aq. 4.12 as a function of the BDT cuts for the spectra 2011 for the different samples studied. Figures of merit are used for BDT cut optimization in which the cut are taken to obtain the maximum efficiency.
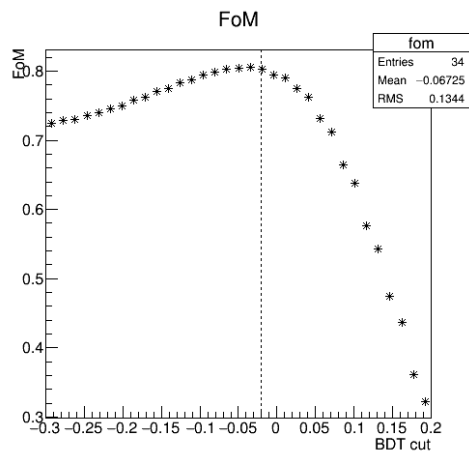
(a) Λ_c^+ DD tracks samples
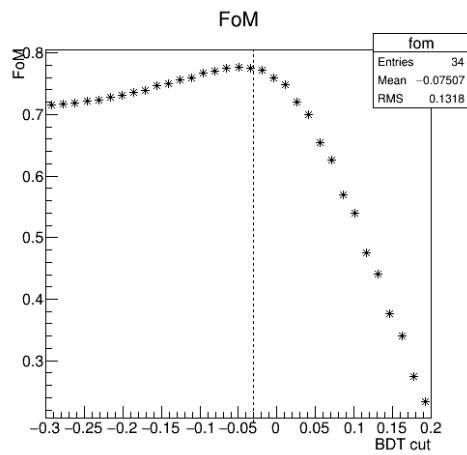
(b) $\bar{\Lambda}_c$ DD tracks samples
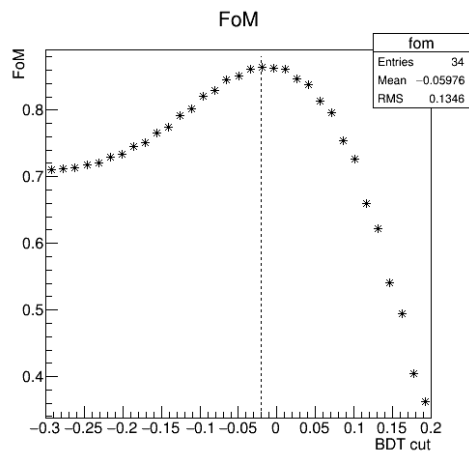
(c) Λ_c^+ LL tracks samples
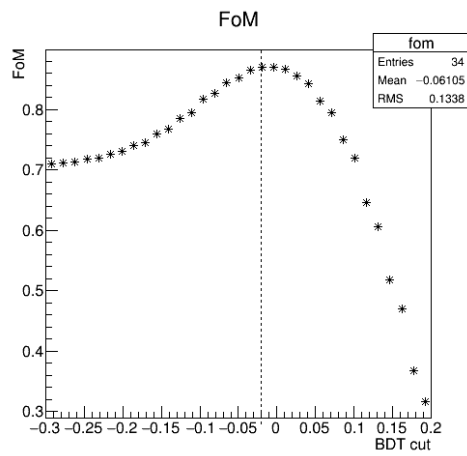
(d) $\bar{\Lambda}_c$ LL tracks samples

Figure 4.16: This figure represents the signal efficiency defined in eq.4.12 as a function of the BDT cuts for the spectra 2012 for the different samples studied. Figures of merit are used for BDT cut optimization in which the cut are taken to obtain the maximum efficiency.

4.6 Signal Shapes and Adjustment of the Mass Spectra

The events generated by Monte-Carlo are used to obtain the signal shapes. The invariant mass distribution reconstructed from simulated events is fitted with a Double Crystal Ball function (DCB) [73] with shared mean μ and different width σ. The mathematical description of a Crystal Ball PDF of variable m is given by:

$$P(m; \alpha; n; \mu; \sigma) = N \cdot \begin{cases} exp\Big(-(m-\mu)^2/2\sigma^2\Big), & if -(m-\mu)/\sigma > -\alpha \quad (4.13) \\ (\frac{n}{|\alpha|})^n exp\big(-\frac{\alpha^2}{2}\big)\big(\frac{n-\alpha^2}{|\alpha|} - \frac{m-\mu}{\sigma}\big)^{-n}, & if -\frac{(m-\mu)}{\sigma} \leq -\alpha \quad (4.14) \end{cases}$$

where N is the normalization factor and m is the invariant mass. The turnover point is denoted (α) and the tail parameter (n) models the left or the right tail of signal mass distribution. Although the two functions in equation (4.14) are independent of the sign of the parameter α, the sign of α determines on which side (of the Crystal Ball (CB) function) the tail should appear, where a positive α means the tail is on the left side of the CB while negative α means the tail is on the right side. All the signal shapes are fitted simultaneously in order to obtain the ratios of the widths, which are used as "constrained parameters" in the final PDF aiming to fit the real data.

Tab.4.8 summarizes the parameters obtained from the fits, which are shown in Fig.4.17 and 4.18. The extracted parameters $\alpha 1$, $\alpha 2$, n1, n2, f2 are fixed parameters in the nominal fit to the real data.

(a) M(Λ_c^+) for DD tracks

(b) M($\bar{\Lambda}_c$) for DD tracks

(c) M(Λ_c^+) for LL tracks

(d) M($\bar{\Lambda}_c$) for LL tracks
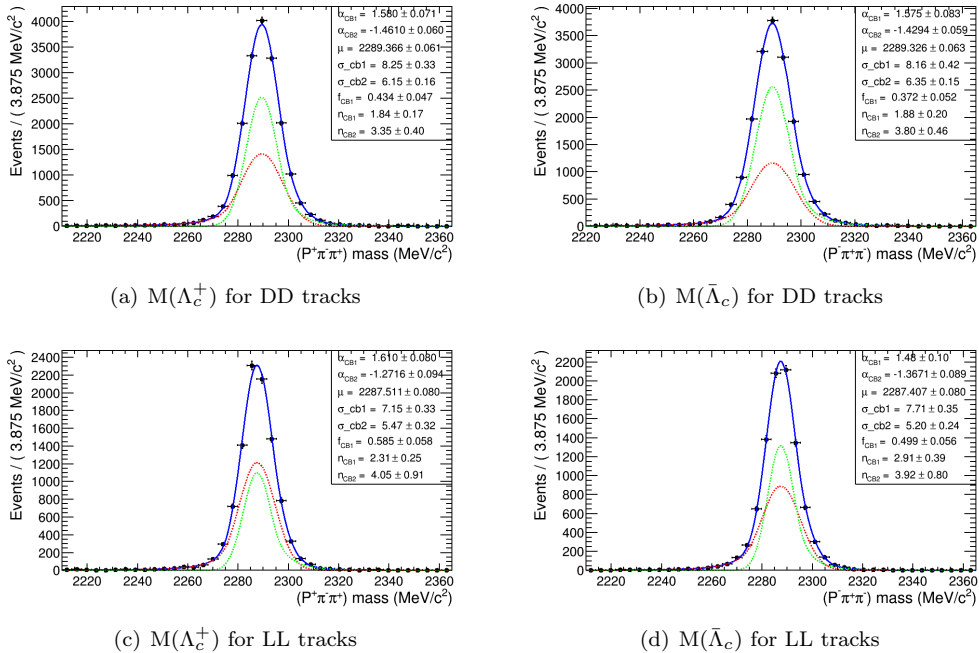
Figure 4.17: Signal invariant mass distribution fitted using double crystal ball for the spectra 2011.

The invariant mass range used to produce these fits starts from 2210 MeV/c^2. It is worth noticing that the nominal fit to the data starts also from the same range 2210 MeV/c^2.

One here should stress on the difference shown in Tab.4.8 indicating a clear ≈ 2 MeV shift in the Λ_c^+ mass spectrum between LL and DD samples.

Year	Particle	Track	μ MeV	$\sigma 1$	$\sigma 2$	$\alpha 1$	$\alpha 2$	n1	n2	f
2011	Λ_c^+	LL	2287.511 ± 0.080	7.15 ± 0.33	5.47 ± 0.32	1.610 ± 0.080	-1.2716 ± 0.094	2.31 ± 0.25	4.05 ± 0.91	0.585 ± 0.058
		DD	2289.366 ± 0.061	8.25 ± 0.33	6.15 ± 0.16	1.580 ± 0.071	-1.4610 ± 0.060	1.84 ± 0.17	3.35 ± 0.40	0.434 ± 0.047
	$\bar{\Lambda}_c^-$	LL	2287.407 ± 0.080	7.71 ± 0.35	5.20 ± 0.24	1.48 ± 0.10	-1.3671 ± 0.089	2.91 ± 0.39	3.92 ± 0.80	0.499 ± 0.056
		DD	2289.326 ± 0.063	8.16 ± 0.42	6.35 ± 0.15	1.575 ± 0.083	-1.429 ± 0.095	1.88 ± 0.20	3.80 ± 0.20	0.372 ± 0.052
2012	Λ_c^+	LL	2287.514 ± 0.073	7.23 ± 0.25	5.67 ± 0.29	1.602 ± 0.062	-1.2552 ± 0.088	2.14 ± 0.18	4.00 ± 0.78	0.641 ± 0.050
		DD	2289.284 ± 0.052	7.98 ± 0.19	5.80 ± 0.15	1.557 ± 0.045	-1.1884 ± 0.047	2.61 ± 0.21	3.47 ± 0.41	0.544 ± 0.032
	$\bar{\Lambda}_c^-$	LL	2287.511 ± 0.079	6.61 ± 0.39	6.06 ± 0.53	1.61 ± 0.10	-1.146 ± 0.11	2.19 ± 0.27	6.6 ± 5.4	0.608 ± 0.089
		DD	2289.254 ± 0.052	8.09 ± 0.18	5.77 ± 0.314	1.680 ± 0.051	-1.2851 ± 0.046	2.21 ± 0.18	3.38 ± 0.36	0.525 ± 0.035

Table 4.8: Fit parameters of the Λ_c^+ invariant mass.

(a) M(Λ_c^+) for DD tracks

(b) M($\bar{\Lambda}_c$) for DD tracks

(c) M(Λ_c^+) for LL tracks

(d) M($\bar{\Lambda}_c$) for LL tracks
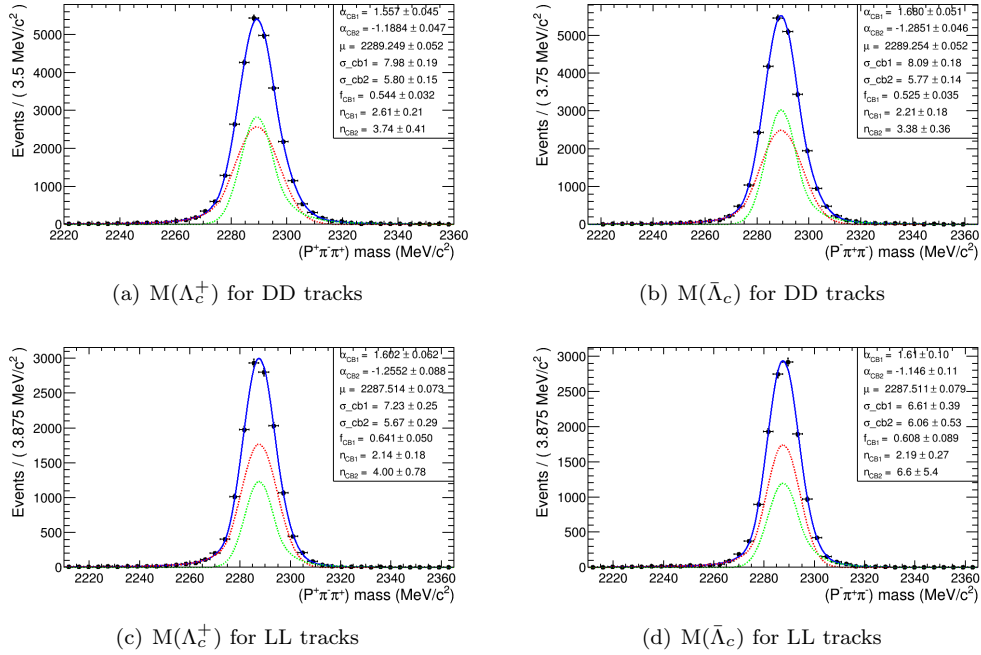
Figure 4.18: Signal invariant mass distribution fitted using double crystal ball for the spectra 2012.

4.6.1 Partially-reconstructed background shapes

The partially-reconstructed backgrounds with no mis-identified particles are modeled by a Gaussian resolution. The generalized Gaussian function for a variable (m) is given by the analytical expression:

$$f(m, \mu, \sigma) = \beta \cdot exp\bigg(- (m - \mu)^2/2\sigma^2 \bigg) \tag{4.15}$$

where β is a normalization factor. The shapes of these backgrounds are obtained from MC-generated events of the reconstructed decay $\Lambda_c^+ \longrightarrow (\Sigma^0 \longrightarrow \Lambda\gamma)\pi^+$. The shape parameters obtained are then fixed in the nominal fit to data and the yields are set free to float.

4.6.2 Combinatoric shapes

Exponential function is used to model the combinatorial backgrounds. This function requires one variable to be determined, which is the slope used to describe the decrease of combinatorial background as a function of the reconstructed invariant mass.

A note here is in order regarding the choice of an exponential model as the baseline against other shapes for the combinatorics. The only valuable information about the combinatorics for most of the samples studied in this analysis lies in the RHSB of the data. The left-handed region of the invariant mass distribution of most of the samples is populated by the partially reconstructed background. Since the techniques of the adjustment of an exponential shape requires a leverage on the left-handed part of the invariant mass distribution, it is likely that its fit can absorb overlooked background contributions coming from other partially reconstructed decays of very low statistics. These considerations drove us to the choice of the exponential model for the fit model.

4.7 Fit results

In this section, we present the fit results and the measurement of the yields in the BaryonPCR model which is used to implement semileptonic decays using realistic dynamics [74].The form factors are being taken from [75].

The Λ_c^+ decay signal yields are determined by the fit and are then used are used to do the final fit of the angular distributions, with proper propagation of the statistical errors taking into account correlations. There are also associated errors that are propagated as systematic uncertainties of the angular distribution derivation. The next section is dedicated to the efficiency derivation.

Fig.4.19 and 4.20 display the fit results of the simultaneous fit to the invariant mass spectra using the BaryonPCR model 2011 data. Fig.4.21 and 4.22 show the fit results for the 2012 data. The fit parameters are taken from MC summarized in Tab.4.8, where it shows which parameters are shared and not shared.
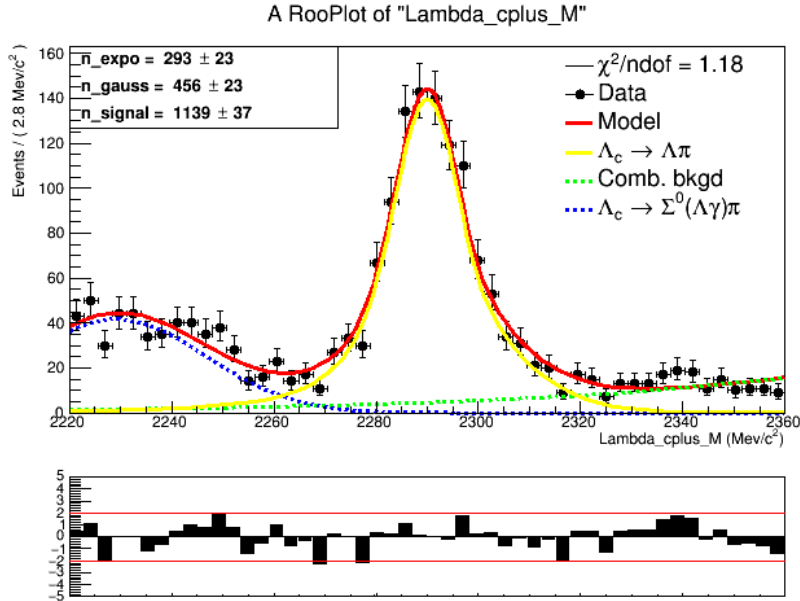
(a) M(Λ_c^+) for DD tracks
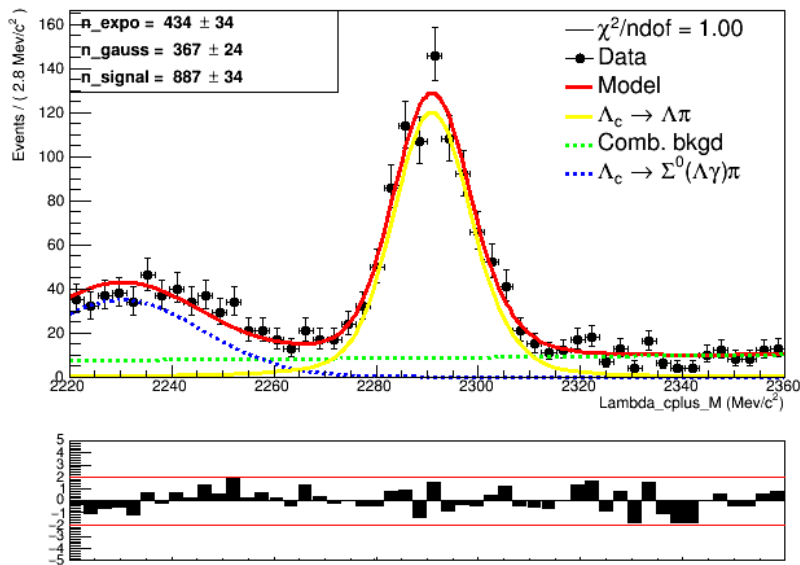
(b) M($\bar{\Lambda}_c$) for DD tracks

Figure 4.19: Fit results for the $\Lambda_c^+ \longrightarrow \Lambda\pi$ DD spectra for different track and particle type using the BaryonPCR data of 2011.
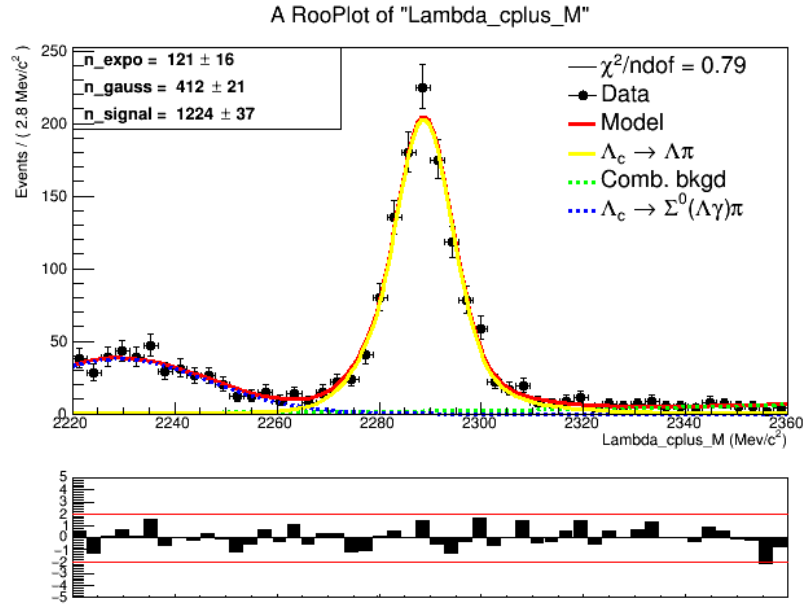
(a) $M(\Lambda_c^+)$ for LL tracks
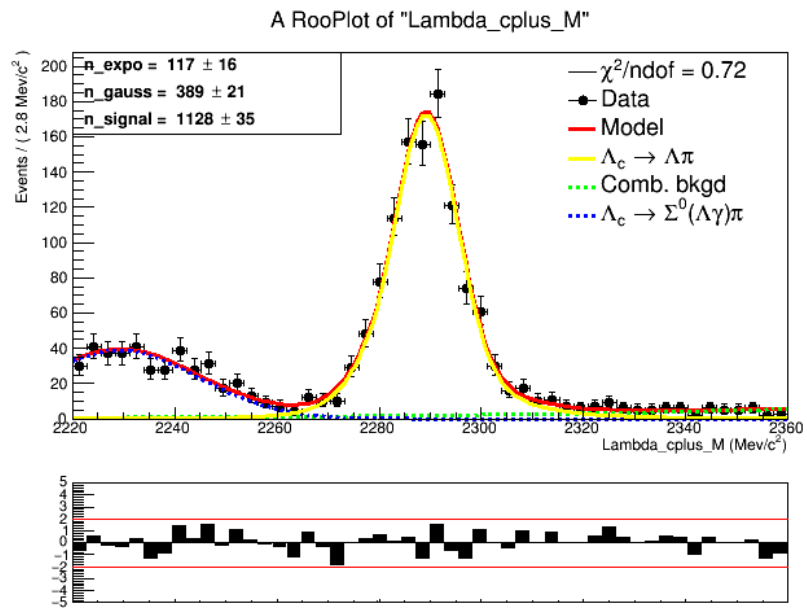
(b) $M(\bar{\Lambda}_c)$ for LL tracks

Figure 4.20: Fit results for the $\Lambda_c^+ \longrightarrow \Lambda\pi$ LL spectra for different track and particle type using the BaryonPCR data of 2011.

(a) $M(\Lambda_c^+)$ for DD tracks

(b) $M(\bar{\Lambda}_c)$ for DD tracks
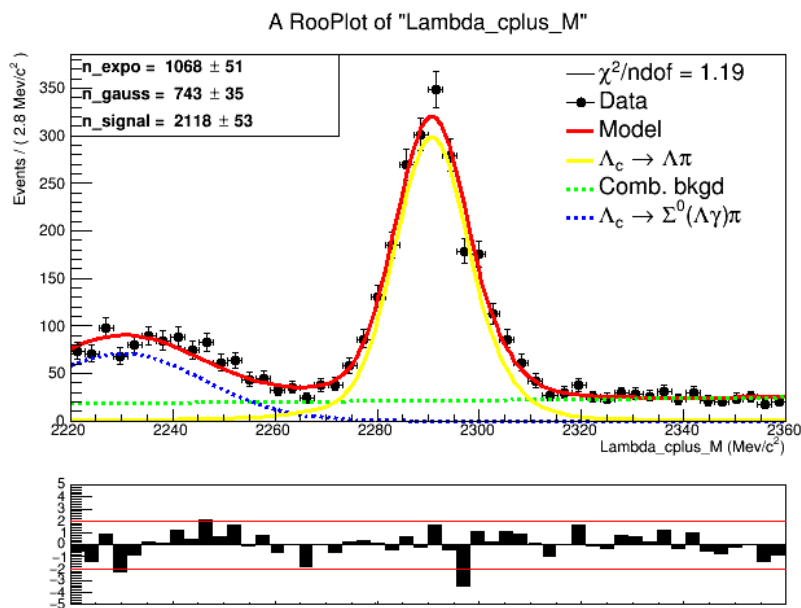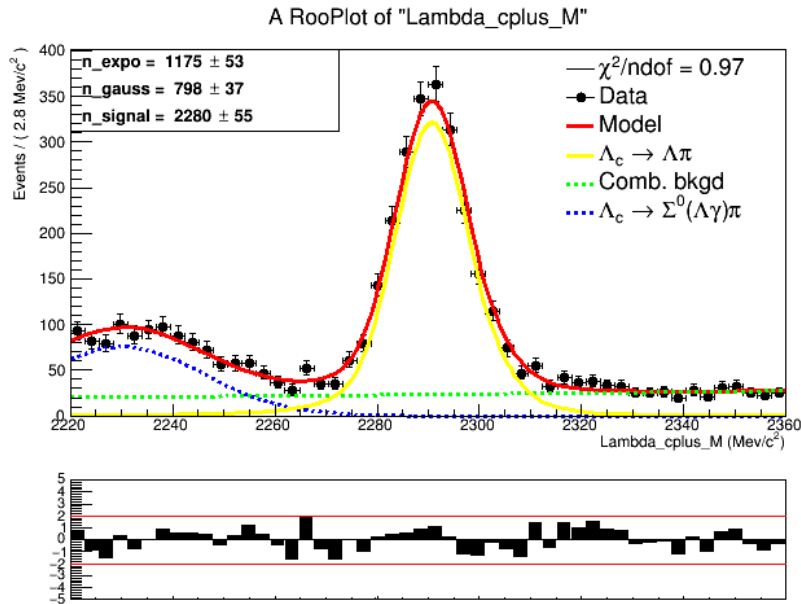
Figure 4.21: Fit results for the $\Lambda_c^+ \longrightarrow \Lambda\pi$ DD spectra for different track and particle type using the BaryonPCR data of 2012.

(a) $M(\Lambda_c^+)$ for LL tracks

(b) $M(\bar{\Lambda}_c)$ for LL tracks
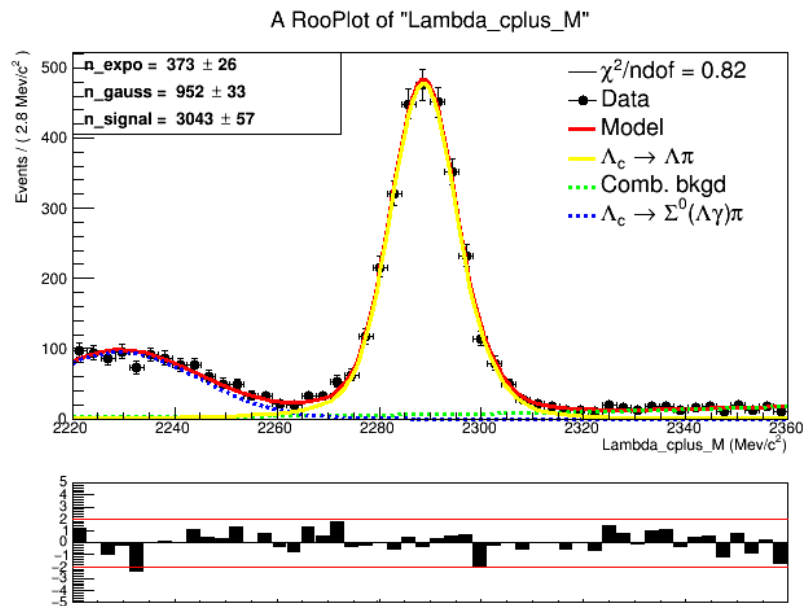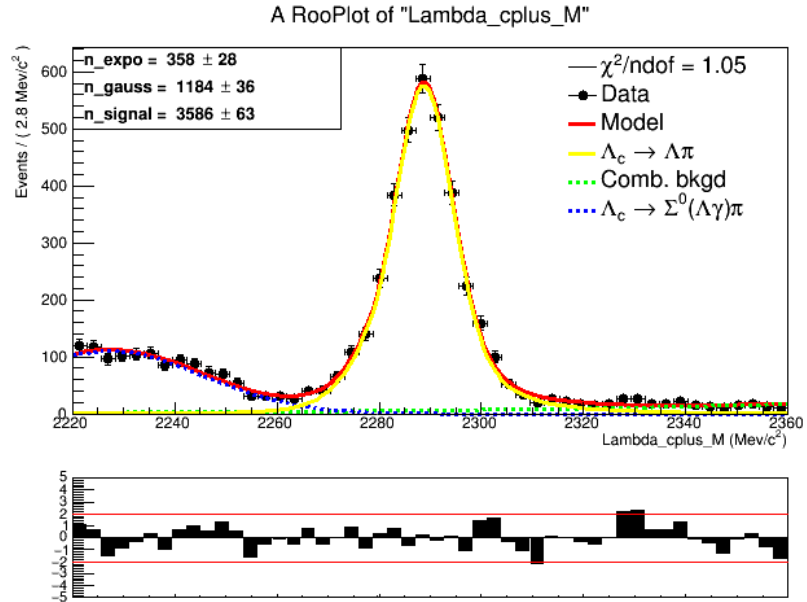
Figure 4.22: Fit results for the $\Lambda_c^+ \longrightarrow \Lambda\pi$ LL spectra for different track and particle type using the BaryonPCR data of 2012.

4.8 Production Yield

The LHC machine is designed to deliver a luminosity $L \approx 2 \times 10^{32} cm^{-2} s^{-2}$ for 2012 and $L \approx 1 \times 10^{32} cm^{-2} s^{-2}$ for 2011. The expected $b\bar{b}$ cross section is approximately $300 \pm 0.01 \mu b$ ([76]), and by that the annual yield of the $b\bar{b}$ pairs at the LHCb will reach 10^{12}:

$$N_{b\bar{b}} \approx L.\sigma_{b\bar{b}}.10^7 \approx 10^{12}$$

For our decay channel, the annual production yield is given by the following equation:

$$N_{signal}^{exp} = 2 \times L_{year}^{int} \times \sigma_{b\bar{b}} \times f_s(b \rightarrow \Lambda_b^0) \times BF_{VIS} \times \epsilon_{gen} \qquad (4.16)$$

The factor 2 added due to the fact that there are particles and antiparticles coming from the $b\bar{b}$ pair. L_{year}^{int} is the integrated luminosity of one nominal year - 1(2011) and 2(2012) fb^{-1}. The hadronization probability is given by $f_s(b \rightarrow \Lambda_b^0) = 12\%$, BF_{VIS} is the visible branching fraction of the desired decay and ϵ_{gen} is the generator efficiency. For $\Lambda_b^0 \longrightarrow \Lambda_c^+ \mu^- \nu_\mu$, the branching fraction is calculated from:

$$\begin{aligned} BF_{VIS} &= BF(\Lambda_b^0 \longrightarrow \Lambda_c^+ \mu^- \nu_\mu) \times BF(\Lambda_c^+ \longrightarrow \Lambda \pi^+) \times BF(\Lambda \longrightarrow p^+ \pi^-) \\ &= 5.3 \times 10^{-4} \end{aligned} \qquad (4.17)$$

Where

$$\begin{aligned} BF(\Lambda_b^0 \longrightarrow \Lambda_c^+ \mu^- \nu_\mu) &= (6.5_{-1.3}^{+1.4})\% \\ BF(\Lambda_c^+ \longrightarrow \Lambda \pi^+) &= (1.3 \pm 0.07)\% \\ BF(\Lambda \longrightarrow p^+ \pi^-) &= (63.9 \pm 0.5)\% \end{aligned}$$

The preceding analysis allows us to infer the different efficiencies: $\epsilon_{trigger}$, $\epsilon_{kin-cuts}$, ϵ_{BDT}

We define $\epsilon_i = \frac{N_i}{N_t}$ to be the efficiency of the selection
where
- N_i is number of events passing the cut.
- N_t is number of events before the cut.

year	luminosity(fb^{-1})	N_{total}	$\epsilon_{trigger}$	$\epsilon_{kin-cuts}$	ϵ_{BDT}	N_{exp}	N_{meas}
2011	1.11	128254	49.5%	13.2%	53.1%	4450	4378
2012	2.08	352297	50.5%	12.9%	48.6%	11154	11027

Table 4.9: Number of expected signal events and measured one for years 2011 and 2012.

Tab.4.9 shows the expected signal coming from $\Lambda_b^0 \longrightarrow \Lambda_c^+ \mu^- \nu_\mu$ decay and the measured number of events for the whole data sample (years 2011-2012). N_{exp} represents the number of the expected events departing from equation 4.16, whereas the N_{meas} represents the number of signal events obtained from the fits, by adding the signal yield of the two samples Λ_b and $\bar{\Lambda}_b$ for each year 2011 and 2012.

4.9 Corrections applied on MC (reweighting)

4.9.1 Reweighting the Λ_b^0 Transverse momentum P_T

Fig.4.23 shows a comparison between the Λ transverse momentum P_T for the hadronic decay $\Lambda_b^0 \rightarrow \Lambda_c^+(\rightarrow \Lambda(p\pi^-)\pi^+)\mu^- \bar{\nu}_\mu$ for all the data samples and years.

As seen in all the spectra, the curves are all normalized to have the unit area. One can easily observe the difference between the simulated spectrum (green) and the measured one (blue). This could lead to a false determination of the efficiency, and thus all the MC samples should be re-weighted to simulate the right kinematic conditions.

Fig.4.23 shows also that we have achieved the desired aim in matching the kinematics properties of the daughter particles between MC and data for different conditions (the rest of figures are again in the appendix B: Corrections applied on MC (reweighting)).
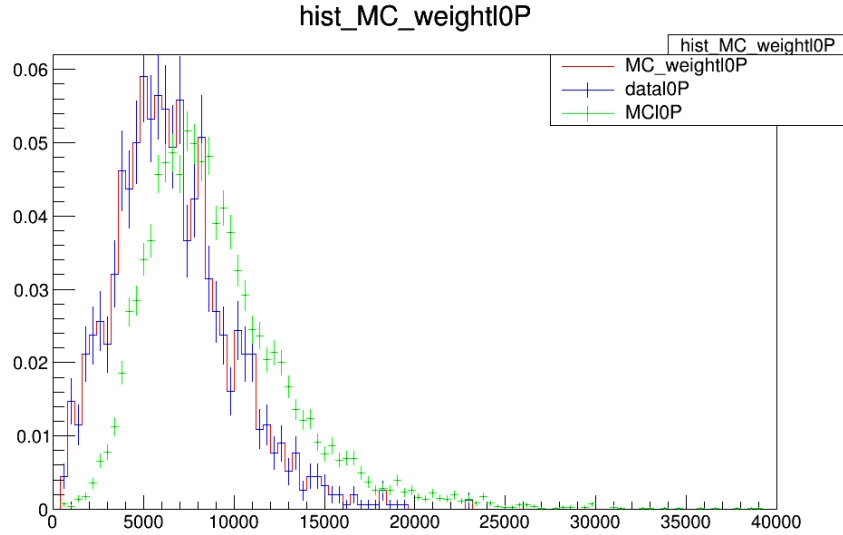
(a) P_T of Λ_b^0 for LL tracks
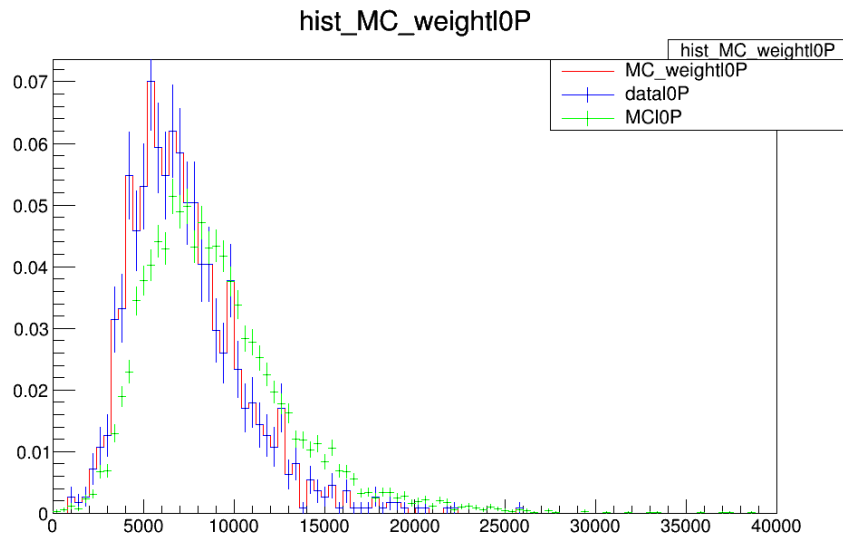
(b) P_T of $\bar{\Lambda}_b^0$ for LL tracks

Figure 4.23: Comparison between the normalized Λ_b^0 P_T before and after reweighting for LL track and particle type using the data of 2011. The blue color represents the side-band-subtracted data and the MC is represented by the green color. The red color represents the re-weighted MC events that clearly match the real data shown in blue.

4.9.2   Reweighting the track multiplicity

The simulated track multiplicity is not in agreement with the data measured by the LHCb detector. This will affect a lot the study performed and especially the PID performance. So the best thing to be done is to re-weight the track multiplicity of

the MC samples to simulate the real data samples.

Fig.4.24 show a comparison between the track multiplicity for all the data samples and years. Again the curves are all normalized to have the unity. And again there is a clear difference between the simulated spectrum (green) and the measured one (blue).

However, the re-weighted MC (red) shows also that we have a clear matching of the kinematics properties of the particles between MC and data.
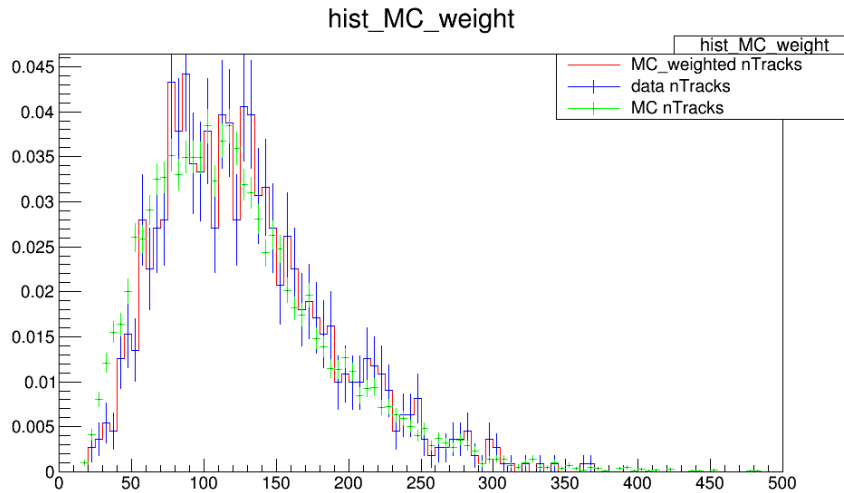
(a) Track multiplicity for DD tracks
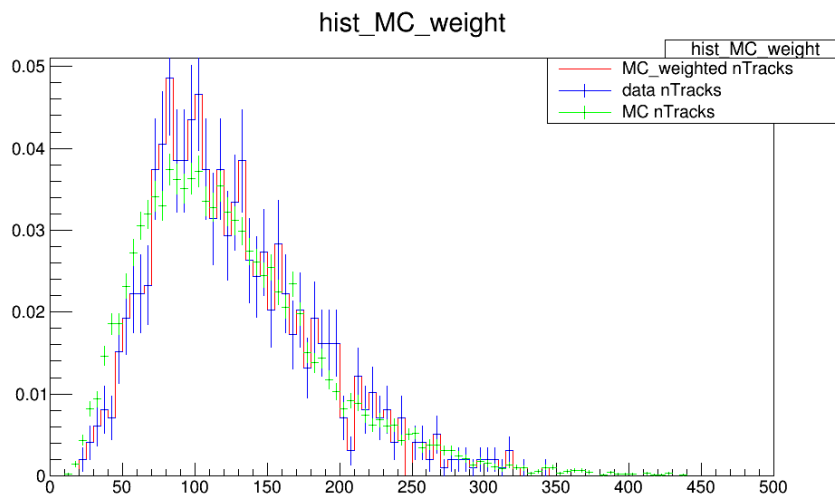
(b) Track multiplicity for DD tracks

Figure 4.24: Comparison between the normalized track multiplicity before and after reweighting for DD tracks and particle types using the data of 2011. The blue color represents the sideband-subtracted data and the MC is represented by the green color. The red color represents the re-weighted MC events that clearly match the real data shown in blue.

4.10   Angular Distributions after reweighting

We use the sPlot [72] technique to compare MC and data. The angular distributions, after reweighting, are showing discrepancies between data and MC as indicated in Figs. 4.25 to 4.28 for the data sample 2011 and in Figures 4.29 to 4.32 for the data sample 2012. This could mean the presence of unknown dynamics in the data spectra. The next step to be done (after reweighting) is to unfold both the MC and data because the Λ_b^0 momentum was determined up to two-fold ambiguity. The last step is the correction for the global efficiency of the LHCb detector.
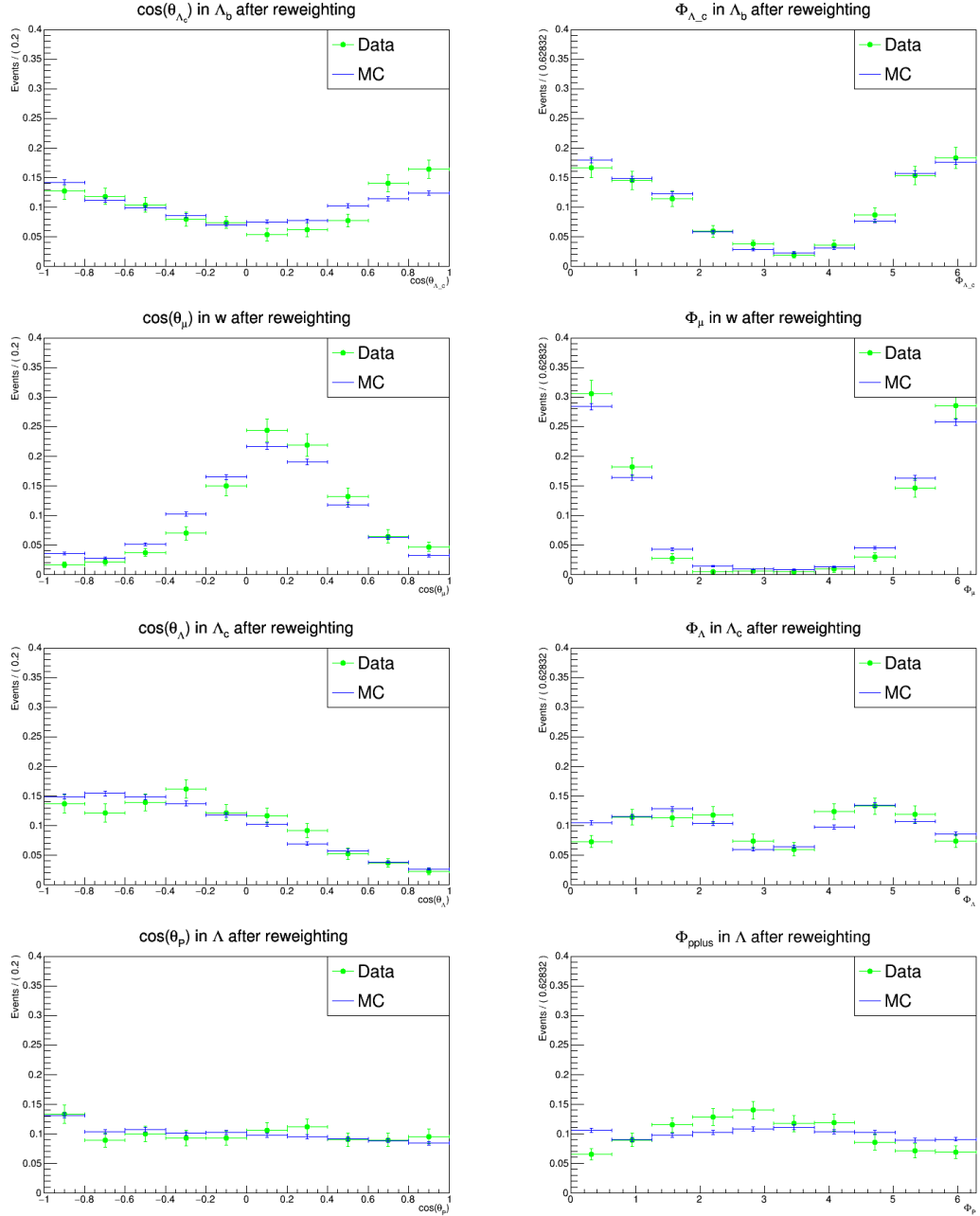
Figure 4.25: Comparison between MC (represented in blue) and Data (represented in green) of the angular distributions spectra for particles of type DD for data 2011 after reweighting.
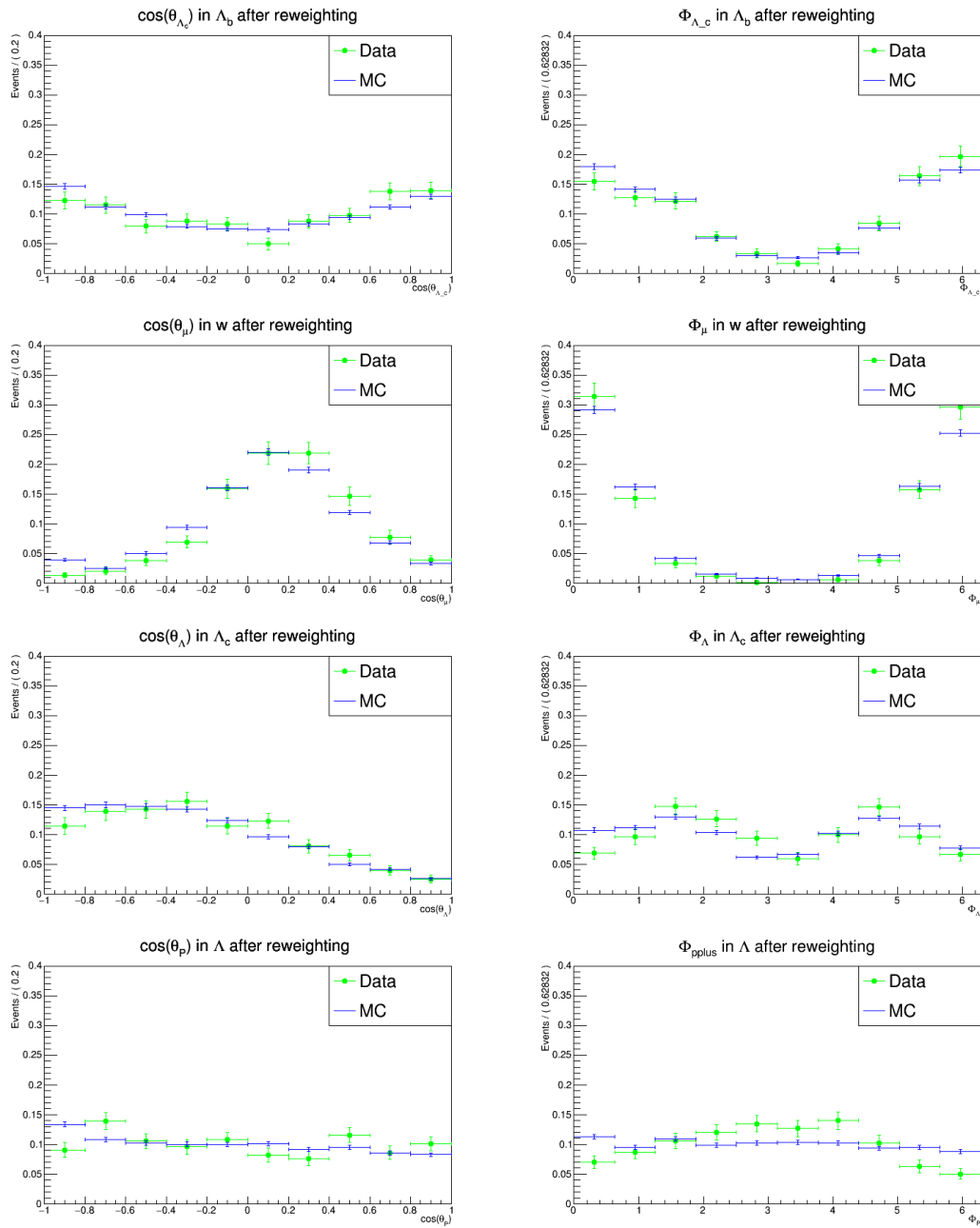
Figure 4.26: Comparison between MC (represented in blue) and Data (represented in green) of the angular distributions spectra for anti-particles of type DD for data 2011 after reweighting.
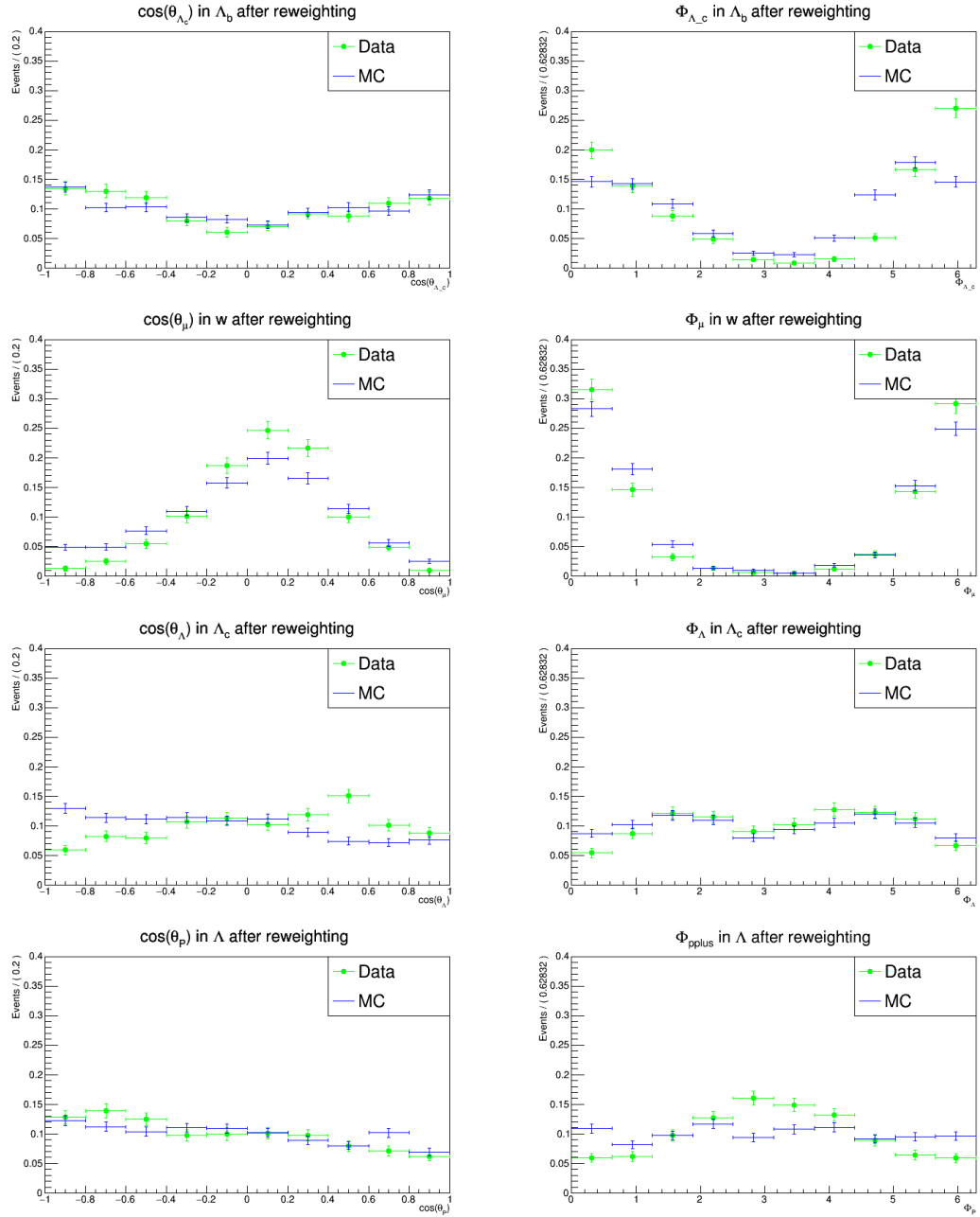
Figure 4.27: Comparison between MC (represented in blue) and Data (represented in green) of the angular distributions spectra for particles of type LL for data 2011 after reweighting.
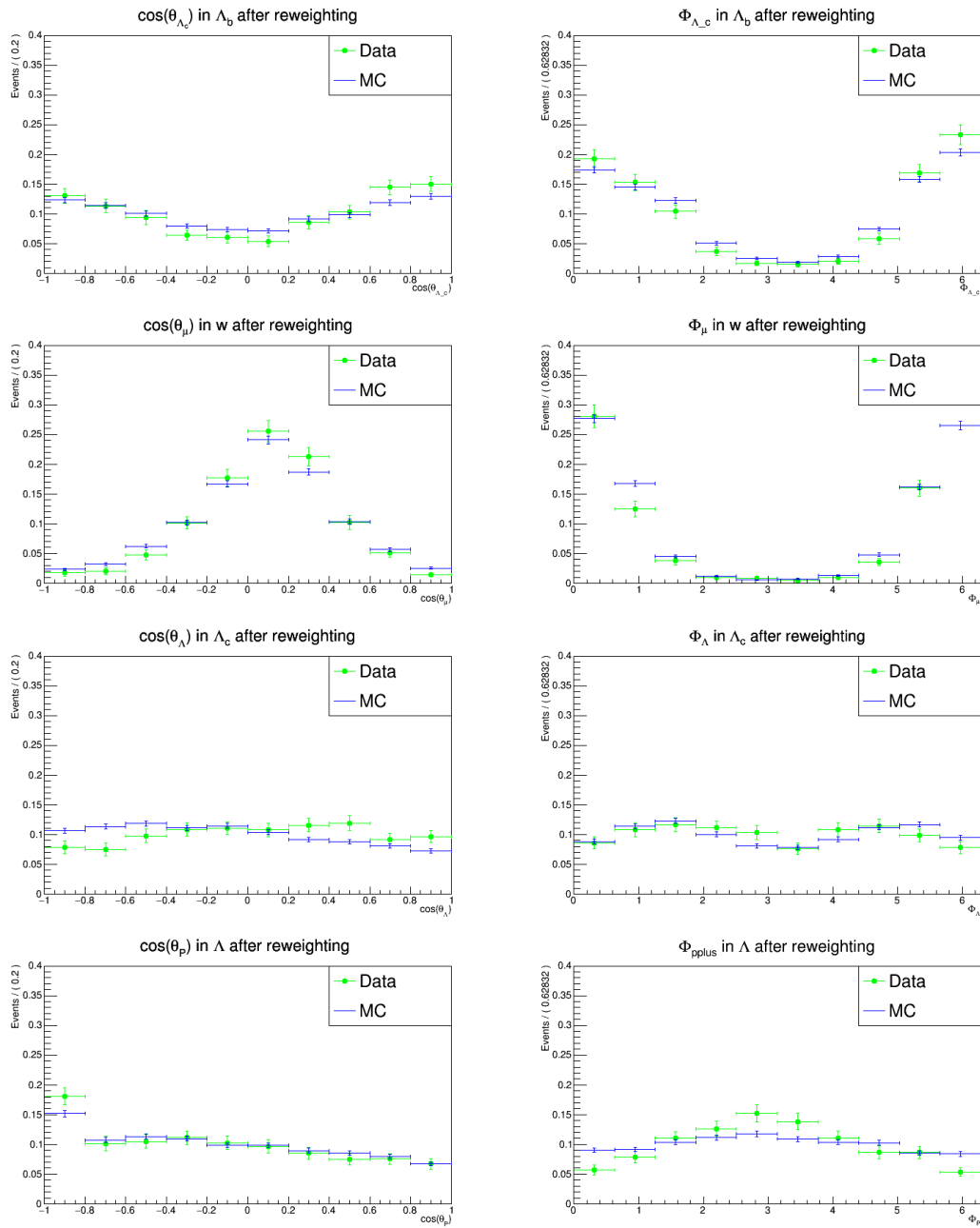
Figure 4.28: Comparison between MC (represented in blue) and Data (represented in green) of the angular distributions spectra for anti-particles of type LL for data 2011 after reweighting.
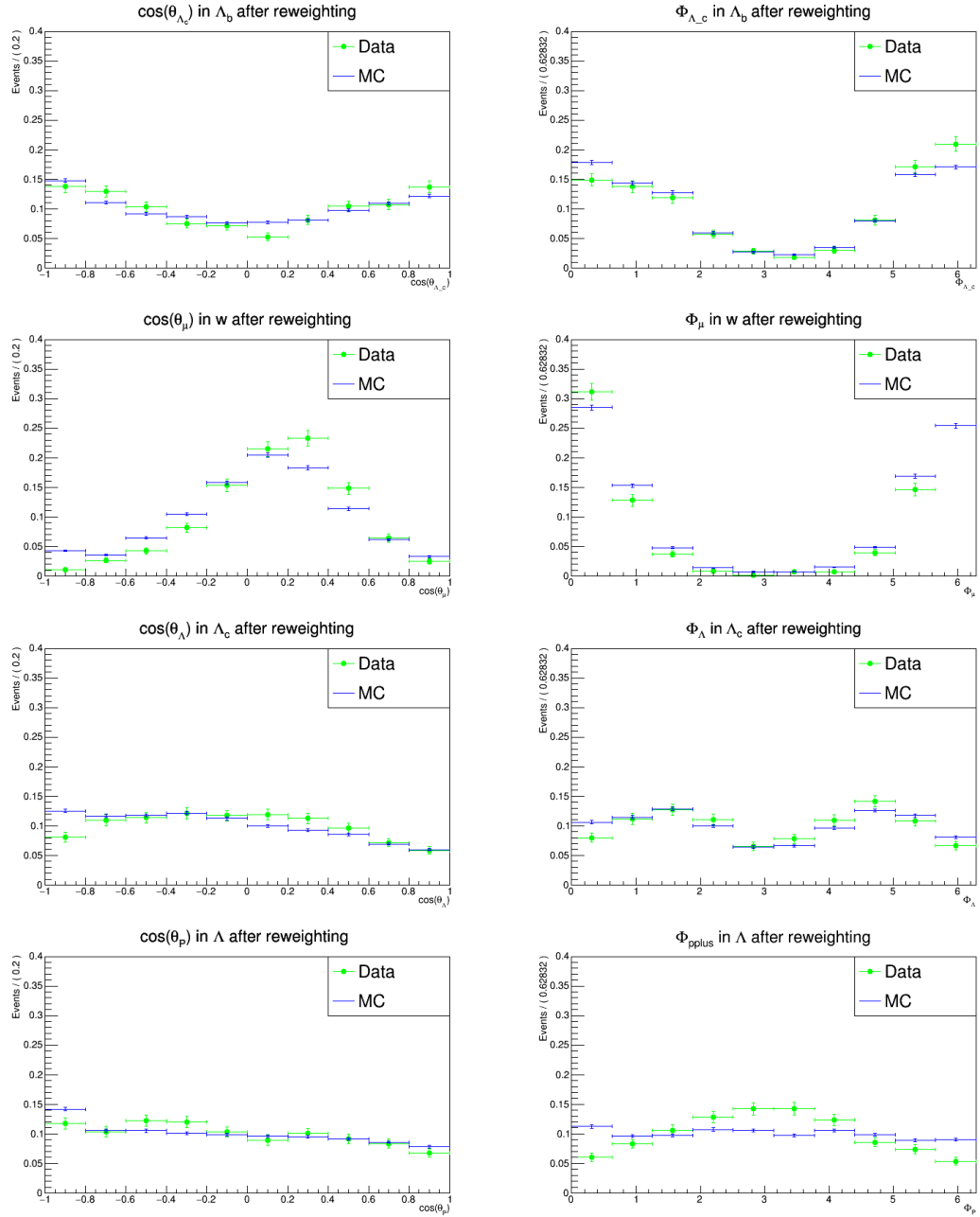
Figure 4.29: Comparison between MC (represented in blue) and Data (represented in green) of the angular distributions spectra for particles of type DD for data 2012 after reweighting.
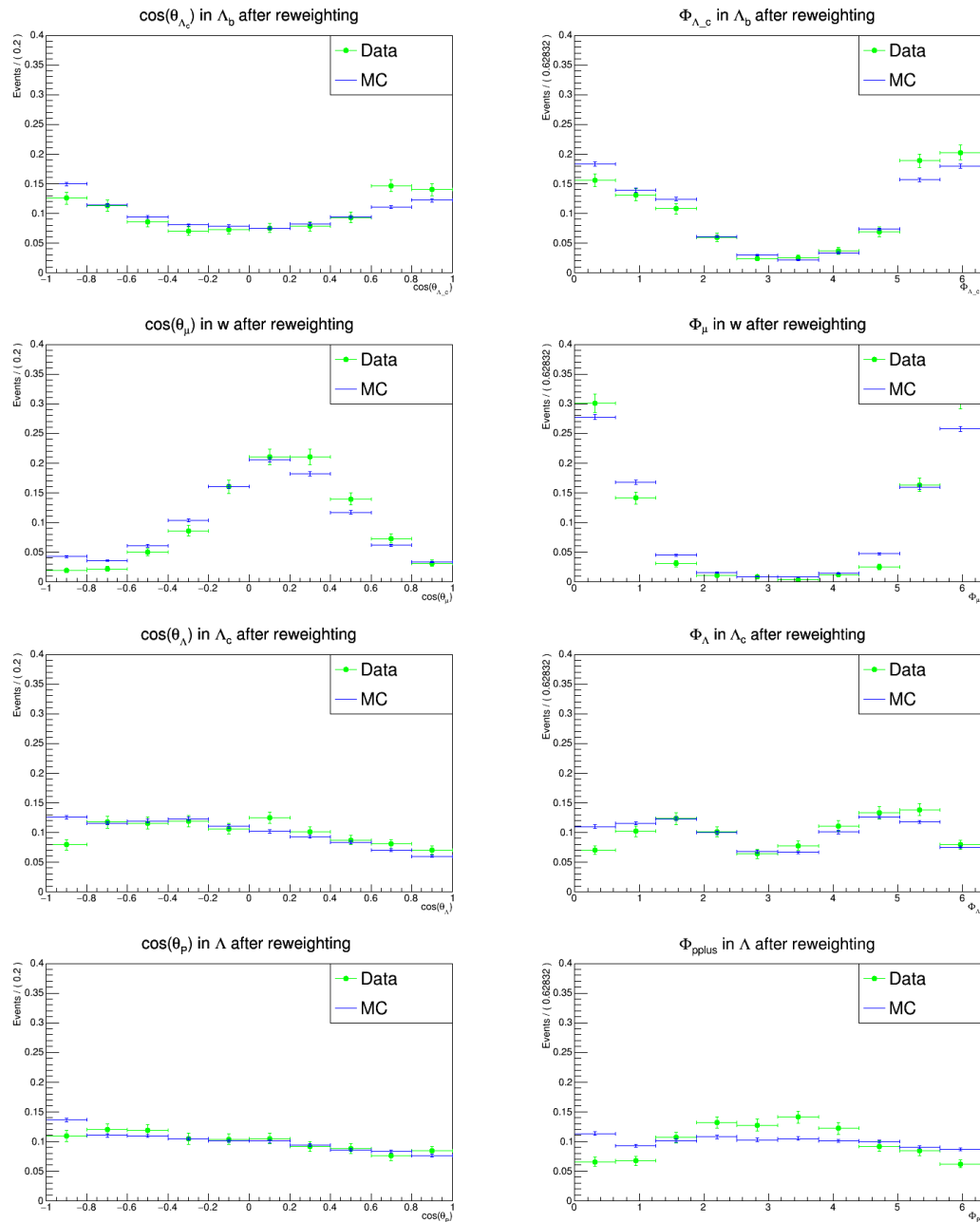
Figure 4.30: Comparison between MC (represented in blue) and Data (represented in green) of the angular distributions spectra for anti-particles of type DD for data 2012 after reweighting.
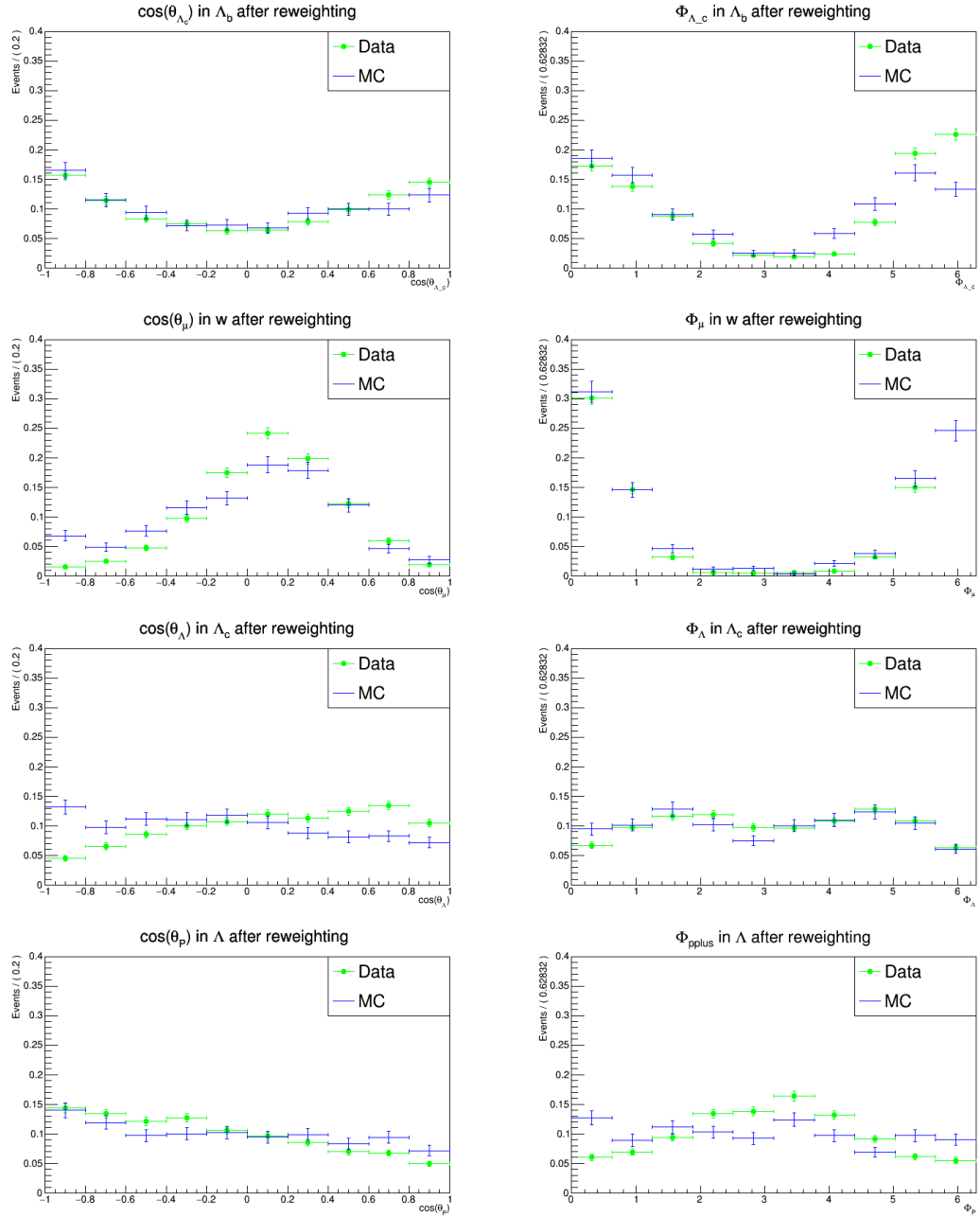
Figure 4.31: Comparison between MC (represented in blue) and Data (represented in green) of the angular distributions spectra for particles of type LL for data 2012 after reweighting.
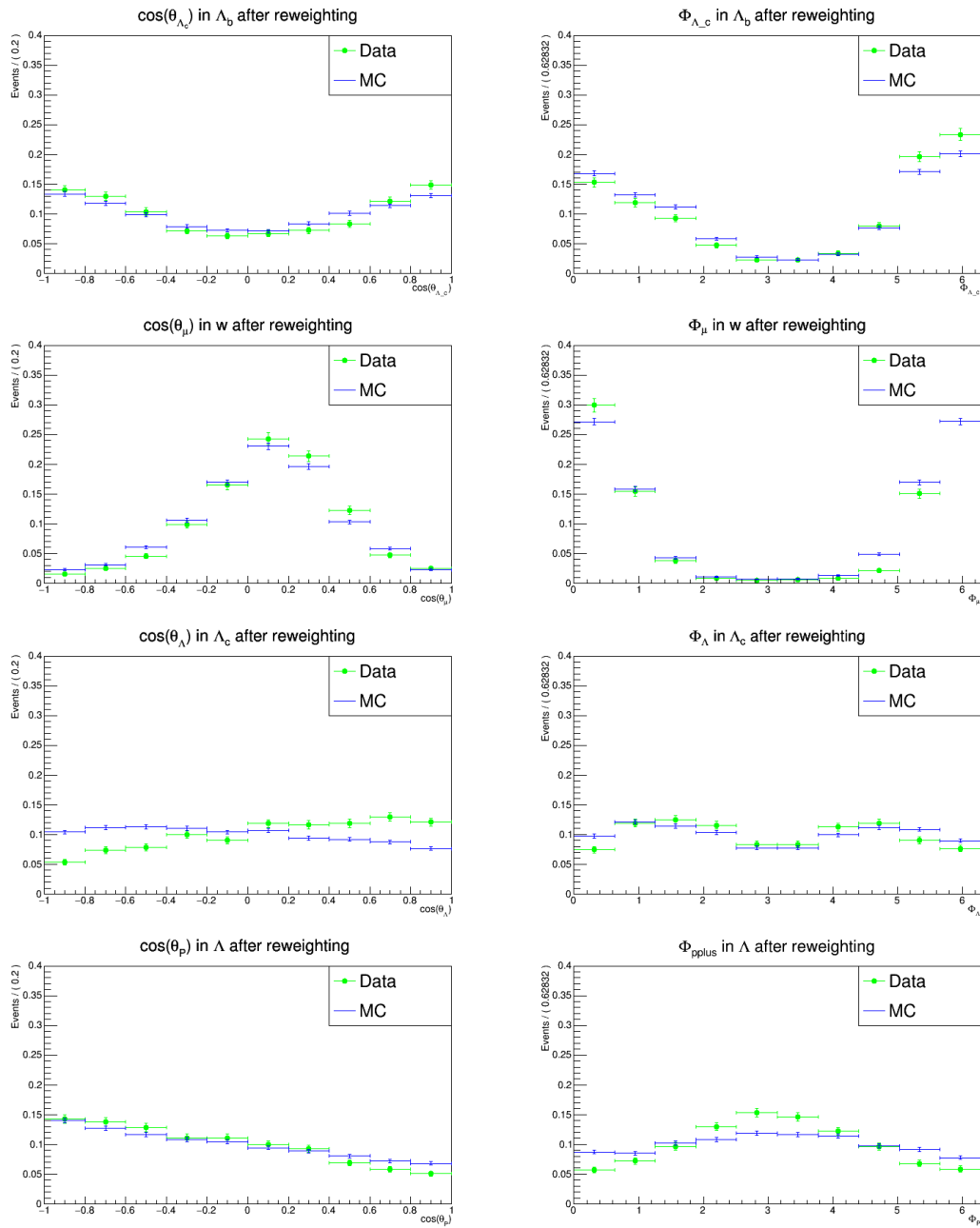
Figure 4.32: Comparison between MC (represented in blue) and Data (represented in green) of the angular distributions spectra for anti-particles of type LL for data 2012 after reweighting.

4.11   Angular acceptance

The LHCb detector induces a significant acceptance effect on the reconstruction of the angular distributions of the studied decays. For $\Lambda_b^0 \longrightarrow \Lambda_c^+ \mu\nu$, the available MC is generated according to BaryonPCR model, where the decays of the intermediate resonance are generated with the PHSP (phase-space) model for both $\Lambda_c^+ \longrightarrow \Lambda\pi$ and $\Lambda \longrightarrow p\pi$. The angular distributions at the generator level are therefore not flat since there have been some dynamics introduced to generate them. The aim of that is to see how the MC evolve. The results of the $\Lambda_b^0 \longrightarrow \Lambda_c^+ \mu\nu$ are shown in Figs. 4.33 and 4.34.
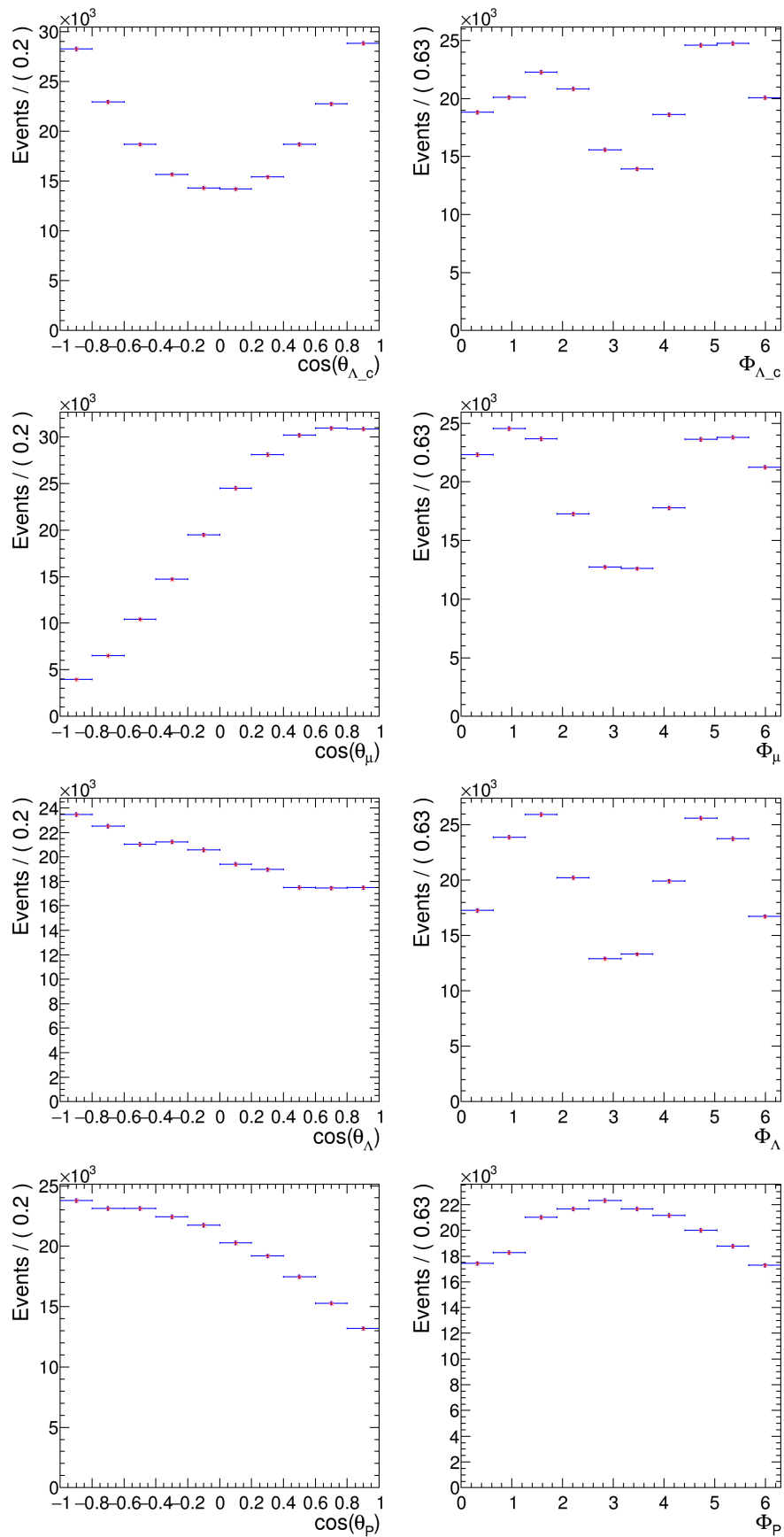
Figure 4.33: The angular distributions spectra for data 2011 at generator level.
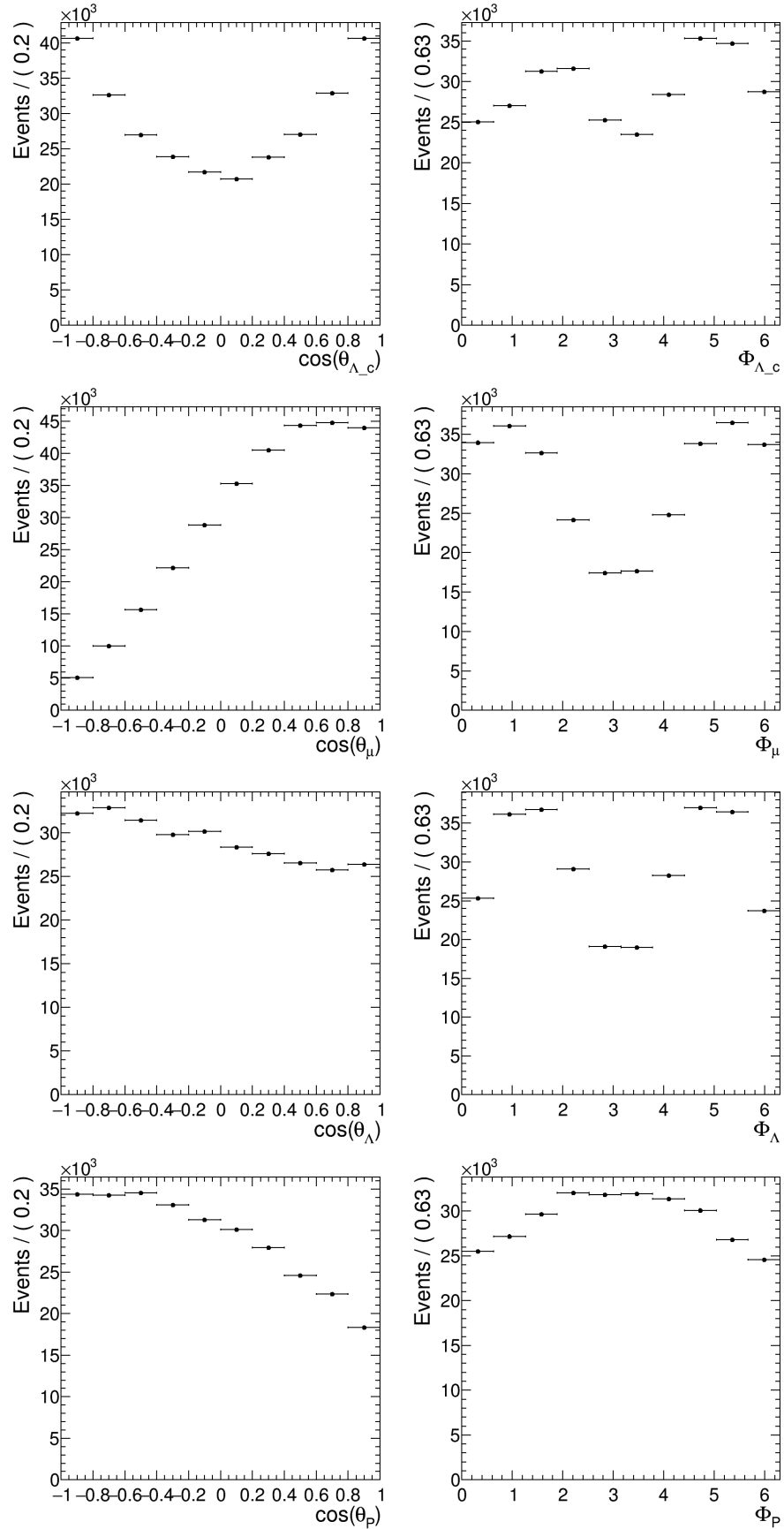
Figure 4.34: The angular distributions spectra for data 2012 at generator level.

4.12   Unfolding and Efficiency Determination

4.12.1   The Unfolded Angular distributions

The RooUnfold package [77] implanted in ROOT provides a common framework to evaluate and use different unfolding algorithms. It currently provides implementations or interfaces for the Iterative Bayes, Singular Value Decomposition, and TUnfold methods, as well as bin-by-bin and matrix inversion reference methods. Common tools provide co-variance matrix evaluation and multi-dimensional unfolding. A test suite allows comparisons of the performance of the algorithms under different truth and measurement models.

In this study, the Singular Value Decomposition method [78] is being used in order to remove the known effects of measurement resolutions, systematic biases, and detection efficiency which helps determining the "true" distribution. The response matrix is responsible for parametrizing the resolution effect for the reconstructed events and is inverted using singular value decomposition, which allows for a linear implementation of the unfolding algorithm.

For 1-dimensional true and measured distribution bins T_i and M_j, the response matrix element R_{ji} gives the fraction of events from bin T_i that end up measured in bin M_j. The response matrix is usually determined using Monte Carlo simulation (training), with the true values coming from the generator output. The normalization to the number of events is retained in order to minimize uncertainties due to the size of the training sample.

The SVD unfolding algorithm require a regularization parameter to prevent the statistical fluctuations being interpreted as structure in the true distribution. Therefore, the regularization needs to be tuned according to the distribution, binning, and sample statistics in order to minimize the bias due to the choice of the training sample while retaining small statistical fluctuations in the unfolding result.

4.12.2   The Unfolded Spectra Using Regularization Parameter

The correct choice of the regularization parameter, k, is of particular importance for the SVD method. A too-small value will bias the unfolding result towards the MC truth input, a too-large value will give a result that is dominated by unphysically enhanced statistical fluctuations. This needs to be tuned for any given distribution, number of bins, and approximate sample size-with k between 2 and the number of bins. (Using k=1 means getting only the training truth input as result without any corrections. Basically regularizing away any differences, and only keep the leading term which is, by construction, the MC truth input.) Hocker and Kartvelishvili's paper [79] (section 7) describes how to choose the optimum value for k. In this analysis, the k-value has been chosen to be equal to 3, where as the number of bins was chosen to be 10.

The unfolded error matrix includes the contribution of uncertainties on the response matrix due to finite MC training statistics.

The unfolded angular spectra are obtained by applying the response matrix to the measured spectra

$$N^i_{unfolded} = \sum_j R_{ij} N^j_{reco}$$

where $N^i_{unfolded}$ and N^j_{reco} are the unfolded and the measured spectra respectively. The results of the different angular distributions spectra ($\cos\theta$ and ϕ of Λ_c^+ in Λ_b^0 rest frame) for different samples (year : 2011, long long particles) are given in Figs.4.37 and 4.38. Each figure consists of three sub-figures: response matrix, co-variance matrix, and finally the comparison between the true-unfolded-

reconstructed angular spectra for each particle. For the rest of the particles see appendix B.

4.12.3 Unfolded MC

To be sure that every thing works well and to see the effect of the detector on the angular distribution, the MC samples have been also unfolded just after the reweighting procedure. We also exposed those samples to efficiency corrections using equation 4.18

$$\epsilon(x_i) = \frac{dN_{reco}[x_i]}{dN_{gen}[x_i]} \tag{4.18}$$

so that the distributions now look to be are more realistic,as seen in Figs. [4.35-4.36].
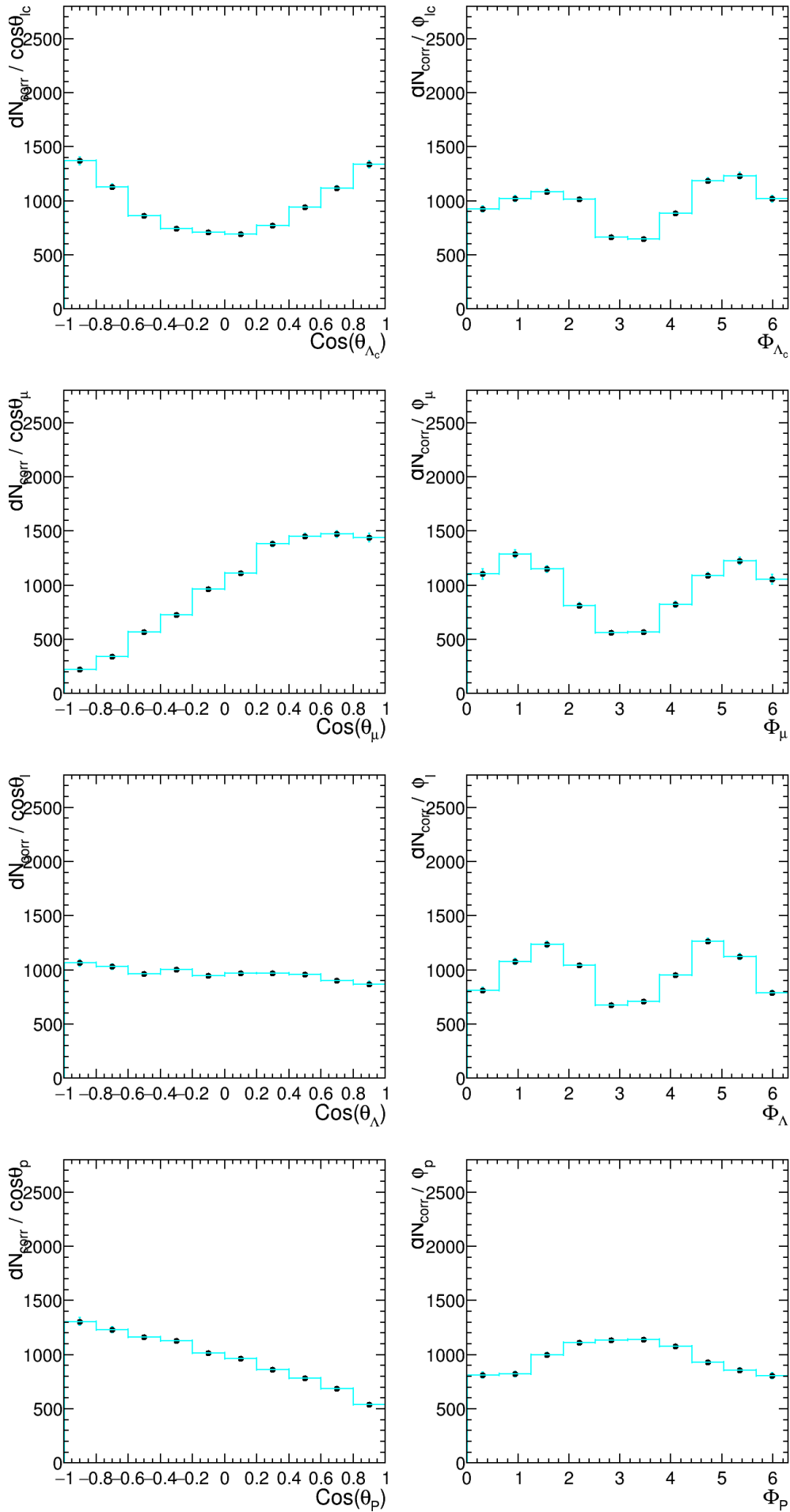
Figure 4.35: The unfolded MC spectra $\cos\theta$ and ϕ of the particles in their mother rest frame for the year 2011, particles, LL tracks.
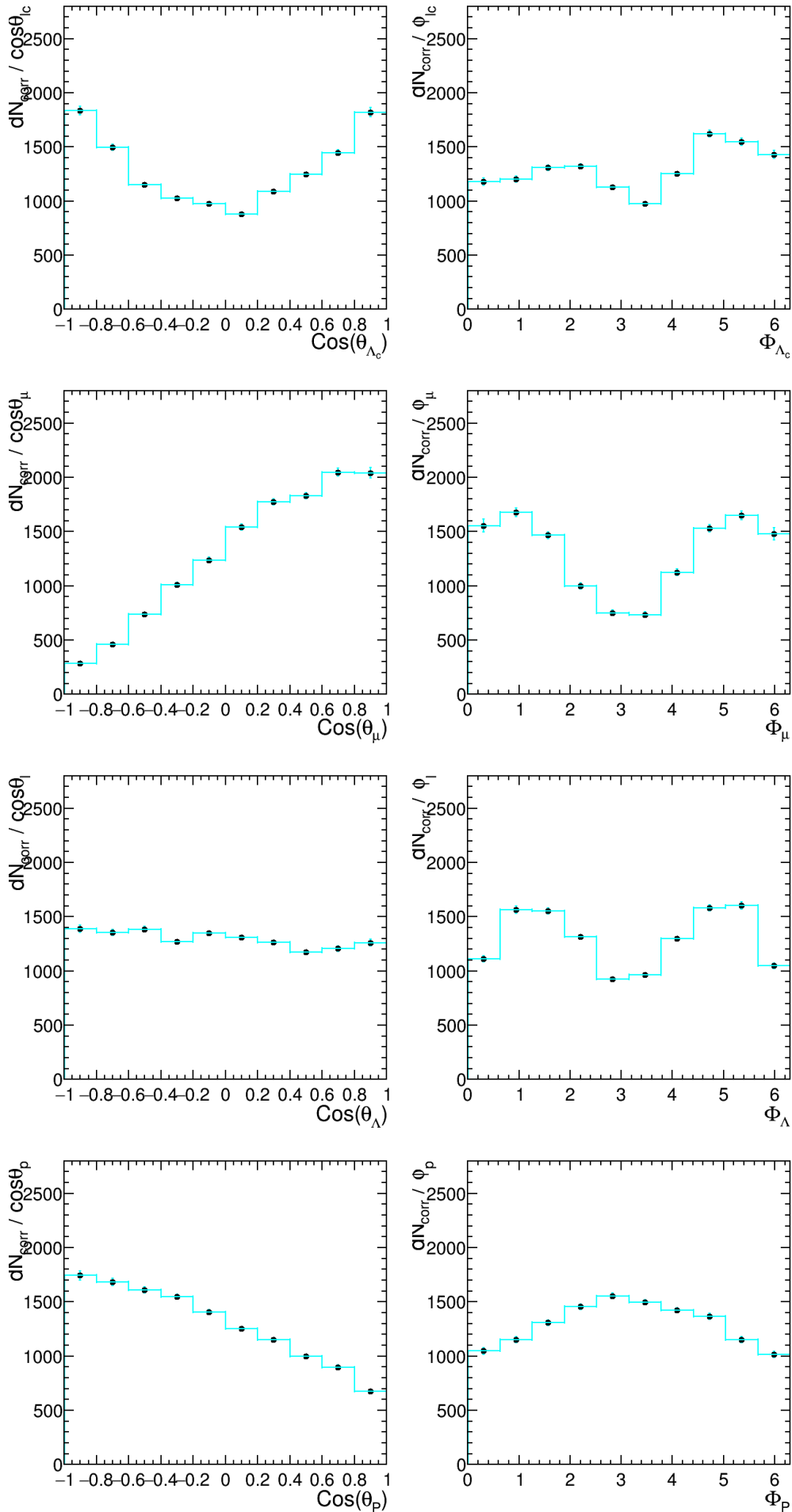
Figure 4.36: The unfolded MC spectra $\cos\theta$ and ϕ of the particles in their mother rest frame for the year 2012, particles, LL tracks.

4.12.4 Unfolded Data

Fig.4.37 and 4.38 show the response matrix deduced from the generated MC and the reconstructed one. The two figures also show the comparison between the generated angular distributions, the reconstructed ones and the unfolded angular distributions. Here we just plot one of the data samples, for the rest see appendix B.
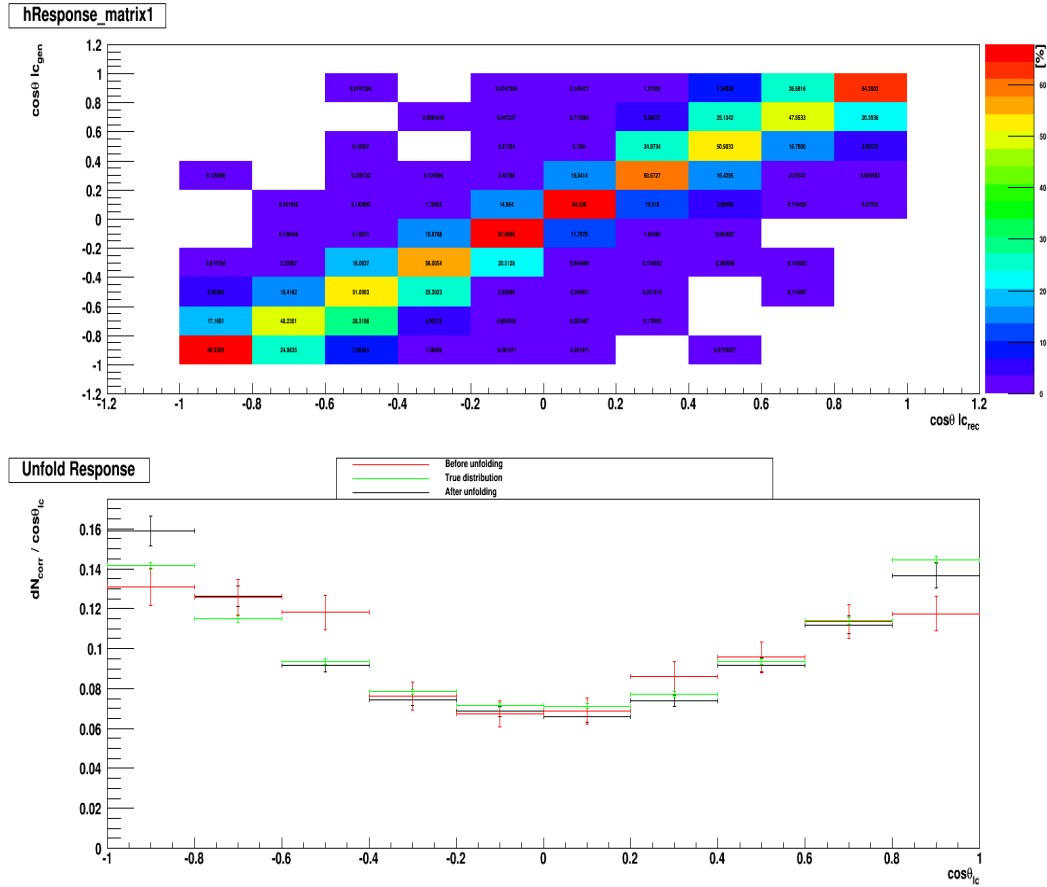
Figure 4.37: The angular distributions spectra $\cos\theta$ of Λ_c^+ in Λ_b^0 rest frame for the year 2011, particles, LL tracks. The top one represents the response matrix that gives the fraction of events from true bin T_i that end up in measured bin M_i. The bottom shows the distributions of the data before unfolding in red, the true distributions in green and the data being unfolded in black.
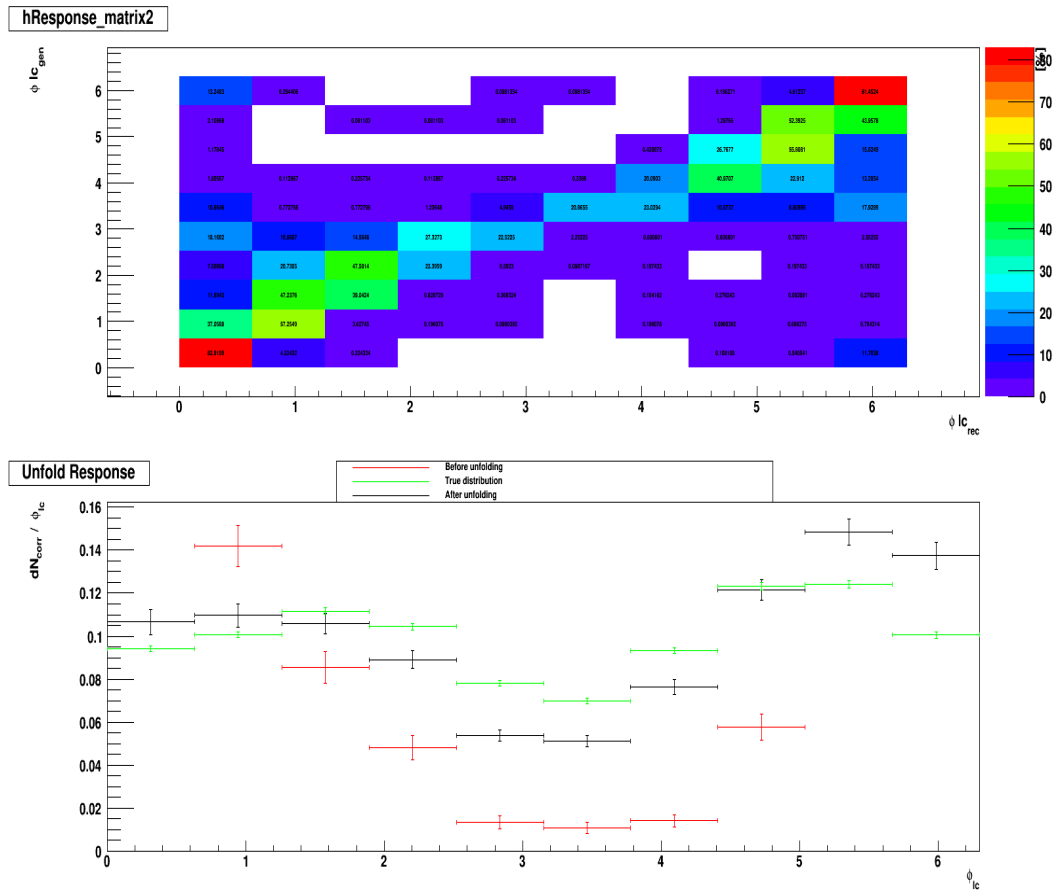
Figure 4.38: The angular distributions spectra ϕ of Λ_c^+ in Λ_b^0 rest frame for the year 2011, particles, LL tracks. The top one represents the response matrix that gives the fraction of events from true bin T_i that end up in measured bin M_i. The bottom shows the distributions of the data before unfolding in red, the true distributions in green and the data being unfolded in black.

Note: In order to take into account the correlations between the experimental data points introduced by the unfolding procedure, we perform a χ^2 fit with a "weight matrix" being the inverse of the non-diagonal covariance matrix [80].

We first start by setting the definition for the covariance matrix used in our study. The covariance matrix is defined as the matrix whose element in the i, j position is the covariance between the i-th and j-th elements of a random vector. A random vector is a random variable with multiple dimensions. Each element of the vector is a scalar random variable. Each element has either a finite number of observed empirical values or a finite or infinite number of potential values.

Because the covariance of the i-th random variable with itself is simply that random variable's variance, each element on the principal diagonal of the covariance matrix is the variance of one of the random variables. Because the covariance of the i-th random variable with the j-th one is the same thing as the covariance of the j-th random variable with the i-th one, every covariance matrix is symmetric. In addition, every covariance matrix is positive semi-definite.

As a simple expamle, Fig.4.40 shows the covariance matrix of the error bars associated with the ϕ distribution of the proton bin-by-bin.

In order to see more clearly the change in the parameters extracted, we use the same number of bins (10). So it is worth to note that the covariance matrix needed to be inverted is a (10x10) and this makes it more difficult to the study (we almost have 45 Degrees of Freedom). Some of those matrix elements are set by hand to zero while others are rounded to the next digit. The study of this covariance matrix was done by steps:

- Take the diagonal of the matrix (set all the other elements to zero) and check the validity of the model.

- In the next step, add the first and second diagonals (super diagonal + sub diagonal) and again see the effects on the polarization.

- Continue in the same manner with all the other diagonals to have finally the effect of the non-diagonal matrix elements on the polarization of the particles.

Note: It is worth to note that our study has stopped at the level of the second diagonal and the effects are negligible as compared to the real values. The main reason of such stopping is that, at the level of the third diagonal, the covariance matrix starts to be uninvertable (i.e the determinant is equal to zero), making it impossible to know the effects on the polarization. In other words, the effects of those off-diagonals matrix elements don't exist at higher order.

We extract again the fit parameters in order to see the change in the errors after the unfolding method. The results are given in Tab.4.10 and it shows a change in the values of almost 10%. The distribution using the χ^2 fit is shown in Fig.4.39.

Type of Fit	a_{12}	b_6	χ^2/NDF
Model Fit	-0.451±0.035	0.031±0.037	0.18
χ^2 Fit $\pm$ 1st diagonals	-0.422 ± 0.031	0.030 ± 0.02	0.16

Table 4.10: Parameters for the phi of the proton in the Λ rest frame for the sample LL-particles 2011 using the χ^2 Fit.

Since we are using an unfolding procedure, this induces the error on the covaiance matrix elements them selves. So again, Fig.4.41 represents the error on the covariance matrix element-by-element.
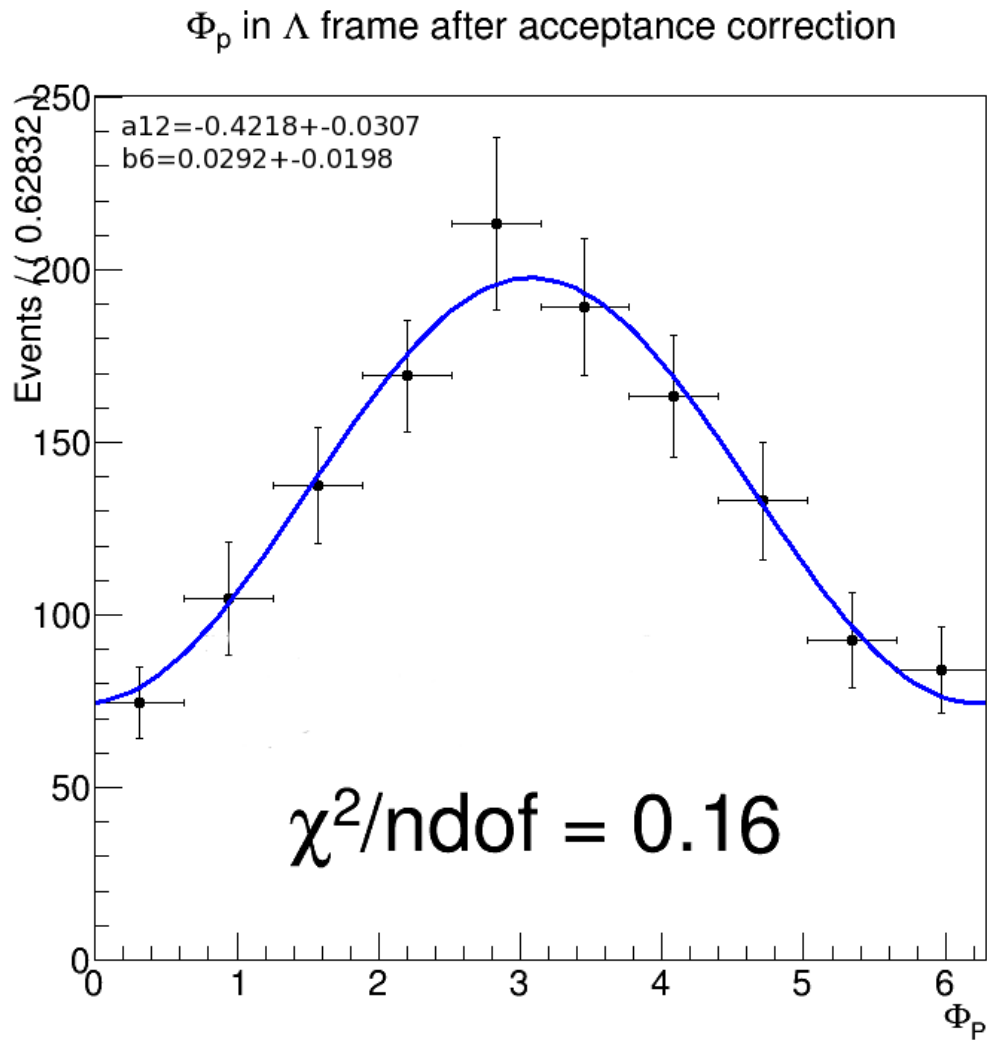
Figure 4.39: Parameters for the phi of the proton in the Λ rest frame for the sample LL-particles 2011.
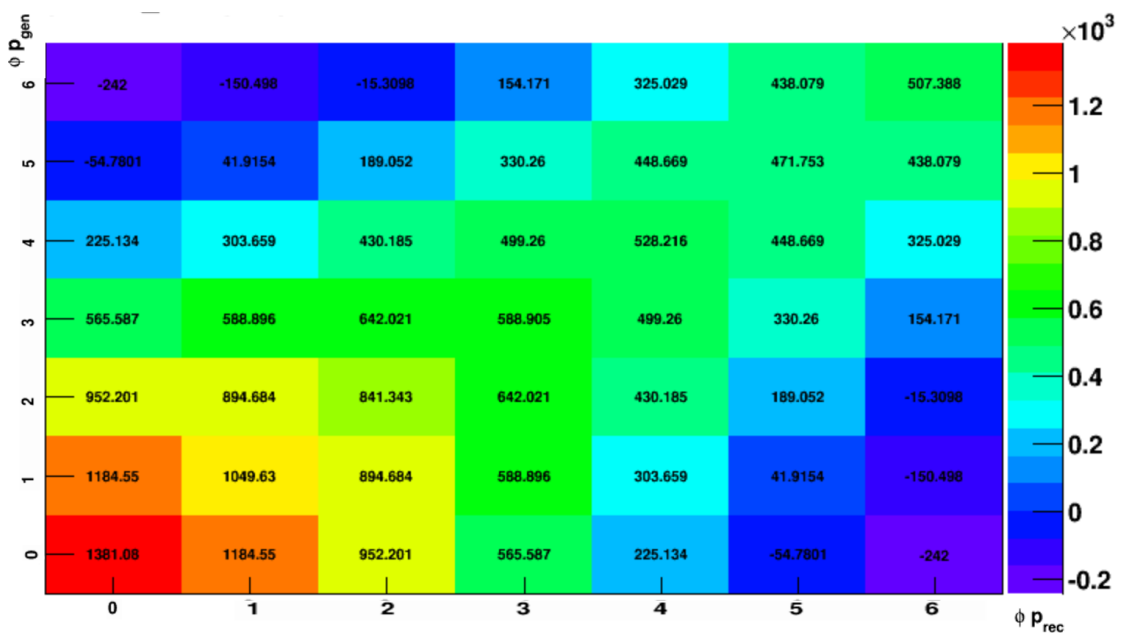
Figure 4.40: Covariance matrix associated to the error bar of the Phi distribution of the proton shown in Fig.4.39.
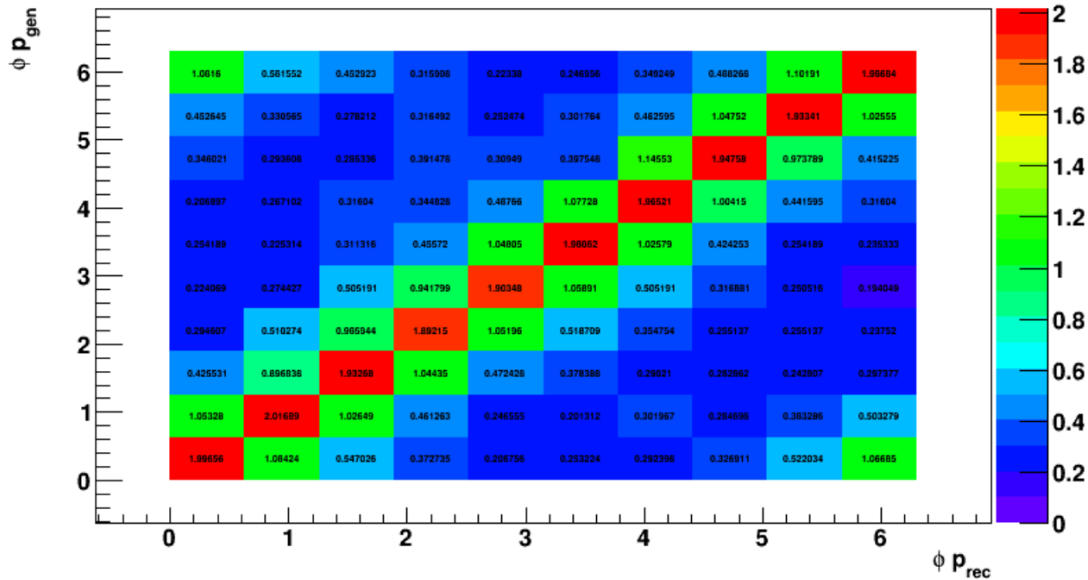
Figure 4.41: Error matrix associated with the covariance matrix shown in Fig.4.40.

4.12.5 Correction of the Data by the Global Efficiency of the LHCb Detector

The strategy of the analysis involves a lot of cuts in order to purify the final data sample used in interpretation of the results. The first efficiency correction applied to the data is the correction for the trigger efficiency. The second term for efficiency losses is due to the stripping, offline, and BDT selections. The last term counting for efficiency losses comes from the LHCb detector that induces a significant acceptance effect on the reconstruction of the angular distributions of the studied decays.

In order to obtain the correct angular distributions spectra needed for this analysis, the later should be corrected by the global efficiency of the detector; since all the data spectra, especially the angular distributions, depend on the LHCb detector acceptance. There are two methods to do that, one from the unfolding and the other is a general relation given in appendix C.

We just stick to the correction provided by the unfolding method and what we do is that we correct the efficiency bin by bin with the help of the equation 4.18.

Figs. 4.42-4.49 shows the angular spectra for the different particles for all data samples after correction by the global efficiency of the LHCb detector.
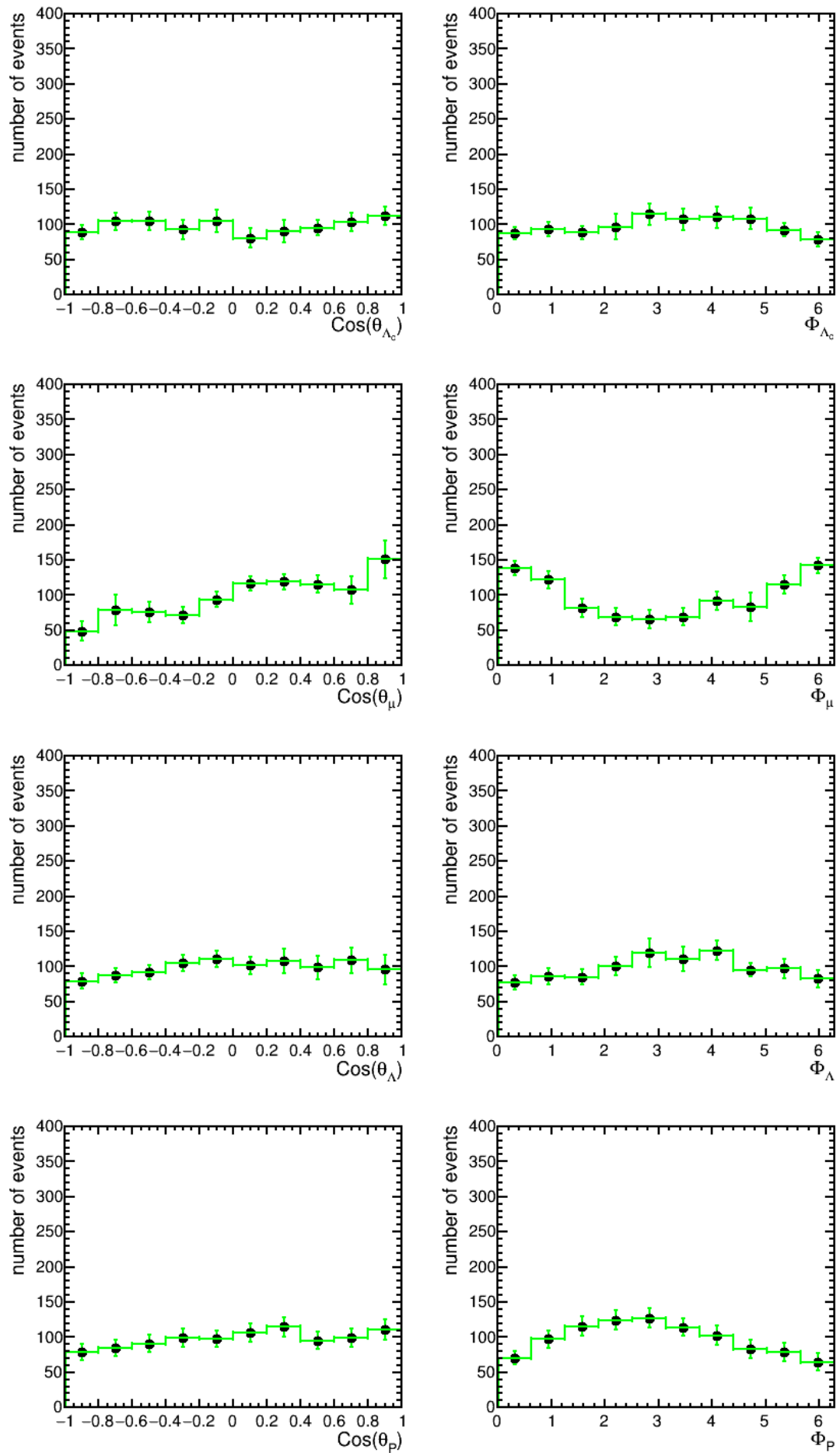
Figure 4.42: The angular distributions spectra after correction by the global efficiency of the LHCb detector for particles of type DD for data 2011.
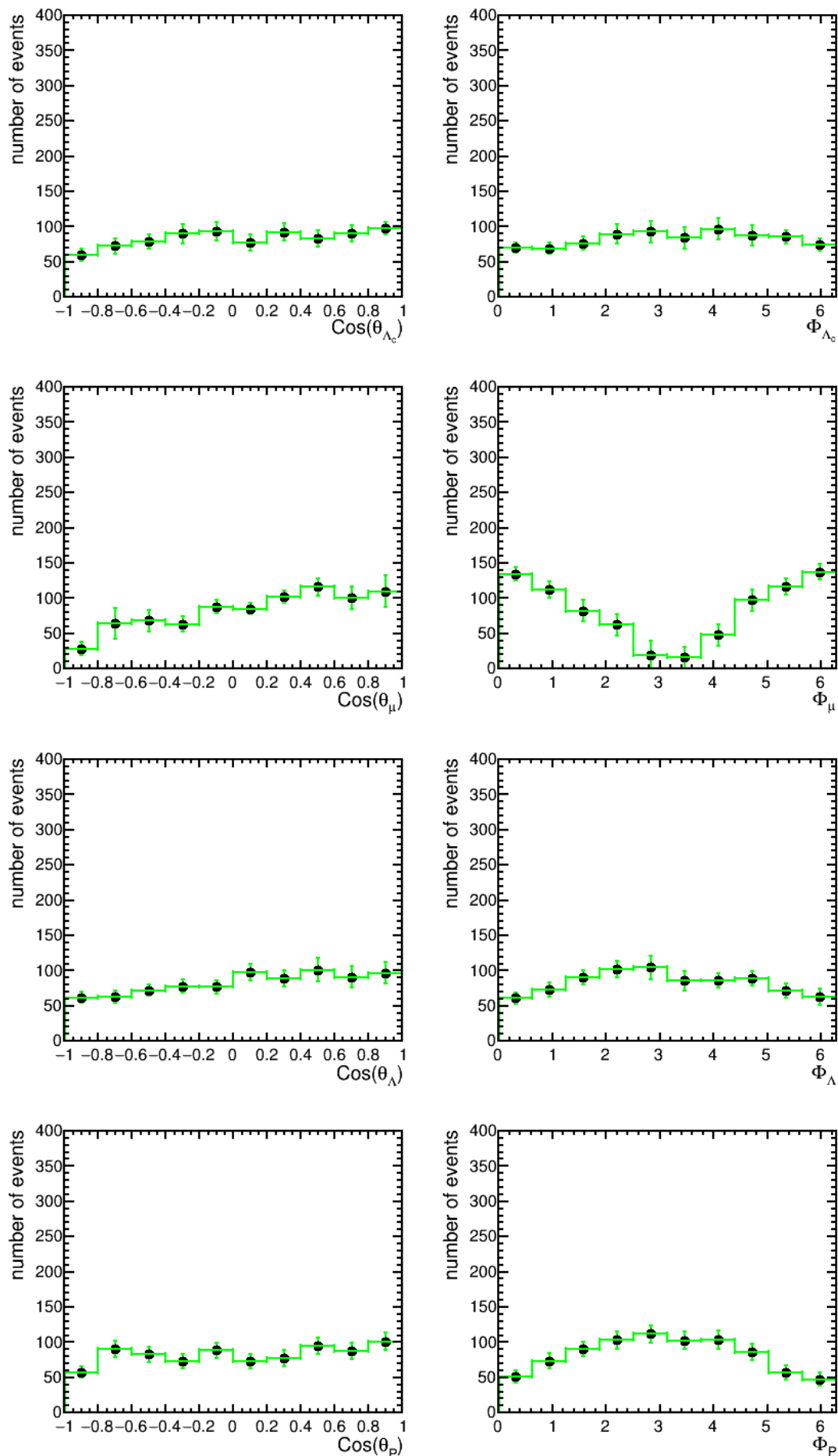
Figure 4.43: The angular distributions spectra after correction by the global efficiency of the LHCb detector for anti-particles of type DD for data 2011.
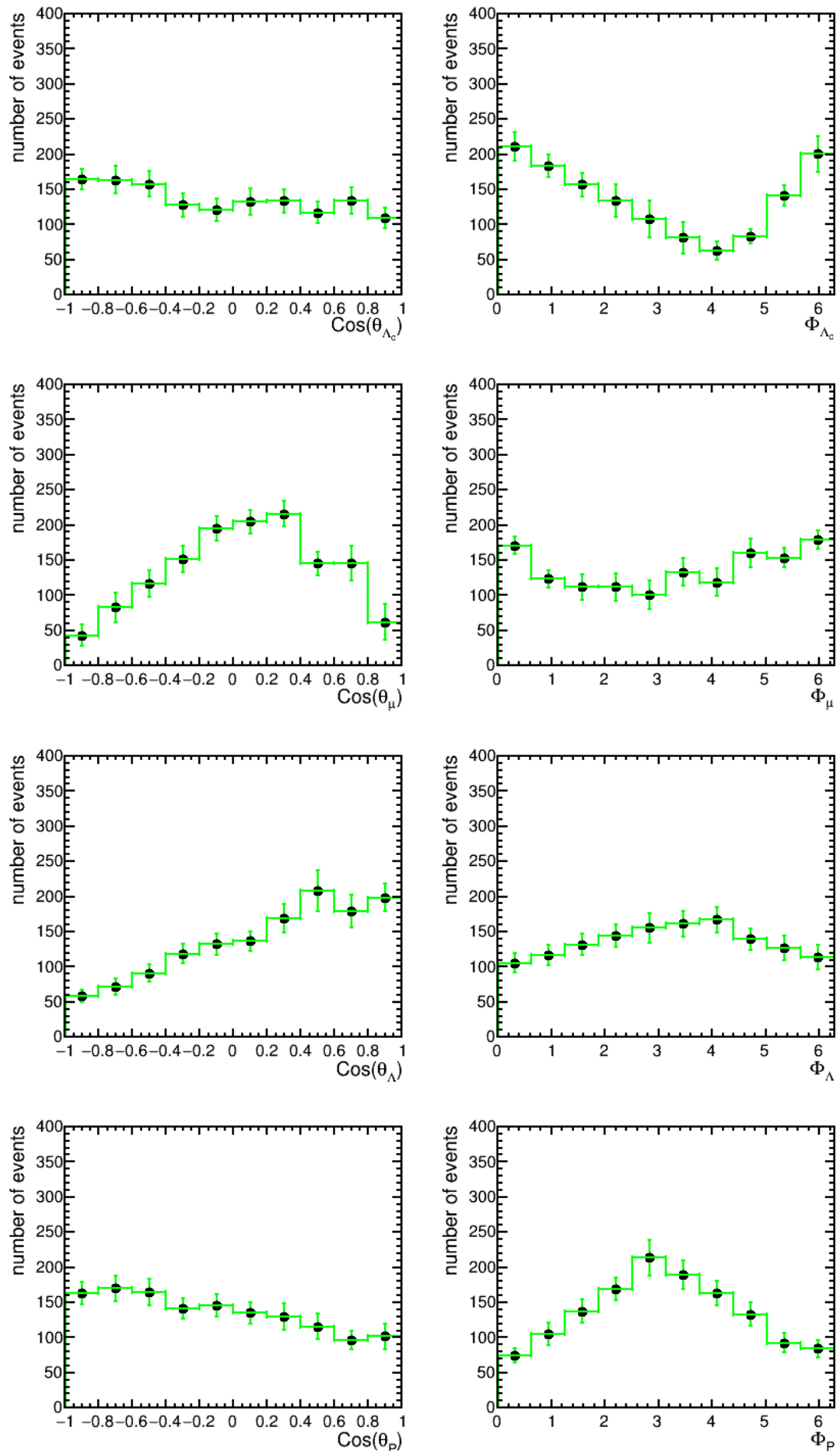
Figure 4.44: The angular distributions spectra after correction by the global efficiency of the LHCb detector for particles of type LL for data 2011.
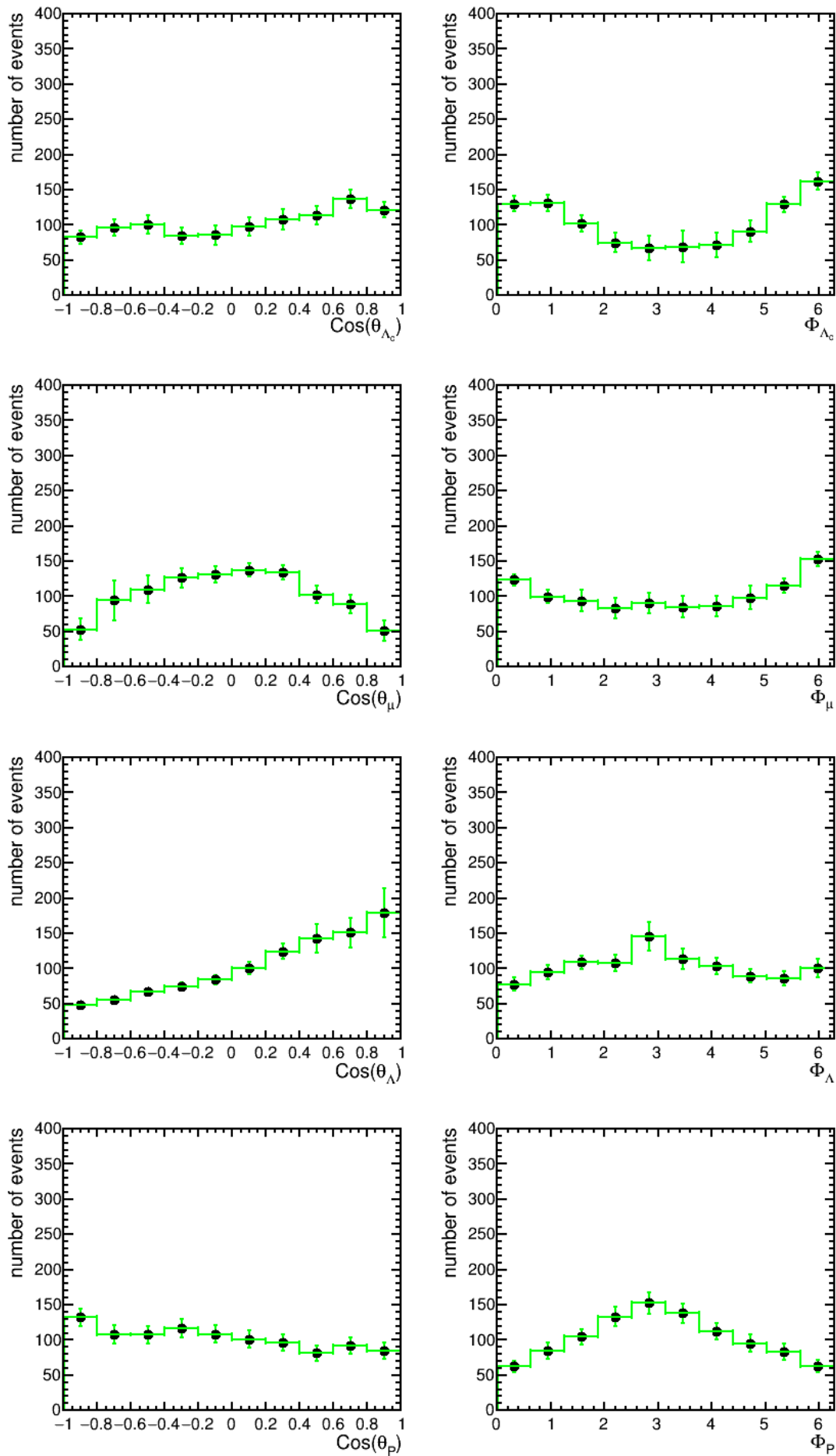
Figure 4.45: The angular distributions spectra after correction by the global efficiency of the LHCb detector for anti-particles of type LL for data 2011.
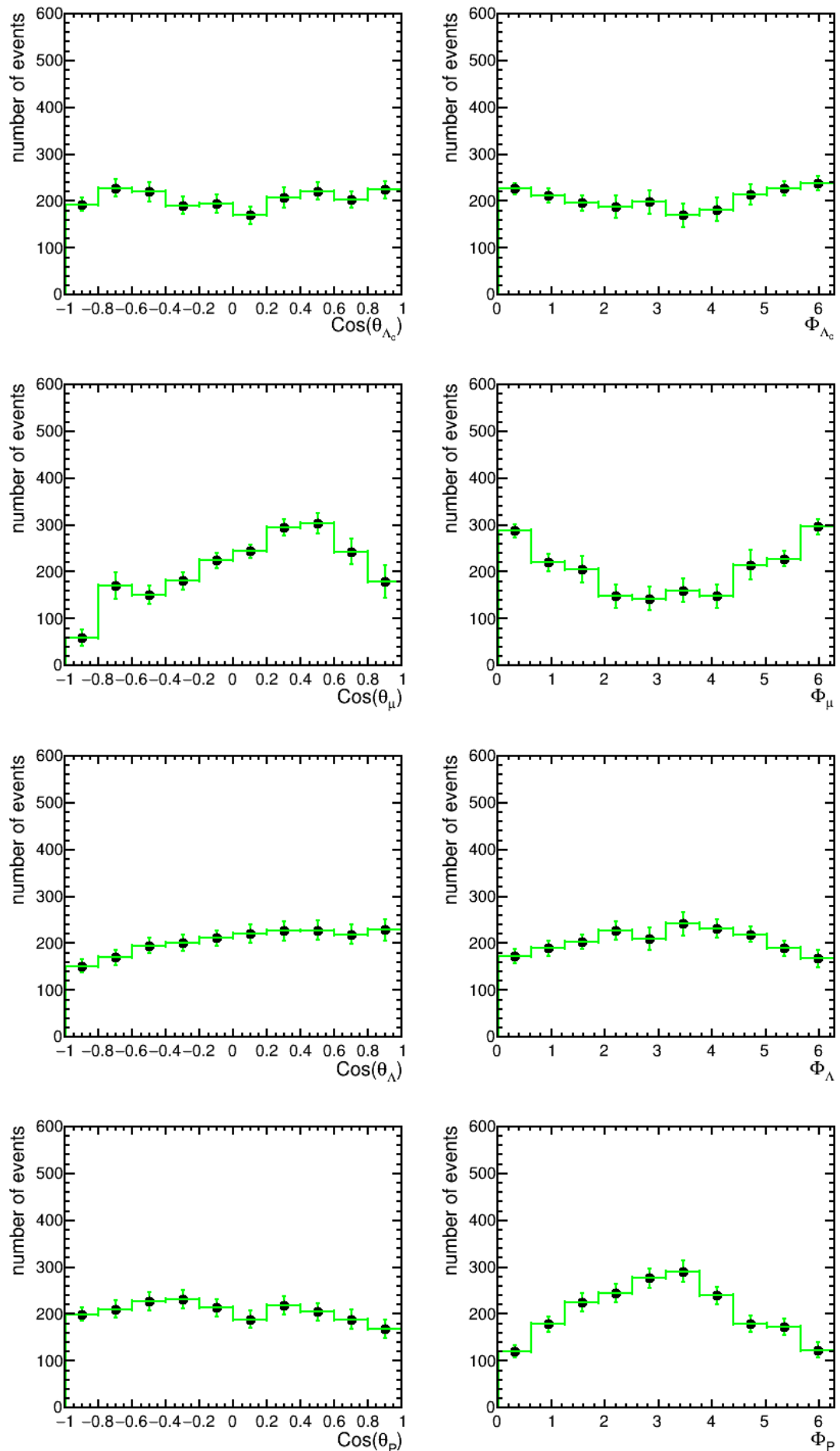
Figure 4.46: The angular distributions spectra after correction by the global efficiency of the LHCb detector for particles of type DD for data 2012.
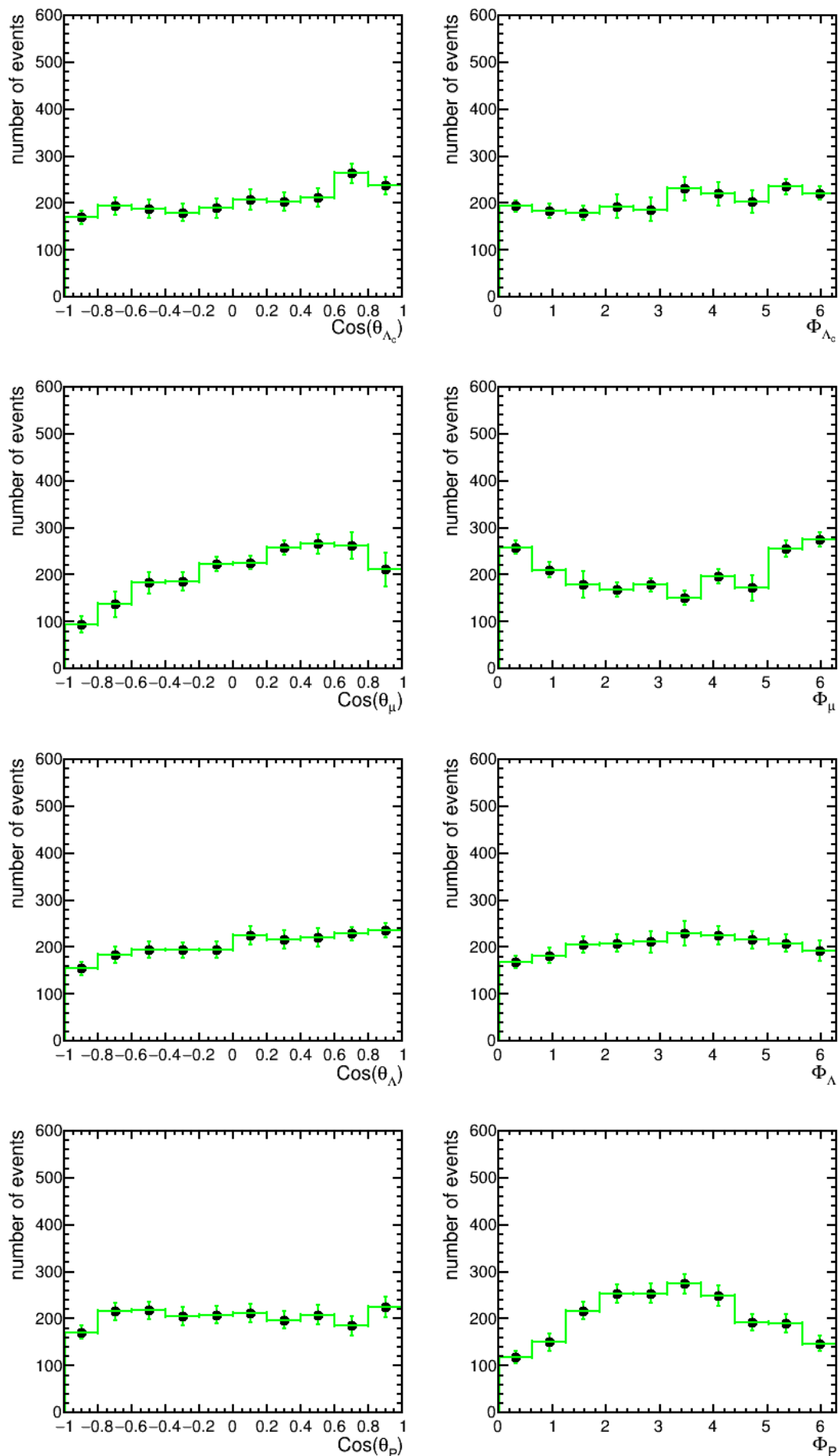
Figure 4.47: The angular distributions spectra after correction by the global efficiency of the LHCb detector for anti-particles of type DD for data 2012.
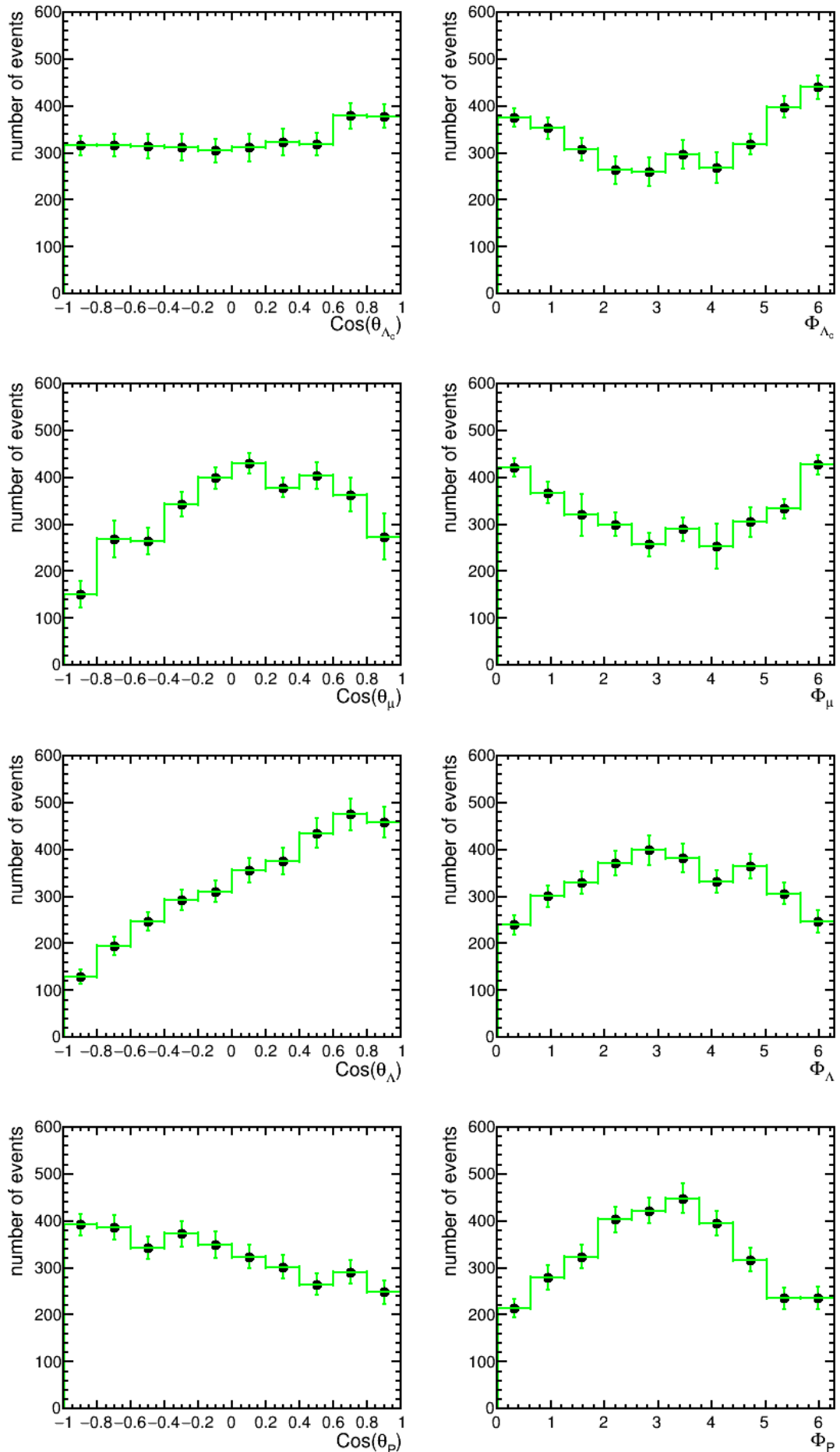
Figure 4.48: The angular distributions spectra after correction by the global efficiency of the LHCb detector for particles of type LL for data 2012.
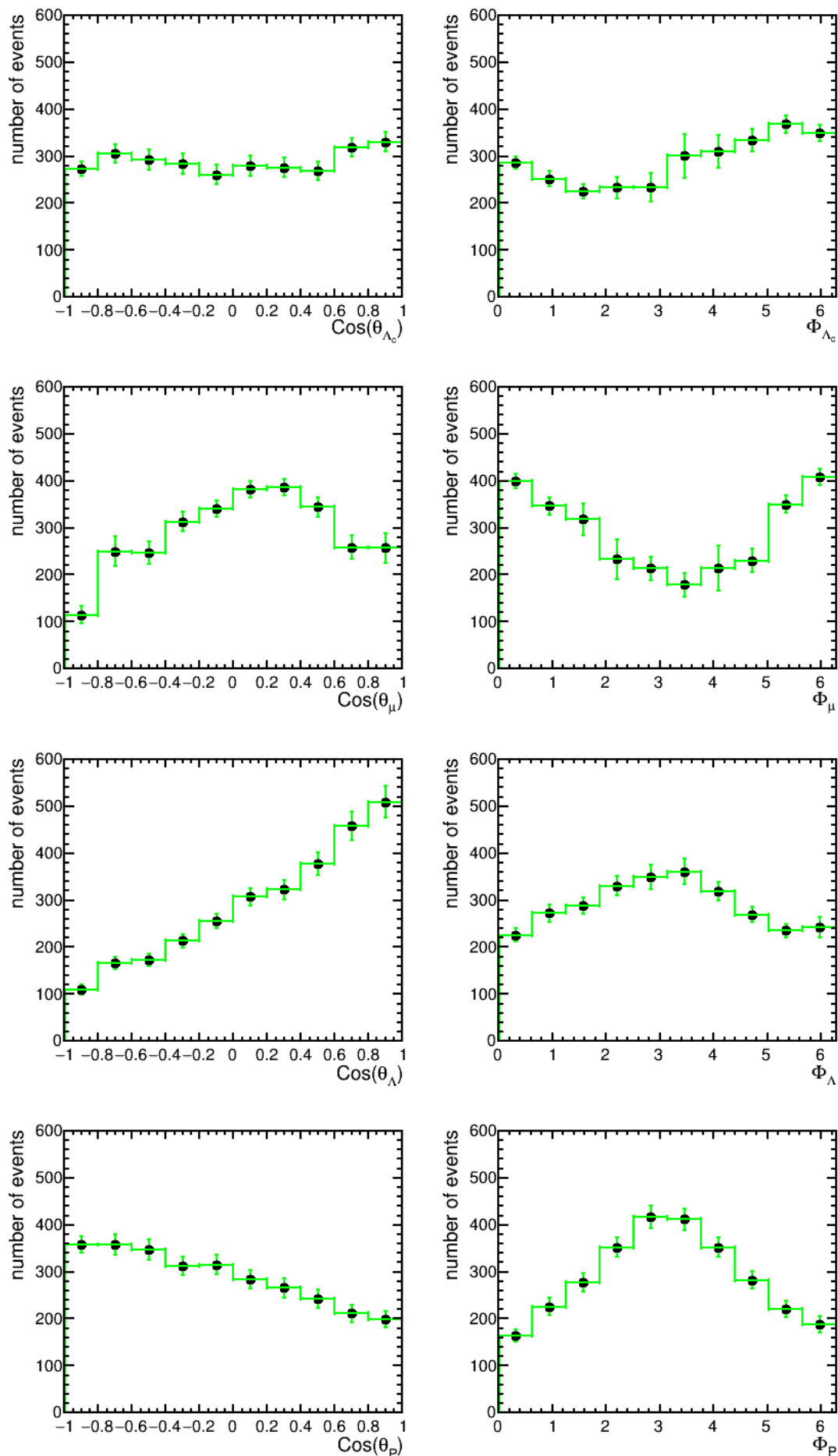
Figure 4.49: The angular distributions spectra after correction by the global efficiency of the LHCb detector for anti-particles of type LL for data 2012.

In this chapter a full analysis study has been performed. The strategy of the analysis concerning reconstruction, selection of the events and the offline cuts has been presented. A new method has been introduced for correcting angular distribution spectra called the Singular Value Decomposition (SVD). In the next chapter we will fit the final spectra, extract the polarization of the different resonances and interpret the final results.

Chapter 5

Interpretation of the Results

Contents

In this chapter we are going to estimate the polarization of the particles(anti-particles) from the final angular distribution spectra presented in the previous chapter. This will give us insights for Time Reversal violation and CP violation in the baryon decays.

5.1   Transformation of Polarization Vector under P and T

In this section, we are interested in developing a method for the determination of the particle polarization. Normally, as has been seen in chapter 3, the angular distribution is given by the following equation:

$$\frac{d\sigma}{d\Omega} \propto 1 + \alpha_{AS}^{Reso}\overrightarrow{P_{Reso}} \cdot \hat{p}_p \tag{5.1}$$

where

- $\hat{p}_p = \frac{\vec{p}}{|\vec{p}|}$ is the unit vector along the momentum of particle in its mother rest frame (Transversity or helicity).

- $\overrightarrow{P_{Reso}}$ is the polarization vector of the mother resonance.

It is worth to mention that the above angular distribution is valid for all types of the frames chosen. So for the **Transversity** frame of the Λ_b^0, the system of coordinates is defined as:

- X-axis is parallel to the incident beam $\vec{e}_x^{\,Trans} = \frac{\vec{P}_p}{|\vec{P}_p|}$.

- Z-axis is orthogonal to the Λ_b^0 production plane $\vec{e}_z^{\,Trans} = \frac{\vec{p}_p \times \overrightarrow{p}_{\Lambda_b}}{|\vec{p}_p \times \overrightarrow{p_{\Lambda_b}}|}$

- Y-axis forms direct frame, $\vec{e}_y^{\,Trans} = \vec{e}_z^{\,Trans} \times \vec{e}_x^{\,Trans}$.

The **Helicity** frame of the daughter particles is constructed from the Transversity frame by two successive rotations $R_y(\theta)$ and $R_z(\phi)$ and a boost along the momentum of the particle.

- Z-axis is parallel to the momentum of the particle $\vec{e}_z^{\,Hel} = \frac{\vec{P}_{part}}{|\vec{P}_{part}|}$.

- Y-axis is perpendicular to the plan of production of the particle. In other words, it is confined with the $\vec{e}_z^{\,Trans}$ in the Transversity frame.

- X-axis is the product of Y-axis and Z-axis. $\vec{e}_x^{\,Hel} = \vec{e}_y^{\,Hel} \times \vec{e}_z^{\,Hel}$

In order to have a clear idea on how the polarization vector of the resonance particles $R^{(i)}$ $(\Lambda_c, \Lambda^0, W^-)$ behave under discrete symmetries; the polarization vector of the resonance is generally given by:

$$\vec{P^R} = P_X^R\vec{e_x} + P_Y^R\vec{e_y} + P_Z^R\vec{e_z} \tag{5.2}$$

The transformation of the vectors $\vec{e_x}, \vec{e_y}, \vec{e_z}$ depends on the choice of the frame. Since the polarization vector is an axial one, it is important to know how its components behave under Parity and Time reversal symmetries. Tab.5.1 summarizes the transformation on the components P_X, P_Y, P_Z by P and T departing from the type of frames left (Helicity frame), right (Transversity frames).

As it has been shown in previous chapters, we are searching for the component of the polarization vector that is odd by T. In this case, we are talking about P_Z^{Trans} of Λ_b^0, P_X^{Hel} of Λ_c, and P_Y^{Hel} of Λ. If this value is different from zero, this means that there is an evidence for Time Reversal violation. It is important to say that the choice of the frame plays an essential role in expressing the different components of the polarization vector and hence on their transformation by T and P.

Observable	P	T	Observable	P	T	Observable	P	T
$\vec{e}_x^{Trans}$	-	-	$\vec{e}_x^{Hel}$	+	+	$\vec{e}_x^{Hel}$	-	-
$\vec{e}_y^{Trans}$	-	-	$\vec{e}_y^{Hel}$	-	-	$\vec{e}_y^{Hel}$	+	+
$\vec{e}_z^{Trans}$	+	+	$\vec{e}_z^{Hel}$	-	-	$\vec{e}_z^{Hel}$	-	-
P_X^{Trans}	-	+	P_X^{Hel}	+	−	P_X^{Hel}	-	+
P_Y^{Trans}	-	+	P_Y^{Hel}	-	+	P_Y^{Hel}	+	−
P_Z^{Trans}	+	−	P_Z^{Hel}	-	+	P_Z^{Hel}	-	+
$\vec{P}_{\Lambda_b^0}^{Trans}$	+	-	$\vec{P}_{\Lambda_c^+}^{Hel}$	+	-	$\vec{P}_{\Lambda}^{Hel}$	+	-

Table 5.1: Effect of Parity and Time Reversal Transformation on the components of the polarization vector in (1) Λ_b^0 Transversity frame, (2) Λ_c Helicity frame, and (3) Λ Helicity frame.

5.2   Final Angular Distribution Spectra

In order to obtain the final fit spectra, the ROOFIT software [81] is being used. This software allows to best fit the angular distributions and extract the fit parameters that directly give an access to the needed polarization.

5.2.1 Λ_c^+ in Λ_b^0 Transversity rest frame

It is important to show the Λ_b^0 helicity frame (Fig.5.1) where the study is done.
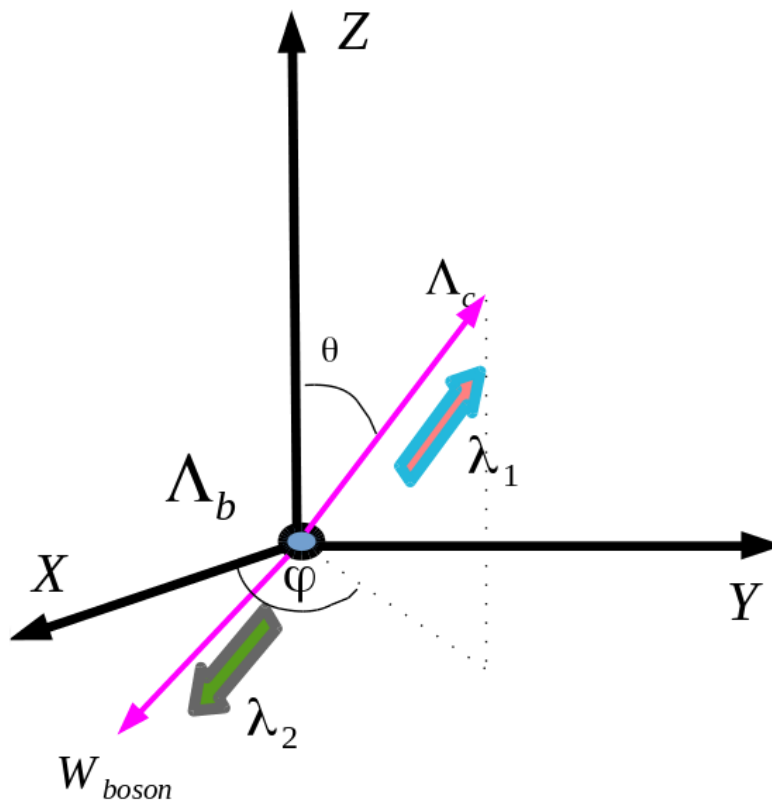
Figure 5.1: Λ_b^0 Transversity frame.

The polar distribution $\cos\theta$

• The polar distribution according to $\cos\theta$ of Λ_c^+ in Λ_b^0 transverse rest frame constructed from the LHCb frame as has been shown early in chapter 3 is given by :

$$\frac{d\sigma}{d\cos\theta_{\Lambda_c^+}} \propto 1 + \alpha_{AS}^{\Lambda_b} P_Z^{\Lambda_b} \cos\theta_{\Lambda_c^+}$$

So in order to model this distribution, a linear function of the form : $1 + a_1\cos\theta$ is being used, and thus $P_Z^{\Lambda_b}$ is given by the following relation $P_Z^{\Lambda_b} = \frac{a_1}{\alpha_{AS}^{\Lambda_b}}$. The associated statistical error with this relation is driven as follows:

$$c = \frac{a}{b} \implies \sigma_c = c\sqrt{\left(\frac{\sigma_a}{a}\right)^2 + \left(\frac{\sigma_b}{b}\right)^2}$$

assuming that a and b are uncorrelated.

Year	Particle	Track	$a_1 = \alpha_{AS}^{\Lambda_b} \times P_Z^{\Lambda_b}$
2011	Λ_c^+	LL	-0.190 ± 0.046
		DD	-0.034 ± 0.055
	$\bar{\Lambda}_c^-$	LL	0.221 ± 0.052
		DD	0.180 ± 0.061
2012	Λ_c^+	LL	0.094 ± 0.030
		DD	0.019 ± 0.038
	$\bar{\Lambda}_c^-$	LL	0.048 ± 0.032
		DD	0.188 ± 0.038

Table 5.2: $P_Z^{\Lambda_b}$ extracted from the polar distribution according to $\cos\theta$ of Λ_c^+ in Λ_b^0 rest frame and the fit parameters for different 2011 and 2012 data samples.

Here it is worth to note that the $P_Z^{\Lambda_b^0}$ is the transverse component of the polarization vector in Λ_b^0 Transversity frame. Figs.5.2 and 5.3 represent the fit $\cos\theta$ of Λ_c^+ in Λ_b^0 Transversity frame. Tab.5.2 shows the values of the slope $a_1 = \alpha_{AS}^{\Lambda_b} \times P_Z^{\Lambda_b}$ of the data 2011-2012 for different samples.

Interpretation of the fit:

The χ^2, or *chi-square*, of the fit which is a statistical quantity used to test whether any given data are well described by some hypothesized function. Such determination is called a *chi-square test for goodness* of fit. The χ^2 of the whole fits is good, but there is difference between the distributions of the LL and the DD samples which is still under study.

The lack of information concerning the value of the decay parameter $\alpha_{AS}^{\Lambda_b}$ prevent us from extracting the $P_Z^{\Lambda_b}$, but one can set an lower limit for this value by $|P_Z^{\Lambda_b}| \geq |a_1|$ ($|\alpha_{AS}^{\Lambda_b}| < 1$).

According to the Tab.5.1, $P_Z^{\Lambda_b^0}$ is considered to be odd under Time Reversal, so any value of this parameter different from zero could be a sign for TRV. According to Tab.5.2, there are some data samples that shows sign for $P_Z^{\Lambda_b^0} \neq 0$ at 4σ within experimental errors. The final particles here, μ and Λ_c^+, neglect the possibility of the final state interaction that could modify any sign of Time Reversal Violation. But in this case, one could not say that $P_Z^{\Lambda_b^0} \neq 0$ could show sign for TRV, because QCD accommodates with a T-odd observables (Λ_b^0 is produced from strong interactions).
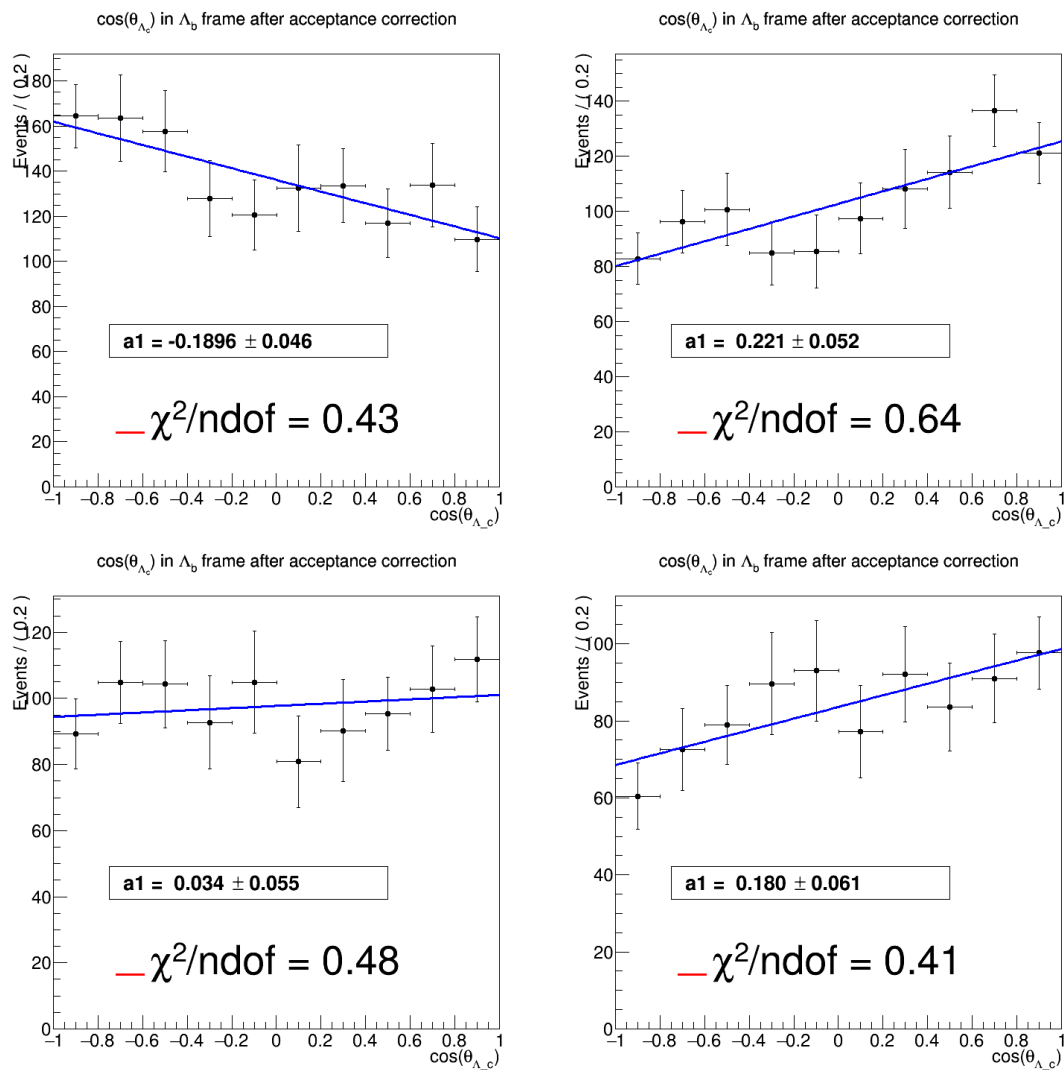
Figure 5.2: Fit results for the angular distributions spectra of $\cos\theta_{\Lambda_c^+}$ in Λ_b^0 rest frame after correction by the global efficiency of the LHCb detector for data 2011: left(right): particles(antiparticles) and up(down): long-long (down-down) tracks.
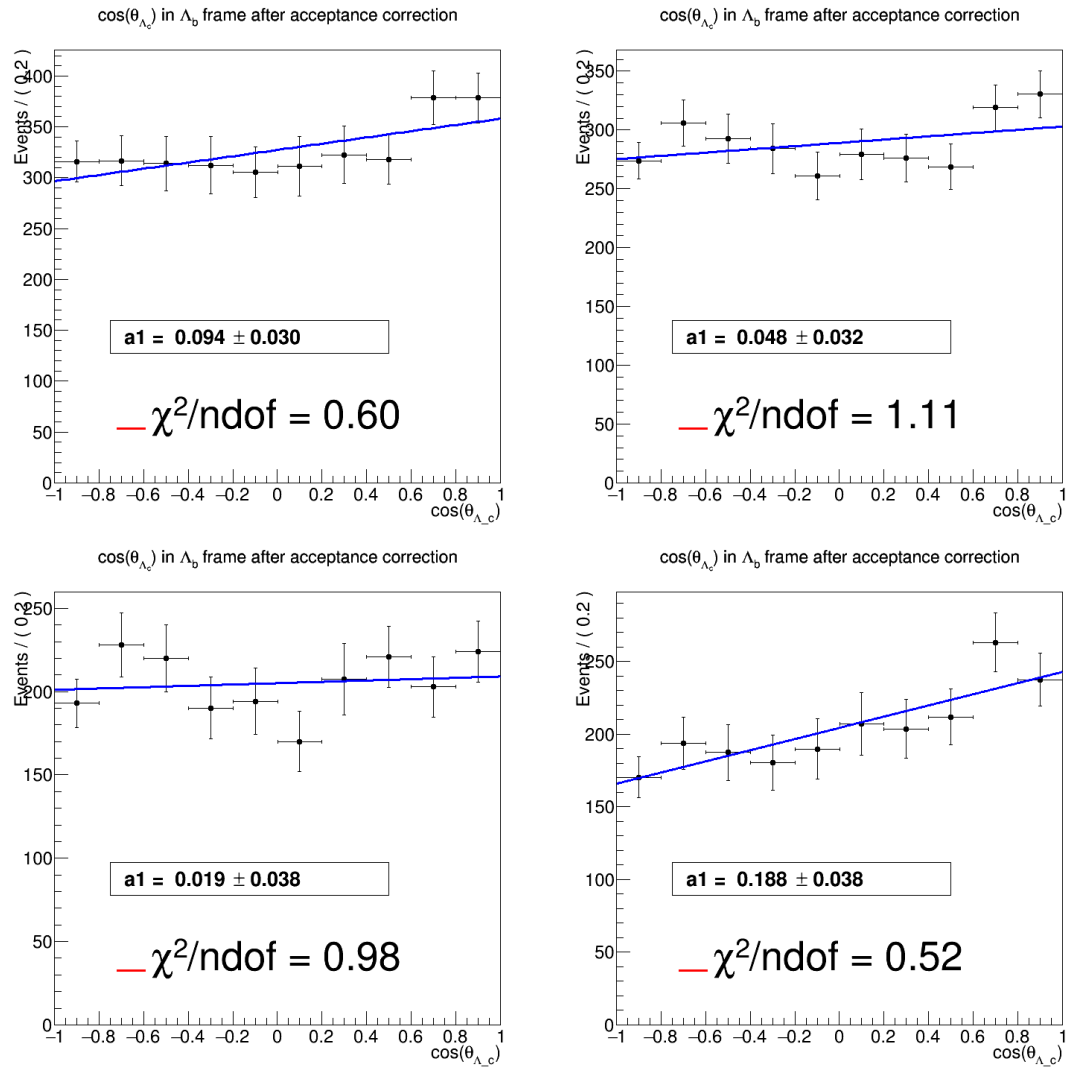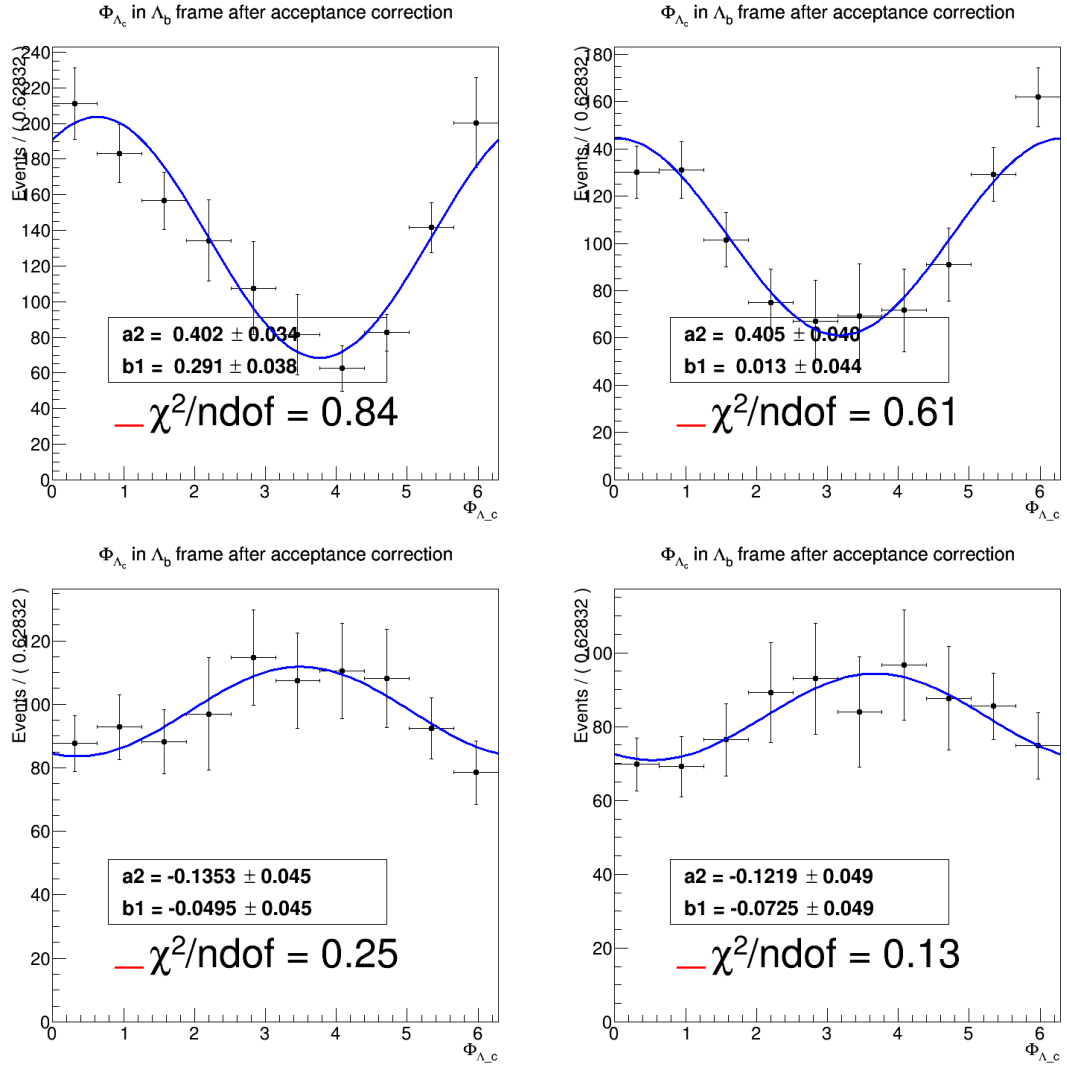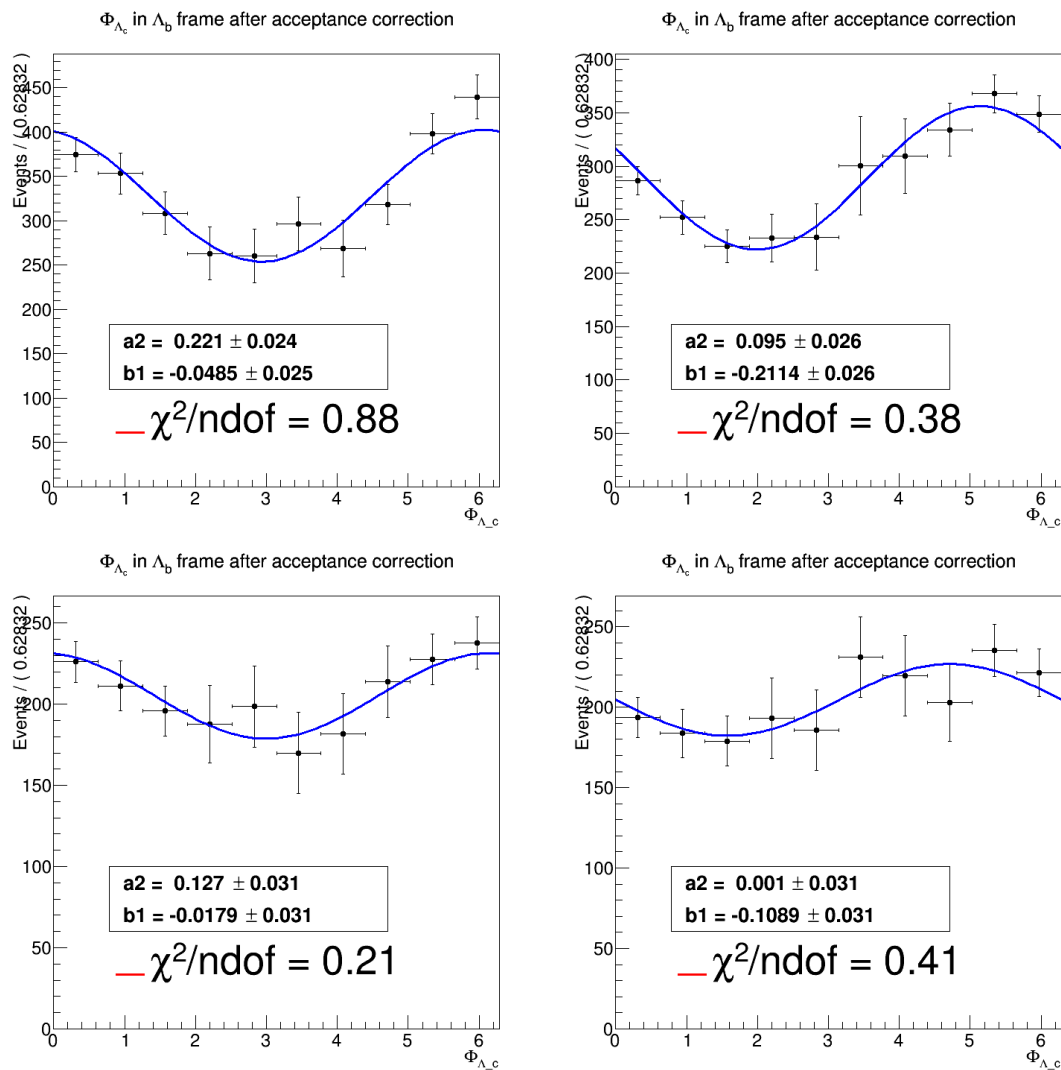
Figure 5.3: Fit results for the angular distributions spectra of Λ_c^+ in Λ_b^0 rest frame after correction by the global efficiency of the LHCb detector for data 2012: left(right), particles(antiparticles), up(down) long-long (down-down) tracks.

The azimuthal distribution ϕ

• The azimuthal distribution according to ϕ of Λ_c^+ in Λ_b^0 rest frame is given by :

$$\frac{d\sigma}{d\phi_{\Lambda_c^+}} \propto 1 + \frac{\pi}{4}\alpha_{AS}^{\Lambda_b}[P_X^{\Lambda_b}\cos\phi_{\Lambda_c^+} + P_Y^{\Lambda_b}\sin\phi_{\Lambda_c^+}]$$

For this distribution, a linear fit of the form $1 + a_2\cos\phi + b_1\sin\phi$ also is taken in the ROOFIT, and by that

$$P_X^{\Lambda_b} = \frac{4*a_2}{\pi\alpha_{AS}^{\Lambda_b}}$$

while

$$P_Y^{\Lambda_b} = \frac{4*b_1}{\pi\alpha_{AS}^{\Lambda_b}}$$

and again the associated error is driven by the same method described above and is given by the following relation:

$$\sigma_c = c\sqrt{\left(\frac{\sigma_a}{a}\right)^2 + \left(\frac{\sigma_b}{b}\right)^2}$$

.

Year	Particle	Track	$a_2 = \frac{\pi}{4}\alpha_{AS}^{\Lambda_b} \times P_X^{\Lambda_b}$	$b_1 = \frac{\pi}{4}\alpha_{AS}^{\Lambda_b} \times P_Y^{\Lambda_b}$
2011	Λ_c^+	LL	0.402 ± 0.034	0.291 ± 0.038
		DD	0.135 ± 0.045	-0.050 ± 0.045
	$\bar{\Lambda}_c^-$	LL	0.405 ± 0.048	0.013 ± 0.044
		DD	-0.122 ± 0.049	-0.073 ± 0.049
2012	Λ_c^+	LL	0.221 ± 0.024	-0.049 ± 0.025
		DD	0.127 ± 0.031	-0.018 ± 0.031
	$\bar{\Lambda}_c^-$	LL	0.095 ± 0.026	-0.211 ± 0.026
		DD	0.001 ± 0.031	-0.109 ± 0.031

Table 5.3: $P_X^{\Lambda_b}$ and $P_Y^{\Lambda_b}$ extracted from the azimuthal distribution according to ϕ of Λ_c^+ in Λ_b^0 rest frame and the fit parameters for different 2011 and 2012 data samples.

Tab.5.3 shows the values of $a_2 = \frac{\pi}{4}\alpha_{AS}^{\Lambda_b} \times P_X^{\Lambda_b}$ and $b_1 = \frac{\pi}{4}\alpha_{AS}^{\Lambda_b} \times P_Y^{\Lambda_b}$ of the data 2011-2012 for different samples.

Figs.5.4 and 5.5 represent the fit ϕ of Λ_c^+ in Λ_b^0 Transversity frame. Due to the lack of information concerning the value of the decay parameter $\alpha_{AS}^{\Lambda_b}$, we were unable to measure the $P_X^{\Lambda_b}$ and $P_Y^{\Lambda_b}$. But again the lower limit has also been set due to $|\alpha_{AS}^{\Lambda_b}| < 1$ ($|P_X^{\Lambda_b}| \geq \frac{4}{\pi}\frac{|a_2|}{|\alpha_{AS}^{\Lambda_b}|}, |P_Y^{\Lambda_b}| \geq \frac{4}{\pi}\frac{|b_1|}{|\alpha_{AS}^{\Lambda_b}|}$).

Interpretation of the fit:

• b_1 values are compatible with zero within the experimental errors for some of the data samples, while others show polarization of the Λ_b^0 along the Y-axis.

• However, the values of a_2 are different from zero, which for sure will result in $P_X^{\Lambda_b}$ non compatible with zero. This indicate that there is polarization of the Λ_b^0 particle along the beam axis represented by the X-axis (in the new constructed frame). This confirms the previous measurements concerning the longitudinal polarization of Λ_b^0 produced in hadronic environments [61].

Figure 5.4: Fit results for the azimuthal distributions spectra of Λ_c^+ in Λ_b^0 rest frame after correction by the global efficiency of the LHCb detector for data 2011: left(right), particles(antiparticles), up(down) long-long(down down) tracks.

Figure 5.5: Fit results for the azimuthal distributions spectra of Λ_c^+ in Λ_b^0 rest frame after correction by the global efficiency of the LHCb detector for data 2012: left(right), particles(antiparticles), up(down) long-long(down down) tracks.

5.2.2 Λ in Λ_c^+ Helicity rest frame

The same method applied for the Λ_c^+ in Λ_b^0 rest frame will be applied for the Λ in Λ_c^+ rest frame and the same methodology and error calculation will be used here and in the next section.

Again, it is important to show the Λ_c helicity frame (Fig.5.6) where the study is done.
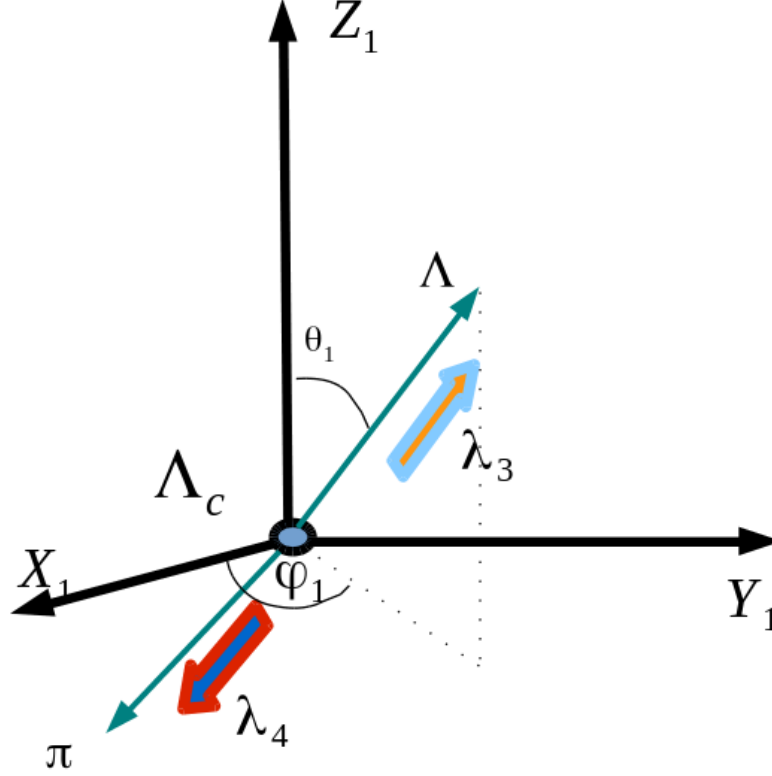
Figure 5.6: Λ helicity frame.
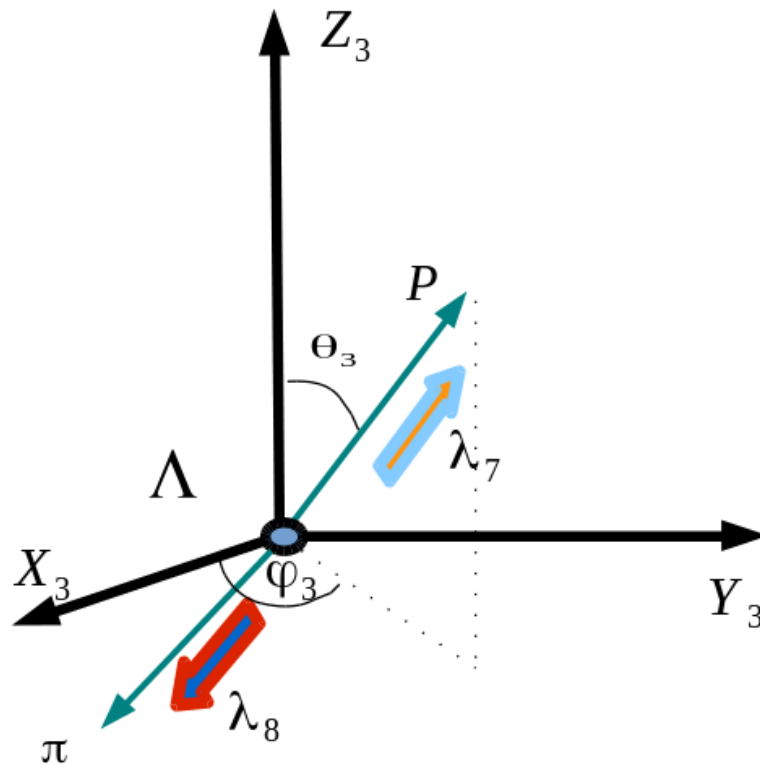
The polar distribution $\cos \theta_1$

• The polar angular distribution of the Λ is :

$$\frac{d\sigma}{d\cos\theta_1} \propto 1 + \alpha_{AS}^{\Lambda_c} P_Z^{\Lambda_c} \cos\theta_1 \qquad (5.3)$$

where $\alpha_{AS}^{\Lambda_c}$ is being measured (PDG 2016) $\alpha_{AS}^{\Lambda_c} = 0.91 \pm 0.15$, and hence is modeled by the linear fit function $1 + a_9 \cos\theta$.

Year	Particle	Track	a_9	$\alpha_{AS}^{\Lambda_c}$	$P_Z^{\Lambda_c} = \rho_{++}^{\Lambda_c} - \rho_{--}^{\Lambda_c}$
2011	Λ_c^+	LL	0.632 ± 0.041	-0.91 ± 0.15	-0.695 ± 0.123
		DD	0.109 ± 0.057	-0.91 ± 0.15	-0.120 ± 0.065
	$\bar{\Lambda}_c^-$	LL	0.658 ± 0.045	0.91 ± 0.15	0.723 ± 0.130
		DD	0.267 ± 0.060	0.91 ± 0.15	0.293 ± 0.081
2012	Λ_c^+	LL	0.596 ± 0.028	-0.91 ± 0.15	-0.655 ± 0.112
		DD	0.201 ± 0.039	-0.91 ± 0.15	-0.208 ± 0.056
	$\bar{\Lambda}_c^-$	LL	0.706 ± 0.026	0.91 ± 0.15	0.776 ± 0.131
		DD	0.193 ± 0.038	0.91 ± 0.15	0.212 ± 0.054

Table 5.4: $P_Z^{\Lambda_c}$ extracted from the polar distribution according to $\cos\theta$ of Λ in Λ_c^+ rest frame and the fit parameters for different 2011 and 2012 data samples .
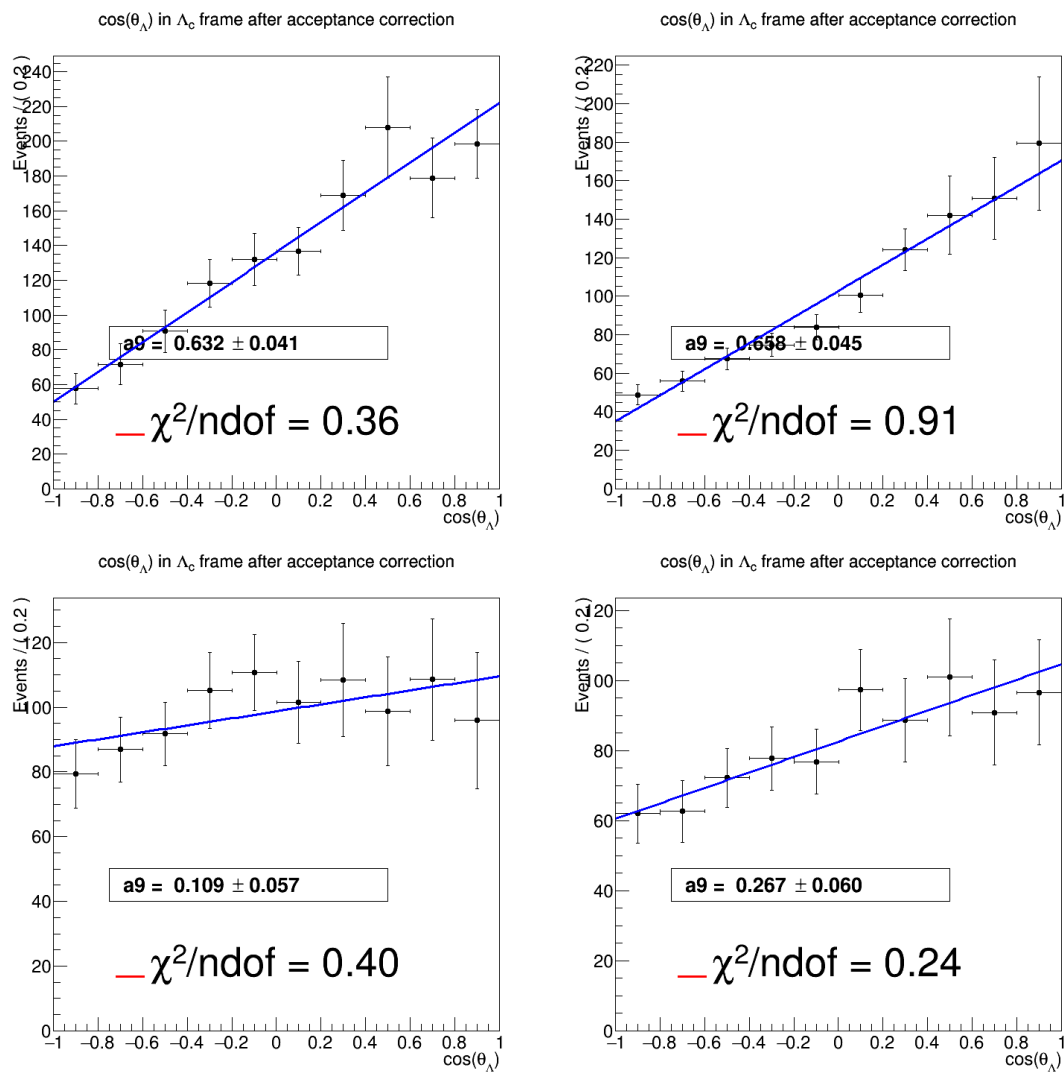
Figure 5.7: Fit results for the angular distributions spectra of Λ in Λ_c^+ rest frame after correction by the global efficiency of the LHCb detector for data 2011: left(right), particles(antiparticles), up(down) long-long(down-down) tracks.
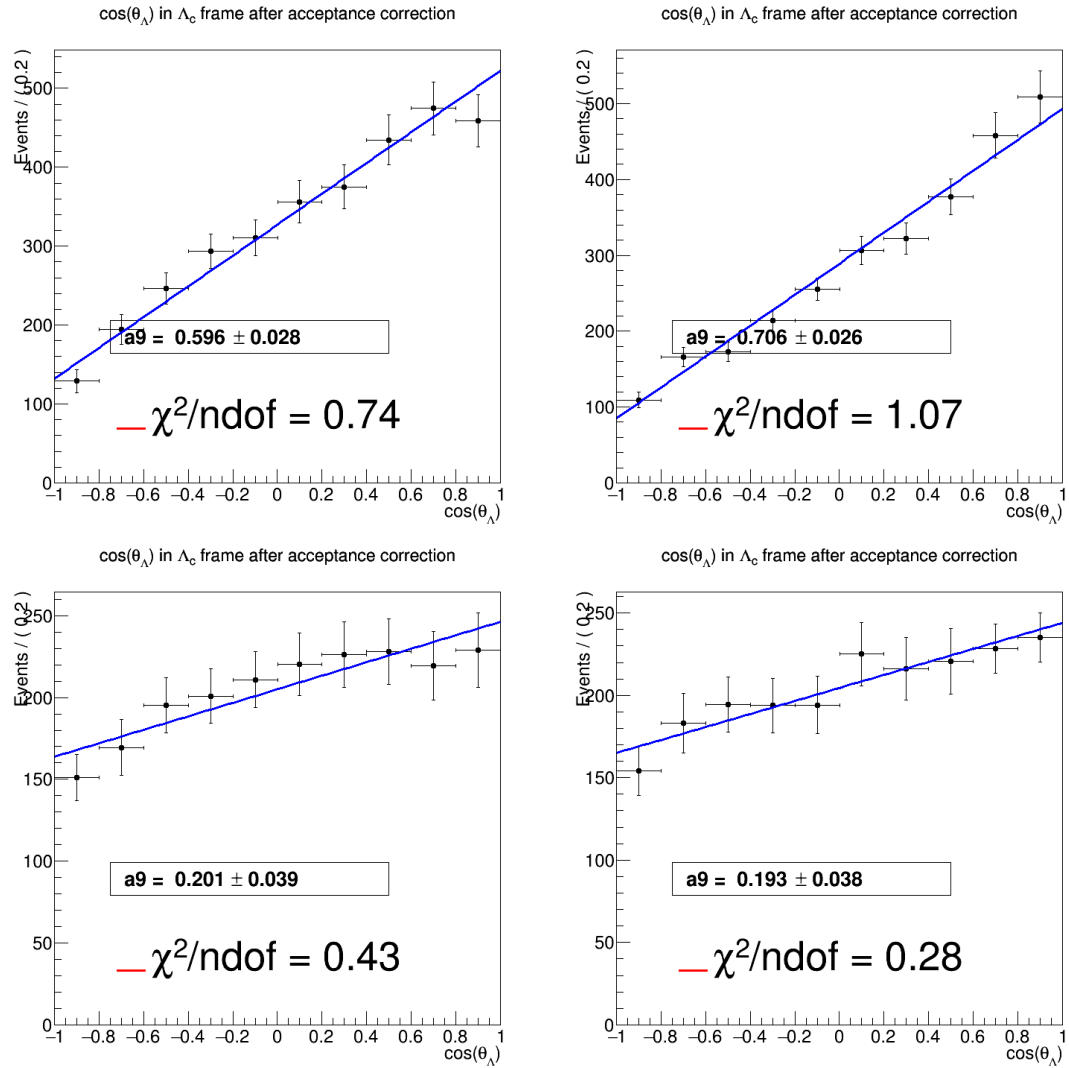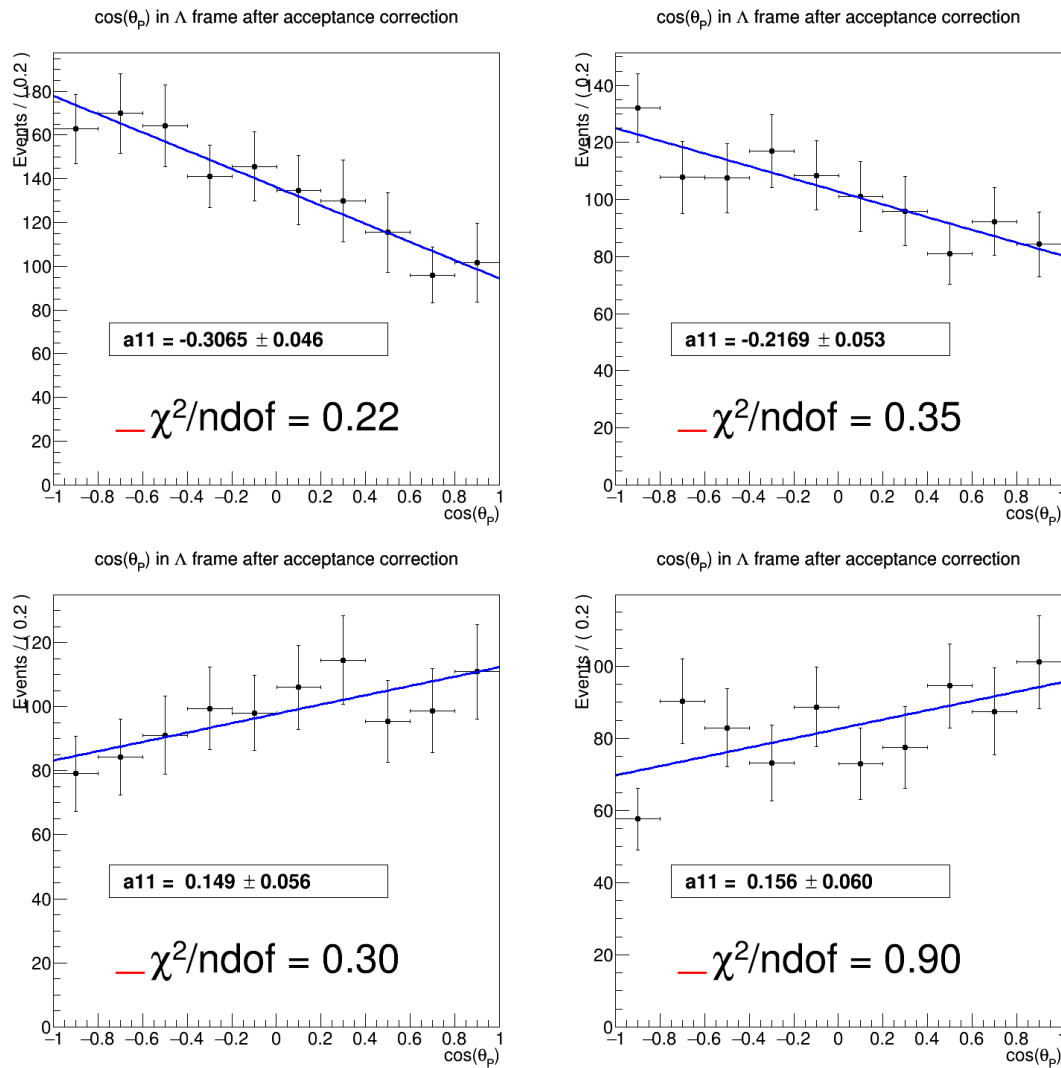
Figure 5.8: Fit results for the angular distributions spectra of Λ in Λ_c^+ rest frame after correction by the global efficiency of the LHCb detector for data 2012: left(right), particles(antiparticles), up(down) long-long(down-down) tracks.

Here, the difference between LL and DD samples (Fig.5.7 and Fig.5.8) raises again in the $P_Z^{\Lambda_c}$ where it is noticed that LL samples show compatible values between particles-anti particles system for both 2011 and 2012, whereas DD doesn't show that compatibility within experimental errors.

The azimuthal distribution ϕ_1

• The azimuthal distribution of the Λ is:

$$\frac{d\sigma}{d\phi_1} \propto 1 + \frac{\pi}{4}\alpha_{AS}^{\Lambda_c}[P_X^{\Lambda_c}\cos\phi_1 + P_Y^{\Lambda_c}\sin\phi_1] \tag{5.4}$$

And hence is modeled by the linear fit function $1 + a_{10}\cos\phi + b_5\sin\phi$ and are shown in (Fig.5.9 and Fig.5.10)

Year	Particle	Track	a_{10}	b_5	$\alpha_{AS}^{\Lambda_c}$	$P_X^{\Lambda_c}$	$P_Y^{\Lambda_c}$
2011	Λ_c^+	LL	-0.195 ± 0.038	-0.055 ± 0.038	-0.91 ± 0.15	0.273 ±0.069	0.077± 0.054
		DD	-0.182 ± 0.044	-0.073 ± 0.045	-0.91 ± 0.15	0.255 ± 0.075	0.102 ± 0.065
	$\bar{\Lambda}_c^-$	LL	-0.178 ± 0.043	0.061±0.045	0.91 ± 0.15	-0.249 ± 0.072	0.085 ± 0.064
		DD	-0.219 ± 0.049	0.042 ± 0.048	0.91 ± 0.15	-0.307 ± 0.085	0.058 ± 0.067
2012	Λ_c^+	LL	-0.211 ± 0.025	-0.006 ± 0.024	-0.91 ± 0.15	0.295 ± 0.060	0.008 ± 0.033
		DD	-0.151 ± 0.031	-0.026 ± 0.031	-0.91 ± 0.15	0.211 ± 0.055	0.036 ± 0.043
	$\bar{\Lambda}_c^-$	LL	-0.214 ± 0.026	0.035 ± 0.026	0.91 ± 0.15	-0.230 ± 0.061	0.048 ± 0.037
		DD	-0.102 ± 0.031	-0.057 ± 0.031	0.91 ± 0.15	-0.143 ± 0.049	-0.080 ± 0.045

Table 5.5: $P_X^{\Lambda_c}$ and $P_Y^{\Lambda_c}$ extracted from the azimuthal distribution according to ϕ of Λ in Λ_c^+ rest frame and the fit parameters for different 2011 and 2012 data samples.

Interpretation of the fit   According to the Tab.5.1, $P_X^{\Lambda_c^+}$ changes sign under Time Reversal, so it is important to study the values of this T-Odd observable around the central value 0 as shown in Tab.5.6. Any value of this parameter different from zero in absence of final state interaction (FSI) could be a sign for TRV. Tab.5.5, shows the different values of $P_X^{\Lambda_c^+} \neq 0$ for different data samples within experimental errors.

Year	Particle	Track	$P_X^{\Lambda_c}$	Standard Deviation
2011	Λ_c^+	LL	0.273 ± 0.069	4
		DD	0.255 ± 0.075	4
	$\bar{\Lambda}_c^-$	LL	-0.249 ± 0.072	4
		DD	-0.307 ± 0.085	4
2012	Λ_c^+	LL	0.295 ± 0.060	5
		DD	0.211 ± 0.055	4
	$\bar{\Lambda}_c^-$	LL	-0.230 ± 0.061	4
		DD	-0.143 ± 0.049	3

Table 5.6: $P_X^{\Lambda_c}$ and the standard deviation from the central value zero for different 2011 and 2012 data samples.

Further studies are ongoing to see if there is an effect for the FSI on those results. So as a preliminary result, one could say that $P_X^{\Lambda_c^+} \neq 0$ could show sign for TRV around 4σ with a complete compatibility between the values in the LL samples (always the difference between LL and DD).
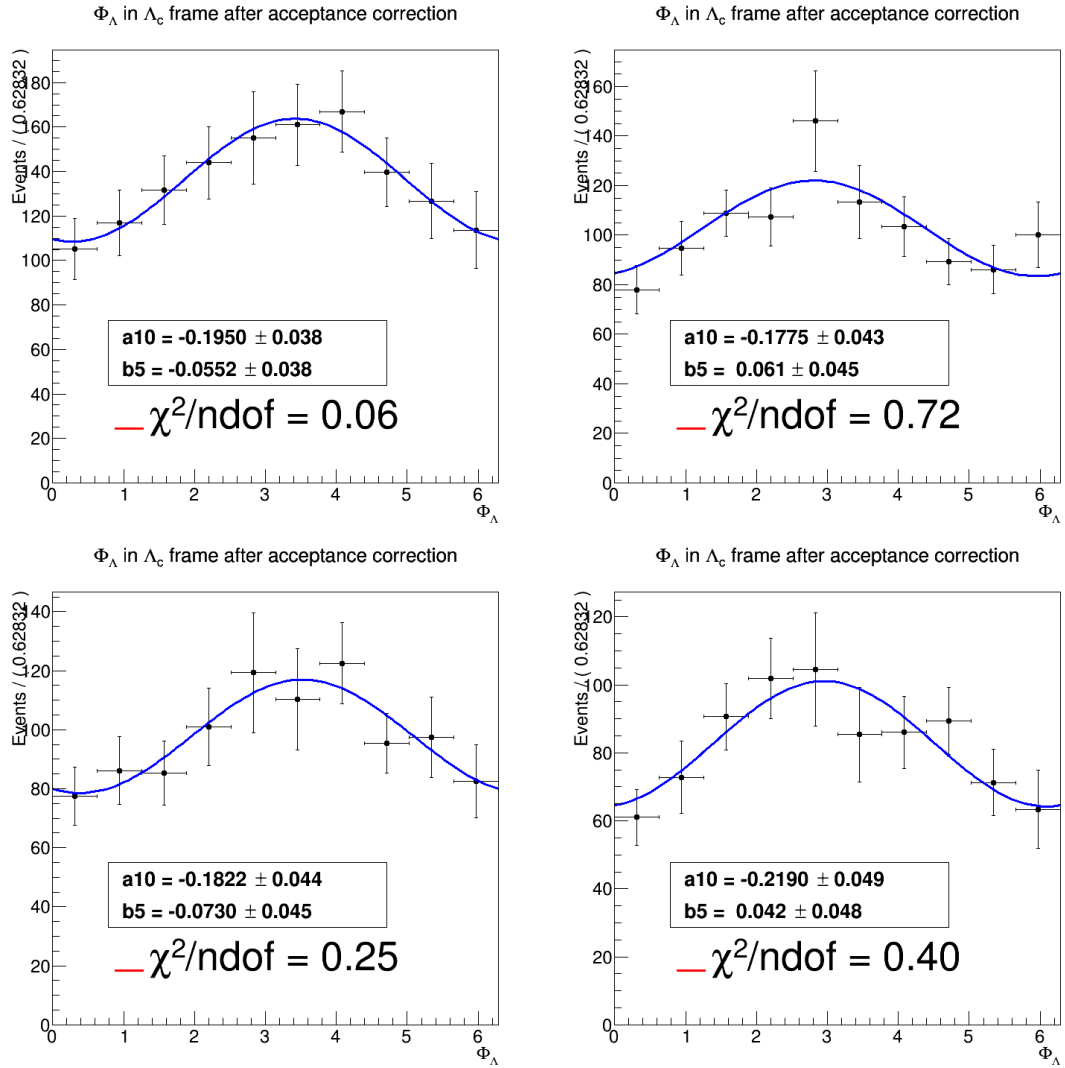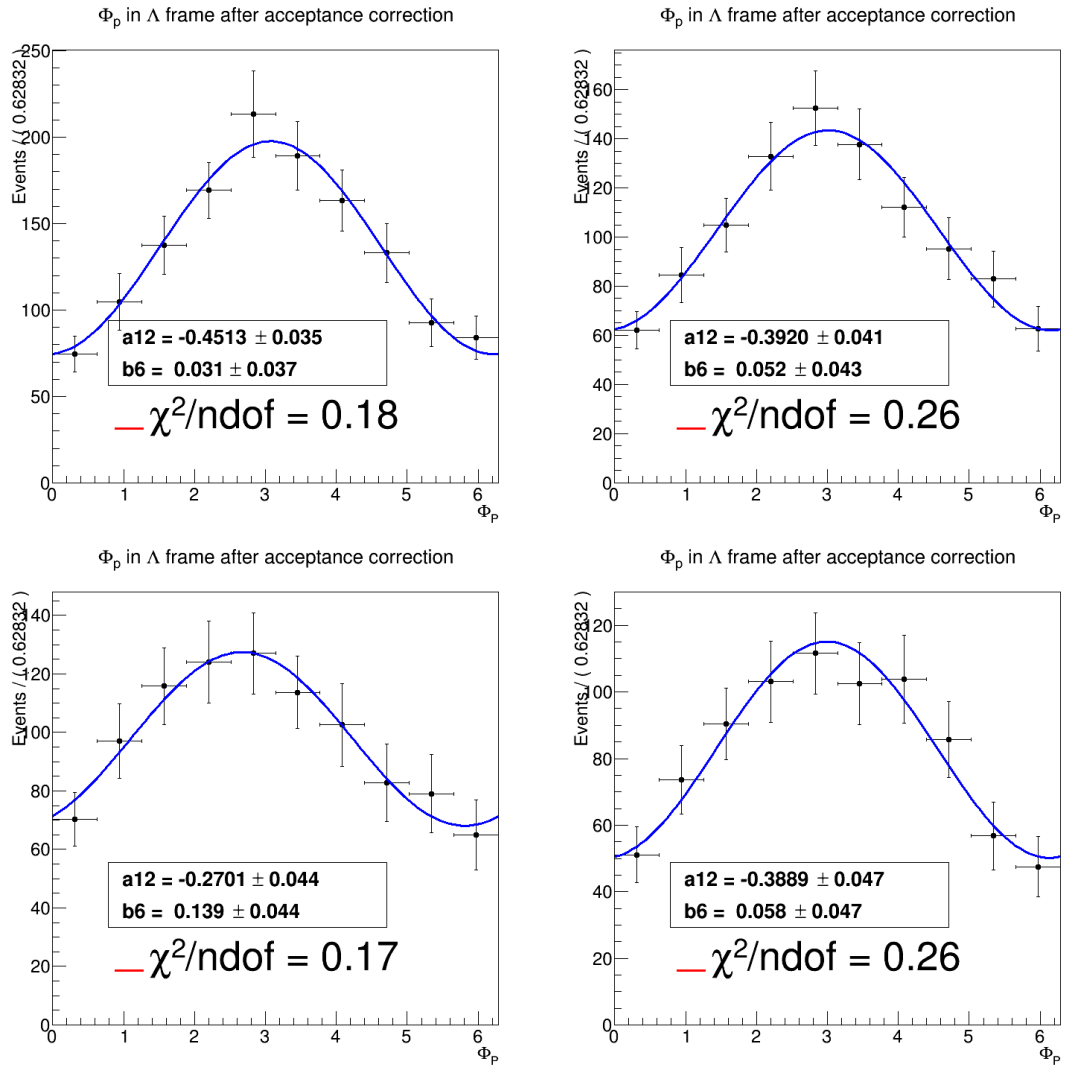
Figure 5.9: Fit results for the azimuthal distributions spectra of Λ in Λ_c^+ rest frame after correction by the global efficiency of the LHCb detector for data 2011: left(right), particles(antiparticles), up(down) long-long(down-down) tracks.
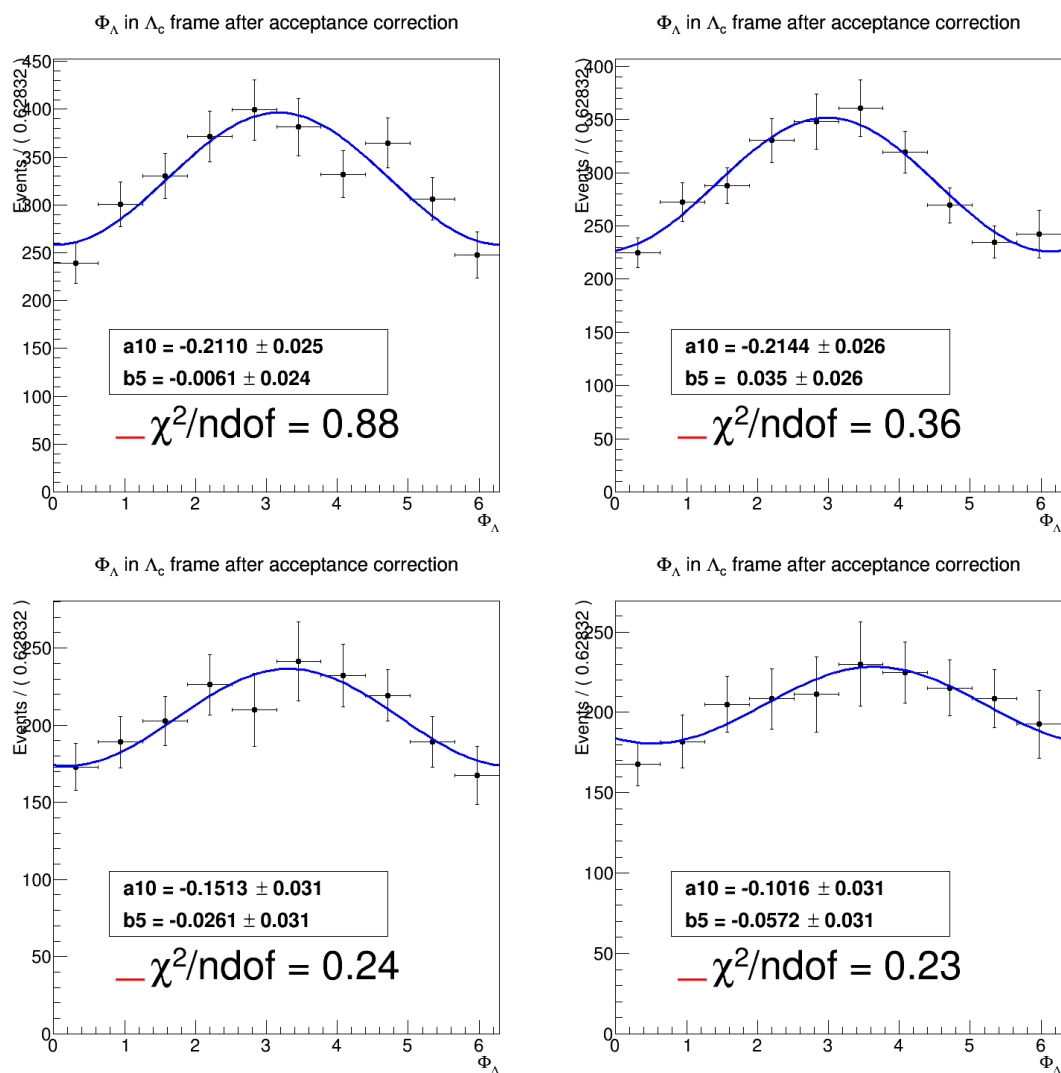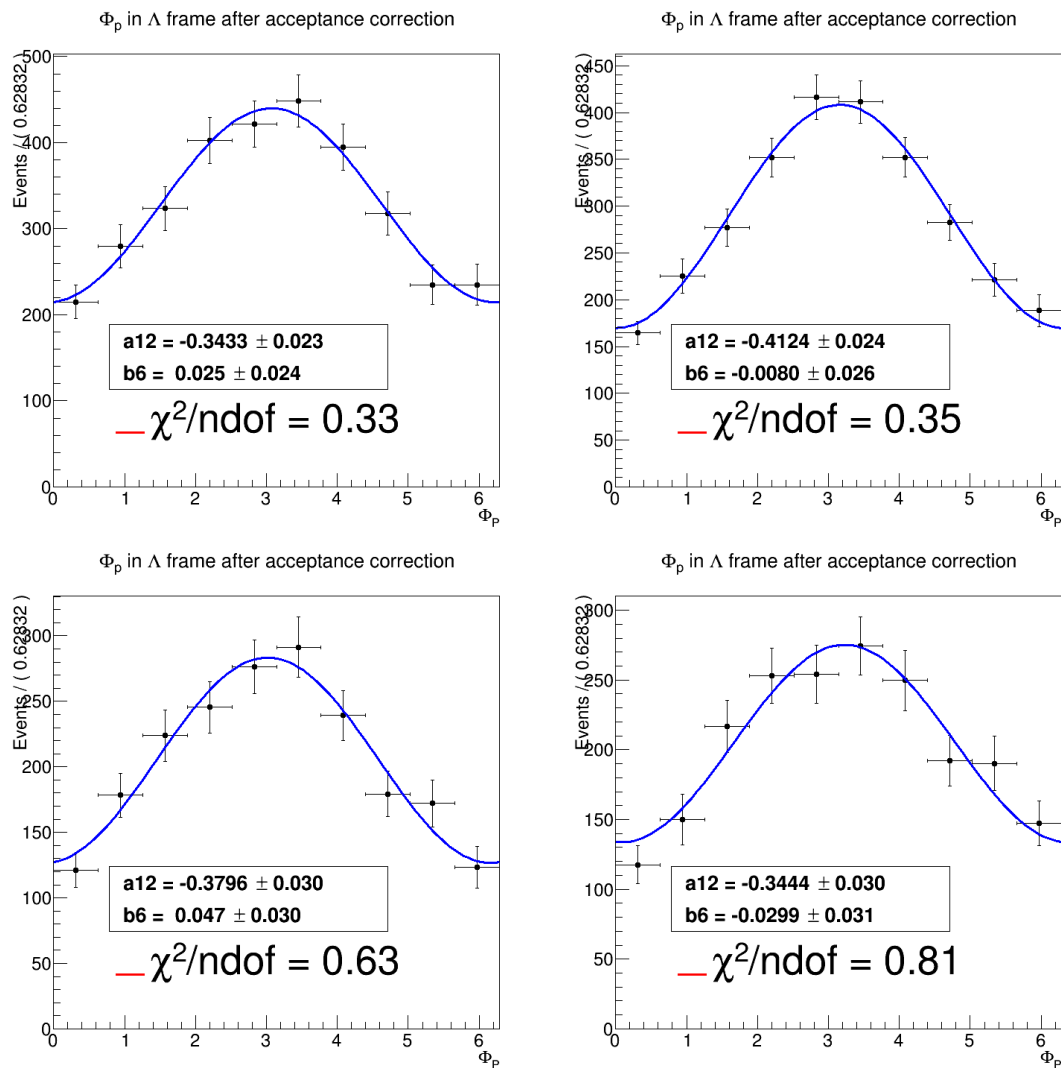
Figure 5.10: Fit results for the azimuthal distributions spectra of Λ in Λ_c^+ rest frame after correction by the global efficiency of the LHCb detector for data 2012: left(right), particles(antiparticles), up(down) long-long(down down) tracks.

5.2.3 Proton in Λ Helicity rest frame

Let us next discuss the last decay from the Λ_b^0 three cascade decay. We are speaking about the hyperon

$$\Lambda \longrightarrow p\pi$$
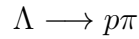
The angular distribution of the proton from the Λ decay is given by the equation 5.5

$$\frac{d\sigma}{d\Omega_1} \propto 1 + \alpha_{AS}^\Lambda \langle\vec{\sigma}\rangle_\Lambda \cdot \hat{p}_p \tag{5.5}$$

where $\hat{p}_p$ is a unit vector along the momentum of the proton in the Λ helicity frame. It is also worth to note that the equation 5.5 acts as an analyzer for the Λ polarization.

Again, it is important to show the Λ helicity frame Fig.5.11 where we are making the study .

Figure 5.11: Λ helicity frame.

The polar distribution $\cos\theta_3$

• The polar angular distribution of the proton is :

$$\frac{d\sigma}{d\cos\theta_3} \propto 1 + P_Z^\Lambda \alpha_{AS}^\Lambda \cos\theta_3 \tag{5.6}$$

And hence is modeled by the linear fit function $1 + a_{11}\cos\theta$ as shown in (Fig.5.12 and Fig.5.13)

Year	Particle	Track	a_{11}	α_{AS}^{Λ}	P_Z^{Λ}
2011	Λ	LL	-0.307 ± 0.046	0.642 ± 0.013	-0.478 ± 0.072
		DD	0.149 ± 0.056	0.642 ± 0.013	0.232 ± 0.087
	$\bar{\Lambda}$	LL	-0.217 ± 0.045	-0.71 ± 0.08	0.306 ± 0.073
		DD	0.156 ± 0.060	-0.71 ± 0.08	-0.220 ± 0.088
2012	Λ	LL	-0.241 ± 0.030	0.642 ± 0.013	-0.375 ± 0.047
		DD	-0.095 ± 0.039	0.642 ± 0.013	0.148 ± 0.060
	$\bar{\Lambda}$	LL	-0.337 ± 0.032	-0.71 ± 0.08	0.475 ± 0.070
		DD	0.033 ± 0.039	-0.71 ± 0.08	-0.046 ± 0.055

Table 5.7: P_Z^{Λ} extracted from the polar distribution according to $\cos\theta$ of proton in Λ rest frame and the fit parameters for different 2011 and 2012 data samples .

Figure 5.12: Fit results for the angular distributions spectra of proton in Λ rest frame after correction by the global efficiency of the LHCb detector for data 2011: left(right), particles(antiparticles), up(down) long-long(down down) tracks.
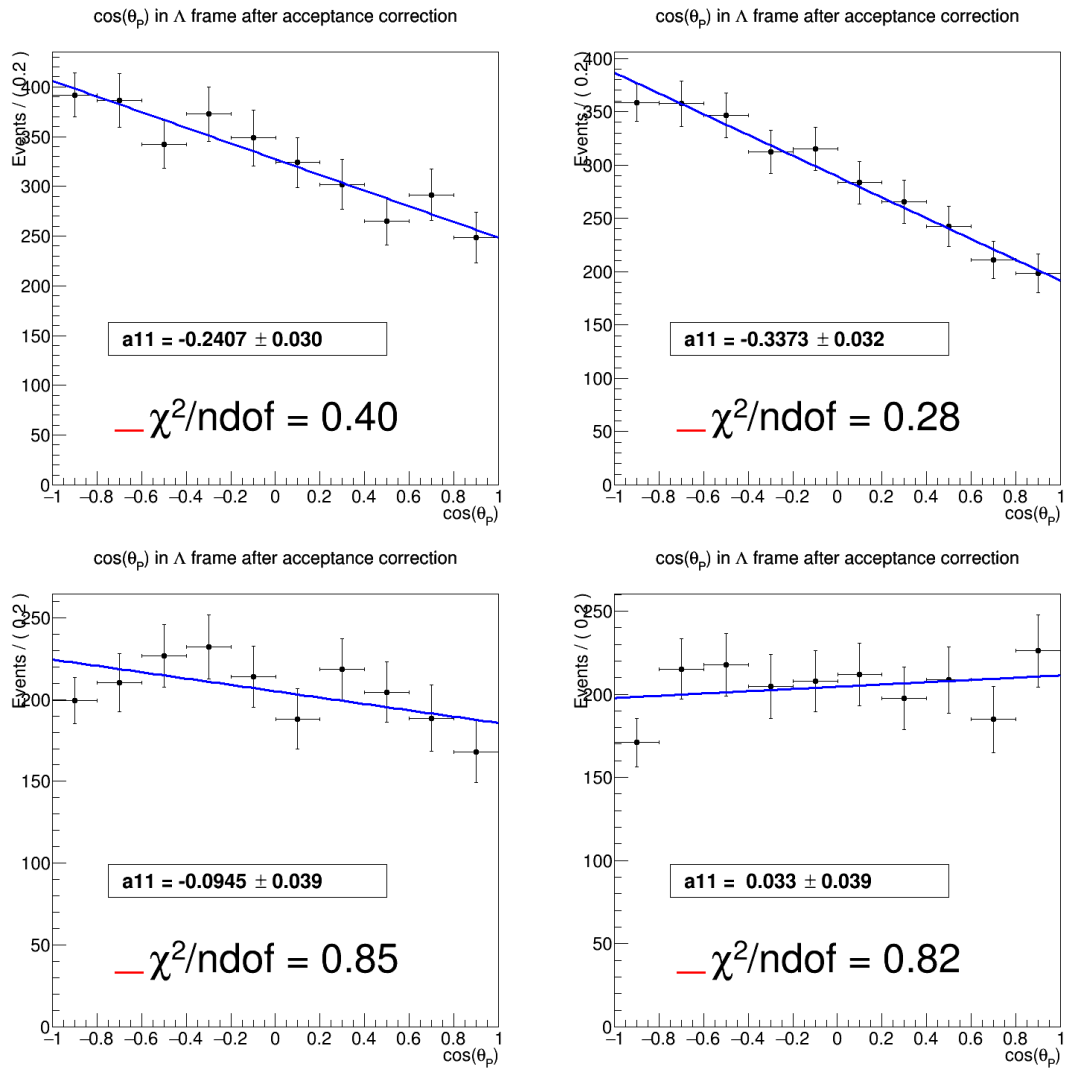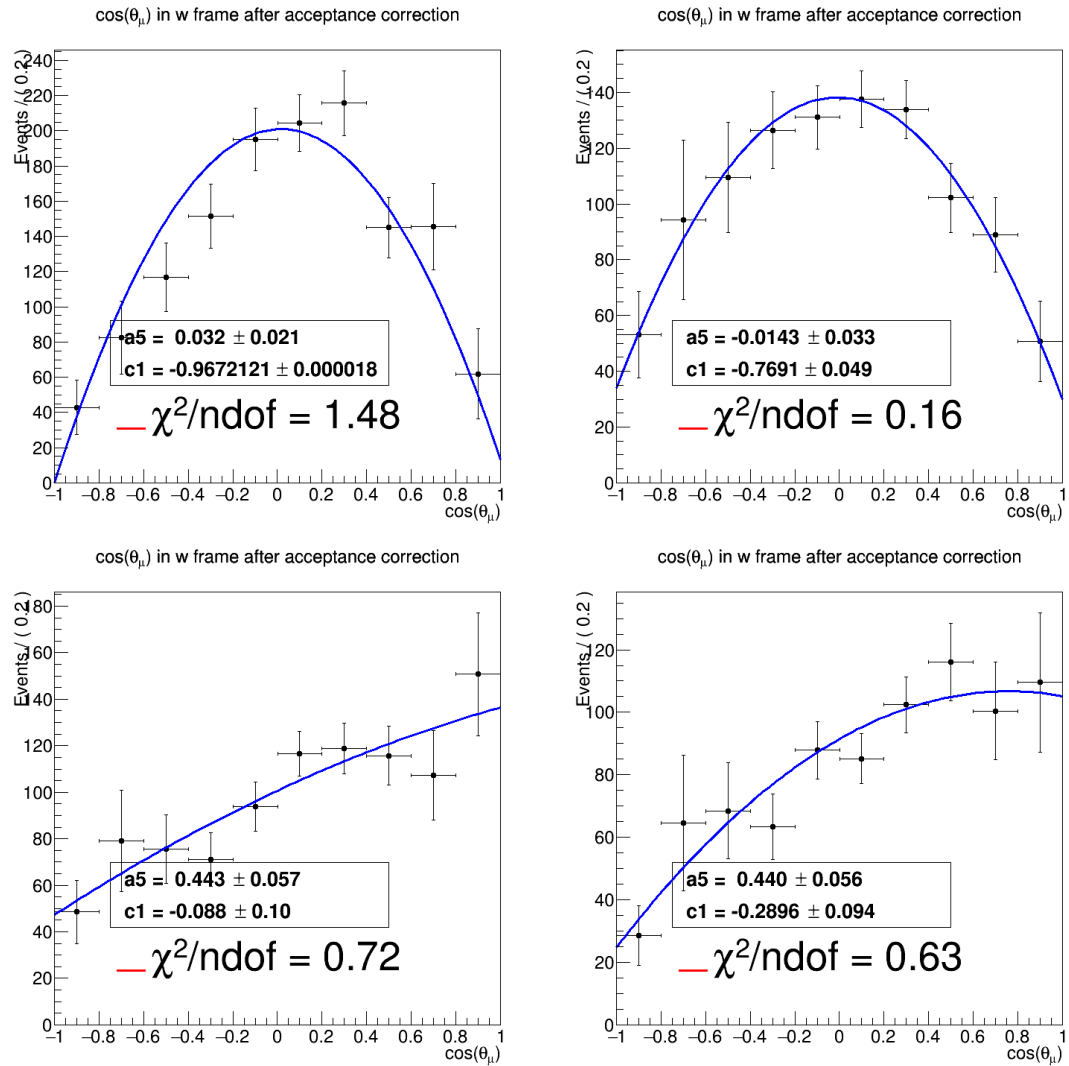
Figure 5.13: Fit results for the angular distributions spectra of proton in Λ rest frame after correction by the global efficiency of the LHCb detector for data 2012: left(right), particles(antiparticles), up(down) long-long(down down) tracks.

The azimuthal distribution ϕ_3

The ϕ_1 distribution of the proton :

$$\frac{d\sigma}{d\phi_3} \propto 1 - \frac{\pi}{4}\alpha_{AS}^\Lambda\{P_X^\Lambda \cos\phi_3 + P_Y^\Lambda \sin\phi_3\} \qquad (5.7)$$

And again it is modeled using the linear fit $1 + a_{12}\cos\phi + b_6\sin\phi$ as shown in (Fig.5.14 and Fig.5.15)

Year	Type	Track	a_{12}	b_6	α_{AS}^Λ	P_X^Λ	P_Y^Λ
2011	Λ	LL	-0.451 ± 0.035	0.031 ± 0.037	0.642 ± 0.013	0.895 ± 0.072	-0.062 ± 0.073
		DD	-0.270 ± 0.044	0.139 ± 0.044	0.642 ± 0.013	0.536 ±0.088	-0.275 ± 0.087
	$\bar\Lambda$	LL	-0.392 ± 0.041	0.052 ±0.043	-0.71 ± 0.08	-0.703 ± 0.108	0.093 ± 0.077
		DD	-0.389 ± 0.047	0.058 ± 0.047	-0.71 ± 0.08	-0.698 ± 0.115	0.104 ± 0.085
2012	Λ	LL	-0.343 ± 0.023	0.025 ± 0.024	0.642 ± 0.013	0.681 ± 0.048	-0.049 ±0.047
		DD	-0.380 ± 0.030	0.047 ± 0.030	0.642 ± 0.013	0.754 ± 0.061	-0.093 ± 0.059
	$\bar\Lambda$	LL	-0.412 ± 0.024	-0.008 ± 0.026	-0.71 ± 0.08	-0.739 ± 0.093	-0.014 ± 0.046
		DD	-0.344 ± 0.030	-0.03 ± 0.031	-0.71 ± 0.08	-0.617 ± 0.087	-0.054 ± 0.055

Table 5.8: P_X^Λ and P_Y^Λ extracted from the azimuthal distribution according to ϕ of proton in Λ rest frame and the fit parameters for different 2011 and 2012 data samples.

Comment on the fit One comment on the fit is that the b_6 is compatible with zero within the experimental error.

Conclusion Polarization of the HyperonΛ Tab.5.9 shows the polarization value for the Hyperon Λ for the different samples and it is given by:

$$|\overrightarrow{P^\Lambda}| = \sqrt{P_X^2 + P_Y^2 + P_Z^2}$$

Year	Type	Track	$|\overrightarrow{P^\Lambda}|$
2011	Λ	LL	1.016 ± 0.101
		DD	0.645 ± 0.140
	$\bar\Lambda$	LL	0.772± 0.136
		DD	0.739±0.146
2012	Λ	LL	0.778 ±0.067
		DD	0.773±0.076
	$\bar\Lambda$	LL	0.878±0.116
		DD	0.621±0.095

Table 5.9: Polarization of Λ for different 2011 and 2012 data samples.

Figure 5.14: Fit results for the azimuthal distributions spectra of proton in Λ rest frame after correction by the global efficiency of the LHCb detector for data 2011: left(right), particles(antiparticles), up(down) long-long(down down) tracks.

Figure 5.15: Fit results for the azimuthal distributions spectra of proton in Λ rest frame after correction by the global efficiency of the LHCb detector for data 2012: left(right), particles(antiparticles), up(down) long-long(down down) tracks.

5.3   Muon in W^*-boson Helicity rest frame

We are going to focus essentially on the following virtual decay: $W^{(*)-} \longrightarrow \mu^- \nu_\mu$, in which there is two spectra to be stressed on:

- $\cos(\theta_\mu)$ and ϕ_μ in W^*-boson rest frame.

It is important to show the W^* helicity frame Fig.5.16 where we are making the study .
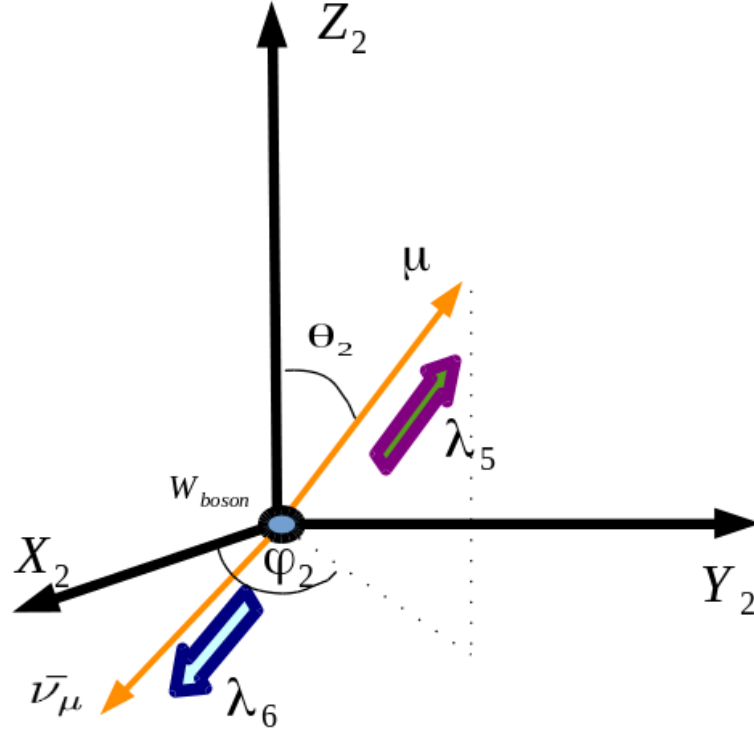
Figure 5.16: W^* helicity frame.

5.3.1 $\cos(\theta_\mu)$ in W^*-boson Helicity rest frame

$$\left. \frac{d\sigma}{d\cos(\theta_\mu)} \right)_{W-r.f} = A_1 \times \left(C_0 + C_1 \cos(\theta_\mu) + C_2 \cos^2(\theta_\mu) \right) \tag{5.8}$$

where A_1 is a <u>normalization dimensional</u> constant used to provide the good dimensions, i.e to have

$\sigma = \int_{-1}^{+1} \left(\frac{d\sigma}{d\cos\theta_l} \right) d(\cos\theta_l) = \left(2C_0 + \frac{2}{3}C_2 \right) \times A_1.$

By neglecting the $|W(--)|^2 \ll |W(+-)|^2$ [82], it is worth to note that the Longitudinal Polarization of the W^*-boson in its rest frame is given by $:P_z^W = \rho_{11}^W - \rho_{-1-1}^W$, where $\overrightarrow{WZ}$ is considered as the quantization axis.

so according to the analytical expression (chapter 3) and in comparison to eq.5.8,

$$C_0 = \frac{|W(+-)|^2}{4}\left(1 + \rho_{00}^W\right)$$

$$C_1 = \frac{|W(+-)|^2}{4}\left(\rho_{11}^W - \rho_{-1-1}^W\right)$$

$$C_2 = \frac{|W(+-)|^2}{4}\left(1 - 3 * \rho_{00}^W\right)$$

For our fit, normalizing eq.5.8 will give $\equiv C_0' + C_1'\cos(\theta_\mu) + C_2'\cos^2(\theta_\mu)$ with :

$$C_0' = \frac{3}{8}\left(1 + \rho_{00}^W\right)$$

$$C_1' = \frac{3}{4}\left(\rho_{11}^W - \rho_{-1-1}^W\right)$$

$$C_2' = \frac{3}{8}\left(1 - 3 * \rho_{00}^W\right)$$

To verify the experimental values, we could check the sum of the diagonal elements of the Polarization density matrix (PDM) that normally should be equal to one:

$$\rho_{00}^W + \rho_{11}^W + \rho_{-1-1}^W = 1 \qquad (5.9)$$

Directly by fitting the $\cos(\theta_\mu)$ spectrum with $1 + a_5\cos(\theta_\mu) + c_1\cos^2(\theta_\mu)$ (as shown in Fig.5.17 and Fig.5.18) one can extract the values of C_0', C_1', C_2' with

- $a_5 = C_1'/C_0' \equiv$ Asymmetry Parameter.

- $c_1 = C_2'/C_0' = \frac{1 - 3\rho_{00}^W}{1 + \rho_{00}^W}$

giving access to the density matrix elements $\rho_{00}^W, \rho_{11}^W, \rho_{-1-1}^W$.

For this study, we limit our-self to calculate the Longitudinal Polarization P_z^W and the density matrix element ρ_{00}^W, where we have:

$$\rho_{00}^W = \frac{1 - c_1}{3 + c_1} \implies \sigma_{\rho_{00}^W} = \frac{4\sigma_{c_1}}{(c_1 - 1)(c_1 + 3)}$$

$$P_z^W = \frac{2a_5}{3 + c_1} \implies \sigma_{P_z^W} = P_z^W\sqrt{\left(\frac{2\sigma_{a_5}}{a_5}\right)^2 + \left(\frac{\sigma_{c_1}}{3 + c_1}\right)^2}$$

Year	Particle	Track	$a_5 = C_1'/C_0'$	$c_1 = C_2'/C_0'$	P_Z^W	ρ_{00}^W
2011	W^+	LL	0.032 ± 0.021	-0.967 ± 0.000018	0.031 ± 0.041	$0.967 \pm 1.7e^{-05}$
		DD	0.433 ± 0.057	0.088 ± 0.10	0.280 ± 0.074	0.295 ± 0.041
	W^-	LL	-0.014 ± 0.033	-0.769 ± 0.049	-0.012 ± 0.059	0.792 ± 0.039
		DD	0.440 ± 0.056	-0.287 ± 0.094	0.513 ± 0.131	0.474 ± 0.051
2012	W^+	LL	0.186 ± 0.022	-0.573 ± 0.035	0.153 ± 0.036	0.648 ± 0.023
		DD	0.301 ± 0.029	-0.592 ± 0.045	0.250 ± 0.048	0.661 ± 0.031
	W^-	LL	0.173 ± 0.022	-0.632 ± 0.035	0.146 ± 0.037	0.689 ± 0.024
		DD	0.320 ± 0.033	-0.404 ± 0.053	0.401 ± 0.083	0.540 ± 0.031

Table 5.10: P_z^W and ρ_{00}^W extracted from the $\cos\theta_\mu$ distribution of the μ in the W^*-boson rest frame and the fit parameters for different 2011 and 2012 data samples.

Figure 5.17: Fit results for the angular distributions spectra of μ in W^*-boson rest frame after correction by the global efficiency of the LHCb detector for data 2011: left(right), particles(antiparticles), up(down) long-long(down-down) tracks.
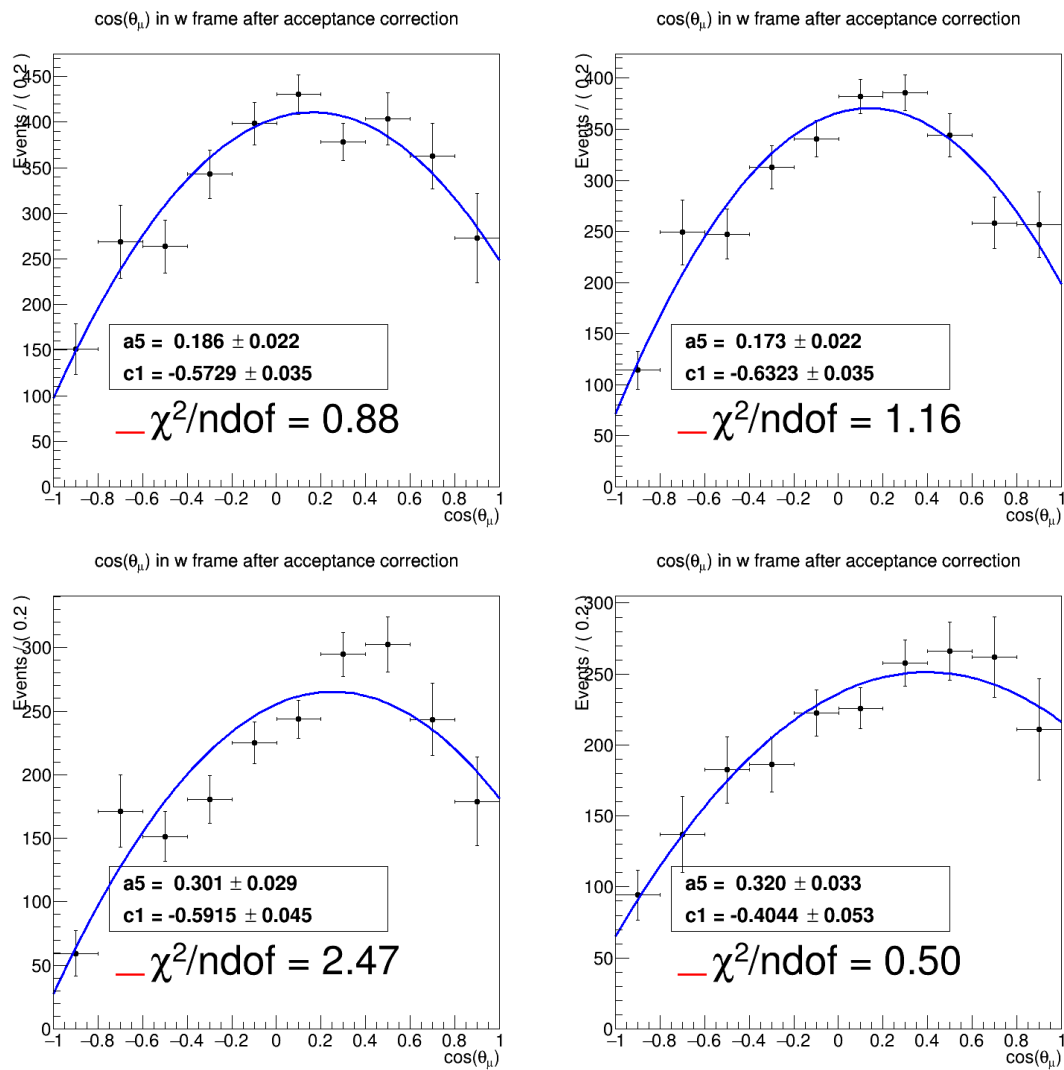
Figure 5.18: Fit results for the angular distributions spectra of μ in W^*-boson rest frame after correction by the global efficiency of the LHCb detector for data 2012: left(right), particles(antiparticles), up(down) long-long(down-down) tracks.

The same problems concerning LL and DD arise here again. Fig. 5.17 and 5.18 show completely different angular distribution shapes between LL and DD within the same year. P_z^W and ρ_{00}^W in the LL samples within 2011-2012 are in very good compatibility.

5.3.2 ϕ_μ in W^*-boson Helicity rest frame

The azimuthal distribution of the muon in the W^*-boson rest frame is given by the following equation:

$$\left.\frac{d\sigma}{d\phi_\mu}\right)_{W-r.f} = A_2 \times \left(D_0 + D_1\cos(\phi_\mu) + D_2\sin(\phi_\mu)\right) \quad (5.10)$$

where A_2 again is a <u>normalization dimensional</u> constant used to provide the good dimensions, in which one can say that:

$$\sigma = \int_0^{2\pi}\left(\frac{d\sigma}{d\phi_l}\right)d(\phi_l) = \left(2\pi D_0\right) \times A_2.$$

So by normalizing the azimuthal distribution and neglecting $|w(--)|^2$, we get (as shown in Fig.5.19 and Fig.5.20) :

$$\left.\frac{d\sigma}{d\phi_\mu}\right)_{W-r.f} = \frac{1}{2\pi}\left(1 + D_1'\cos(\phi_\mu) + D_2'\sin(\phi_\mu)\right) \quad (5.11)$$
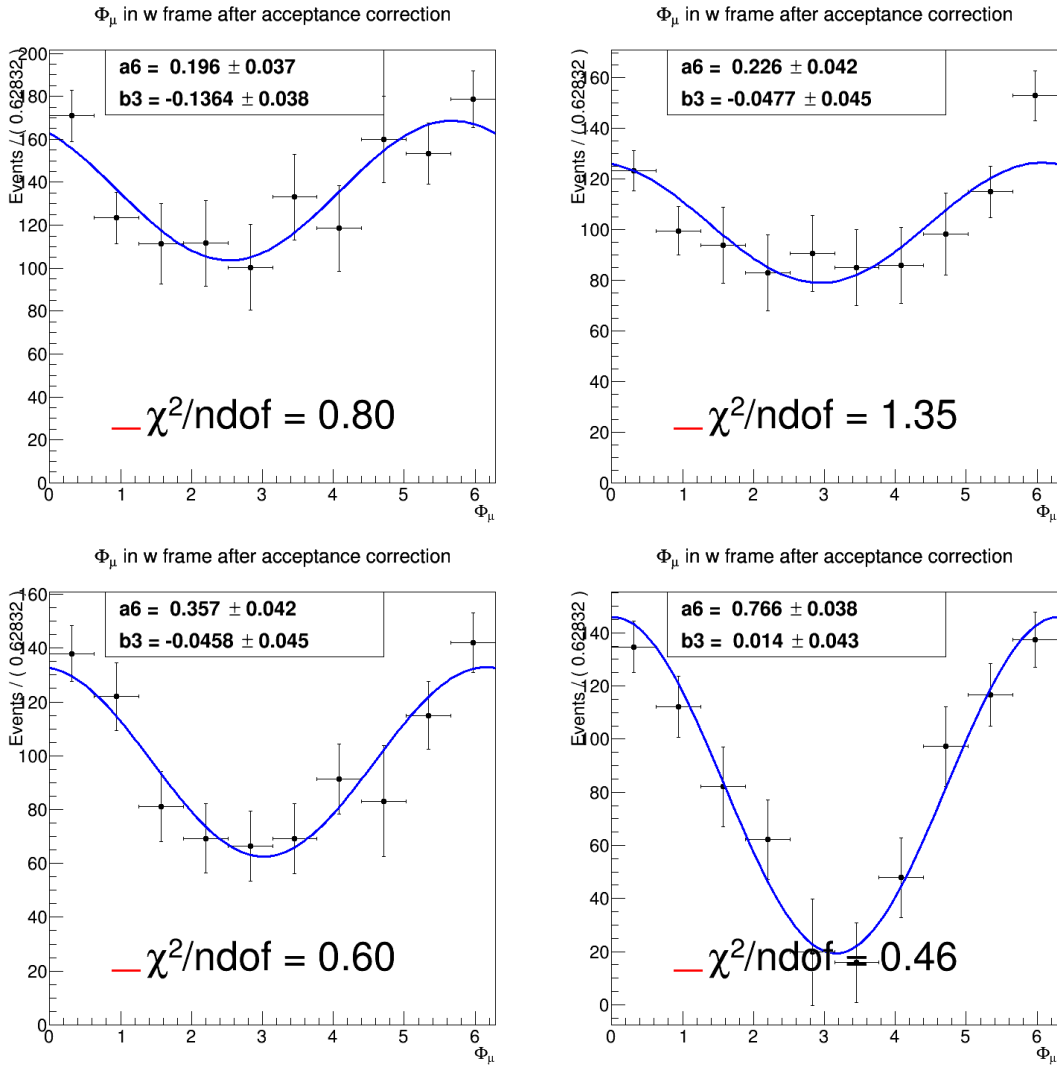
Figure 5.19: Fit results for the azimuthal distributions spectra of μ in W^*-boson rest frame after correction by the global efficiency of the LHCb detector for data 2011: left(right), particles(antiparticles), up(down) long-long(down-down) tracks.

Again, only the results relevant to the LL samples are reliable. A small comment here is about the non flat distribution of the μ in the W^* frame given by the
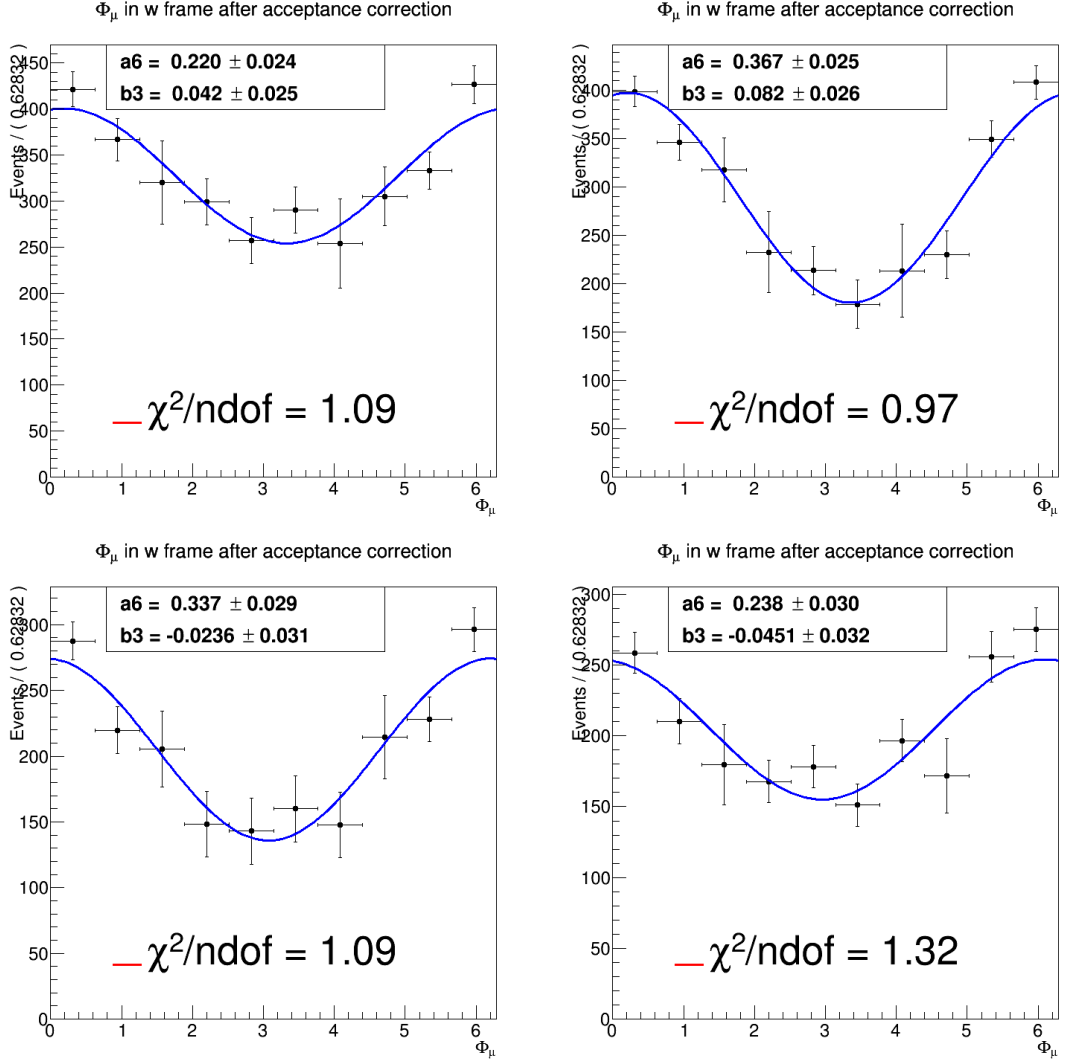
Figure 5.20: Fit results for the azimuthal distributions spectra of μ in W^*-boson rest frame after correction by the global efficiency of the LHCb detector for data 2012: left(right), particles(antiparticles), up(down) long-long(down-down) tracks.

Year	Particle	Track	$a_6 = D_1/D_0$	$b_3 = D_2/D_0$
2011	W^+	LL	0.196 ± 0.037	-0.136 ± 0.038
		DD	0.357 ± 0.042	-0.046 ± 0.045
	W^-	LL	0.226 ± 0.042	-0.048 ± 0.045
		DD	0.766 ± 0.038	0.014 ± 0.043
2012	W^+	LL	0.220 ± 0.024	0.042 ± 0.025
		DD	0.337 ± 0.029	-0.024 ± 0.031
	W^-	LL	0.367 ± 0.025	0.082 ± 0.026
		DD	0.238 ± 0.030	-0.045 ± 0.032

Table 5.11: Parameters extracted from the ϕ_μ distribution of the μ in the W^*-boson rest frame for different 2011 and 2012 data samples.

variable $a_6 = D_1/D_0$. Such distribution clearly gives a sign for a polarized $\mu\bar{\nu}$ system which is a promising result . W^* being virtual will arise the question: could the W-boson in a top decay show a sign of polarization?

5.4   Systematic uncertainties

There are several sources of systematical uncertainties that affect the value of the polarization extracted in the previous sections. Since we are concerned with the T-Odd observables, the systematic uncertainties are just examined for those observables. The different sources examined in this study are listed in Tab.5.12. It is also worth to note that other important systematics have not been considered by the lack of time. So there will be a complete study for those missing systematics in the coming future. There is also the tracking efficiency being which is not yet understood for DD tracks, many studies are done but till now there is no clear reasons that could explain the difference seen between LL and DD tracks.

Before listing those systematical errors one should stress emphasis on how to calculate them. Lets consider the value of the $a = b \pm \sigma_b$ slope extracted from the angular distribution before any modification done on our study. Make the modification (for calculation of the systematics: change BDT cuts, model, ...etc) and the new value would be $a' = b' \pm \sigma_{b'}$. So the change in the slope would be $a - a'$ and the associated error will be $\sigma_{sys}^2 = \sigma_b^2 + \sigma_{b'}^2$

• Concerning the systematic uncertainties on the BDT cuts, we change the cuts taken by $\pm 10\%$ and the angular distributions are fitted again. The new fluctuations are considered systematic errors on the BDT cuts and are assigned a value of 0.0063.

• Λ_c^+ signal has been fitted (from MC) using a Double Crystal Ball function [73], however, it could be fitted by a two Gaussian functions also. This causes a change in the slope of the $\cos \theta_{\Lambda_c^+}$ in Λ_b^0 rest frame and the error associated is 0.007.

• The next term that counts for systematic uncertainties is the total PDF of the Λ_c^+ mass spectrum, where we refit the BKG with first order degree polynomial instead of exponential function, and the partially reconstructed decay $(\Lambda_c^+ \rightarrow \Lambda \gamma \pi^+)$ is fitted with a Gaussian, this causes the slope to change and the error associated is 0.001.

• The choice of binning also has its own effect on the results. Changing from 10 bins to 14 introduces on the slope a change by 0.0002. The incorrect modeling of the Λ_b^0 kinematics (before and after reweighting) is considered a source of systematic uncertainties due to the change it makes on the slope, so we assume a 0.0002 systematic error for this procedure.

• The uncertainty on the SVD unfolding and the regularization is obtained by repeating the unfolding procedure with different values of the regularization parameter k. For us, the choice of k was k=3, so we used k=4, k=5, and k=6 to extract this systematic uncertainty. We plotted the angular distributions for all particles using the different regularization parameters as shown in Fig.5.21, and we see the effect of the value k on the different distributions. By that way we were able to assign a 0.002 systematic uncertainty to this procedure.

• Concerning the uncertainty on the MC statistics, we use half of our MC samples, make all the fits again and see the effect on the slope also. we assume a 0.0021 systematic error for this procedure.
• There is also the uncertainty associated to correlation between the error bars of the angular distributions, we assume a 10% systematic error for this procedure.

Item	$P_Z^{\Lambda_b}$	$P_X^{\Lambda_c}$	P_Y^{Λ}
BDT cuts $\pm 10\%$	0.0063	0.008	0.0094
Λ_c^+ signal fit	0.007	0.0079	0.0081
PDF fit for signal and BKG	0.001	0.0015	0.0021
Binning choice 10-14	0.0002	0.00026	0.00028
Λ_b^0 kinematics dependencies	0.004	0.0047	0.005
unfolding procedure	0.002	0.039	0.0051
MC statistics	0.0021	0.0024	0.0026
sum	0.0106	0.0131	0.0147

Table 5.12: Summary of the systematic uncertainties.
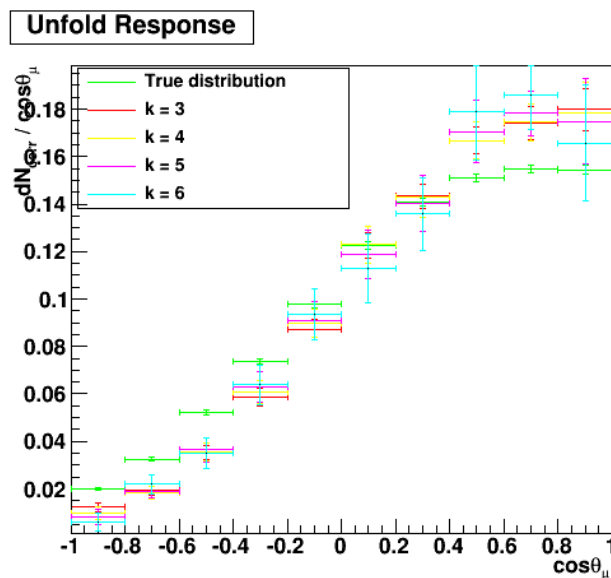
Figure 5.21: Difference between the reconstructed and unfolded angular spectra for different k-values.

Chapter 6

Conclusions and Perspectives

A study of the Time Reversal Symmetry violation in the heavy baryon decays is ongoing.We have developed a method that permits to settle a direct way to test TRV. The decay $\Lambda_b^0 \to \Lambda_c^+(\to \Lambda(p\pi^-)\pi^+)\mu^-\bar{\nu}_\mu$ was chosen for elaborating our searches. This study is being performed with the help of the data recorded by the LHCb detector for the years 2011-2012 of luminosity $1fb^{-1}$ and $2fb^{-1}$ respectively with $\approx$ 15k selected events.

In the first part of the study, we developed a kinematical frame work for the chosen decay. Such model, based on the Jacob-Wick-Jackson helicity formalism, enables us to directly measure the polarization of the resonating particles which in turn gives a direct access to test the time reversal symmetry.

In order to very well handle this decay, the Λ_b^0 Transversity frame and the Helicity frames for the resonating particles Λ_c^+ and Λ are constructed. The angular distributions of the particles in their mother rest frames are deduced, and their polarization vector components are extracted. It is worth to mention that either the normal component or the transverse component of the polarization vector is odd by the TR symmetry, which could be a sign of TRV in the absence of final state interactions.

In the next part, the MC simulations for the decay $\Lambda_b^0 \to \Lambda_c^+(\to \Lambda(p\pi^-)\pi^+)\mu^-\bar{\nu}_\mu$ are generated according to BaryonPCR model whereas the resonating particles are generated according to phase-space. A series of selection criteria has been applied to the data and the MC to purify the final results as much as possible. The presence of the neutrino results in a missing energy and momentum needed to be corrected. An effective method to perform this correction is the unfolding method. It is used to correct both the data and MC.
After that, the final results are corrected with the global efficiency of the detector. The final angular distributions are plotted and analyzed to extract the polarization.

In the third part, an interpretation of the results has been presented. The angular distributions for the different particles are plotted and the polarization of the particles are extracted.
Some systematic uncertainties have been partially taken into account. The run 1 data has been analyzed, and since this decay shows promising results.

Preliminary Test of Time Reversal Symmetry

Some components of the polarization vector have proved to change sign under Time Reversal (T-ODD). This depends on the choice of the frame that we are taking: Transverse frame or the Helicity one. So, the concerned components, as

shown in Tab.5.1, are P_Z^{Trans}, P_X^{Hel}, and P_Y^{Hel}.

• A lower limit for the P_Z^{Trans} of the $\vec{P}_{\Lambda_b^0}^{Trans}$ polarization vector was set. According to Tab.6.1, it is clear that there no sign for TRV within the statistical and systematical errors because Λ_b^0 is mainly produced by strong interactions.

Year	Particle	Track	$a_1 = \alpha_{AS}^{\Lambda_b} \times P_Z^{\Lambda_b}$
2011	Λ_b^0	LL	-0.190 ± 0.046(stat) ± 0.011(sys)
	Λ_b^0	LL	0.221 ± 0.052(stat) ± 0.011(sys)
2012	Λ_b^0	LL	0.094 ± 0.030(stat) ± 0.011(sys)
	Λ_b^0	LL	0.048 ± 0.032(stat) ± 0.011(sys)

Table 6.1: $P_Z^{\Lambda_b}$ extracted from the polar distribution according to $\cos\theta$ of Λ_c^+ in Λ_b^0 rest frame and the fit parameters for different 2011 and 2012 data samples.

• P_X^{Hel} of the $\vec{P}_{\Lambda_c^+}^{Hel}$ is observed to change sign under TR symmetry. The average standard deviation from zero of all samples within the statistical and systematic uncertainties is listed in Tab.6.2. It has been seen that there is more than 3 σ around the zero value which is an eventual sign of TRV.

$P_X^{\Lambda_c}$	Standard deviation
0.261 ± 0.065(stat) ±0.015(sys)	3.9σ

Table 6.2: $P_X^{\Lambda_c}$ and the standard deviation from the central value zero for different 2011 and 2012 data samples.

• P_Y^{Hel} of the $\vec{P}_{\Lambda}^{Hel}$ of the hyperon Λ is the T-odd observable to be stressed on. The average standard deviation from zero is presented in Tab.6.3, showing one sigma around the zero value within the statistical and systematical errors. So no T-odd effect is seen here.

P_Y^{Λ}	Standard deviation
0.054 ± 0.060(stat) ±0.013(sys)	0.8σ

Table 6.3: P_Y^{Λ} and the standard deviation from zero for different 2011 and 2012 data samples.

Test of CP Symmetry

The analysis developed in this thesis takes into consideration baryons and anti-baryons; this enables to directly test CP in the baryon sector. There are three possibilities to test this symmetry: $\Lambda_b^0 - \bar{\Lambda}_b^0$, $\Lambda_c^+ - \bar{\Lambda}_c^+$ and $\Lambda - \bar{\Lambda}$ systems. We did that by looking to the polarization ratio defined for each particle-antiparticle system.

• For the systems $\Lambda_b^0 - \bar{\Lambda}_b^0$, $\Lambda_c - \bar{\Lambda}_c$ and $\Lambda - \bar{\Lambda}$, no sign of CPV have been seen, however an important longitudinal polarization has been put into evidence in the $(\Lambda, \bar{\Lambda})$ system.

A final word here, we should stress finally on two important results.

• $P_X^{\Lambda_c} = P_{Normal}^{\Lambda_c} \neq 0$ almost greater than 3σ as it has already been shown in the last chapter. This is an indication of T-odd observable. It is worth to note the absence of the strong final state interaction (FSI) between the Λ_c and the system $\mu\nu$, which eventually is an indication for a T violation according to Wolfenstein's theorem (2000).

• Concerning the azimuthal distribution of the muon, we can see clearly that $\frac{dN}{d\phi_\mu} \# 1 + A\cos\phi_\mu + B\sin\phi_\mu$ with $A \neq 0$ and B is equal to zero within the statistical and systematical errors. So a departure from the flat distribution is seen here Figs.(5.19-5.20).

Perspectives

Our next goal is to further study the backgrounds coming from excited Λ_c^+. Analyze the Run 2 data where the LHCb has registered statistics higher than those taken in the Run 1 is to be done also.

Appendices

Appendix A

Angular Distributions

A.1   Calculation of the angular distribution of Λ in Λ_c rest frame:

In the proper transverse frame of $\Lambda_c^+(\Lambda_c^+ XYZ)$ the quantization axis $\overrightarrow{\Lambda_c^+ Z}$ is $||$ to $\vec{n}$, which is perpendicular to the Λ_c^+ production plane.

$\overrightarrow{\Lambda_c^+ Z} || \vec{n} = \frac{\vec{p}_p \times \vec{p}_{\Lambda_c^+}}{|\overrightarrow{\vec{p}_p \times \vec{p}_{\Lambda_c^+}}|}$

Let $M_i = \pm 1/2$ be the projection of the Λ_c^+ spin on the $\overrightarrow{\Lambda_c^+ Z}$ axis, and $\rho^{\Lambda_c^+}$ be the Λ_c^+ polarization density matrix. It is (2×2) hermitian matrix and its elements satisfy the following relations:

$$\rho_{++} + \rho_{--} = 1$$

$$\rho_{+-} = \rho_{-+}^*$$

The initial polarization of Λ_c^+ along the quantization axis $\overrightarrow{\Lambda_c^+ Z}$ is given by :

$$< \vec{S}.\vec{n} >= P_z = (\rho_{++} - \rho_{--})$$

where $\rho_{++}(\rho_{--})$ is the probability of finding the particle with spin projection $+1/2(-1/2)$ along the quantization axis.

Consider the decay $\Lambda_c^+ \to \Lambda(\lambda_1)\pi^+(\lambda_2)$, $\vec{p}_\Lambda(p, \theta, \phi)$ is the momentum of Λ in the Λ_c^+ rest frame, $\lambda_1 = \pm 1/2$ and $\lambda_2 = 0$ are the helicities of Λ and the pion respectively, and finally we denote by $M_f = \lambda_1 - \lambda_2 = \pm 1/2$ to be the projection of the final angular momentum along the axis $(\triangle)||\vec{p}_\Lambda \equiv$ helicity axis.

We have 2 possibilities for the couple (λ_1, λ_2) due to the conservation of the total angular momentum : (-1/2,0) ; (+1/2,0).

The general formalism for the $\Lambda_c^+ \to \Lambda(\lambda_1)\pi^+(\lambda_2)$ decay is based on the Jacob-Wick helicity formalism, and completed by the formalism of Jackson [24]. The decay amplitude is given by the following relation:

$$A_0(M_i) = M_{\Lambda_c^+}(\lambda_1, \lambda_2) D_{M_i, M_f}^{1/2*}(\phi, \theta, 0)$$

with $M_{\Lambda_c^+}(\lambda_1, \lambda_2)$ is the Λ_c^+ hadronic matrix element and it is independent of the polar angle θ and the azimuthal angle ϕ(Wigner's theorem).

$D_{M_i, M_f}^j(\phi, \theta, 0)$ is the general element of the Wigner D-matrix and it depend on the projection of the angular momentum M_i and M_f. It is given by :

$$D_{M_i, M_f}^j(\phi, \theta, 0) = d_{M_i, M_f}^j(\theta) \exp(-i M_i \phi)$$

Consider also the decay $\Lambda(\lambda_1) \longrightarrow p(\lambda_3)\pi^-(\lambda_4)$

The helicity of the proton (λ_3) takes the value $\pm 1/2$, while the helicity of the pion (λ_4) is always equal to zero.

In the helicity rest frame of the Λ, the projection of the total angular momentum along an axis parallel to the proton momentum is designed by $m_1 = \lambda_3 - \lambda_4 = \pm 1/2$

The decay amplitude of the resonance state $\Lambda(\lambda_1) \longrightarrow p(\lambda_3)\pi^-(\lambda_4)$ is given by the following relation: $A_1(\lambda_1) = M_\Lambda(\lambda_3, \lambda_4)D^{1/2*}_{\lambda_1, m_1}(\phi_1, \theta_1, 0) = M_\Lambda(\lambda_3, \lambda_4)d^{1/2}_{\lambda_1, m_1}(\theta_1)\exp(i\lambda_1\phi_1)$

The total amplitude of the decay $\Lambda_c^+ \to \Lambda(\lambda_1)\pi^+(\lambda_2) \longrightarrow p(\lambda_3)\pi^-(\lambda_4)\pi^+(\lambda_2)$

$$A_{tot} = \sum_{\lambda_1, \lambda_2} A_0(M_i)A_1(\lambda_1)$$

$$= \sum_{\lambda_1, \lambda_2} M_{\Lambda_c^+}(\lambda_1, \lambda_2)d^{1/2}_{M_i, M_f}(\theta)\exp(iM_i\phi)M_\Lambda(\lambda_3, \lambda_4)d^{1/2}_{\lambda_1, m_1}(\theta_1)\exp(i\lambda_1\phi_1)$$

where θ_1, ϕ_1 are respectively the polar and the azimuthal angles of the proton in the Λ rest frame.

In the next step we will introduce the polarization density matrix $\rho^{\Lambda_c^+}$, and thus the decay probability is given by :

$$d\sigma \propto \Sigma_{M_i, M_i'}\rho_{M_i, M_i'}A_{tot}A_{tot}^*$$

now we should sum over all the helicities of the final particles and the expression $d\sigma$ becomes:

$$d\sigma \propto \sum_{\lambda_3, \lambda_4}\sum_{M_i, M_i'}\rho_{M_i, M_i'}A_{tot}A_{tot}^*$$

After writing down the explicit form of the total amplitude A_{tot} the probability of the decay takes the form:

$$d\sigma \propto \sum_{\lambda_1, \lambda_2, \lambda_1', \lambda_2'}\sum_{M_i, M_i'}\rho_{M_i, M_i'}M_{\Lambda_c^+}(\lambda_1, \lambda_2)M_{\Lambda_c^+}^*(\lambda_1', \lambda_2')d^{1/2}_{M_i, M_f}(\theta)d^{1/2}_{M_i', M_f'}(\theta)\exp i(M_i - M_i')\phi$$

$$\times |M_\Lambda(\lambda_3, \lambda_4)|^2 d^{1/2}_{\lambda_1, m_1}(\theta_1)d^{1/2}_{\lambda_1', m_1}(\theta_1)\exp i(\lambda_1 - \lambda_1')\phi_1$$

with $m_1 = \lambda_3 - \lambda_4 = \pm 1/2;\quad M_f = \lambda_1 - \lambda_2;\quad M_f' = \lambda_1', \lambda_2'$

finally we have the following integrals to be done:

$$d\sigma(\Lambda)_{\Lambda_c^+} = \int_{\phi_1, \theta_1} d\sigma \times d\phi_1 d\cos\theta_1$$

$$d\sigma(p)_\Lambda = \int_{\phi, \theta} d\sigma \times d\phi d\cos\theta$$

A.2 Calculation of the angular distribution of the proton in the Λ rest frame:

$d\sigma(p)_\Lambda = \sum_{\lambda_1, \lambda_1', M_i, M_i'}\int_{\phi, \theta} d\sigma \times d\phi d\cos\theta$

$\times\{\rho_{M_i, M_i'}M_{\Lambda_c^+}(\lambda_1, 0)M_{\Lambda_c^+}^*(\lambda_1', 0)d^{1/2}_{M_i, M_f}(\theta)d^{1/2}_{M_i', M_f'}(\theta)\exp i(M_i - M_i')\phi\}$

$\times\{|M_\Lambda(1/2, 0)|^2 d^{1/2}_{\lambda_1, 1/2}(\theta_1)d^{1/2}_{\lambda_1', 1/2}(\theta_1) + |M_\Lambda(-1/2, 0)|^2 d^{1/2}_{\lambda_1, -1/2}(\theta_1)d^{1/2}_{\lambda_1', -1/2}(\theta_1)\exp i(\lambda_1 - \lambda_1')\phi_1\}$

The integral over $d\phi$ and having $0 < \phi < 2\pi$ results a Kronecker Delta $\delta_{M_i M'_i}$ and a factor 2π. The resulting $\delta_{M_i M'_i}$ will make the summation over M'_i vanishes and replaces every M'_i by M_i

Making the summation over $M_i = \pm 1/2$ and replacing the reduced Wigner d-matrix by its values and the final expression becomes:

$$d\sigma(p)_\Lambda = \pi |M_\Lambda(1/2,0)|^2 + |M_\Lambda(-1/2,0)|^2 \{|M_{\Lambda_c^+}(1/2,0)|^2 + |M_{\Lambda_c^+}(-1/2,0)|^2\}$$

$$\{1 + \alpha_{AS}^\Lambda \alpha_{AS}^{\Lambda_c^+} \cos\theta_1 - \frac{\pi}{4} \alpha_{AS}^\Lambda P_Z^{\Lambda_c^+} \sin\theta_1 \langle \frac{M_{\Lambda_c^+}(1/2,0) M_{\Lambda_c^+}^*(-1/2,0)}{|M_{\Lambda_c^+}(1/2,0)|^2 + |M_{\Lambda_c^+}(-1/2,0)|^2} \exp(i\phi_1)$$

$$+ \frac{M_{\Lambda_c^+}(-1/2,0) M_{\Lambda_c^+}^*(1/2,0)}{|M_{\Lambda_c^+}(1/2,0)|^2 + |M_{\Lambda_c^+}(-1/2,0)|^2} \exp(-i\phi_1)\rangle\}$$

where $\alpha_{AS}^\Lambda == \frac{|M_\Lambda(1/2,0)|^2 - |M_\Lambda(-1/2,0)|^2}{|M_\Lambda(1/2,0)|^2 + |M_\Lambda(-1/2,0)|^2}$ is the Λ decay parameter.

Appendix B

Figures and Plots of Different Data Samples

B.1 Signal background distribution figures
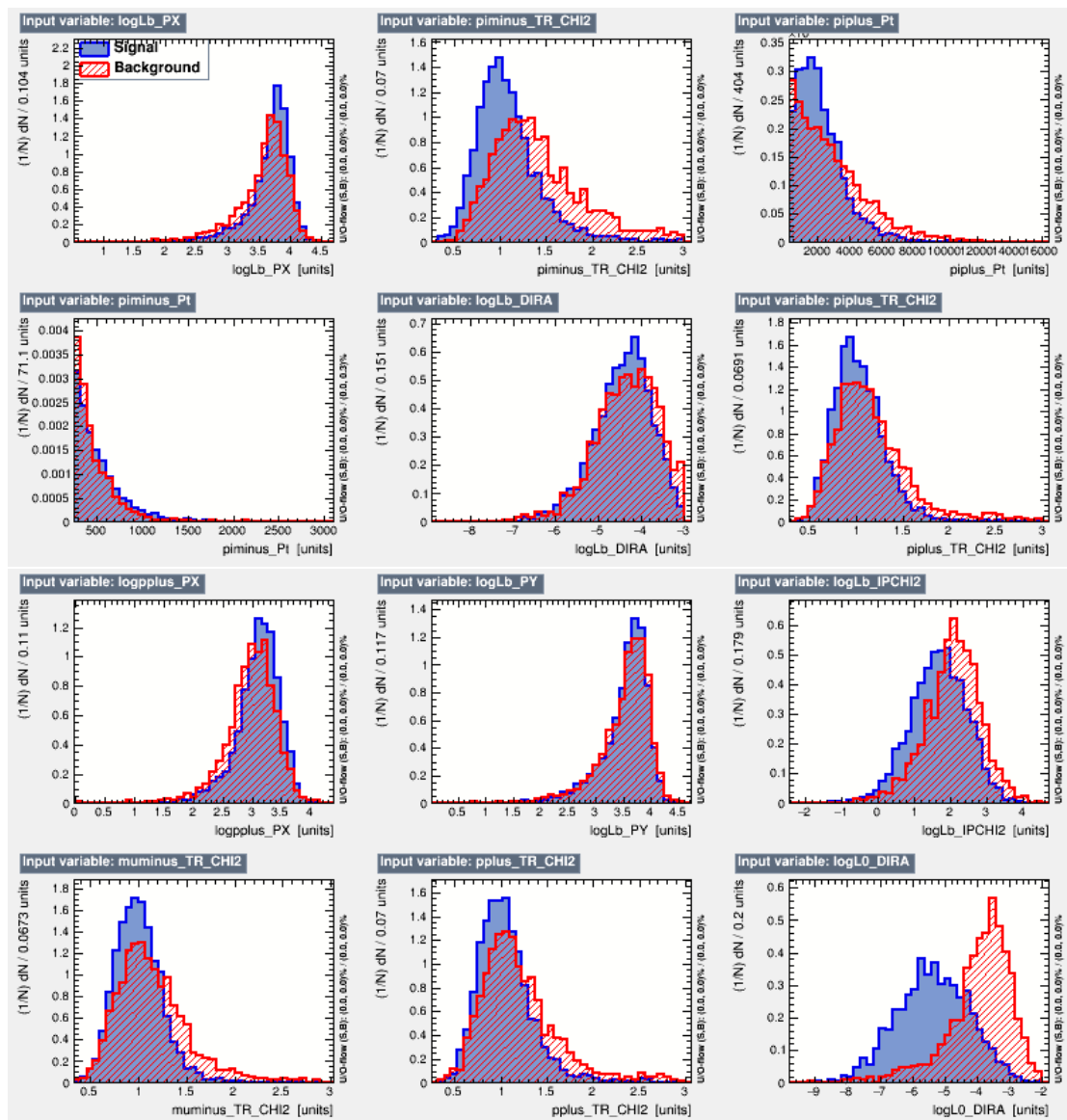
Figure B.1: Distribution of variables used in the training of BDT for 2011 (LL, $\bar{\Lambda}_c$ tracks) , superimposing RHSB background events (in Red) and MC-generated signal events (in Blue).
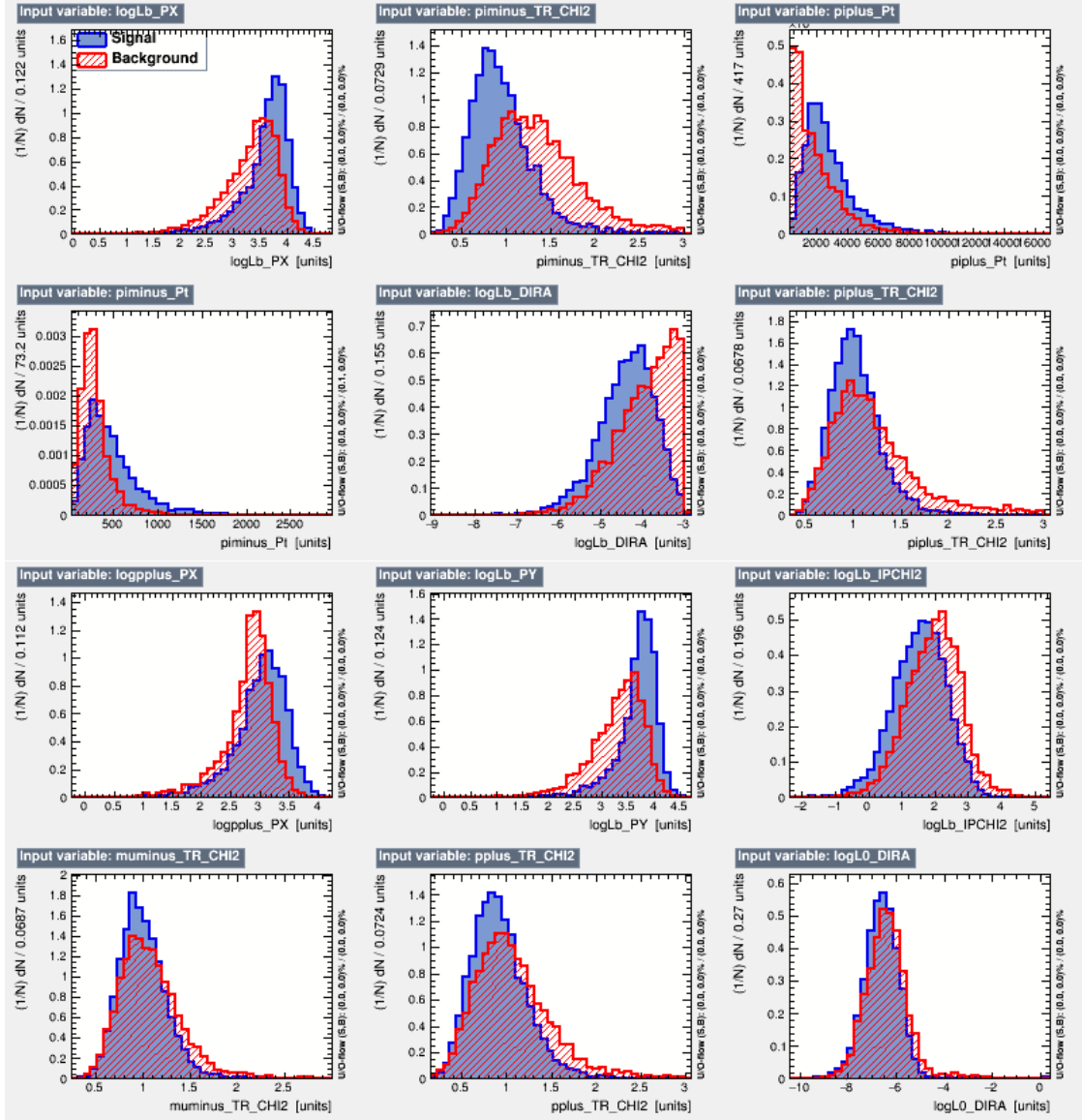
Figure B.2: Distribution of variables used in the training of BDT for 2011 (DD, Λ_c^+ tracks) , superimposing RHSB background events (in Red) and MC-generated signal events (in Blue).

Figure B.3: Distribution of variables used in the training of BDT for 2011 (DD, $\bar{\Lambda}_c$ tracks) , superimposing RHSB background events (in Red) and MC-generated signal events (in Blue).
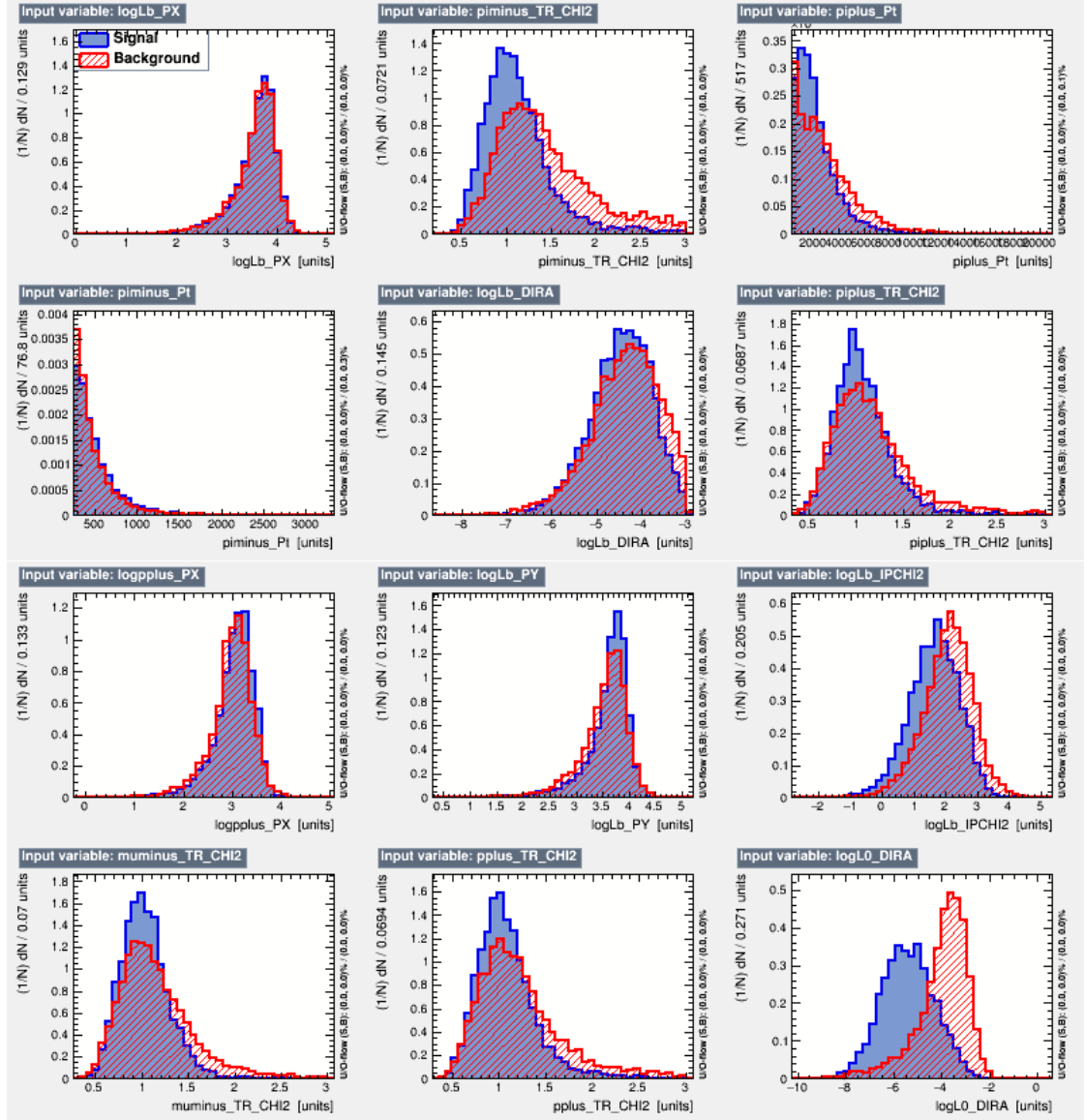
Figure B.4: Distribution of variables used in the training of BDT for 2012 (LL, Λ_c^+ tracks) , superimposing RHSB background events (in Red) and MC-generated signal events (in Blue).

Figure B.5: Distribution of variables used in the training of BDT for 2012 (LL, $\bar{\Lambda}_c$ tracks), superimposing RHSB background events (in Red) and MC-generated signal events (in Blue).
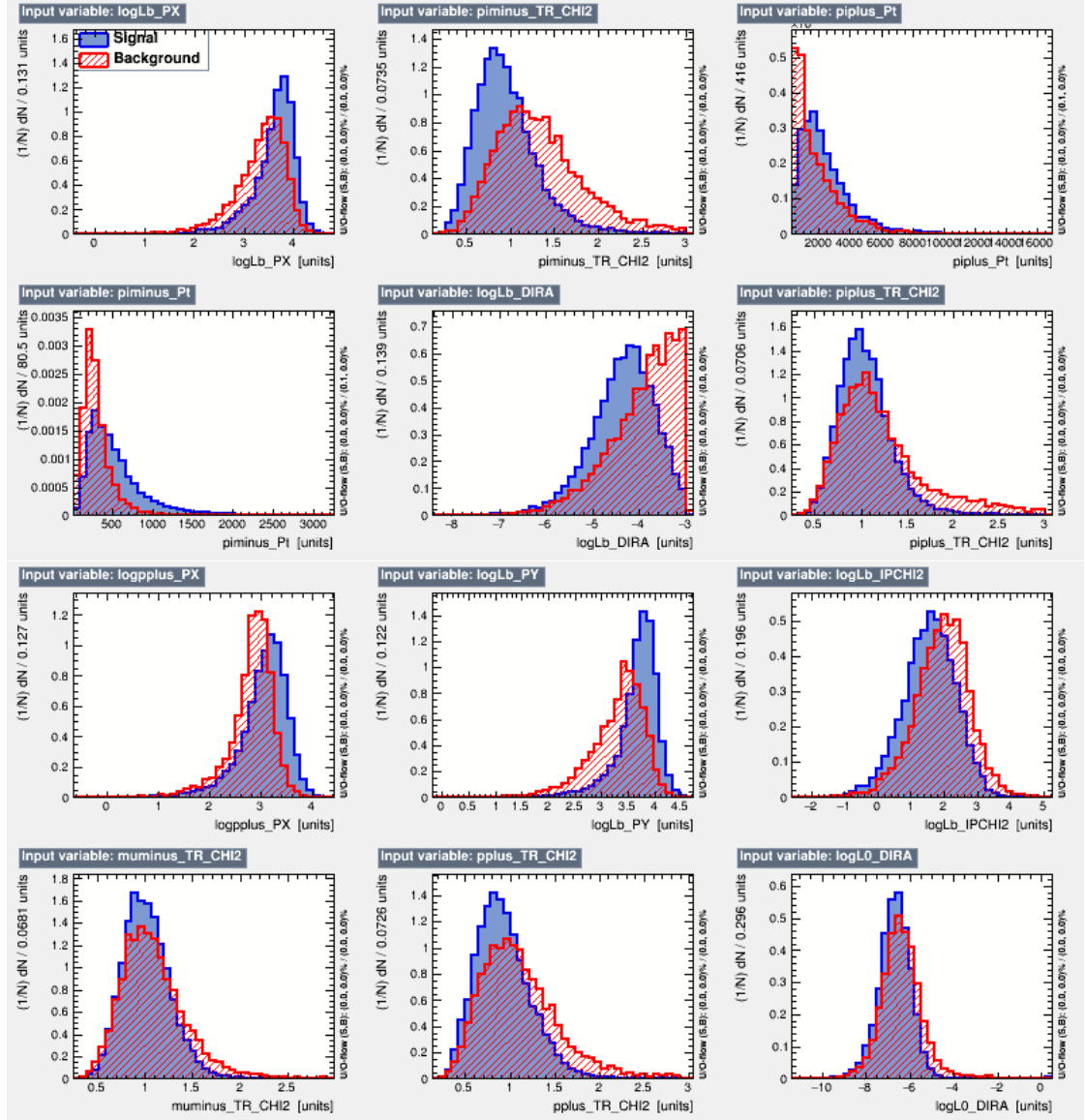
Figure B.6: Distribution of variables used in the training of BDT for 2012 (DD, Λ_c^+ tracks) , superimposing RHSB background events (in Red) and MC-generated signal events (in Blue).

Figure B.7: Distribution of variables used in the training of BDT for 2012 (DD, $\bar{\Lambda}_c$ tracks) , superimposing RHSB background events (in Red) and MC-generated signal events (in Blue).

B.2   Signal Correlation Matrices
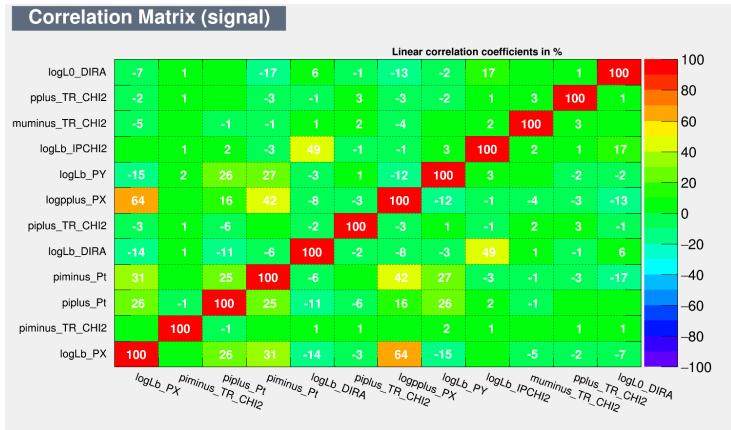
(a) DD Λ_c^+ signal correlation matrix
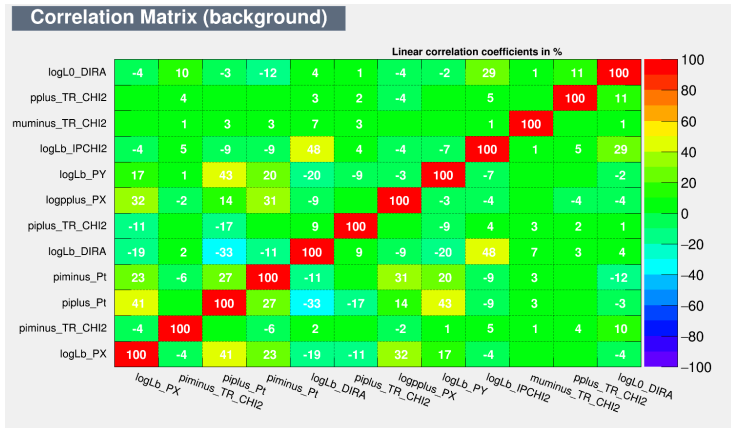
(b) DD Λ_c^+ BKG correlation matrix
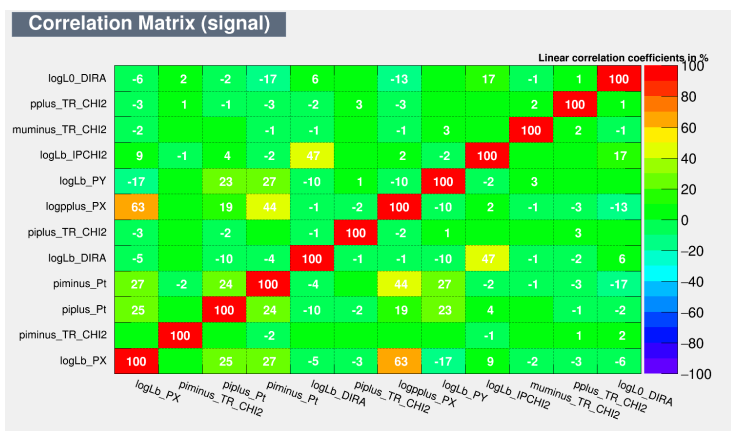
(c) DD $\bar{\Lambda}_c^-$ signal correlation matrix
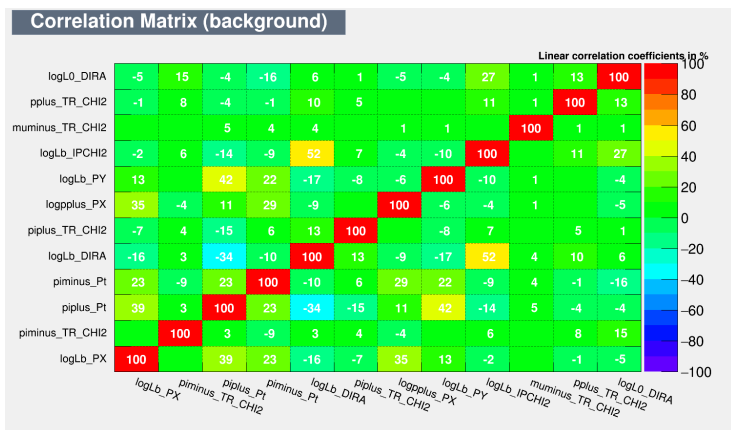
(d) DD$\bar{\Lambda}_c^-$ BKG correlation matrix

Figure B.8: Linear correlation for DD tracks, signal and background (BKG) for 2011 data sample: Λ_c^+ and $\bar{\Lambda}_c^+$.
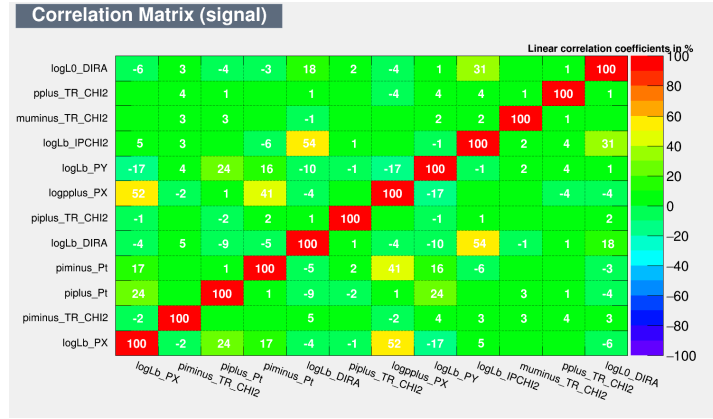
(a) LL Λ_c^+ signal correlation matrix
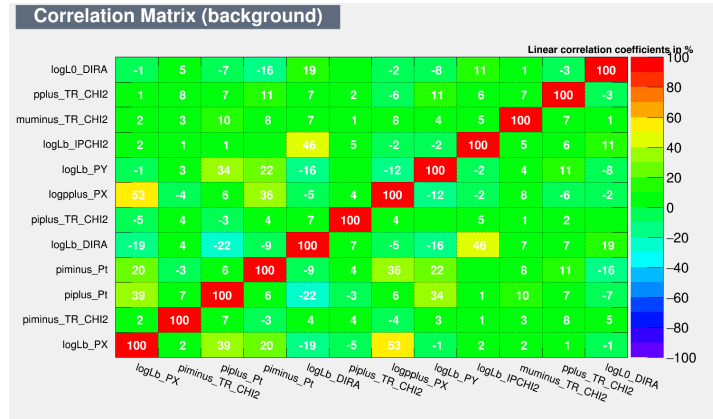
(b) LL Λ_c^+ BKG correlation matrix
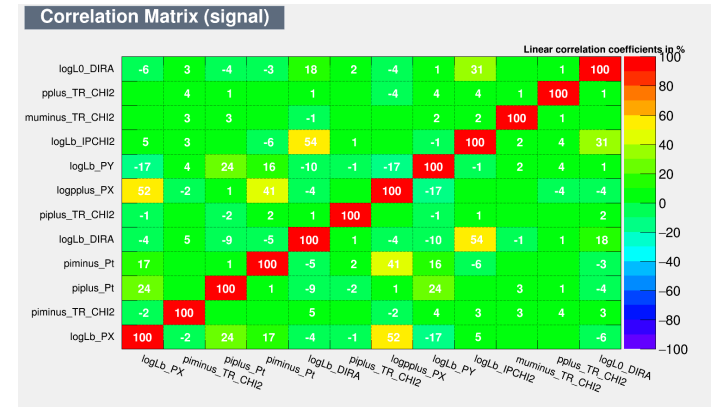
(c) LL $\bar{\Lambda}_c^+$ signal correlation matrix
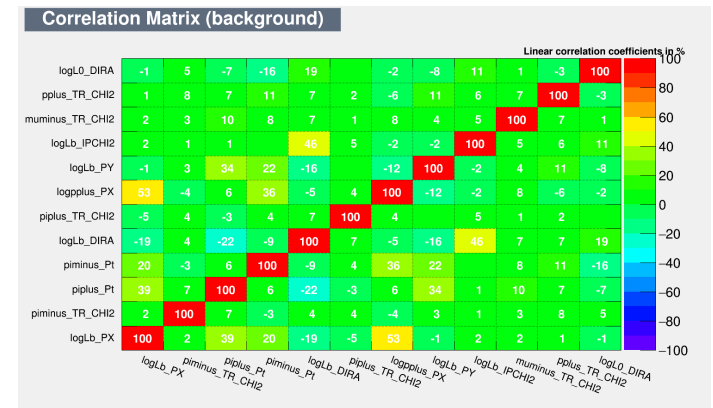
(d) LL $\bar{\Lambda}_c^+$ BKG correlation matrix

Figure B.9: Linear correlation matrix for LL Tracks, signal and BKG for 2011 data sample: Λ_c^+ and $\bar{\Lambda}_c^+$.
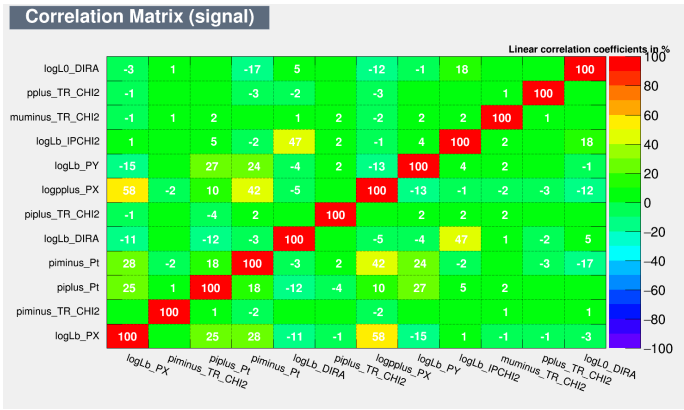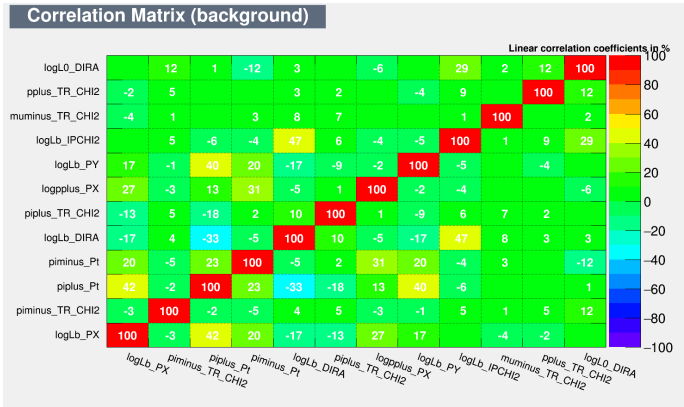
(a) DD Λ_c^+ signal correlation matrix

(b) DD Λ_c^+ BKG correlation matrix
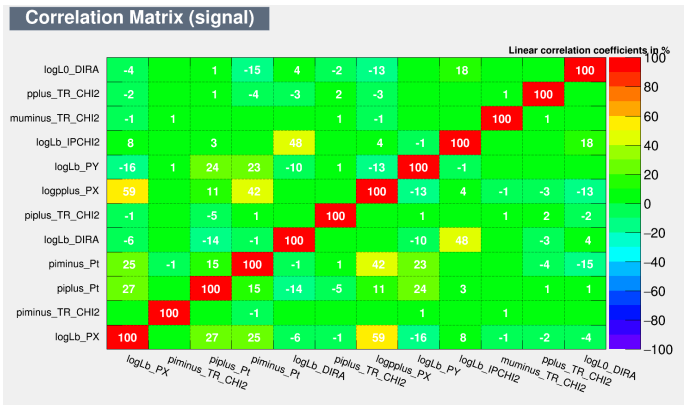
(c) DD $\bar{\Lambda}_c^+$ signal correlation matrix
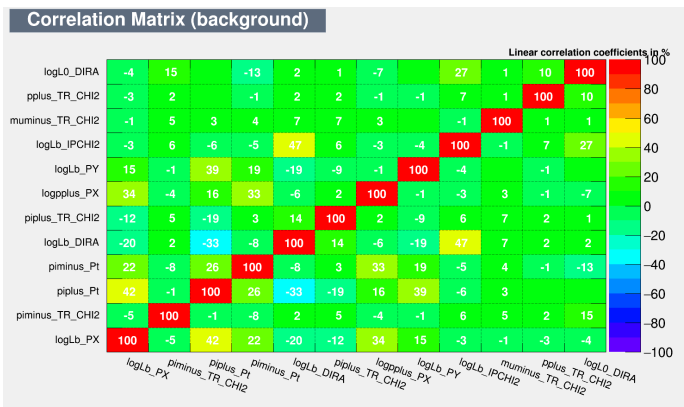
(d) DD $\bar{\Lambda}_c^+$ BKG correlation matrix

Figure B.10: Linear correlation matrix for DD Tracks, signal and BKG for 2012 data sample: Λ_c^+ and $\bar{\Lambda}_c^+$.
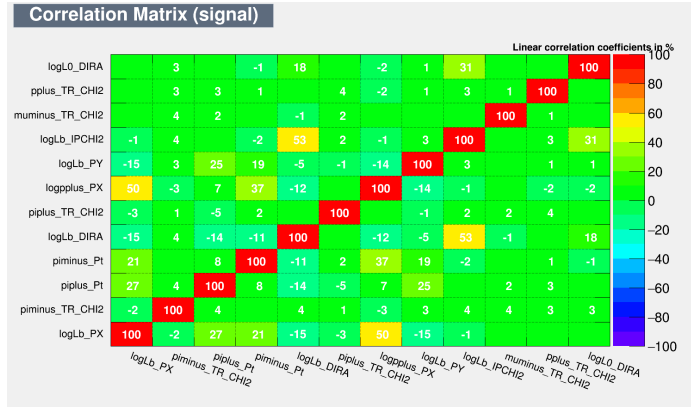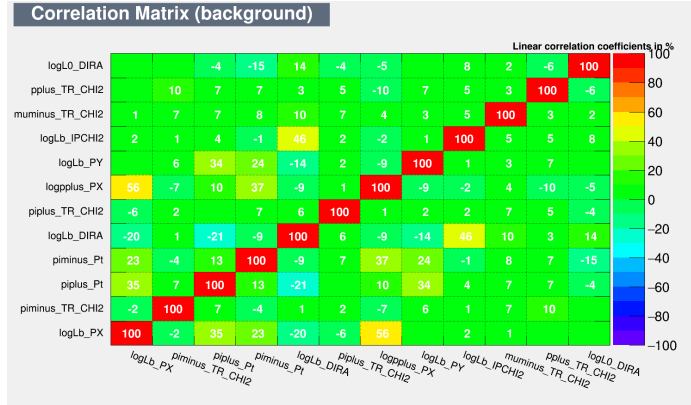
(a) LL Λ_c^+ signal correlation matrix

(b) LL Λ_c^+ BKG correlation matrix
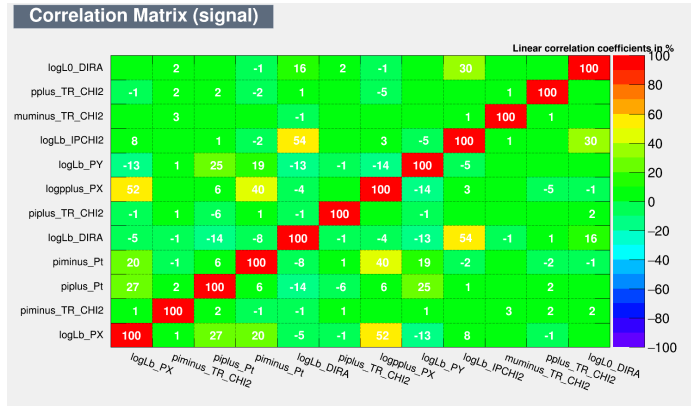
(c) LL $\bar{\Lambda}_c^+$ signal correlation matrix
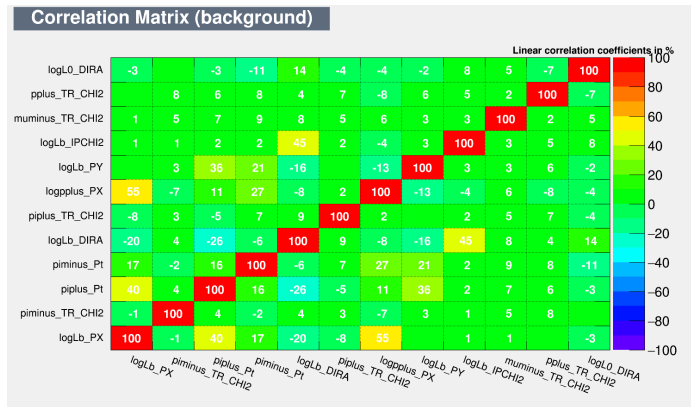
(d) LL $\bar{\Lambda}_c^+$ BKG correlation matrix

Figure B.11: Linear correlation matrix BDT for LL Tracks, signal and background(BKG) for 2012 data sample: Λ_c^+ and $\bar{\Lambda}_c^+$.

B.3 Corrections applied on MC (reweighting)

B.3.1 reweighting the Λ_b^0 Transverse momentum P_T

B.3.2 reweighting the track multiplicity

(a) P_T of Λ_b^0 for LL tracks

(b) P_T of $\bar{\Lambda}_b^0$ for LL tracks
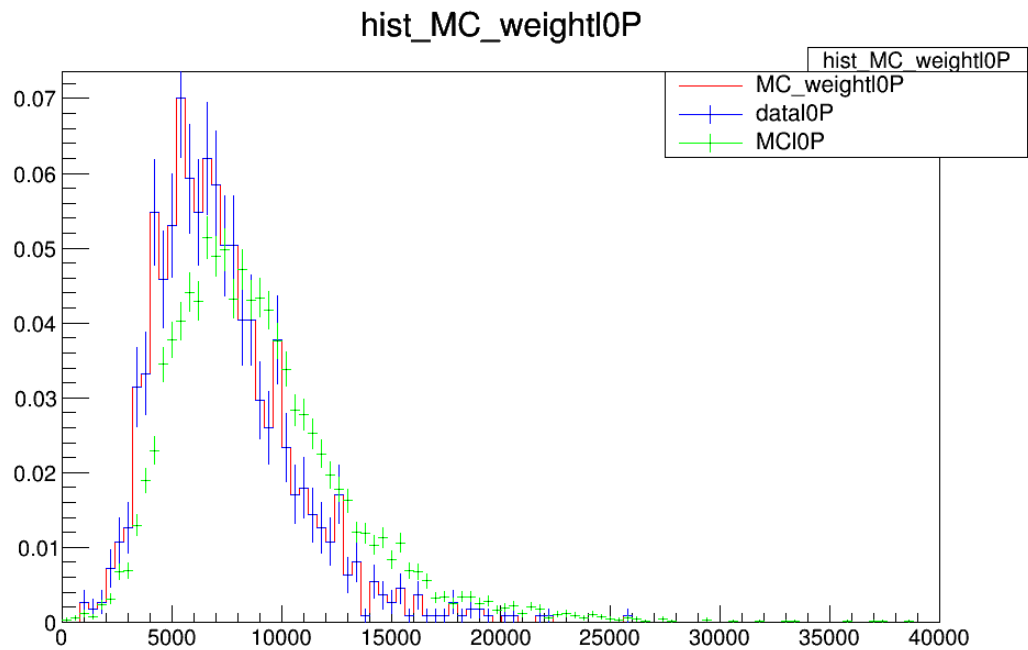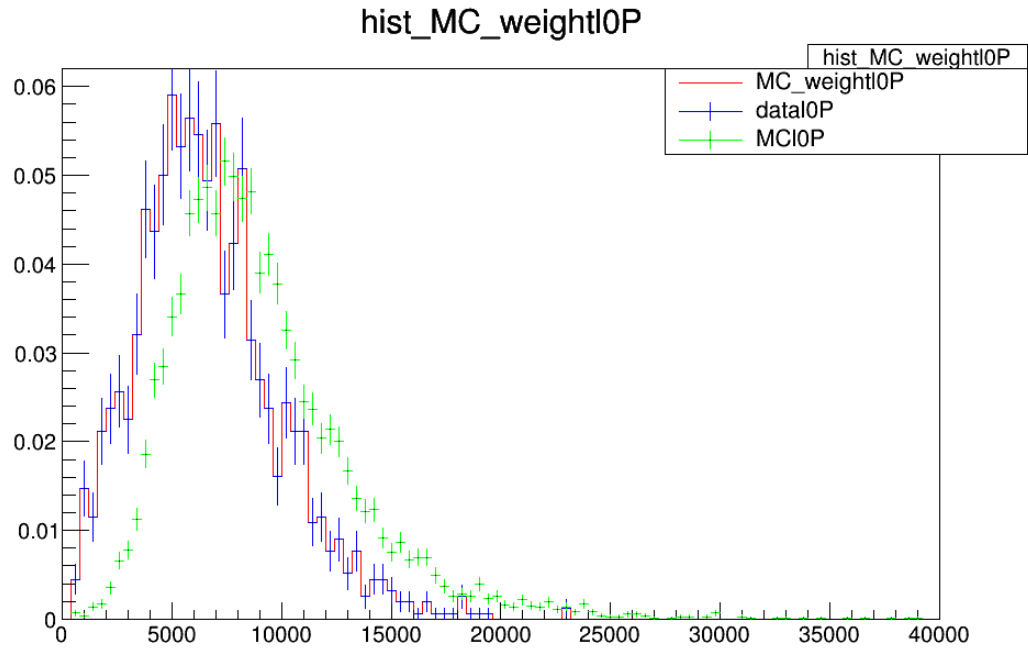
Figure B.12: Comparison between the normalized Λ_b^0 P_T before and after reweighting for LL track and particle type using the data of 2011. The blue color represents the side-band-subtracted data and the MC is represented by the green color. The red color represents the re-weighted MC events.
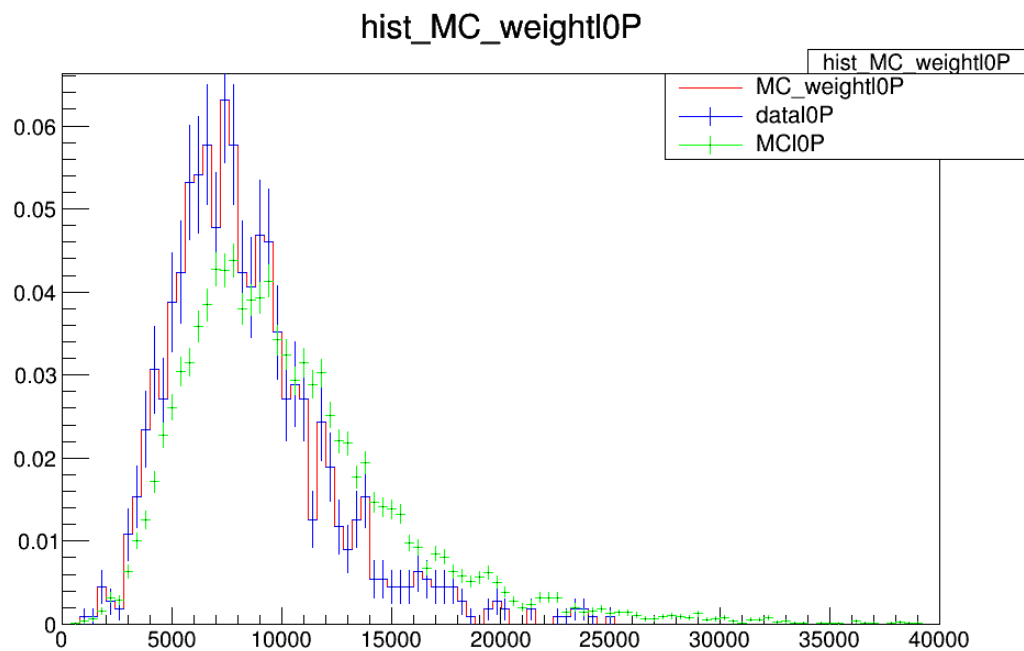
(a) P_T of Λ_b^0 for DD tracks
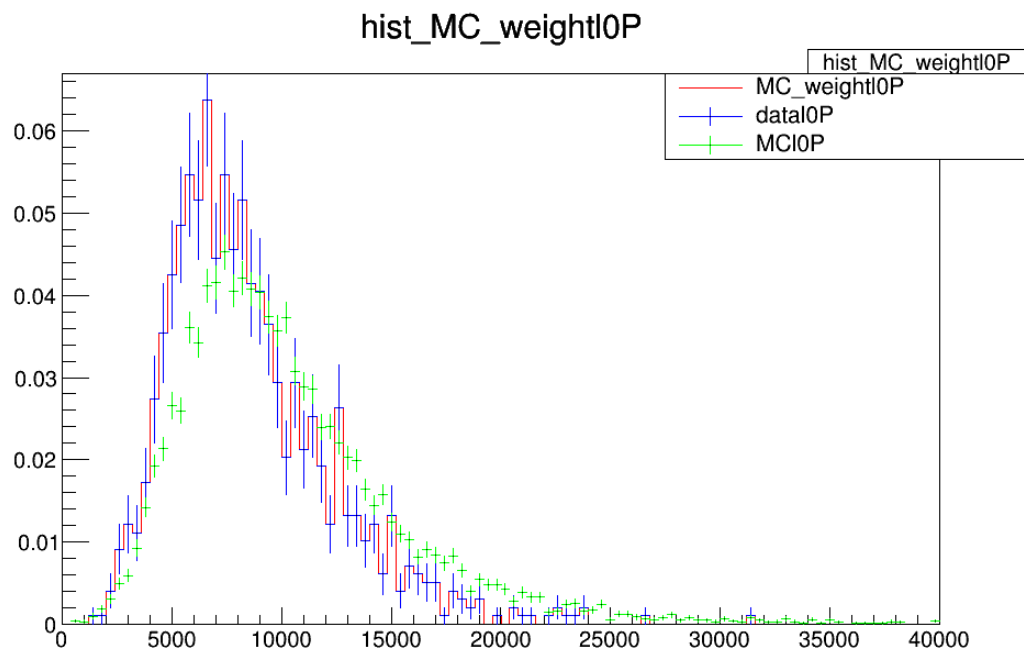
(b) P_T of $\bar{\Lambda}_b^0$ for DD tracks

Figure B.13: Comparison between the normalized Λ_b^0 P_T before and after reweighting for DD tracks and particle type using the data of 2011. The blue color represents the side-band-subtracted data and the MC is represented by the green color. The red color represents the re-weighted MC events.

(a) P_T of Λ_b^0 for LL tracks

(b) P_T of $\bar{\Lambda}_b^0$ for LL tracks
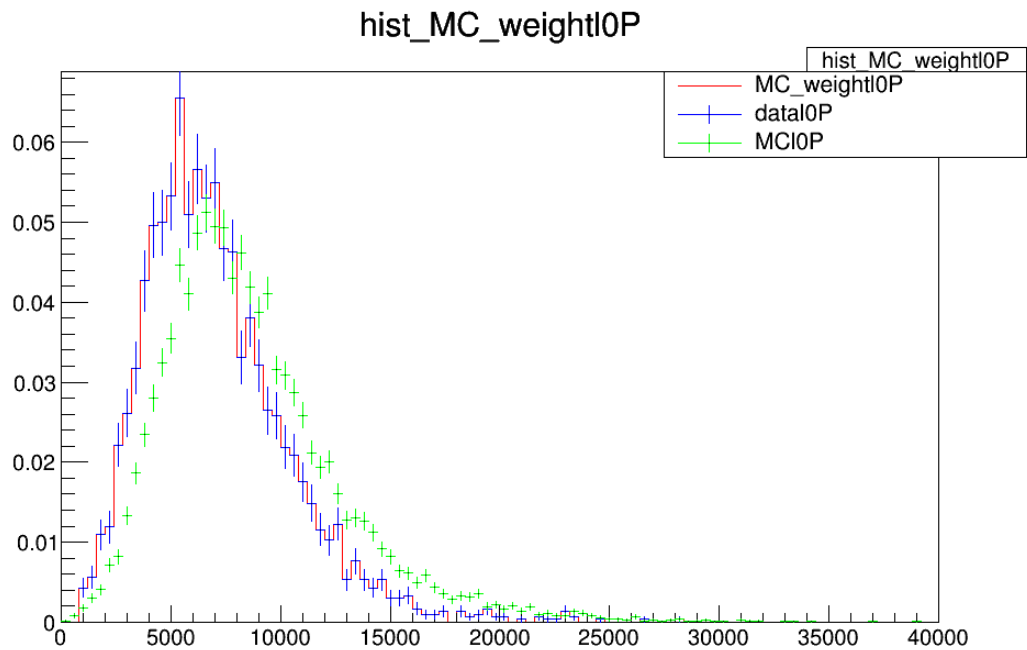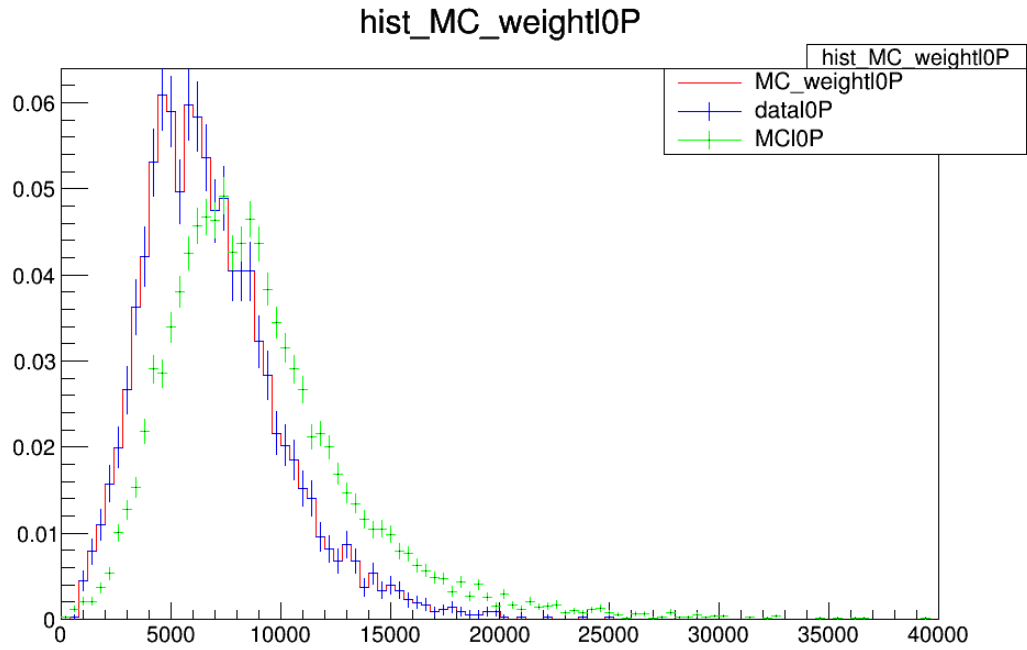
Figure B.14: Comparison between the normalized Λ_b^0 P_T before and after reweighting for LL track and particle types using the data of 2012. The blue color represents the side-band-subtracted data and the MC is represented by the green color. The red color represents the re-weighted MC events.
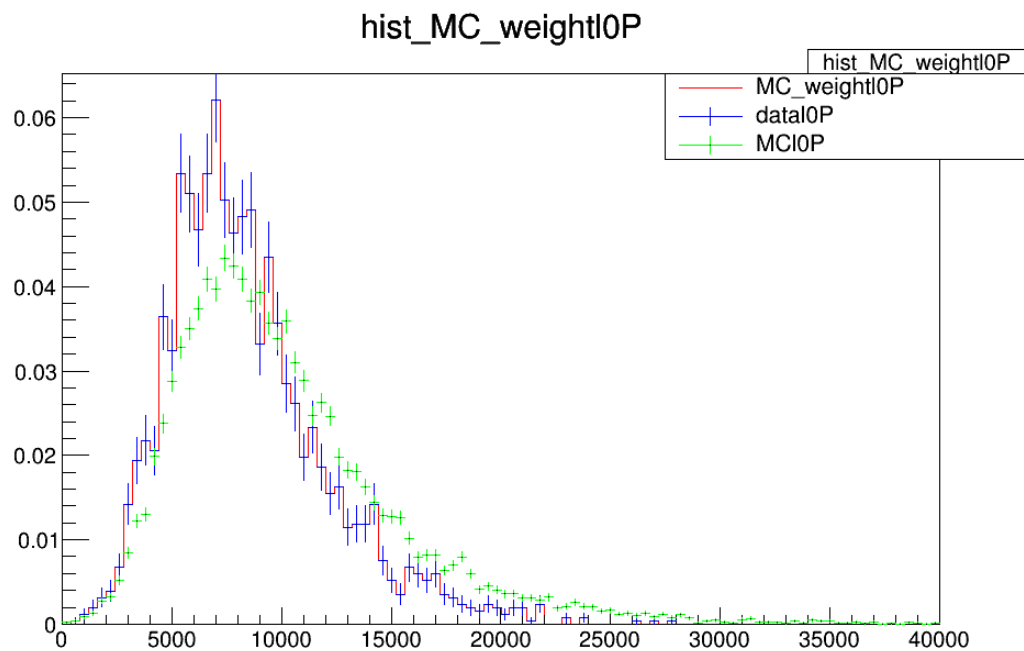
(a) P_T of Λ_b^0 for DD tracks
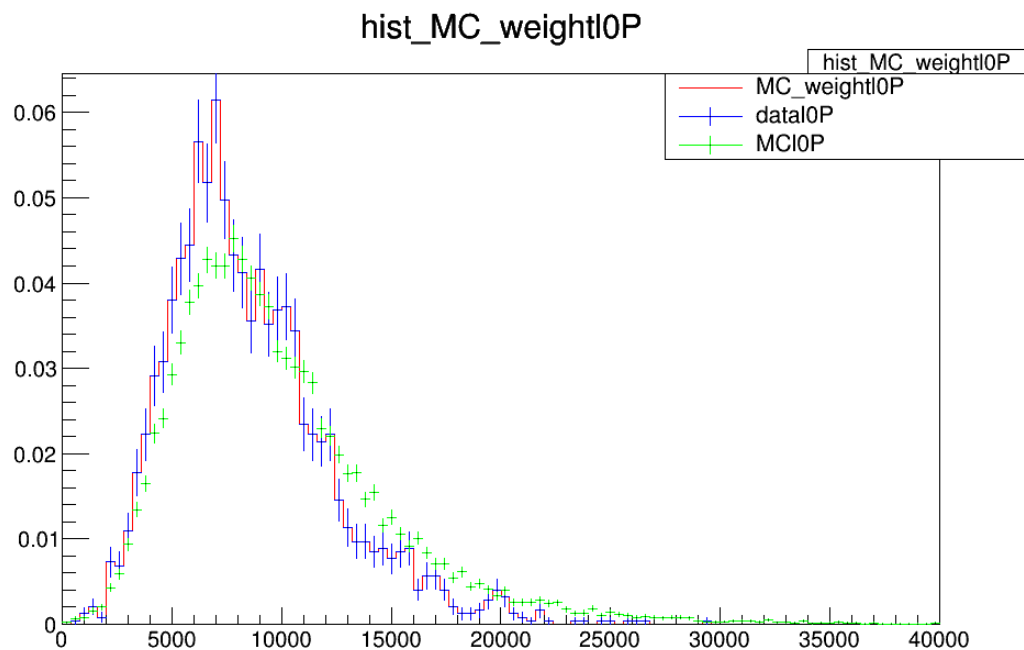
(b) P_T of $\bar{\Lambda}_b^0$ for DD tracks

Figure B.15: Comparison between the normalized Λ_b^0 P_T before and after reweighting for DD track and particle types using the data of 2012. The blue color represents the side-band-subtracted data and the MC is represented by the green color. The red color represents the re-weighted MC events.
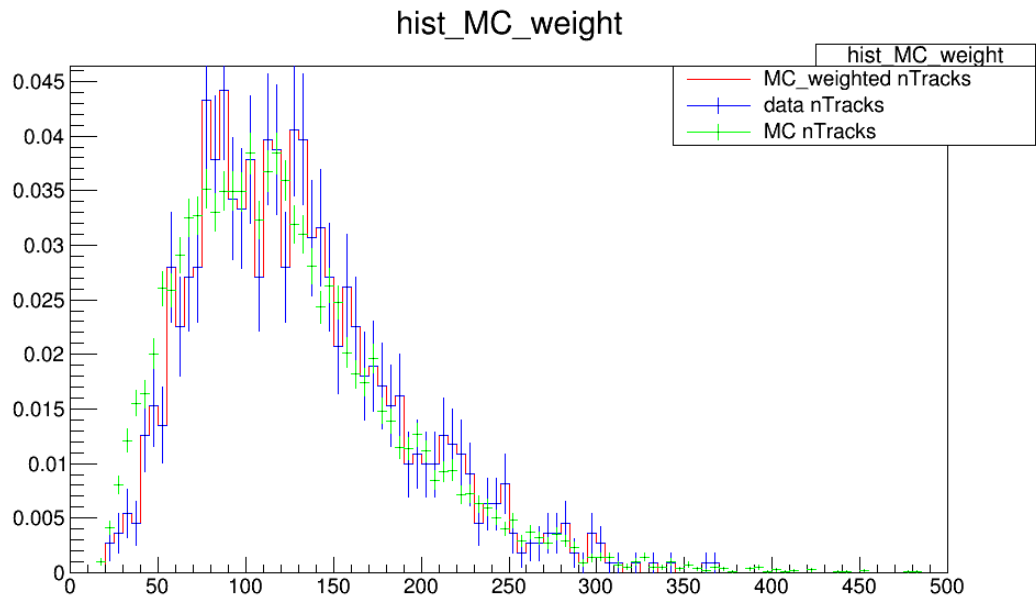
(a) Track multiplicity for DD tracks
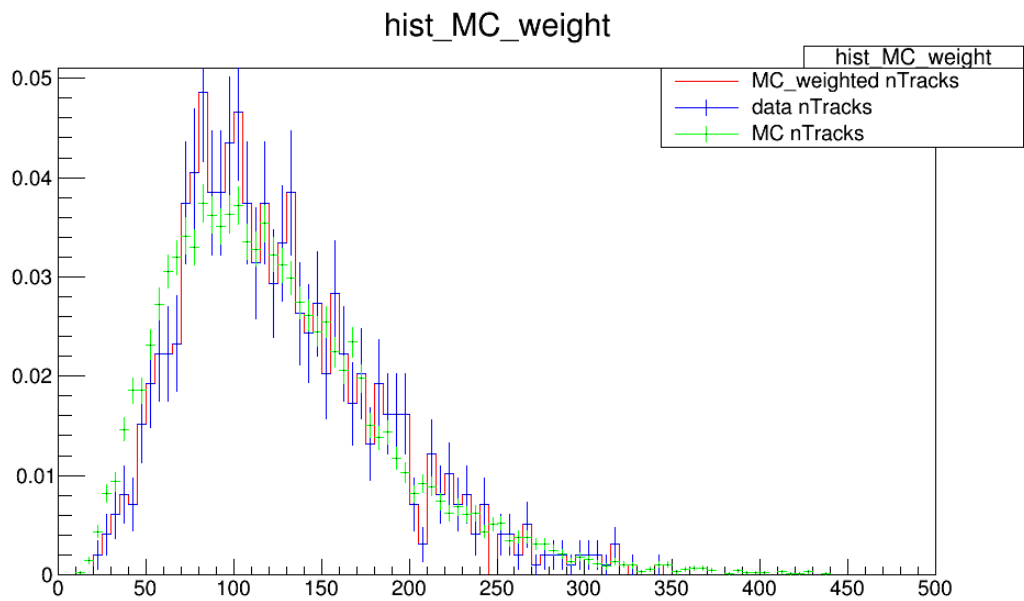
(b) Track multiplicity for DD tracks

Figure B.16: Comparison between the normalized track multiplicity before and after reweighting for DD tracks and particle types using the data of 2011. The blue color represents the sideband-subtracted data and the MC is represented by the green color. The red color represents the re-weighted MC events.
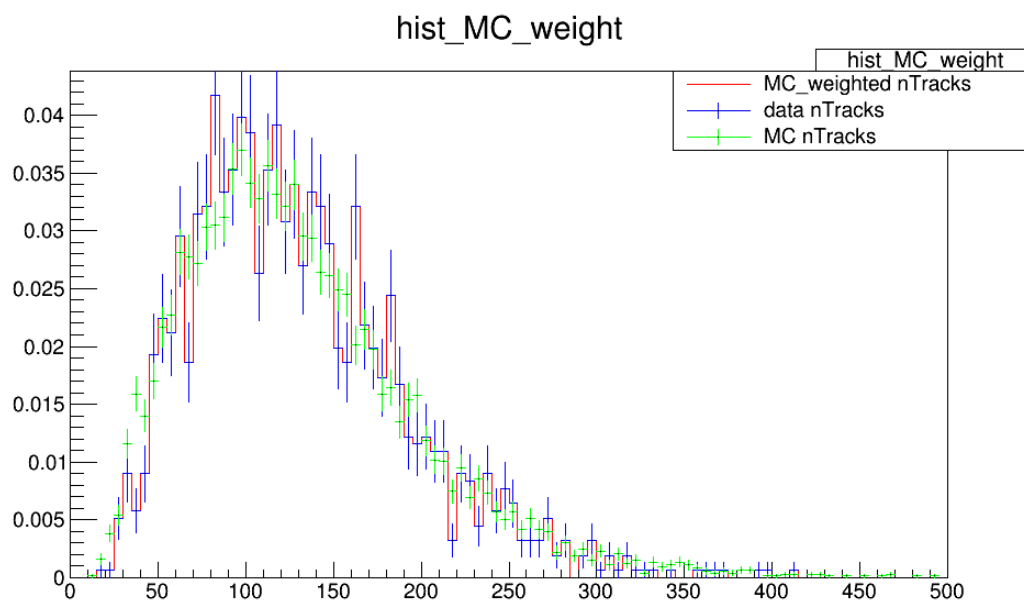
(a) Track multiplicity for LL tracks
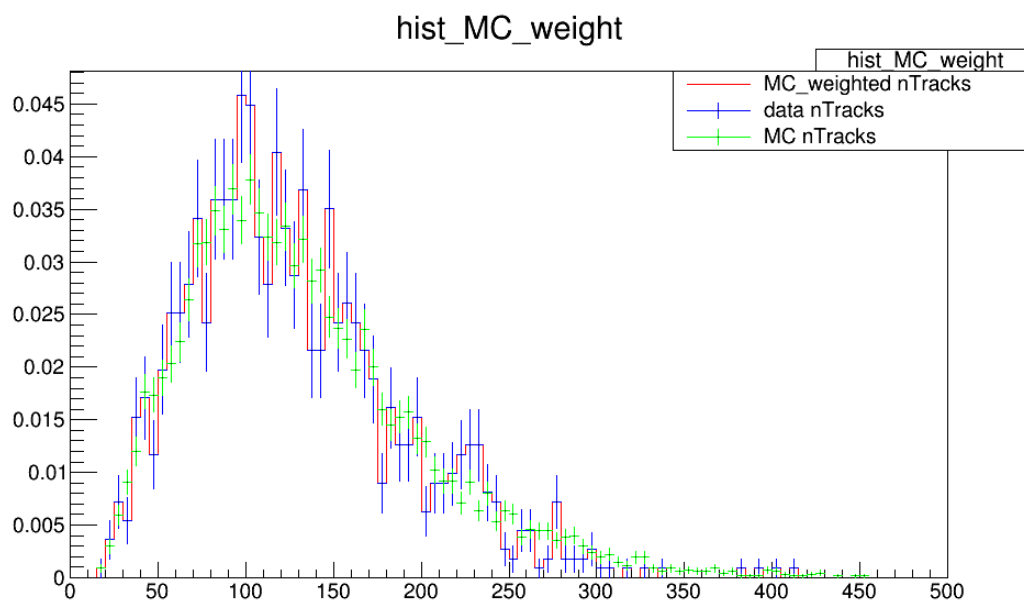
(b) Track multiplicity for LL tracks

Figure B.17: Comparison between the normalized track multiplicity before and after reweighting for LL tracks and particle types using the data of 2011. The blue color represents the side-band-subtracted data and the MC is represented by the green color. The red color represents the re-weighted MC events.
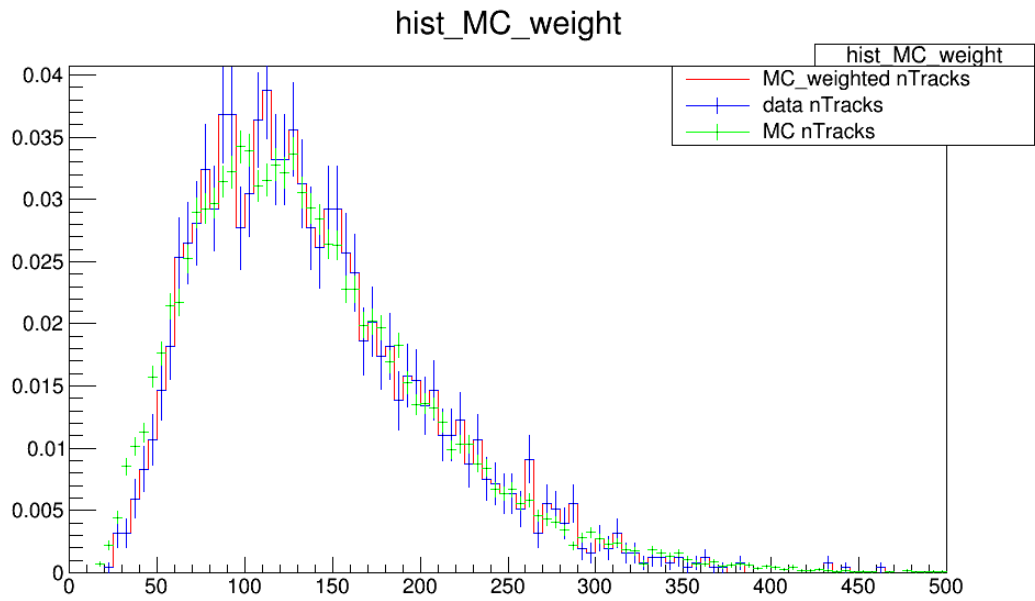
(a) Track multiplicity for DD tracks
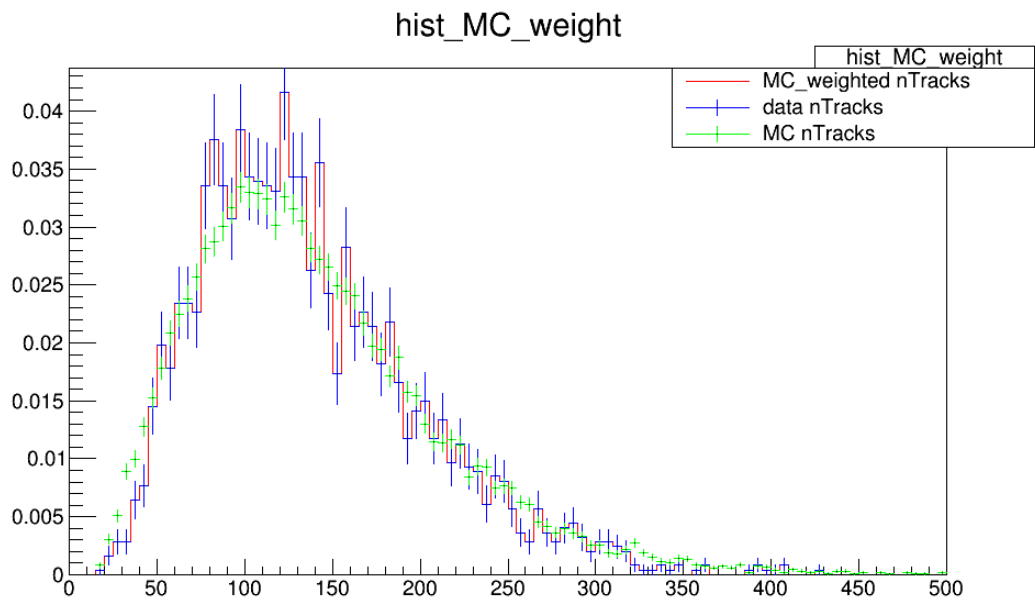
(b) Track multiplicity for DD tracks

Figure B.18: Comparison between the normalized track multiplicity before and after reweighting for DD tracks and particle types using the data of 2012. The blue color represents the side-band-subtracted data and the MC is represented by the green color. The red color represents the re-weighted MC events.
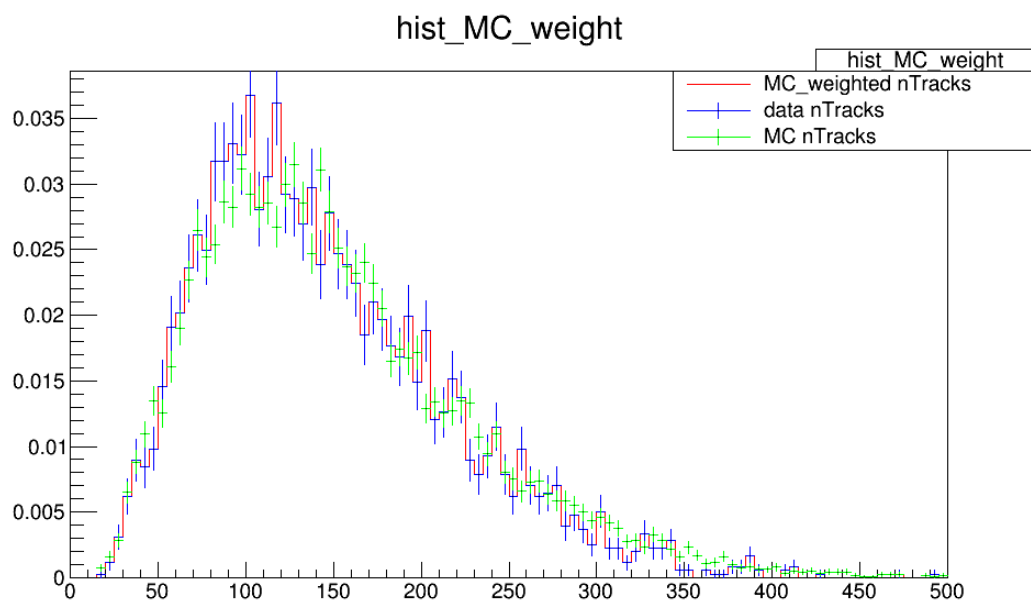
(a) Track multiplicity for LL tracks
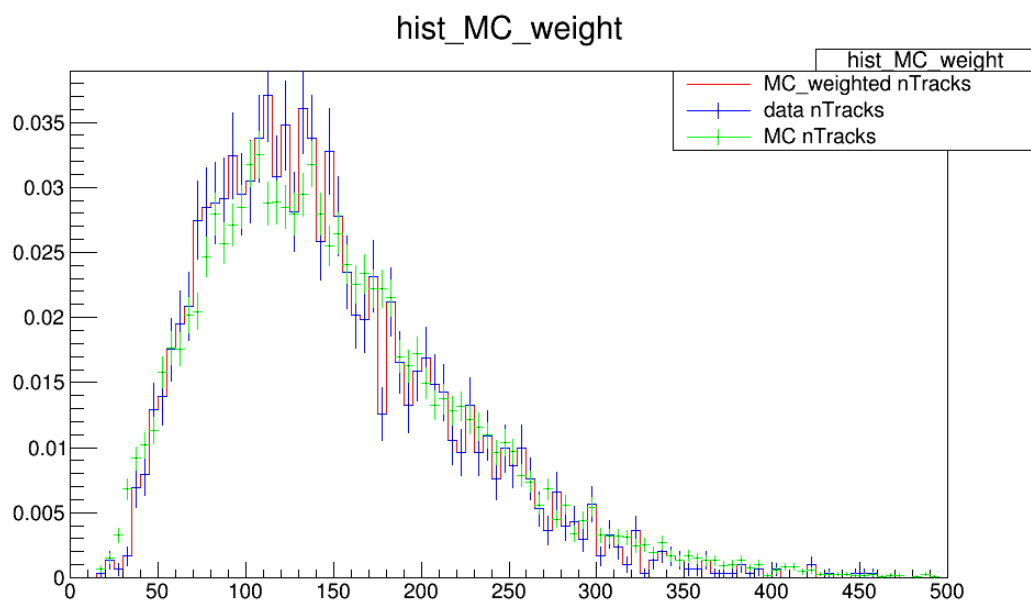
(b) Track multiplicity for LL tracks

Figure B.19: Comparison between the normalized track multiplicity before and after reweighting for LL tracks and particle types using the data of 2012. The blue color represents the side-band-subtracted data and the MC is represented by the green color. The red color represents the re-weighted MC events.

B.4   Unfolded Figures

B.4.1 2011 - DD - particles
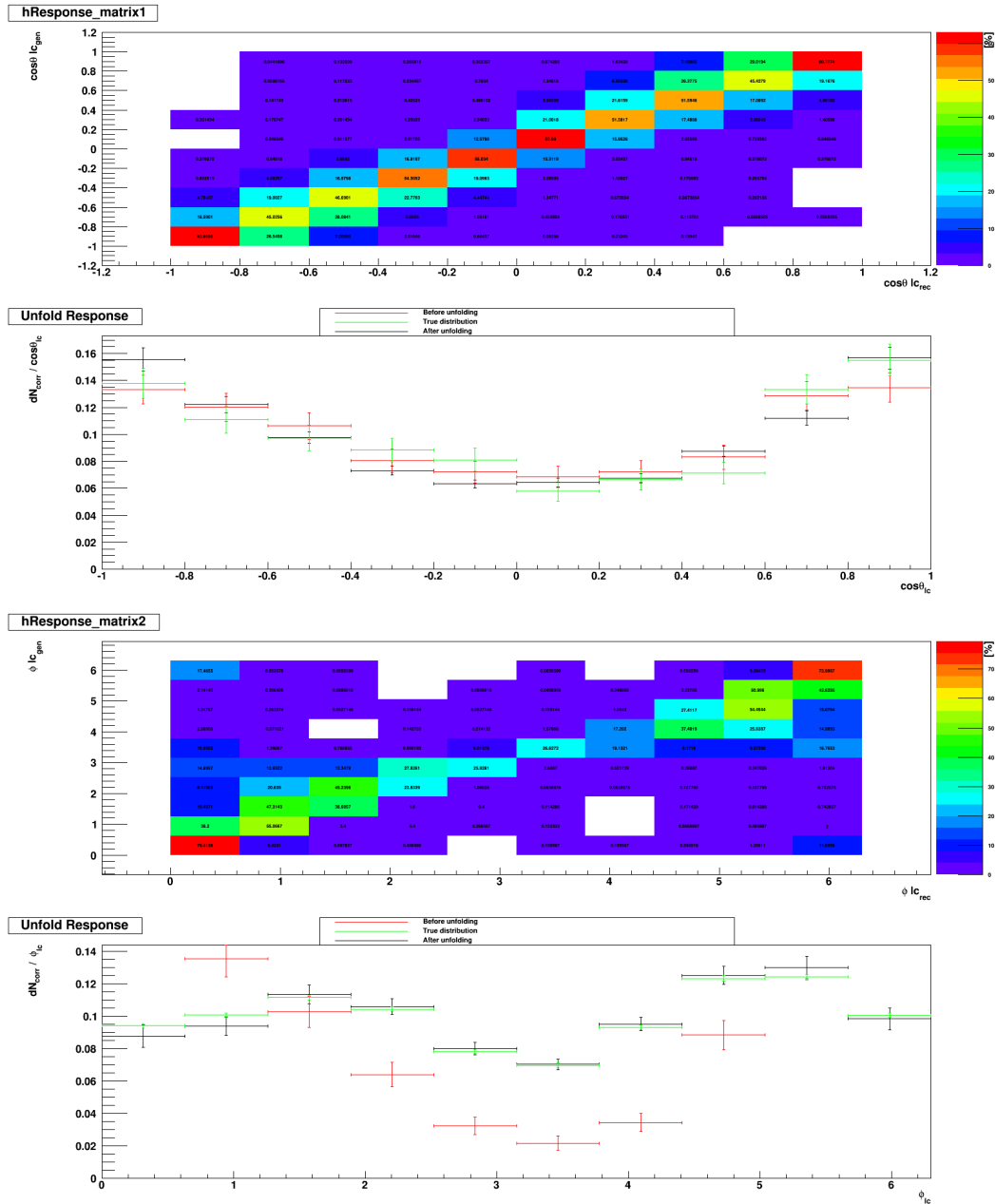
Figure B.20: The angular distributions spectra $\cos\theta$(up) and ϕ(down) of Λ_c^+ in Λ_b^0 rest frame.
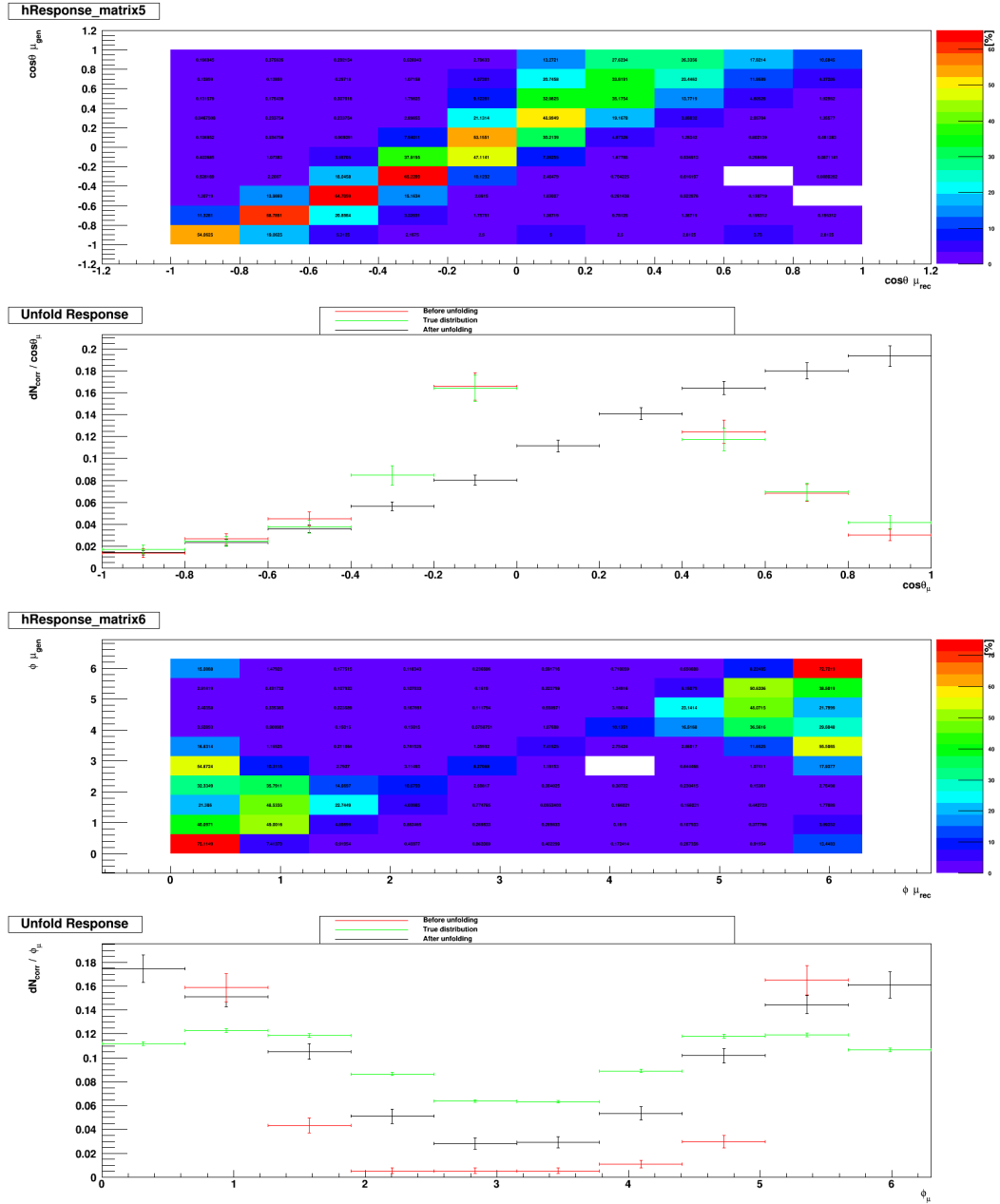
Figure B.21: The angular distributions spectra $\cos\theta$(up) and ϕ(down) of μ in W^*-boson rest frame.
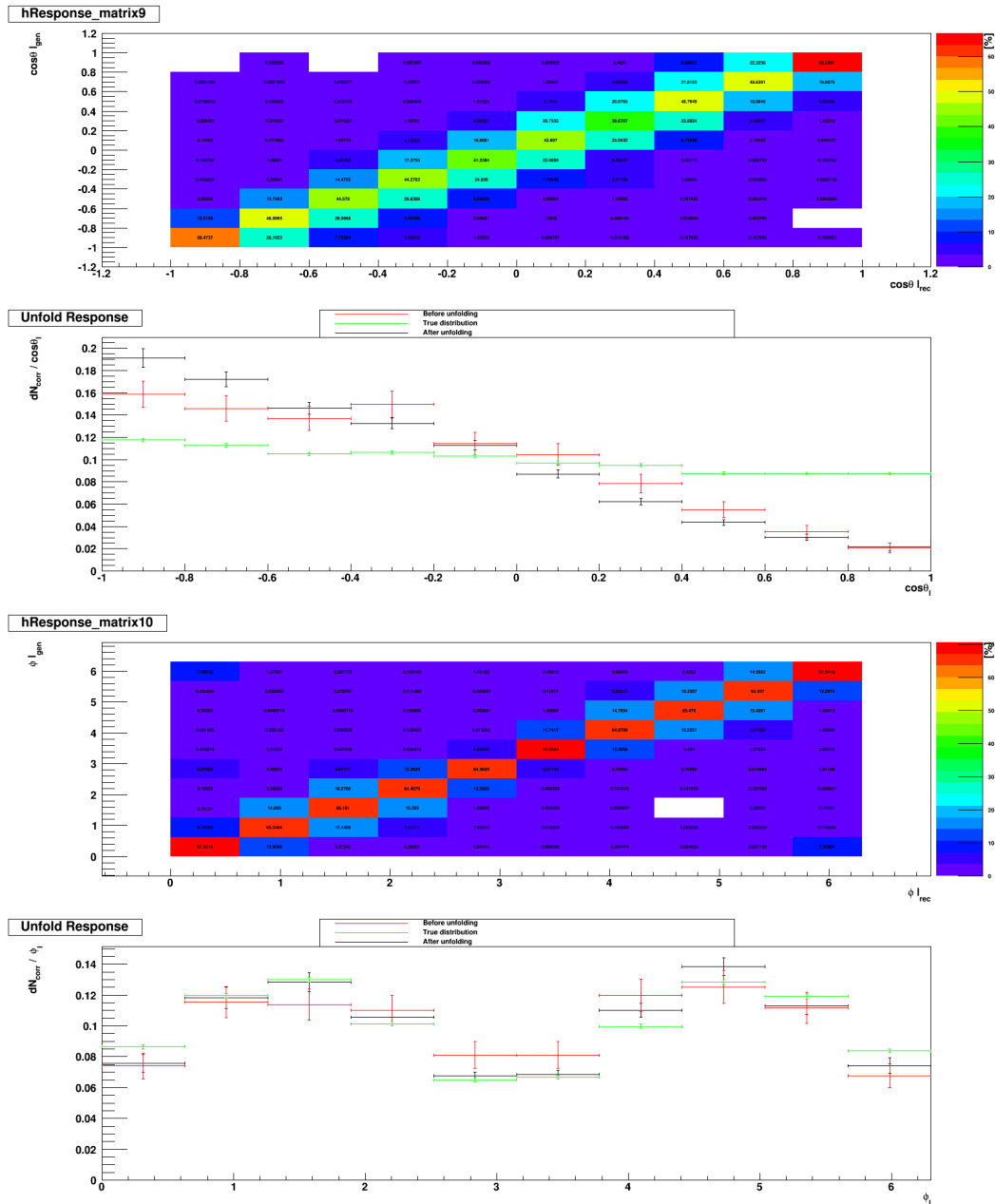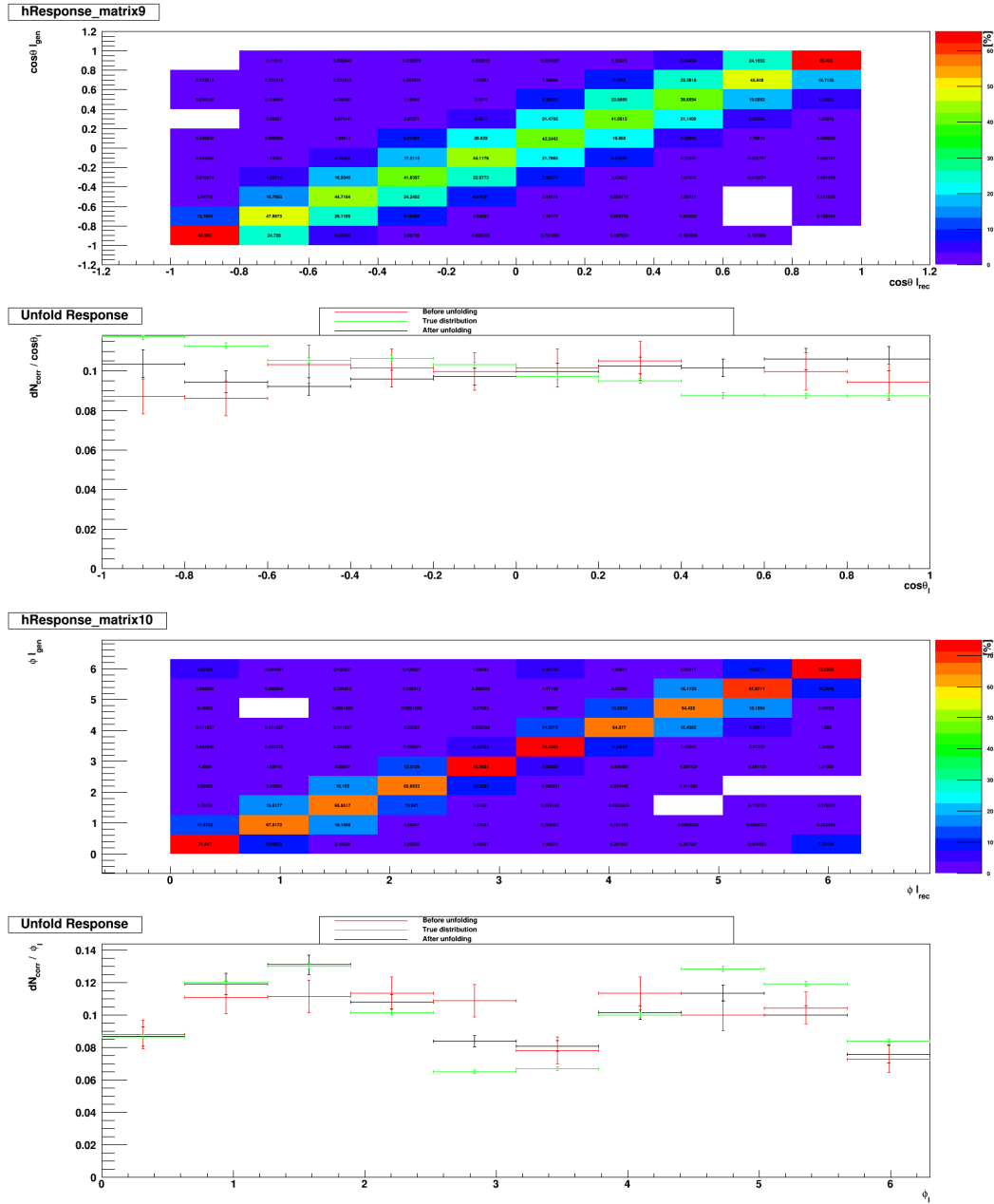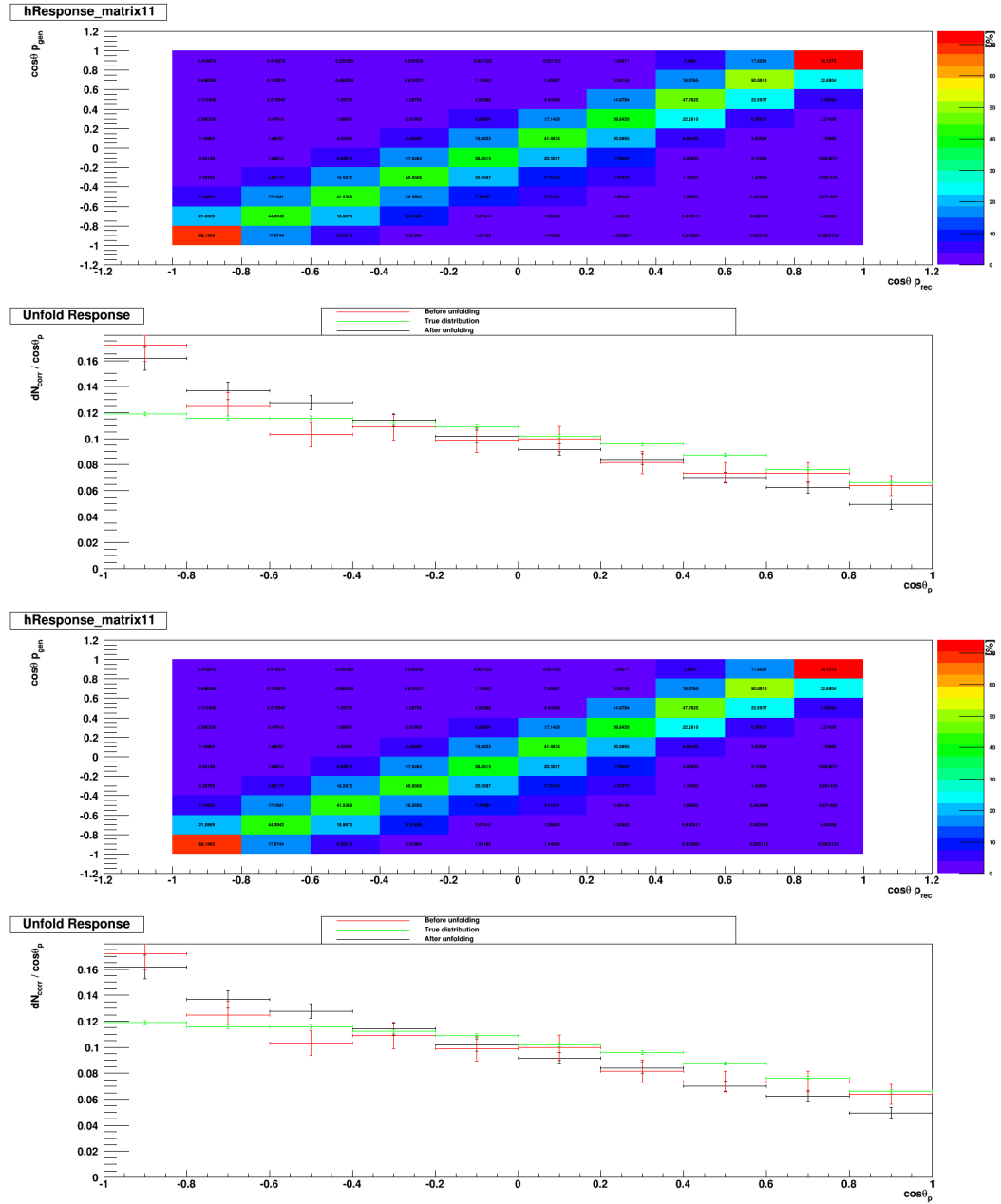
Figure B.22: The angular distributions spectra $\cos\theta$(up) and ϕ(down) of Λ in Λ_c^+ rest frame.
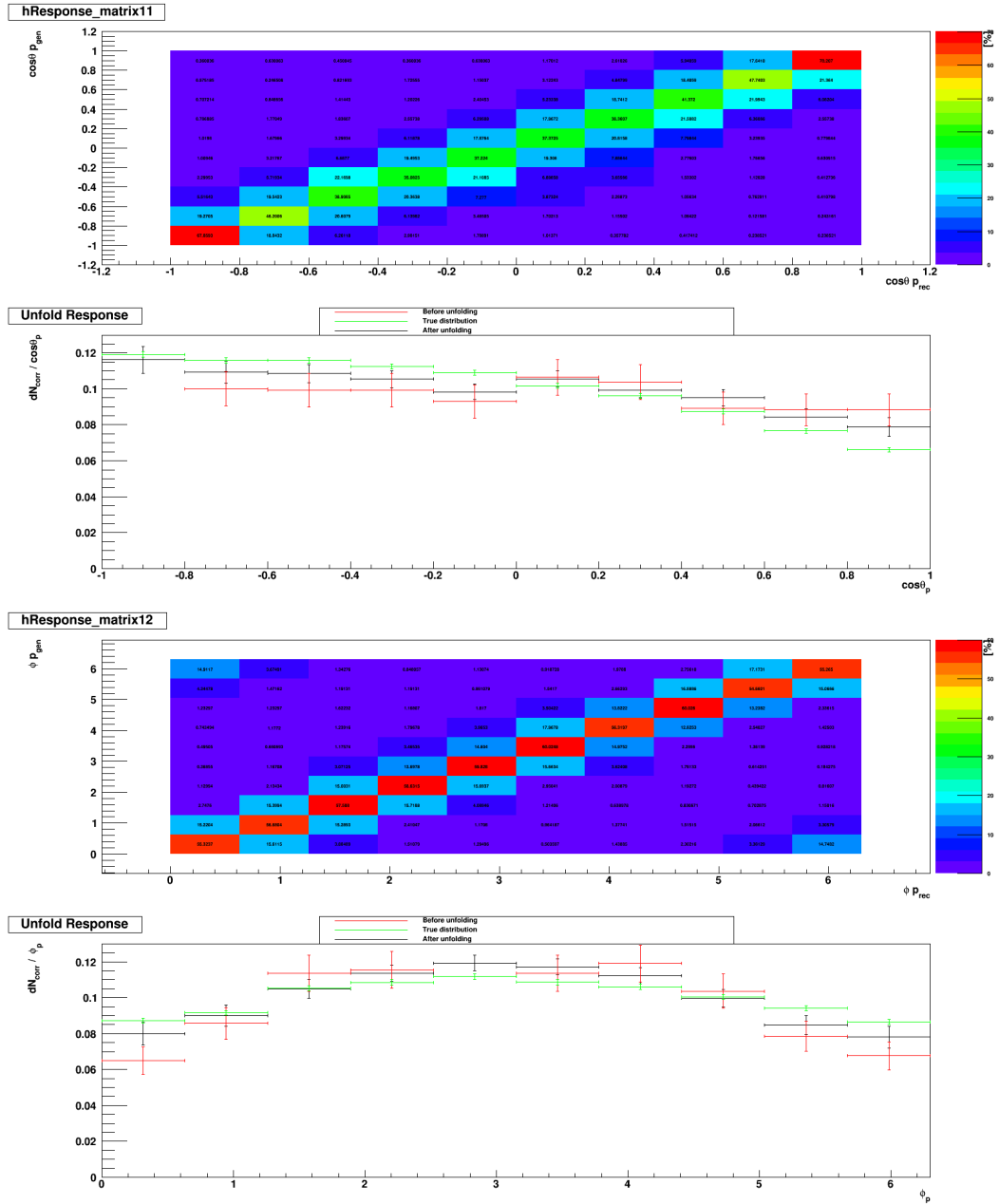
Figure B.23: The angular distributions spectra $\cos\theta$(up) and ϕ(down) of proton in Λ rest frame.
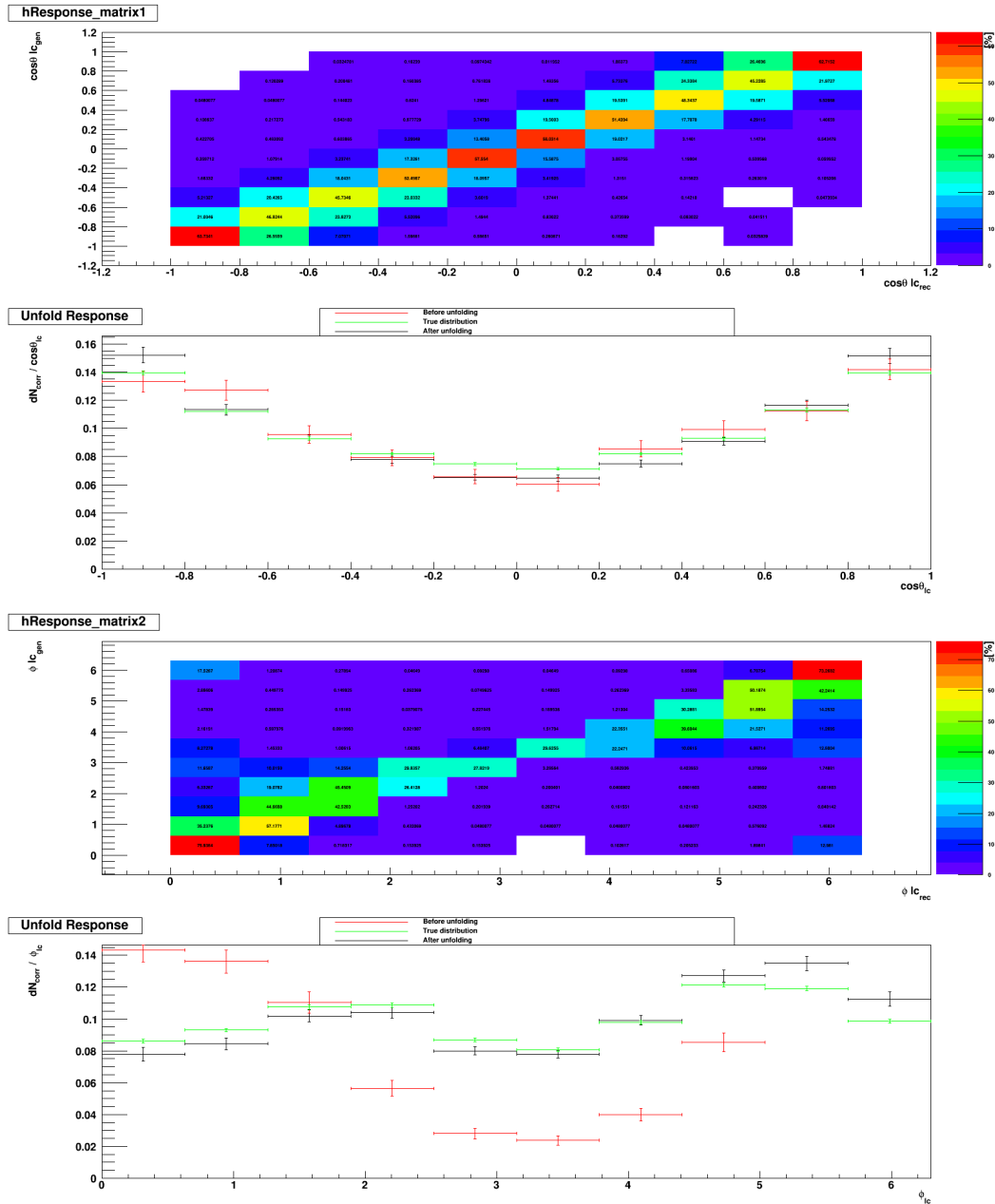
B.4.2   2011 - DD - antiparticles
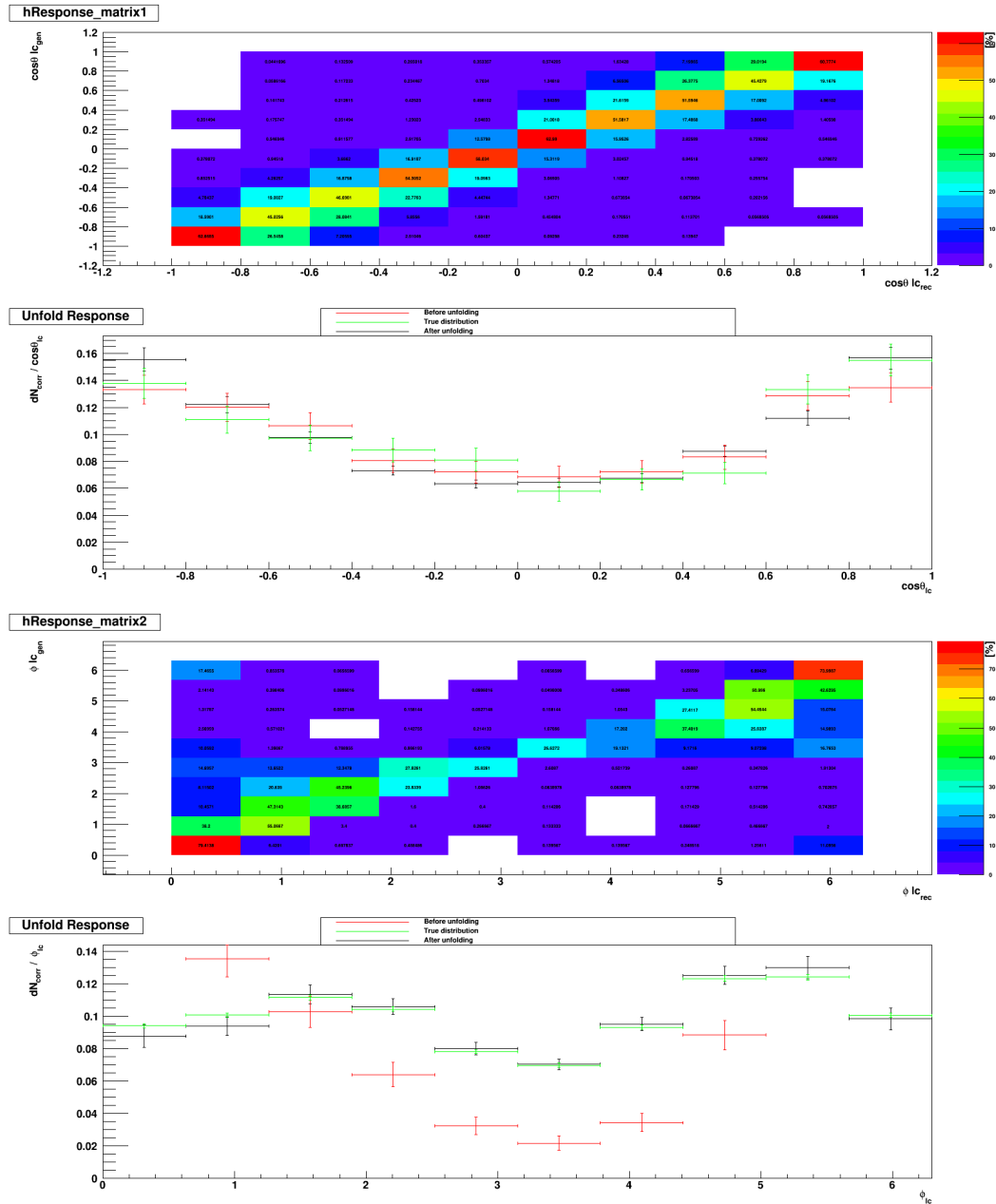
Figure B.24: The angular distributions spectra $\cos\theta$(up) and ϕ(down) of Λ_c^+ in Λ_b^0 rest frame.
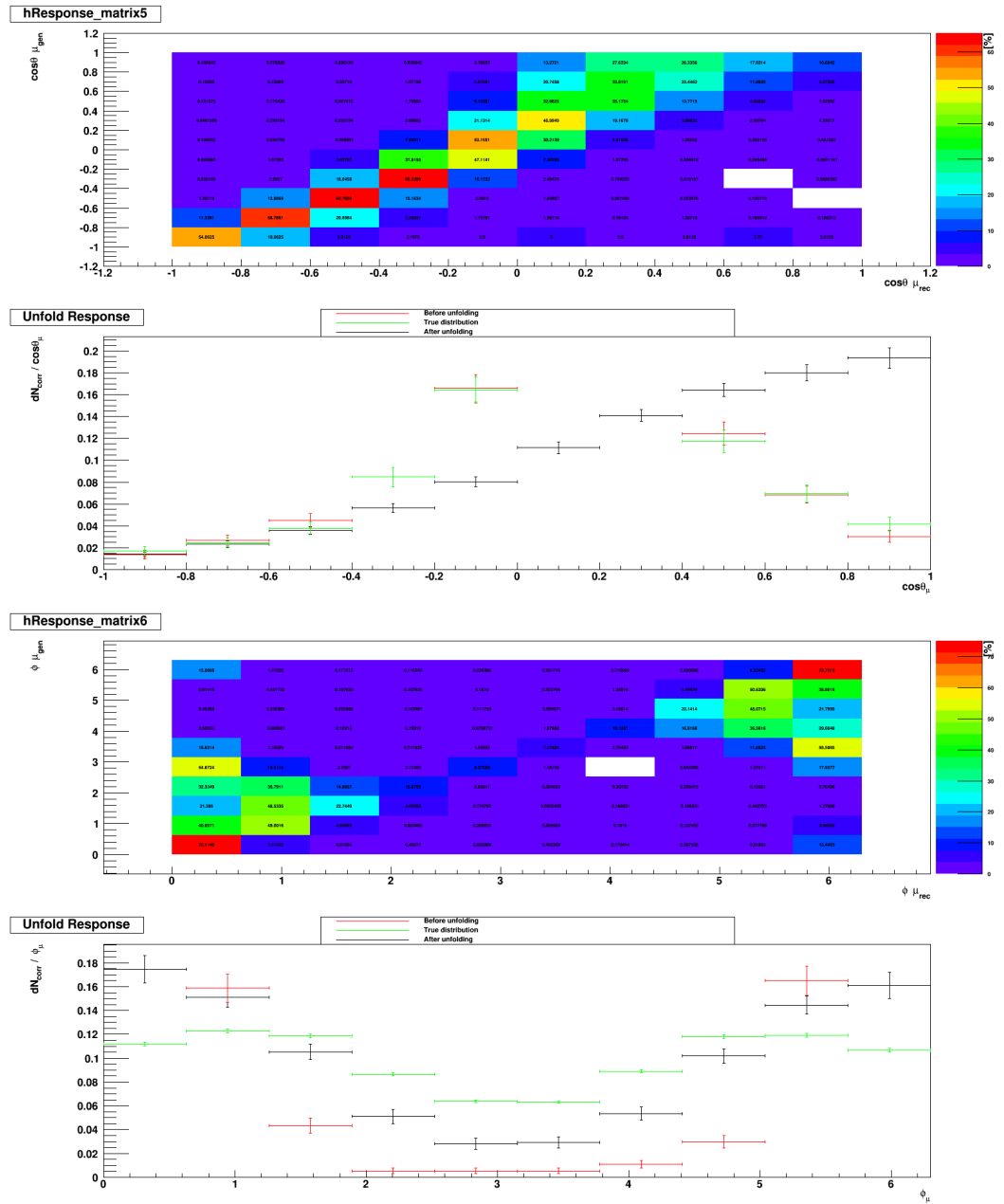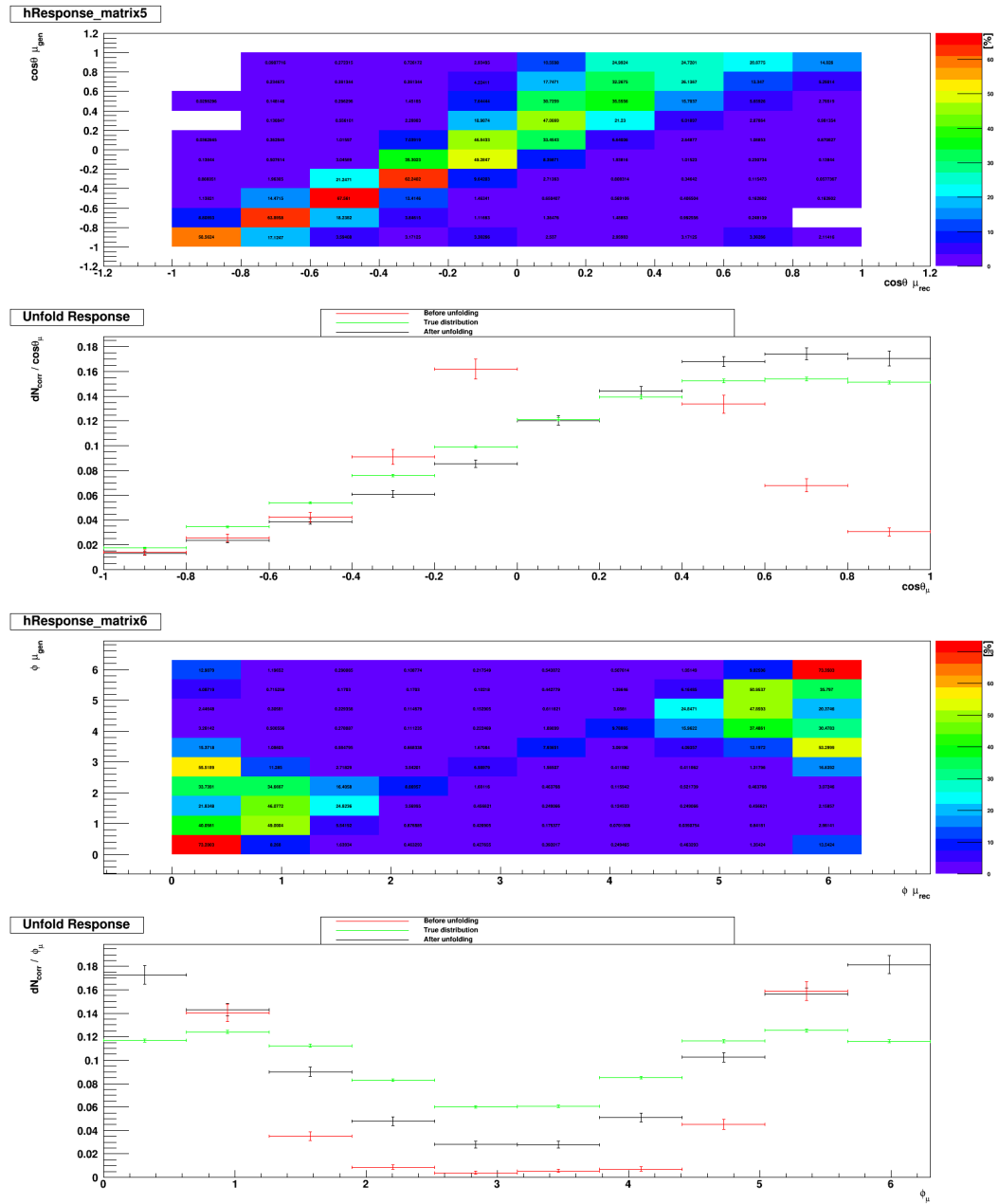
Figure B.25: The angular distributions spectra $\cos\theta$(up) and ϕ(down) of μ in W^*-boson rest frame.
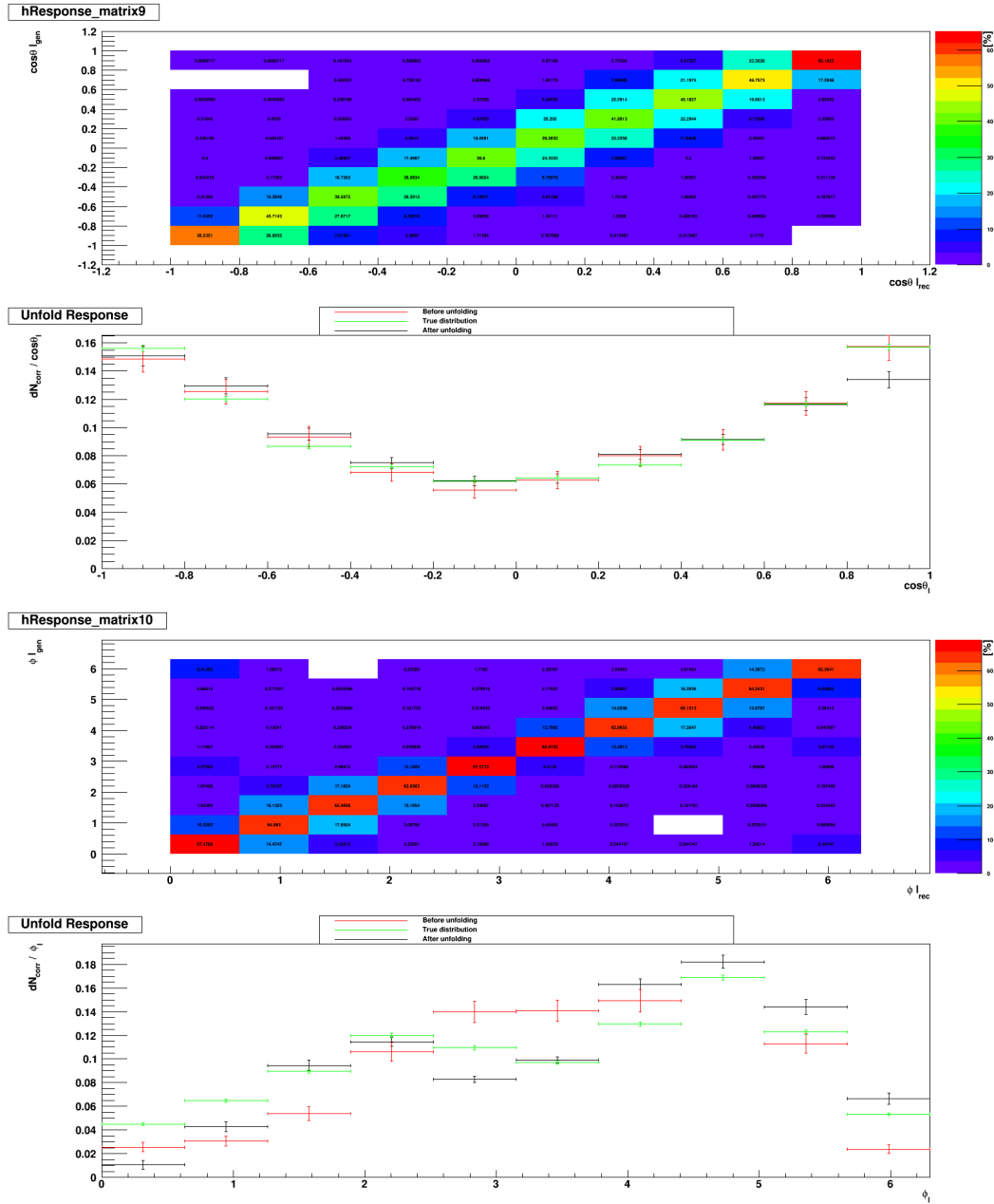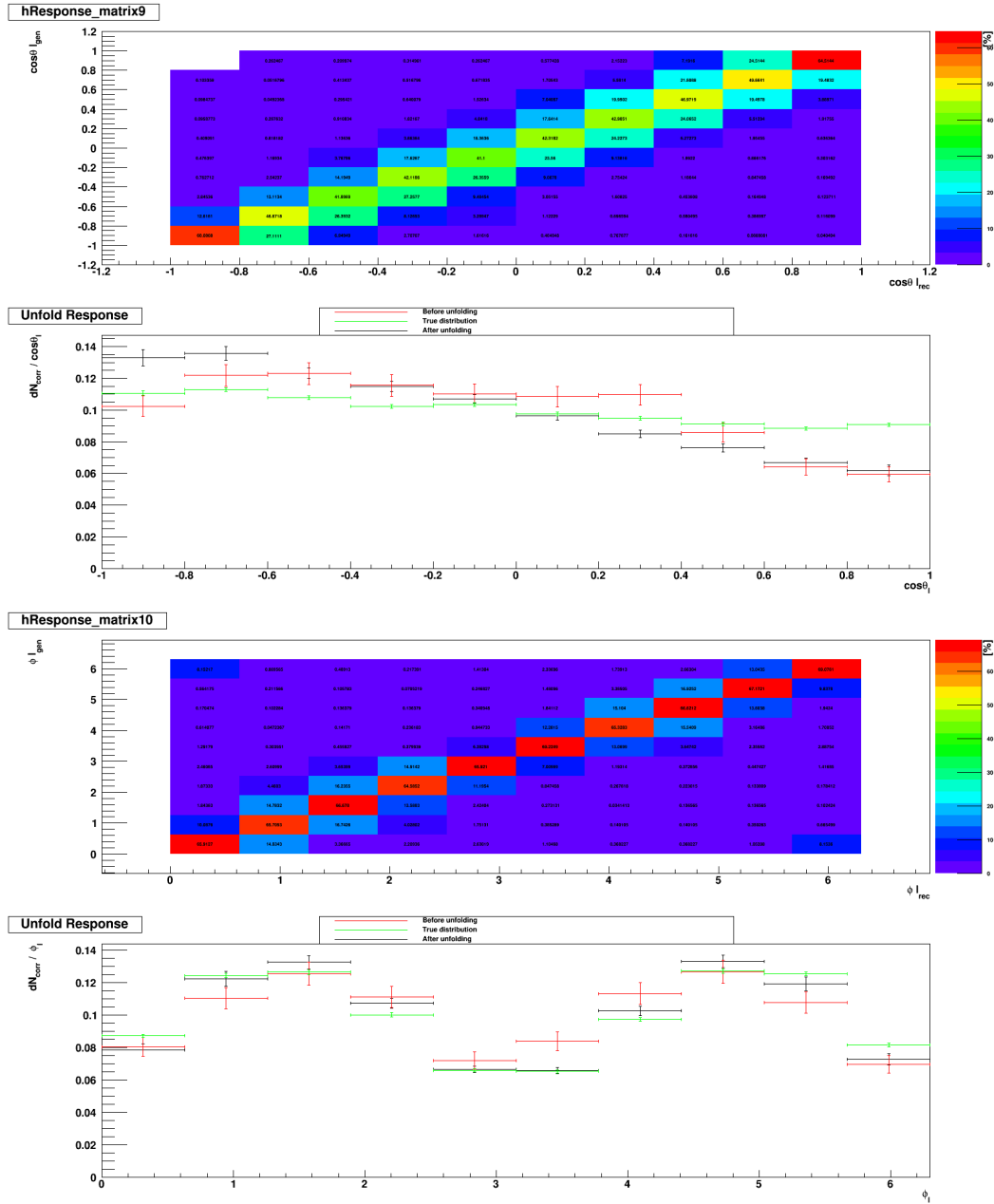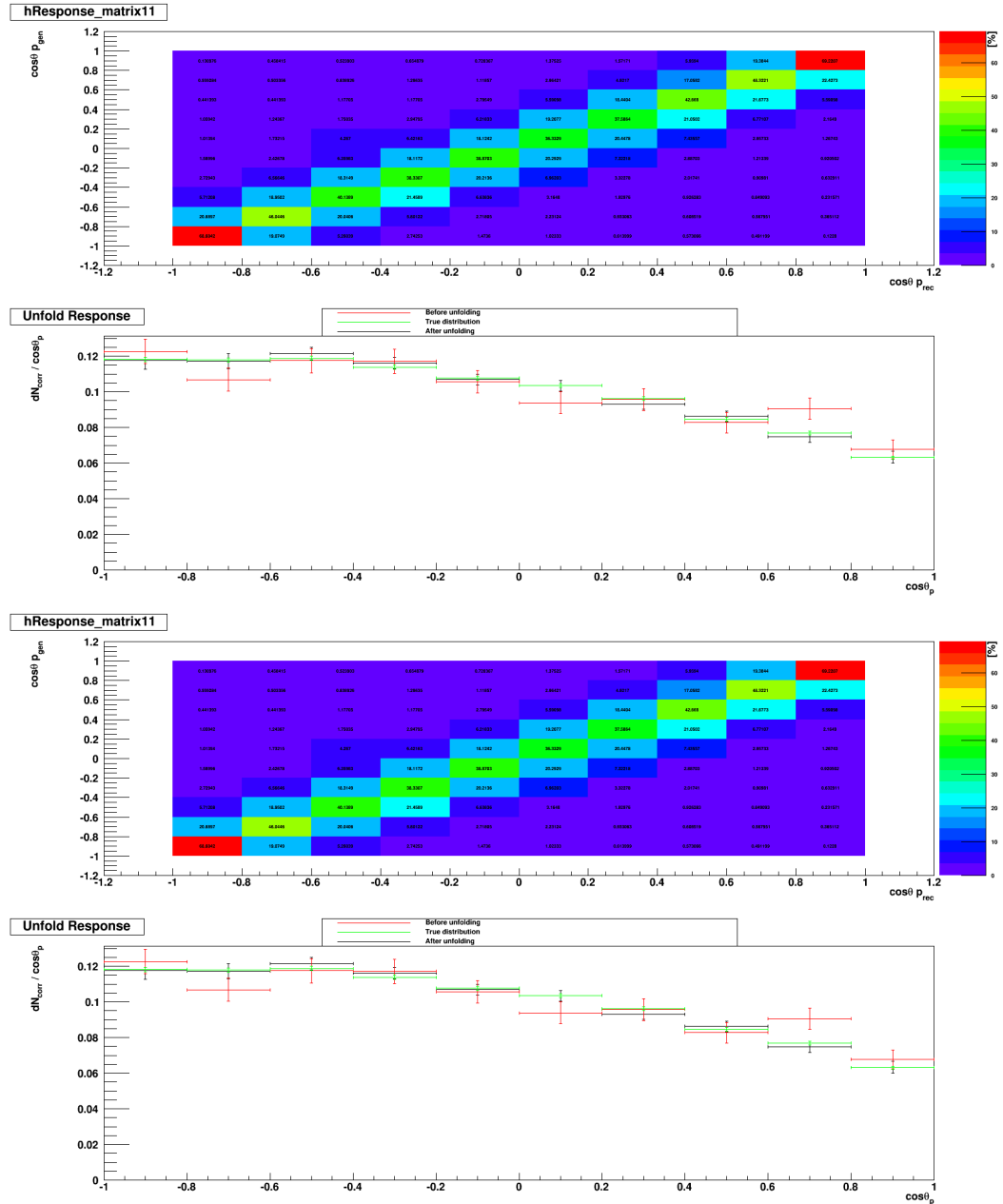
Figure B.26: The angular distributions spectra $\cos\theta$(up) and ϕ(down) of Λ in Λ_c^+ rest frame.
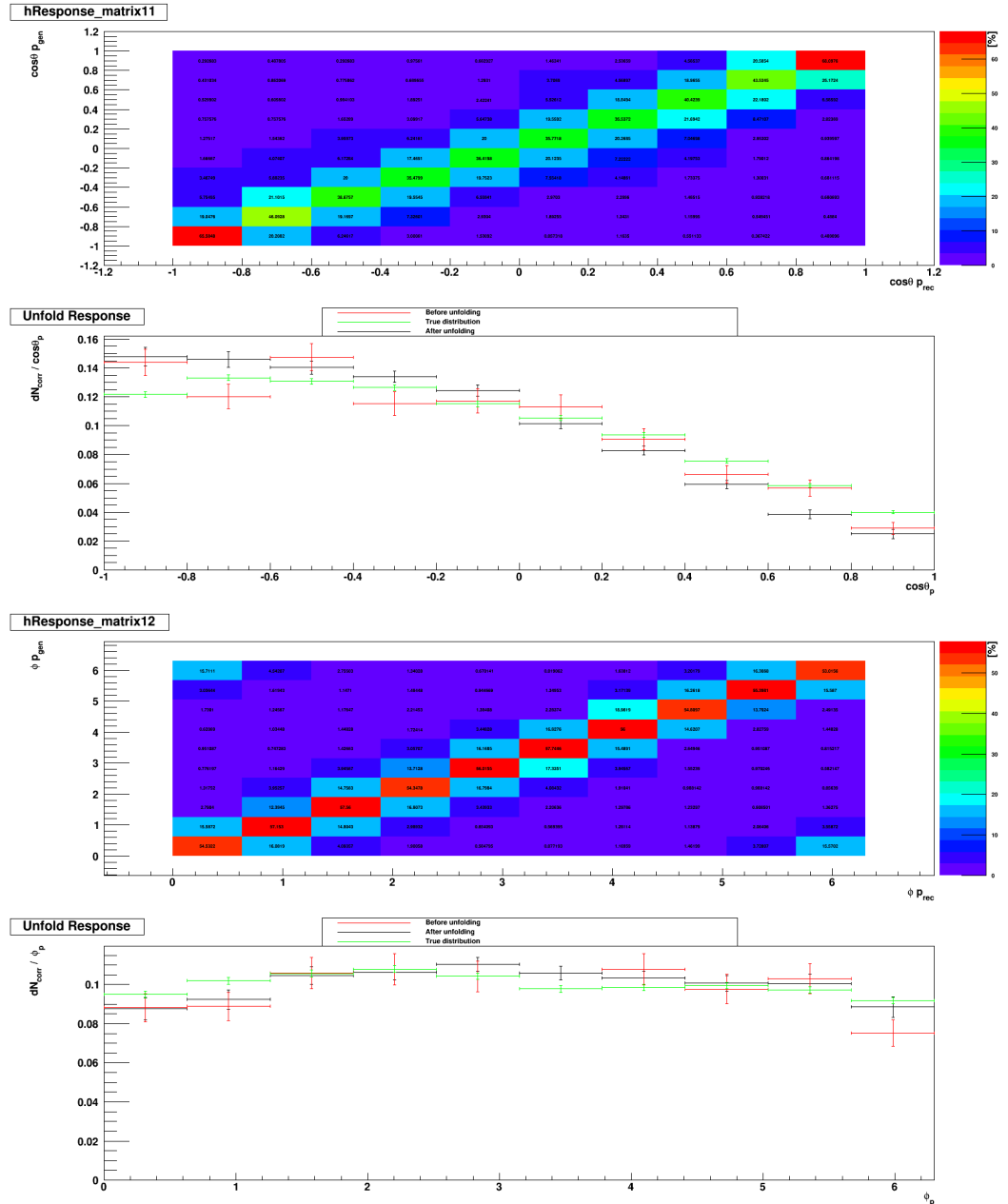
Figure B.27: The angular distributions spectra $\cos\theta$(up) and ϕ(down) of proton in Λ rest frame.

B.4.3 2011 - LL - particles
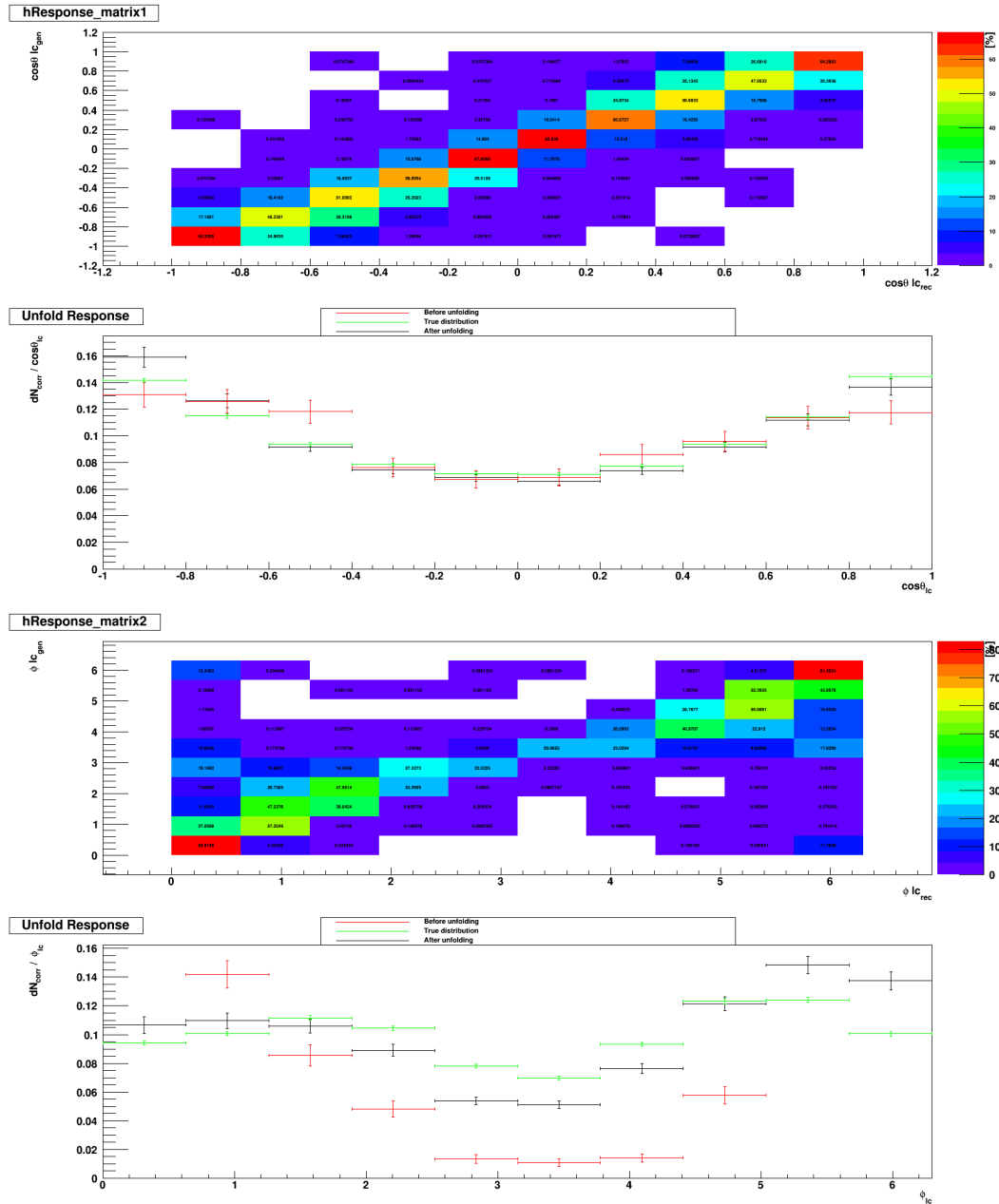
Figure B.28: The angular distributions spectra $\cos\theta$(up) and ϕ(down) of Λ_c^+ in Λ_b^0 rest frame.
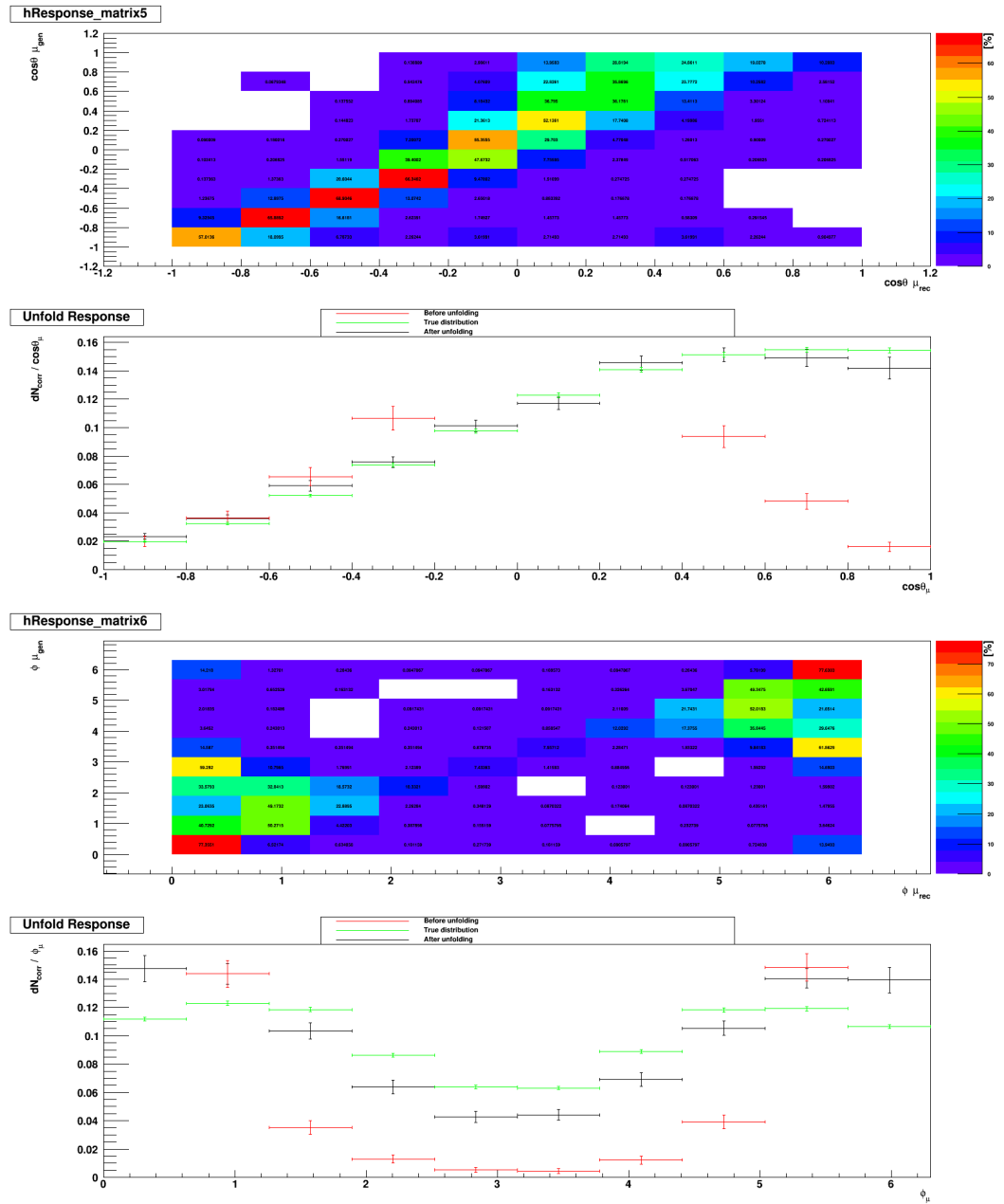
Figure B.29: The angular distributions spectra $\cos\theta$(up) and ϕ(down) of μ in W^*-boson rest frame.
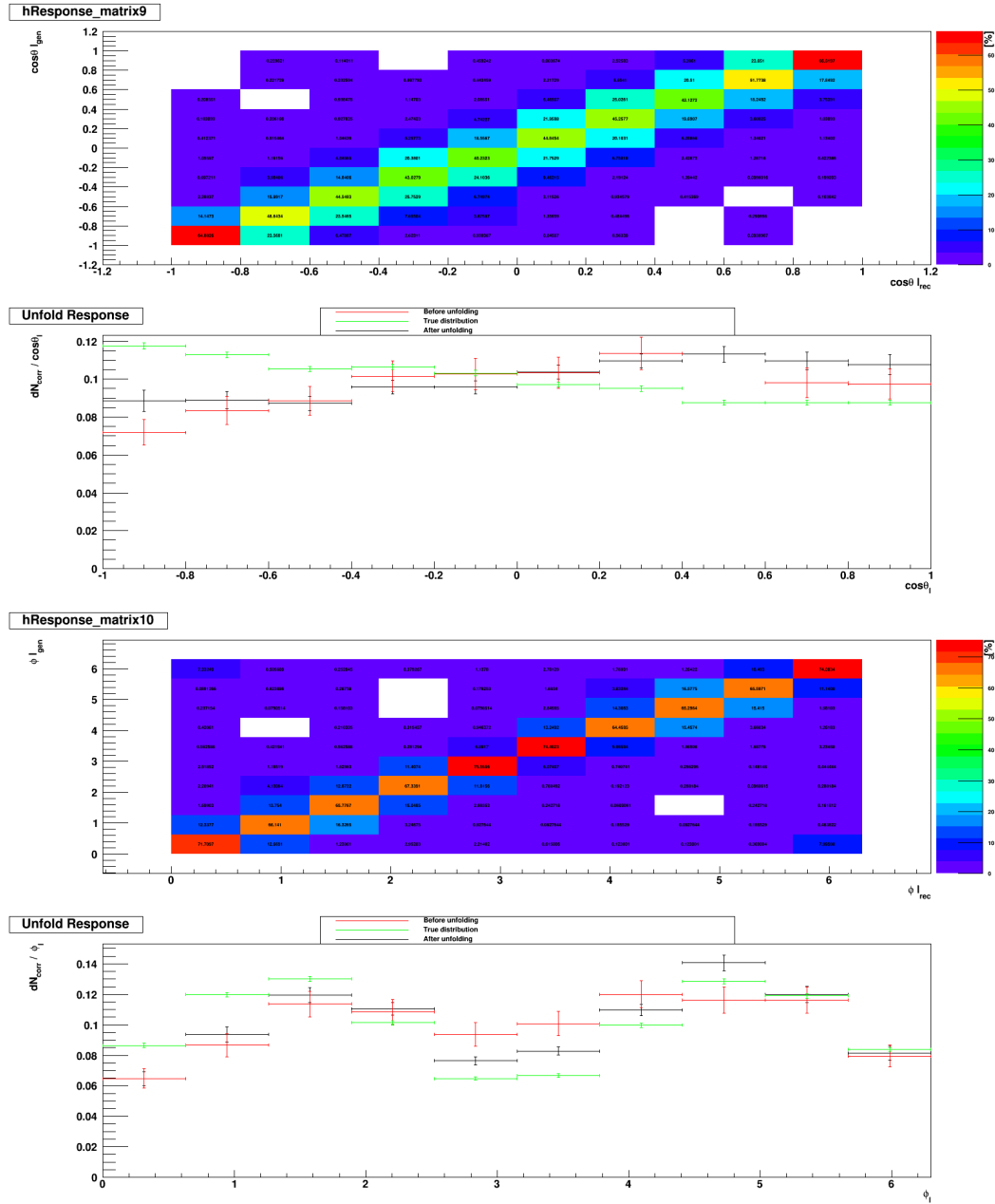
Figure B.30: The angular distributions spectra $\cos\theta$(up) and ϕ(down) of Λ in Λ_c^+ rest frame.
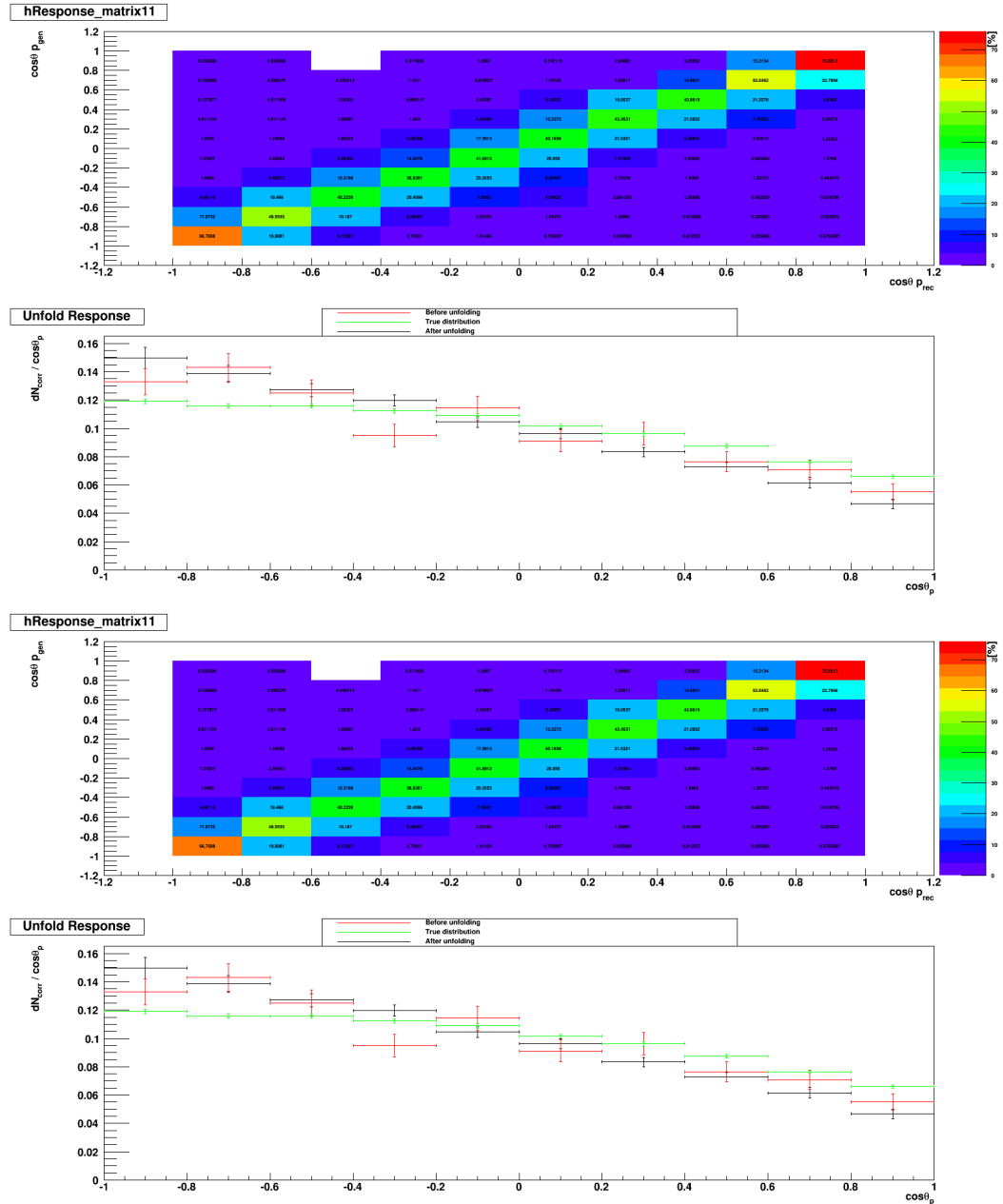
Figure B.31: The angular distributions spectra $\cos\theta$(up) and ϕ(down) of proton in Λ rest frame.
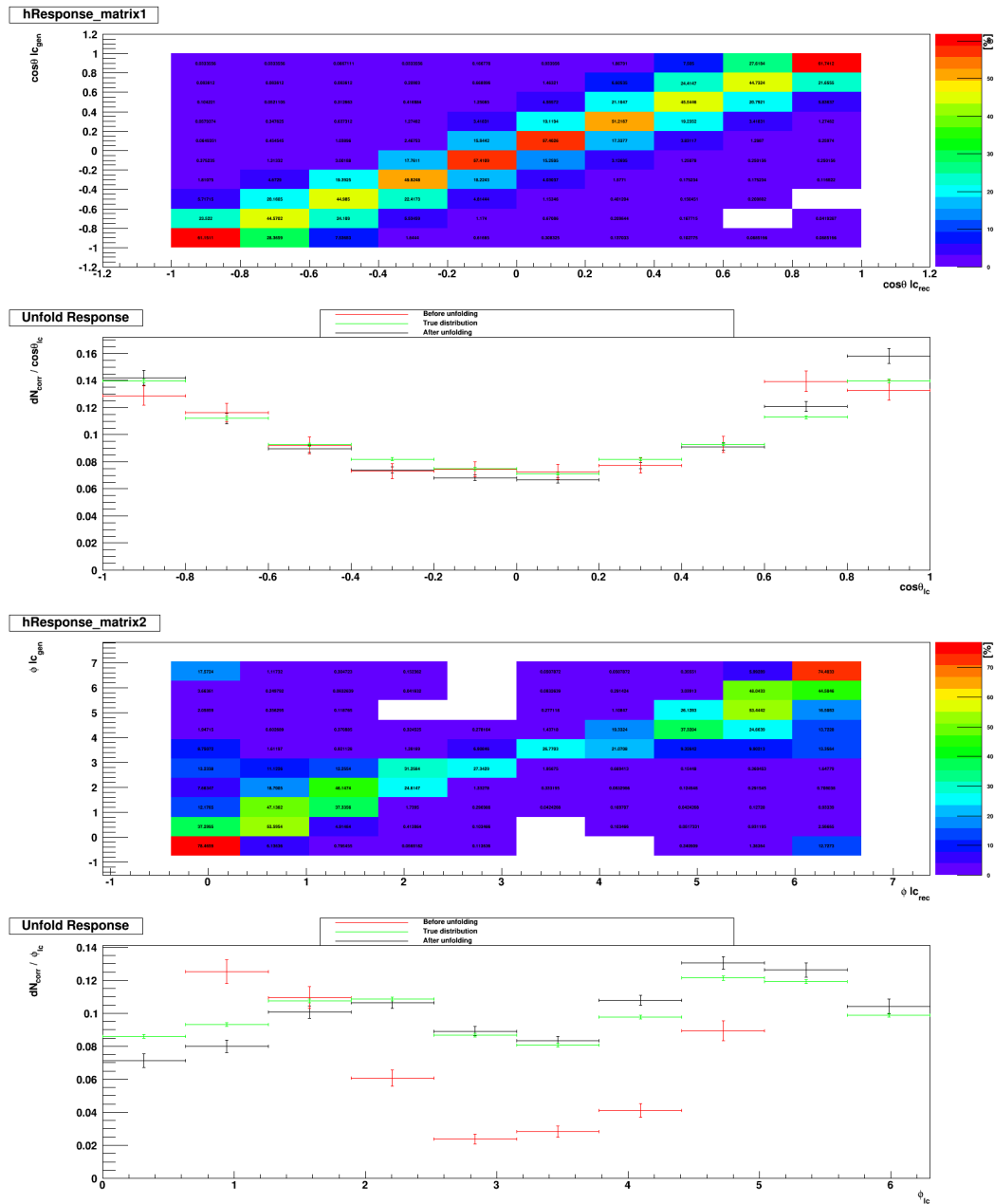
B.4.4   2011 - LL - antiparticles
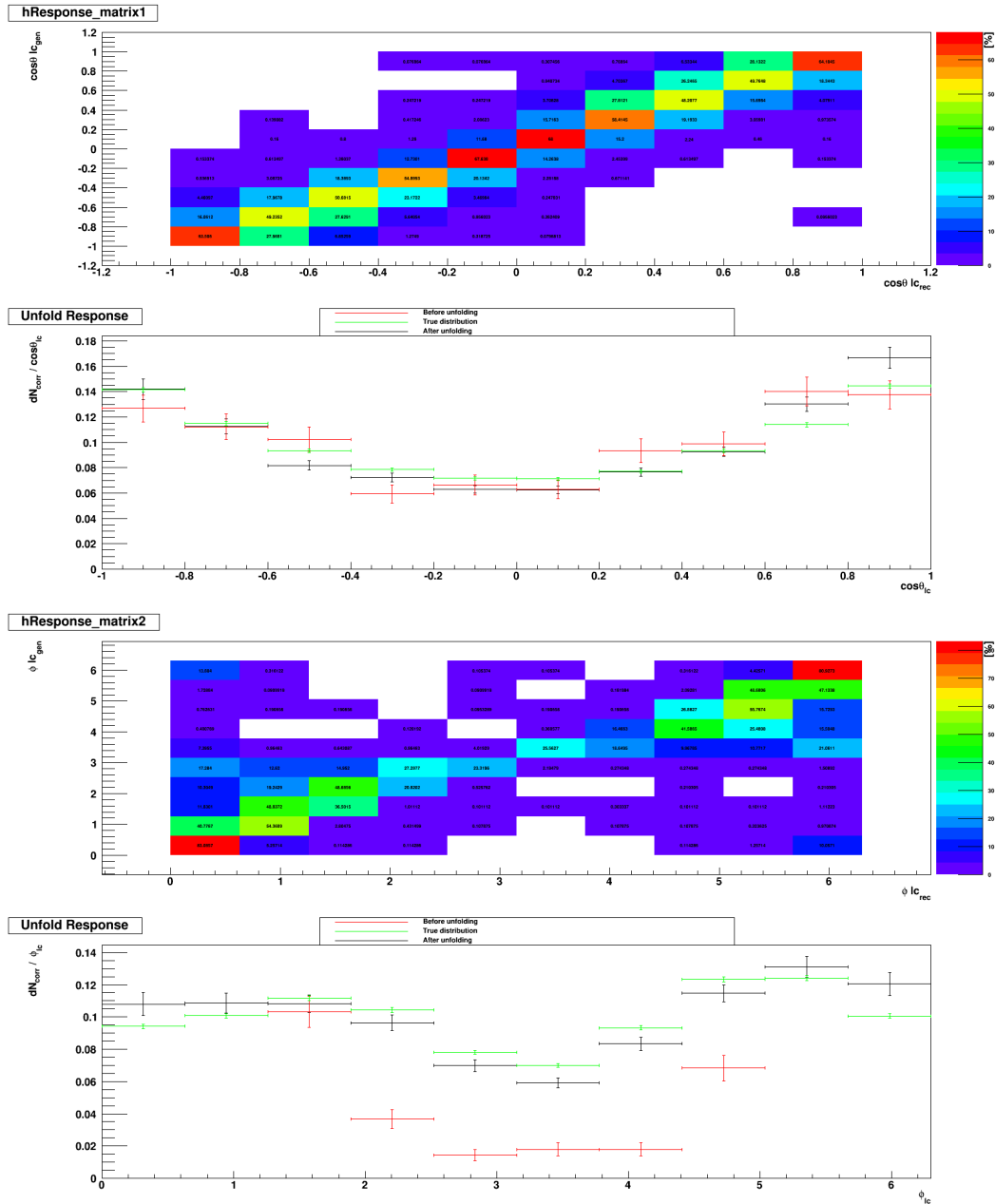
Figure B.32: The angular distributions spectra $\cos\theta$(up) and ϕ(down) of Λ_c^+ in Λ_b^0 rest frame.
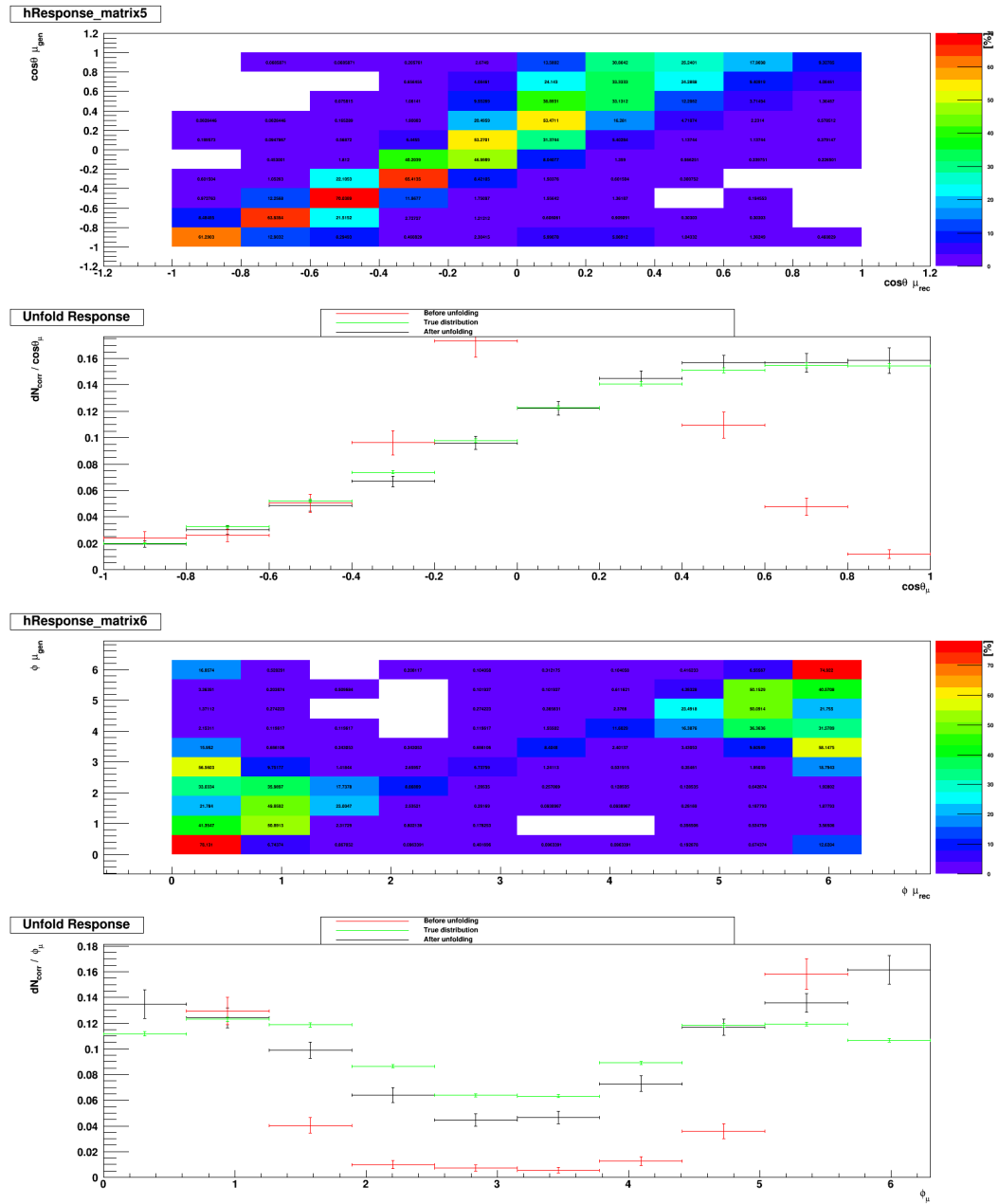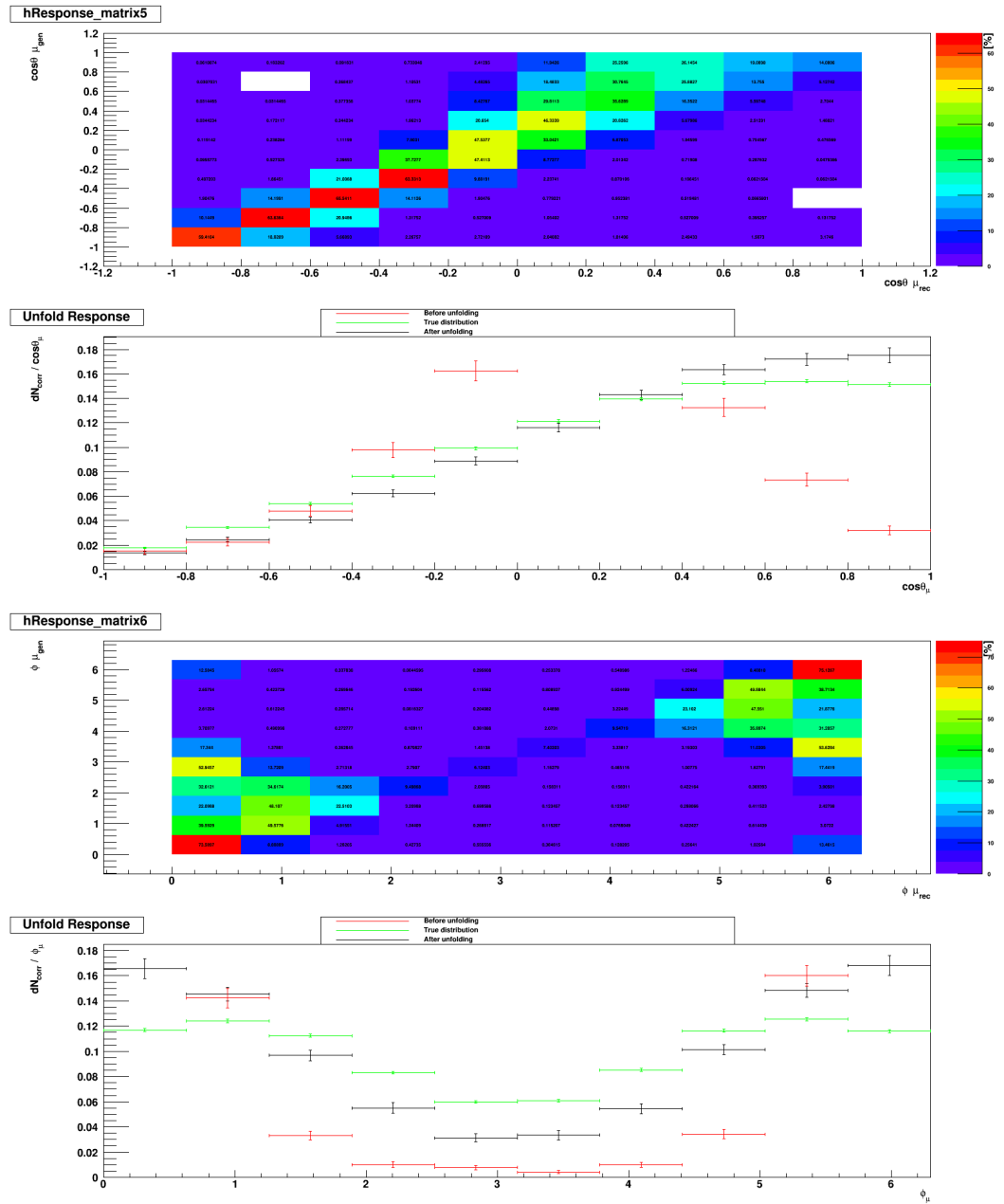
Figure B.33: The angular distributions spectra $\cos\theta$(up) and ϕ(down) of μ in W^*-boson rest frame.
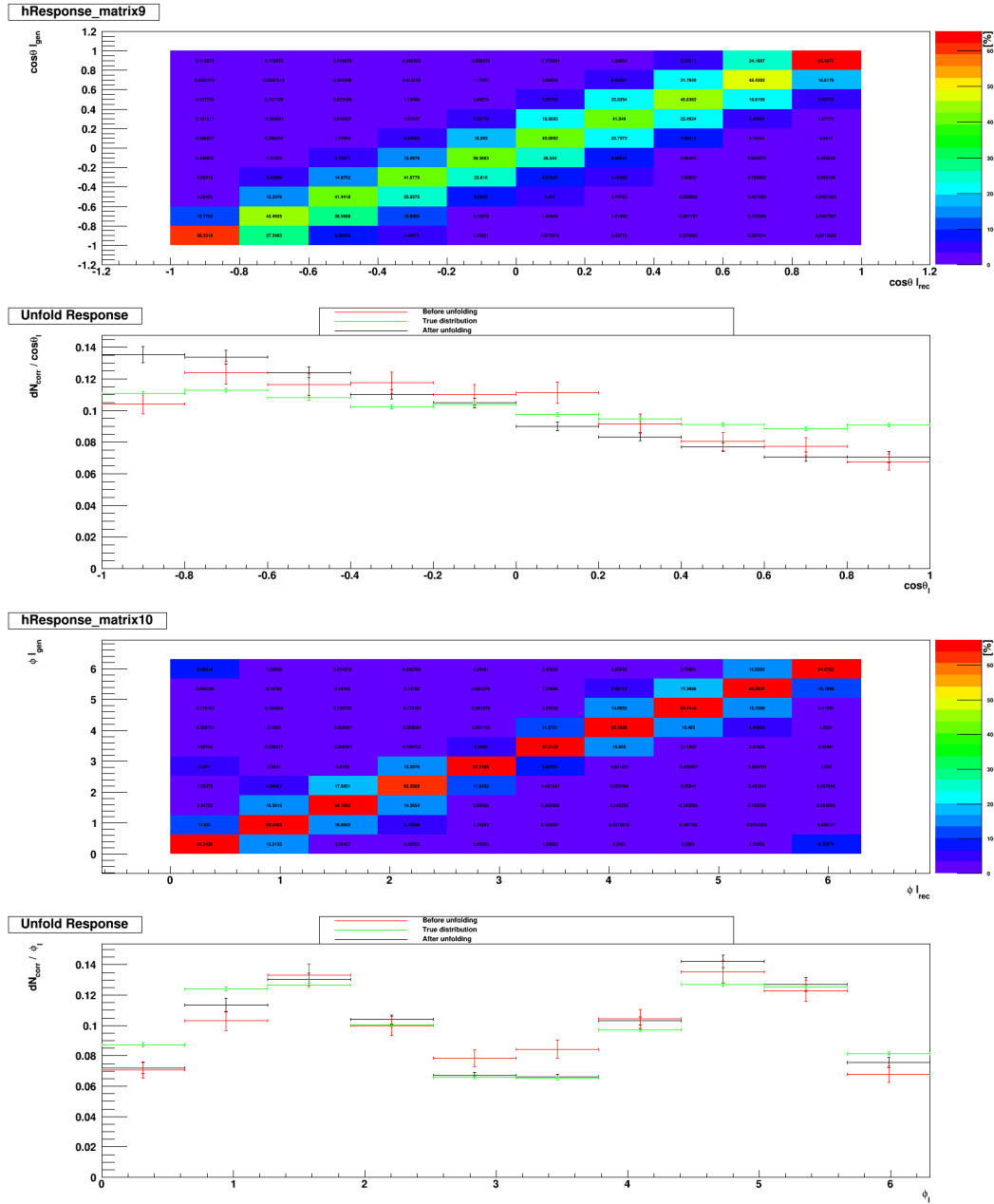
Figure B.34: The angular distributions spectra $\cos\theta$(up) and ϕ(down) of Λ in Λ_c^+ rest frame.

Figure B.35: The angular distributions spectra $\cos\theta$(up) and ϕ(down) of proton in Λ rest frame.

B.4.5   2012 - DD - particles

Figure B.36: The angular distributions spectra $\cos\theta$(up) and ϕ(down) of Λ_c^+ in Λ_b^0 rest frame.

Figure B.37: The angular distributions spectra $\cos\theta$(up) and ϕ(down) of μ in W^*-boson rest frame.
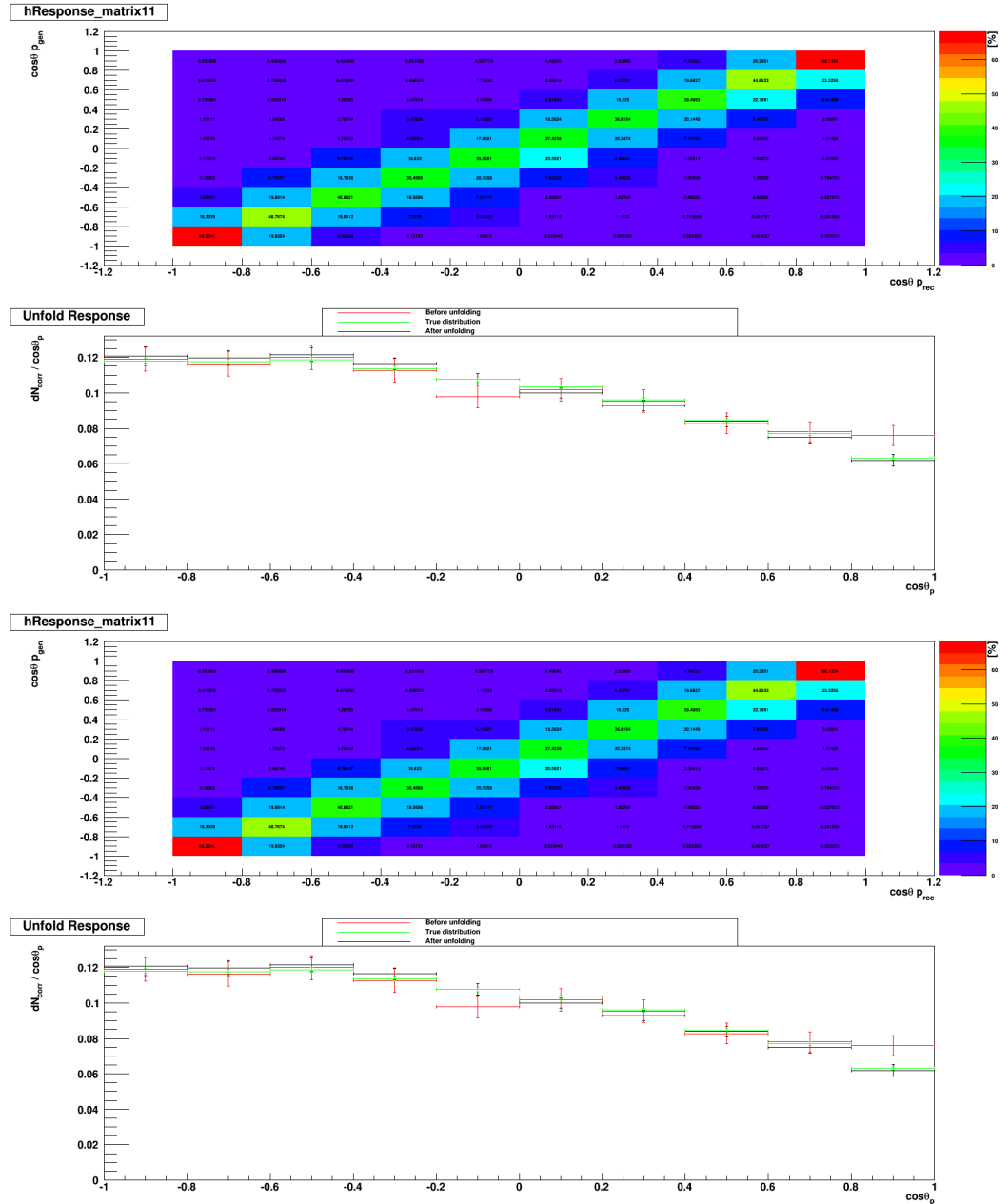
Figure B.38: The angular distributions spectra $\cos\theta$(up) and ϕ(down) of Λ in Λ_c^+ rest frame.

Figure B.39: The angular distributions spectra $\cos\theta$(up) and ϕ(down) of proton in Λ rest frame.
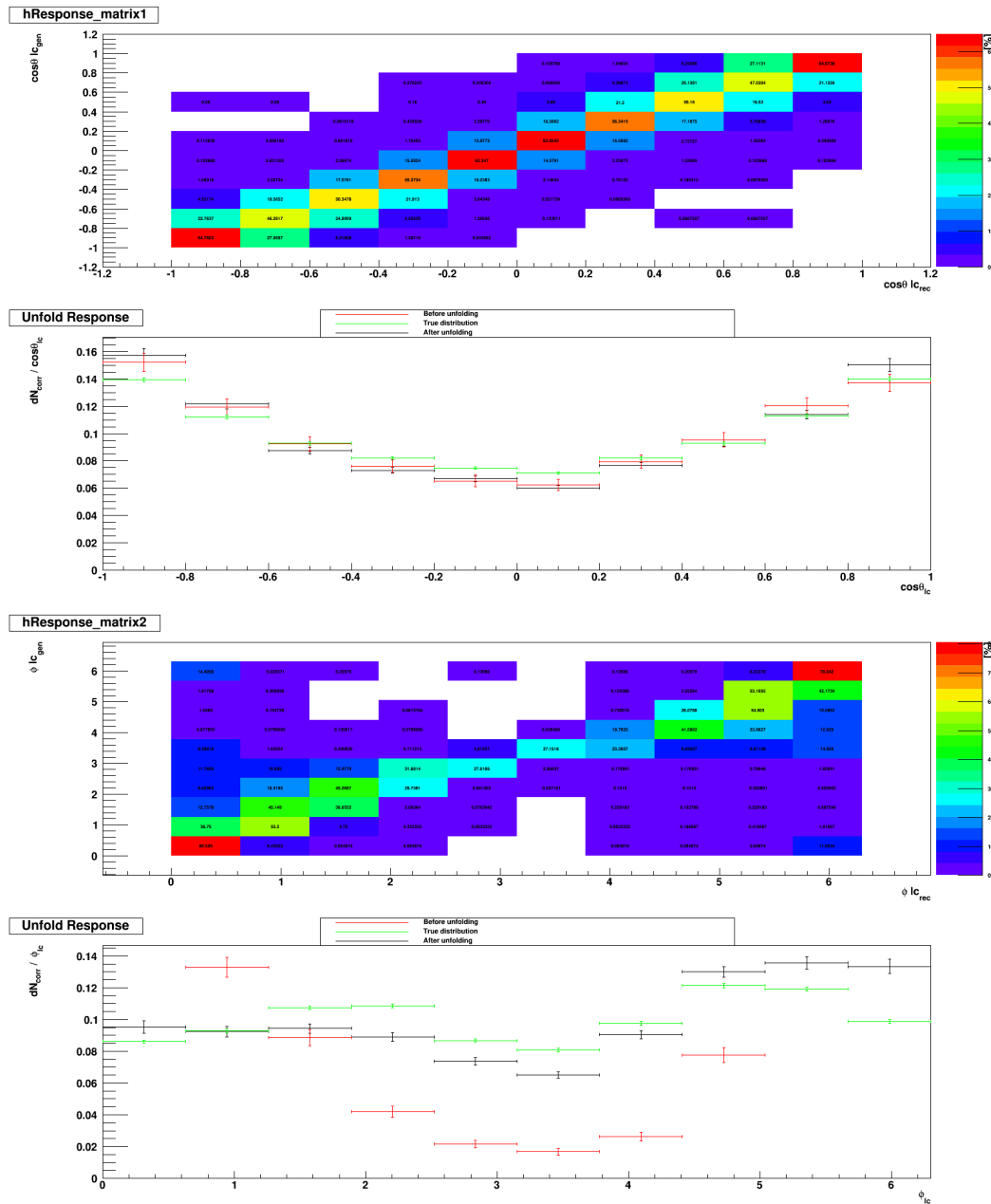
B.4.6   2012 - DD - antiparticles

Figure B.40: The angular distributions spectra $\cos\theta$(up) and ϕ(down) of Λ_c^+ in Λ_b^0 rest frame.
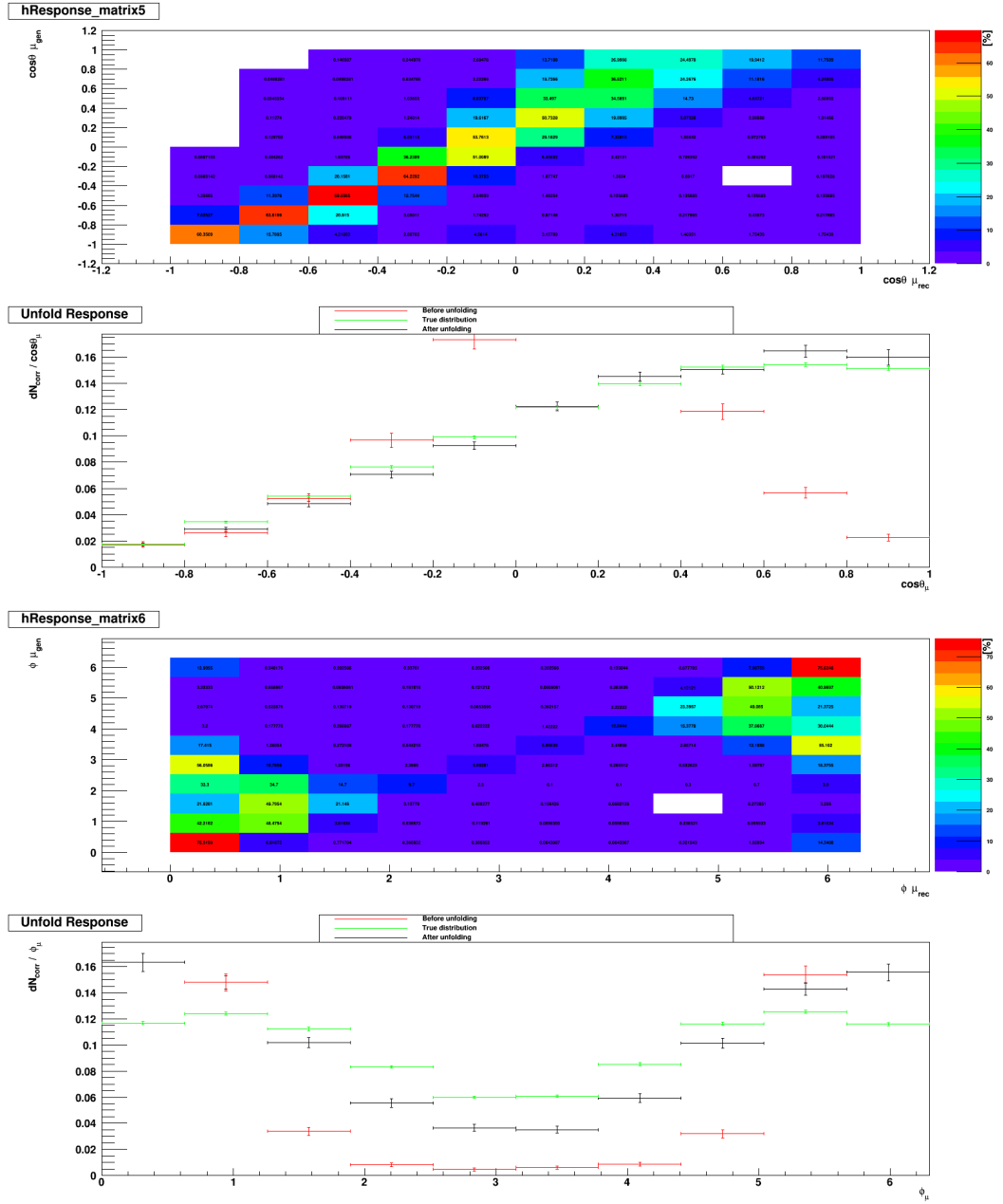
Figure B.41: The angular distributions spectra $\cos\theta$(up) and ϕ(down) of μ in W^*-boson rest frame.
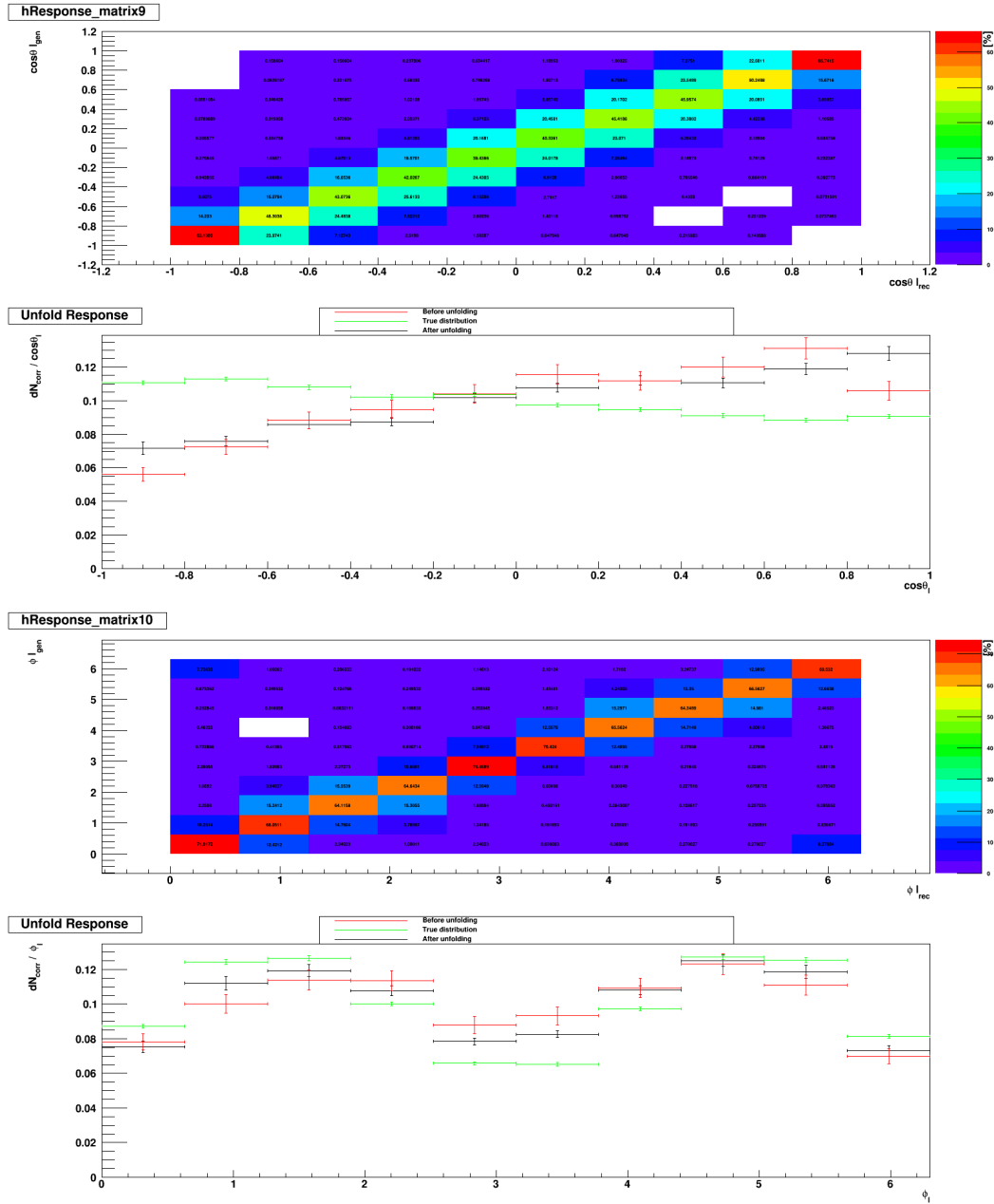
Figure B.42: The angular distributions spectra $\cos\theta$(up) and ϕ(down) of Λ in Λ_c^+ rest frame.

Figure B.43: The angular distributions spectra $\cos\theta$(up) and ϕ(down) of proton in Λ rest frame.

B.4.7   2012 - LL - particles

Figure B.44: The angular distributions spectra $\cos\theta$(up) and ϕ(down) of Λ_c^+ in Λ_b^0 rest frame.

Figure B.45: The angular distributions spectra $\cos\theta$(up) and ϕ(down) of μ in W^*-boson rest frame.
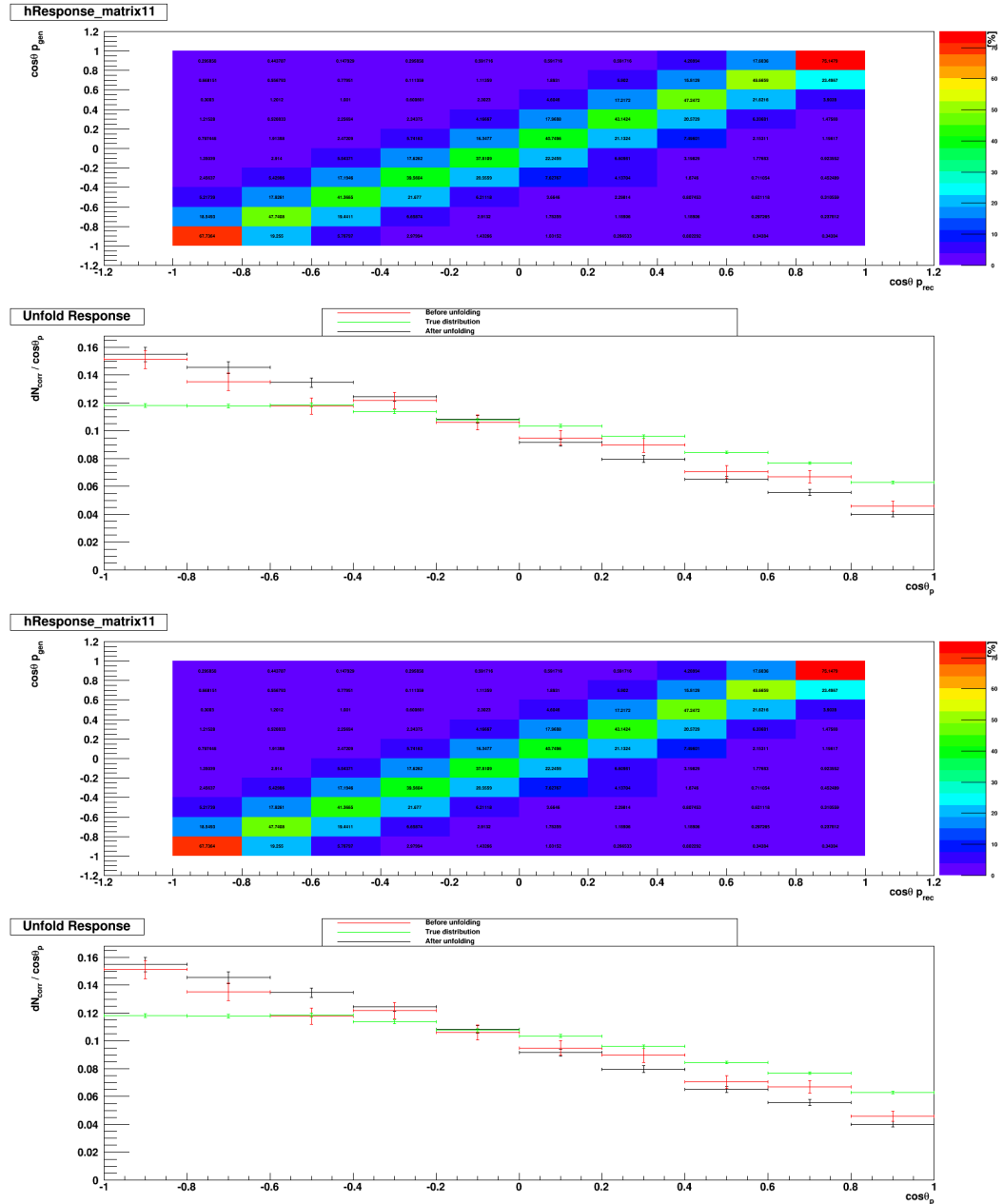
Figure B.46: The angular distributions spectra $\cos\theta$(up) and ϕ(down) of Λ in Λ_c^+ rest frame.

Figure B.47: The angular distributions spectra $\cos\theta$(up) and ϕ(down) of proton in Λ rest frame.
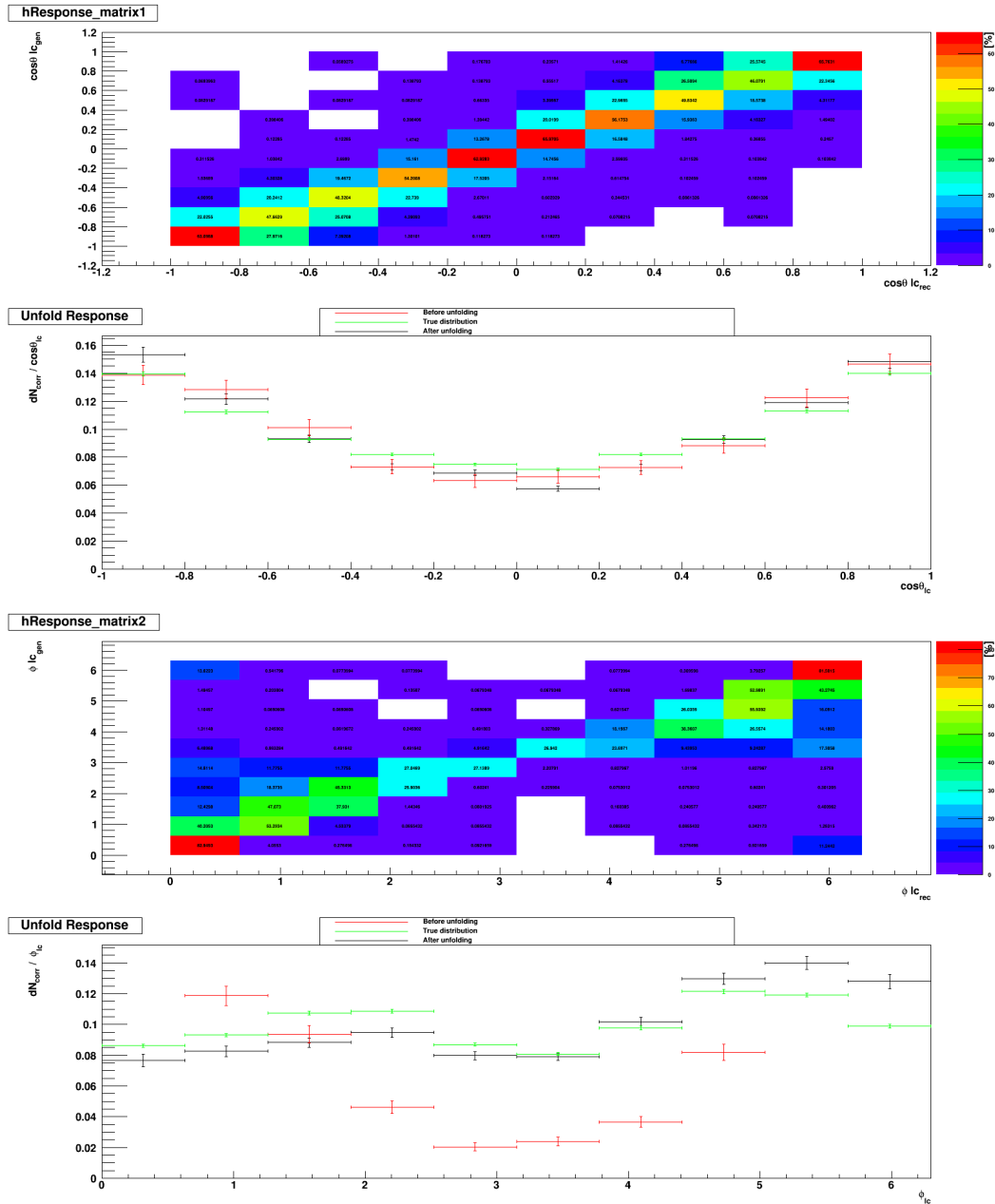
B.4.8 2012 - LL - antiparticles

Figure B.48: The angular distributions spectra $\cos\theta$(up) and ϕ(down) of Λ_c^+ in Λ_b^0 rest frame.
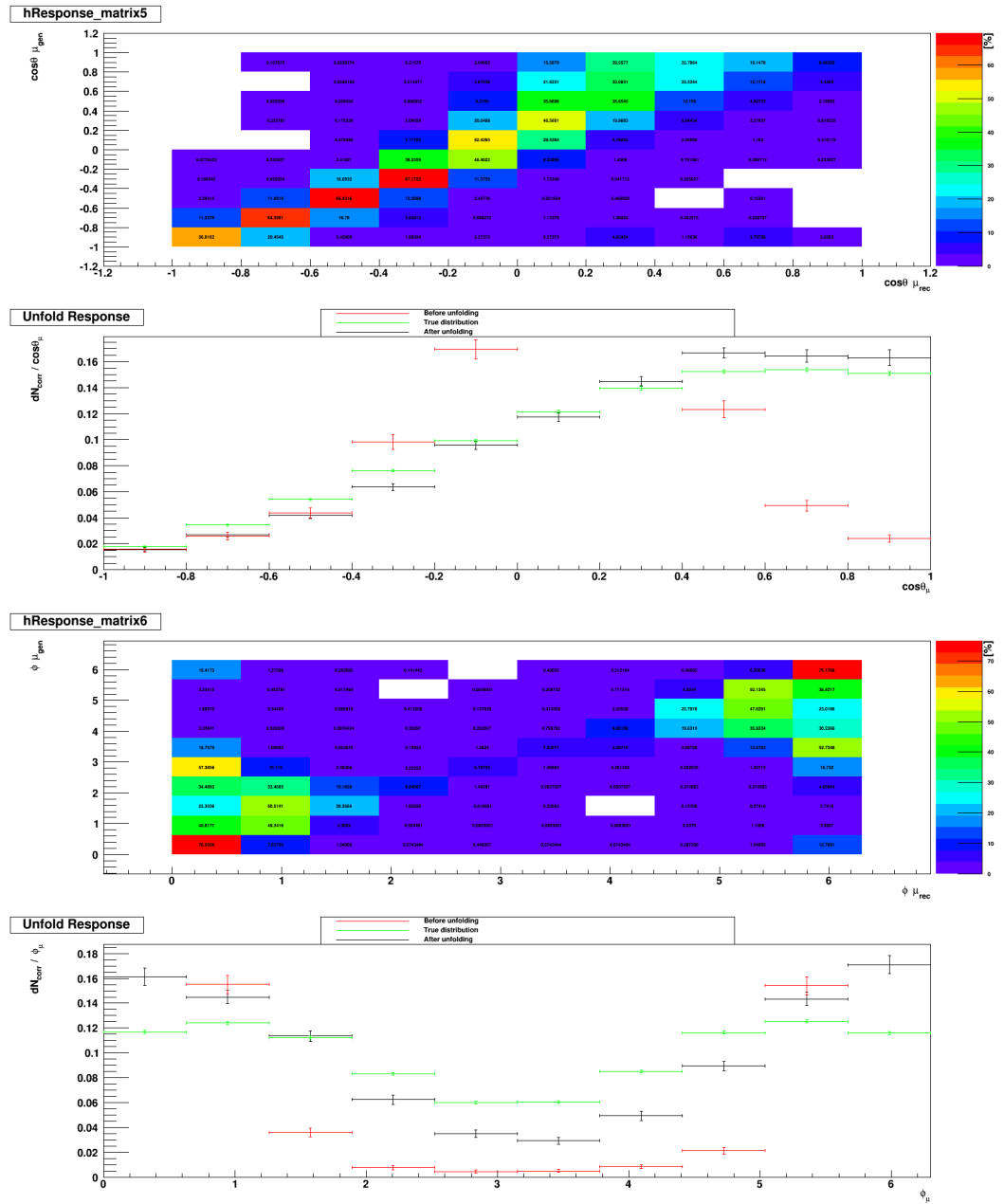
Figure B.49: The angular distributions spectra $\cos\theta$(up) and ϕ(down) of μ in W^*-boson rest frame.
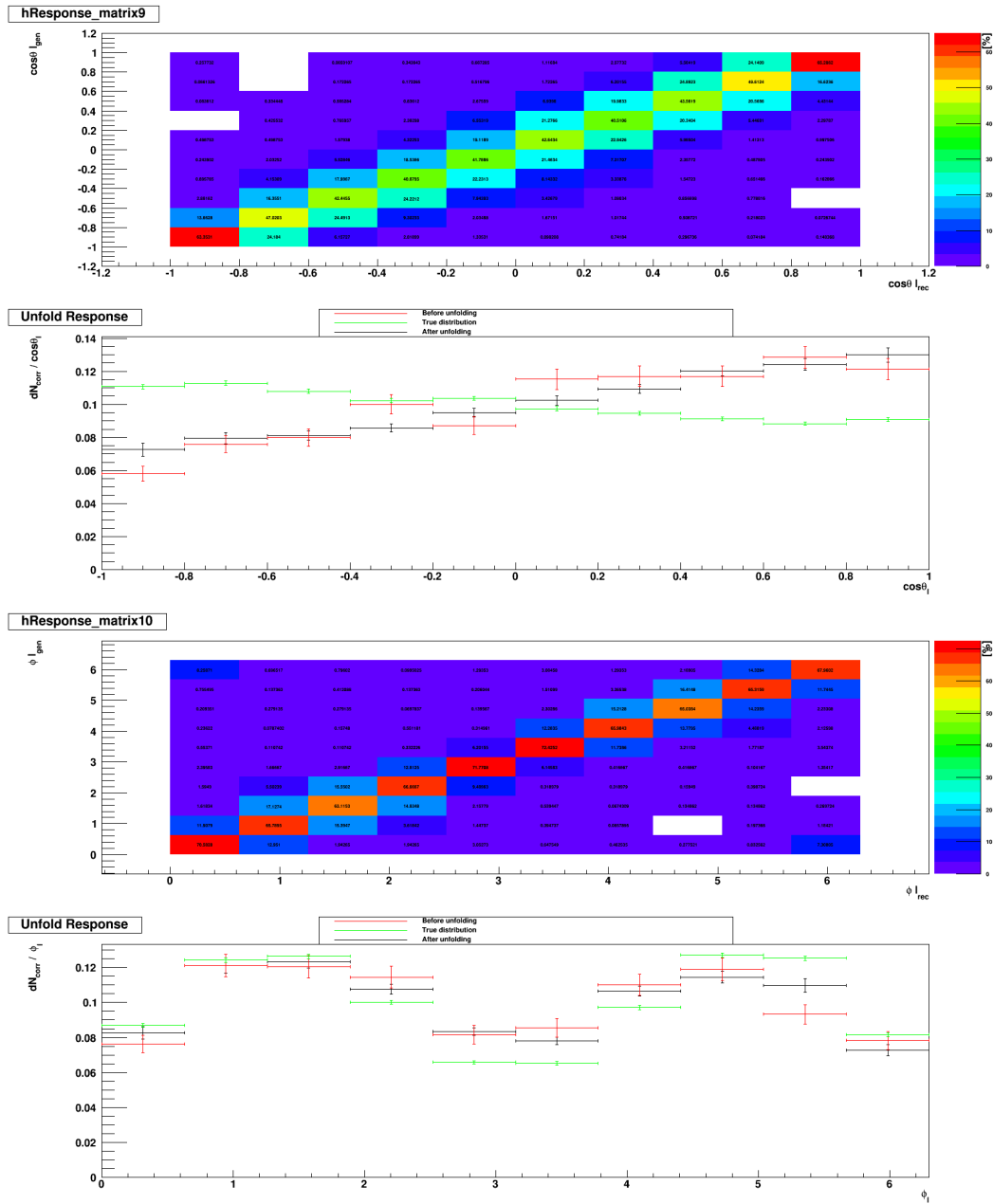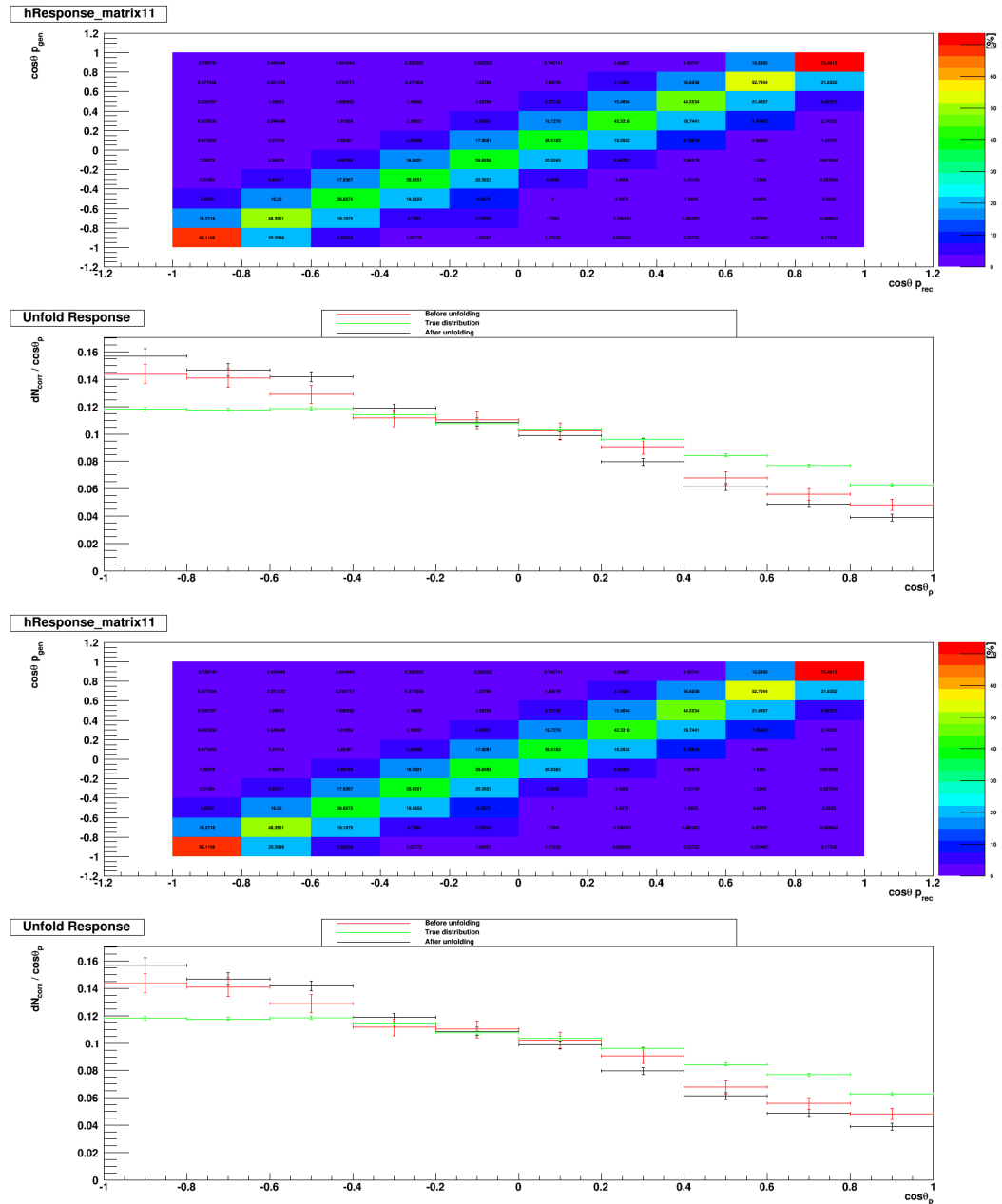
Figure B.50: The angular distributions spectra $\cos\theta$(up) and ϕ(down) of Λ in Λ_c^+ rest frame.

Figure B.51: The angular distributions spectra $\cos\theta$(up) and ϕ(down) of proton in Λ rest frame.

B.5   Unfolded MC Figures

Figure B.52: The unfolded MC spectra $\cos\theta$ and ϕ of the particles in their mother rest frame for data 2011, particles, DD tracks.

Figure B.53: The unfolded MC spectra $\cos\theta$ and ϕ of the particles in their mother rest frame for data 2011, particles, LL tracks.
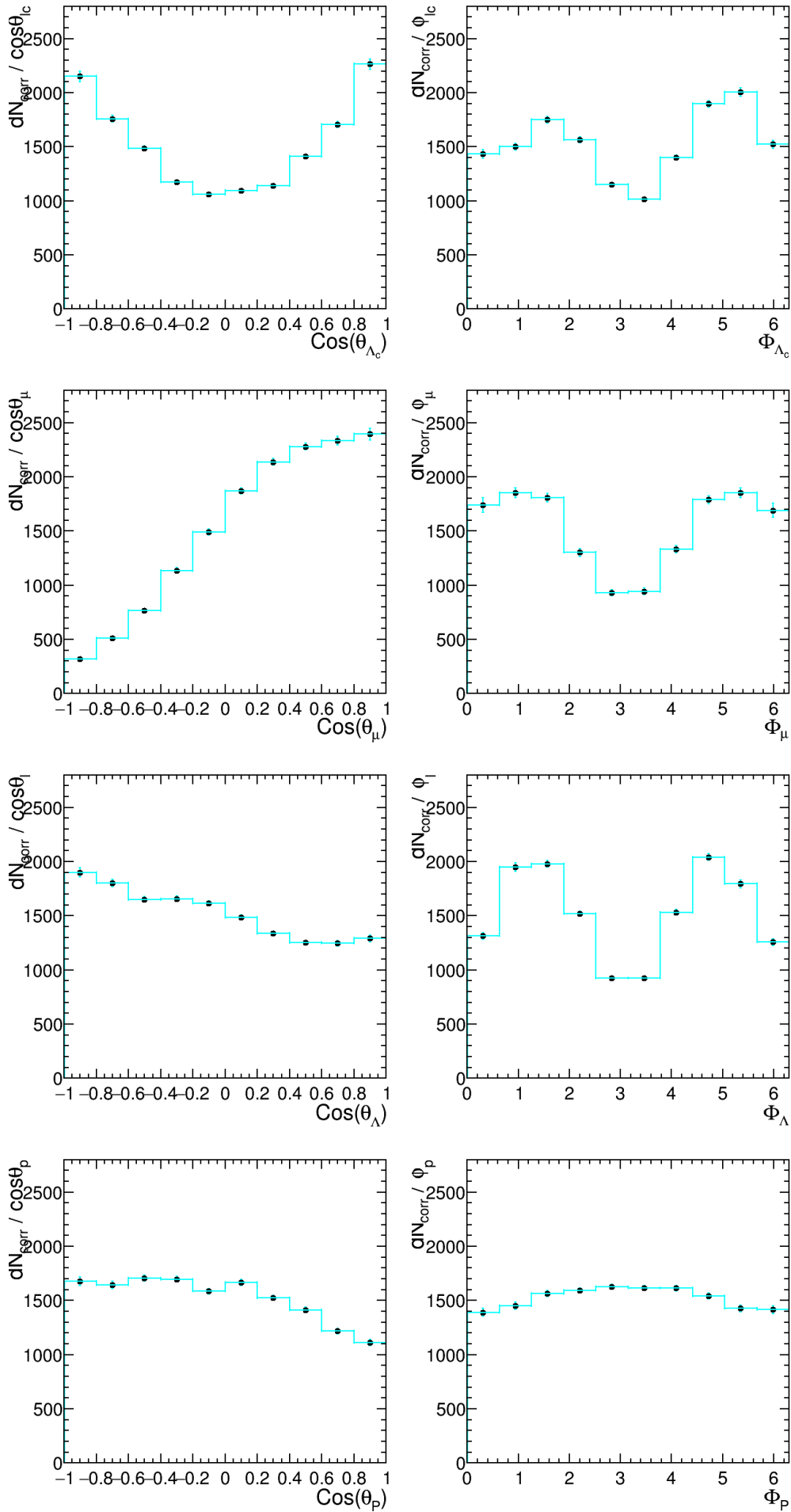
Figure B.54: The unfolded MC spectra $\cos\theta$ and ϕ of the particles in their mother rest frame for data 2012, particles, DD tracks.
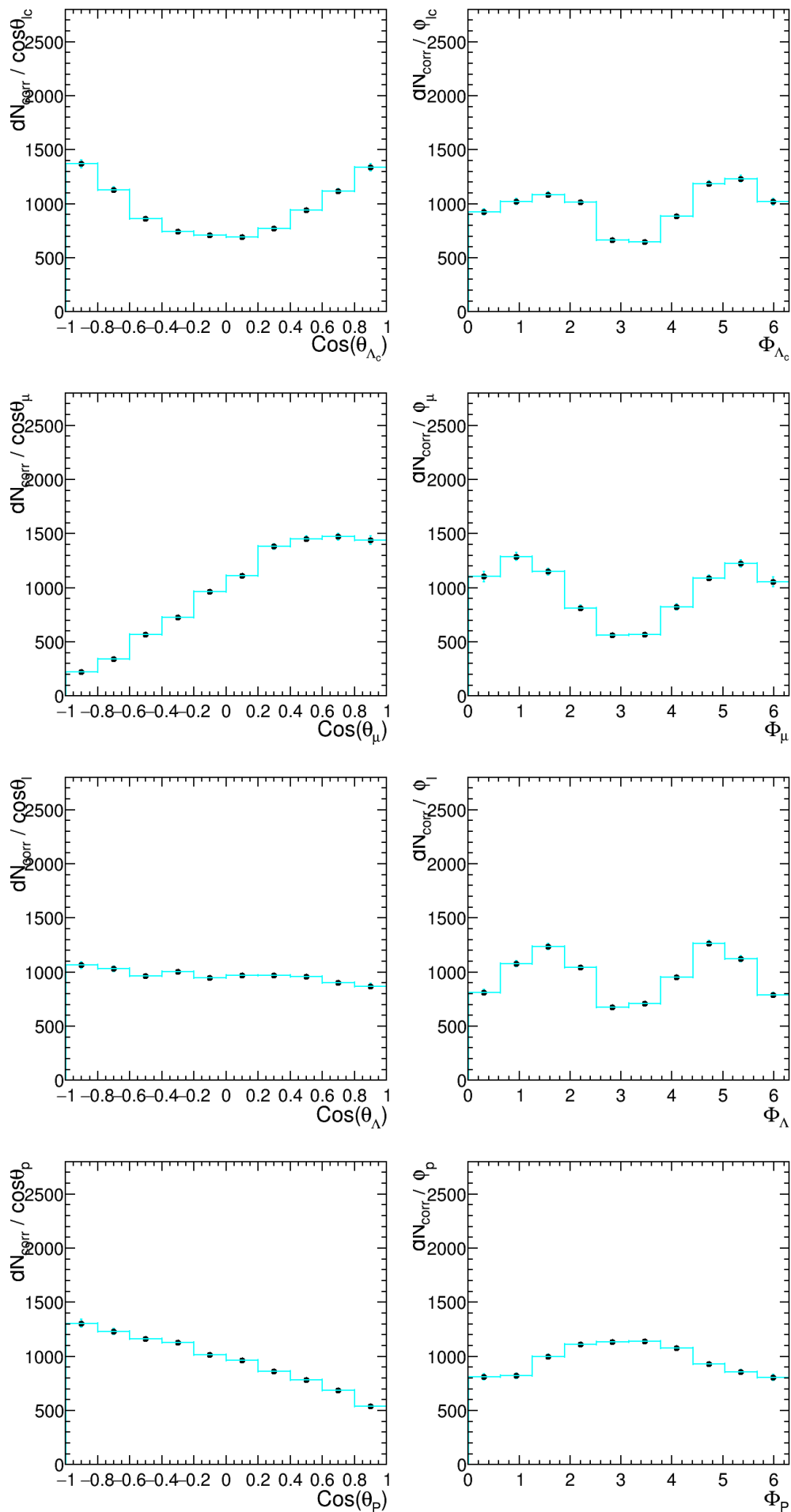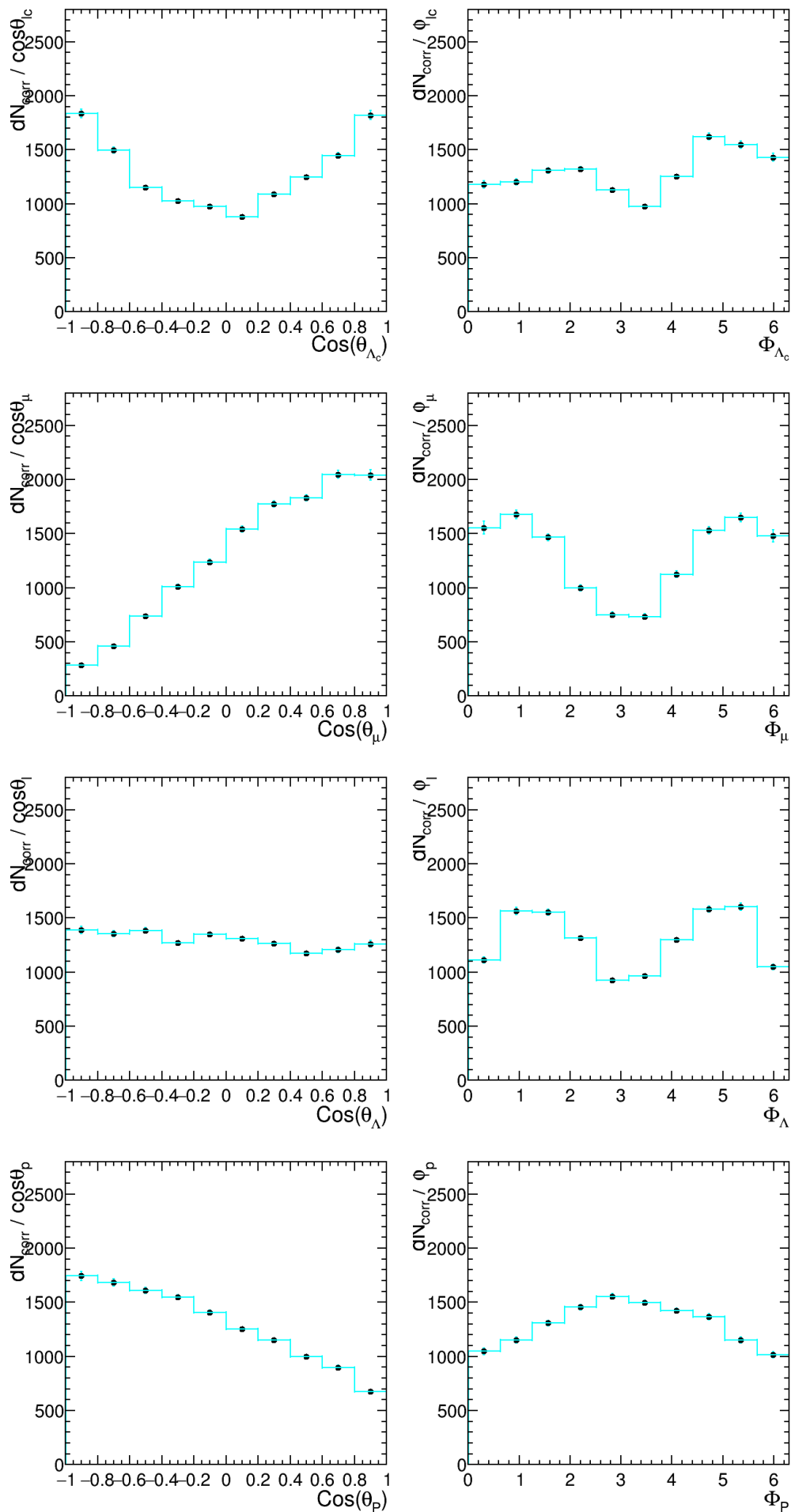
Figure B.55: The unfolded MC spectra $\cos\theta$ and ϕ of the particles in their mother rest frame for data 2012, particles, LL tracks.

Figure B.56: The unfolded MC spectra $\cos\theta$ and ϕ of the particles in their mother rest frame for data 2011, anti-particles, DD tracks.

Figure B.57: The unfolded MC spectra $\cos\theta$ and ϕ of the particles in their mother rest frame for data 2011, anti-particles, LL tracks.
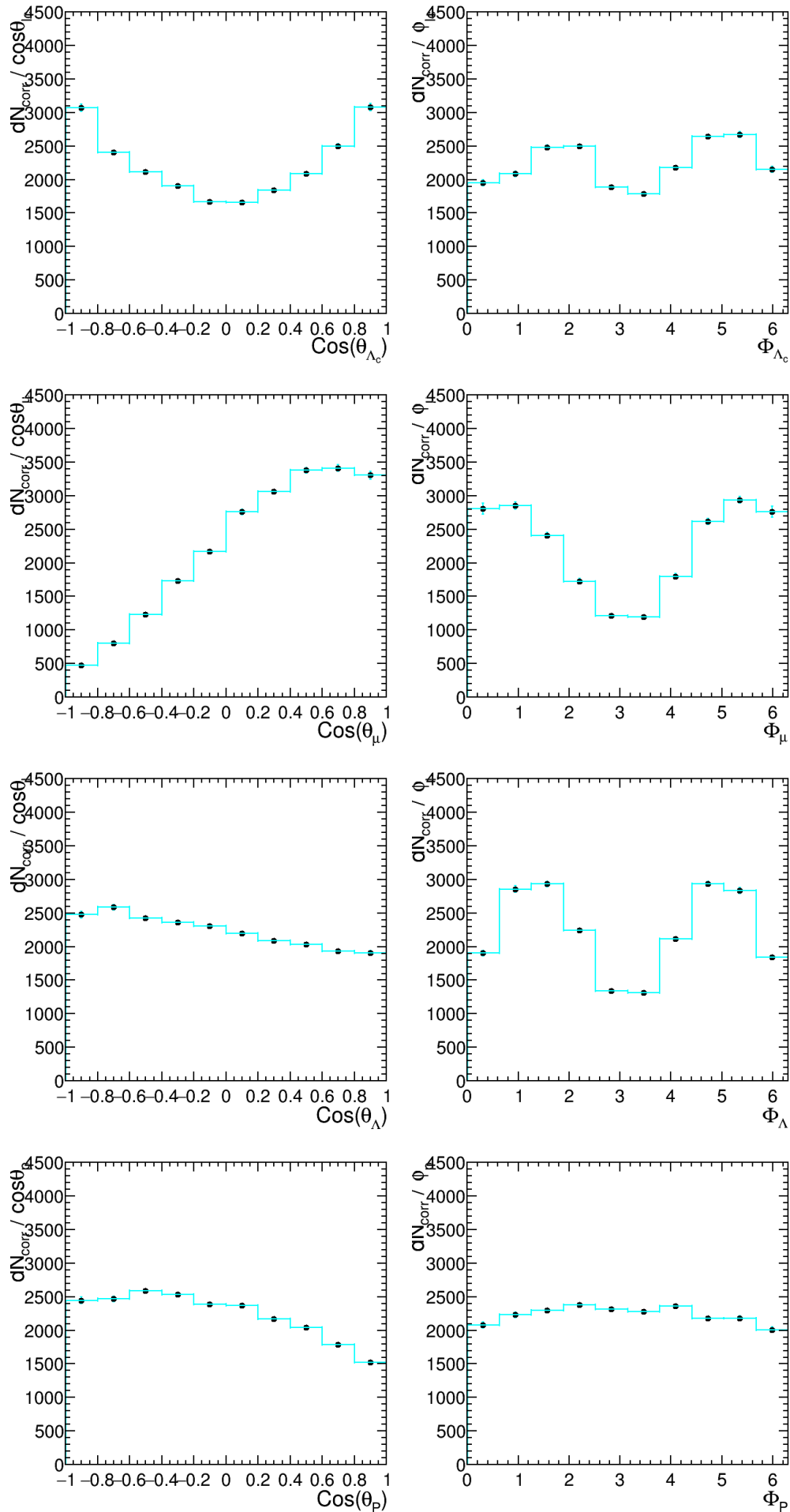
Figure B.58: The unfolded MC spectra $\cos\theta$ and ϕ of the particles in their mother rest frame for data 2012, anti-particles, DD tracks.

Figure B.59: The unfolded MC spectra $\cos\theta$ and ϕ of the particles in their mother rest frame for data 2012, anti-particles, LL tracks.
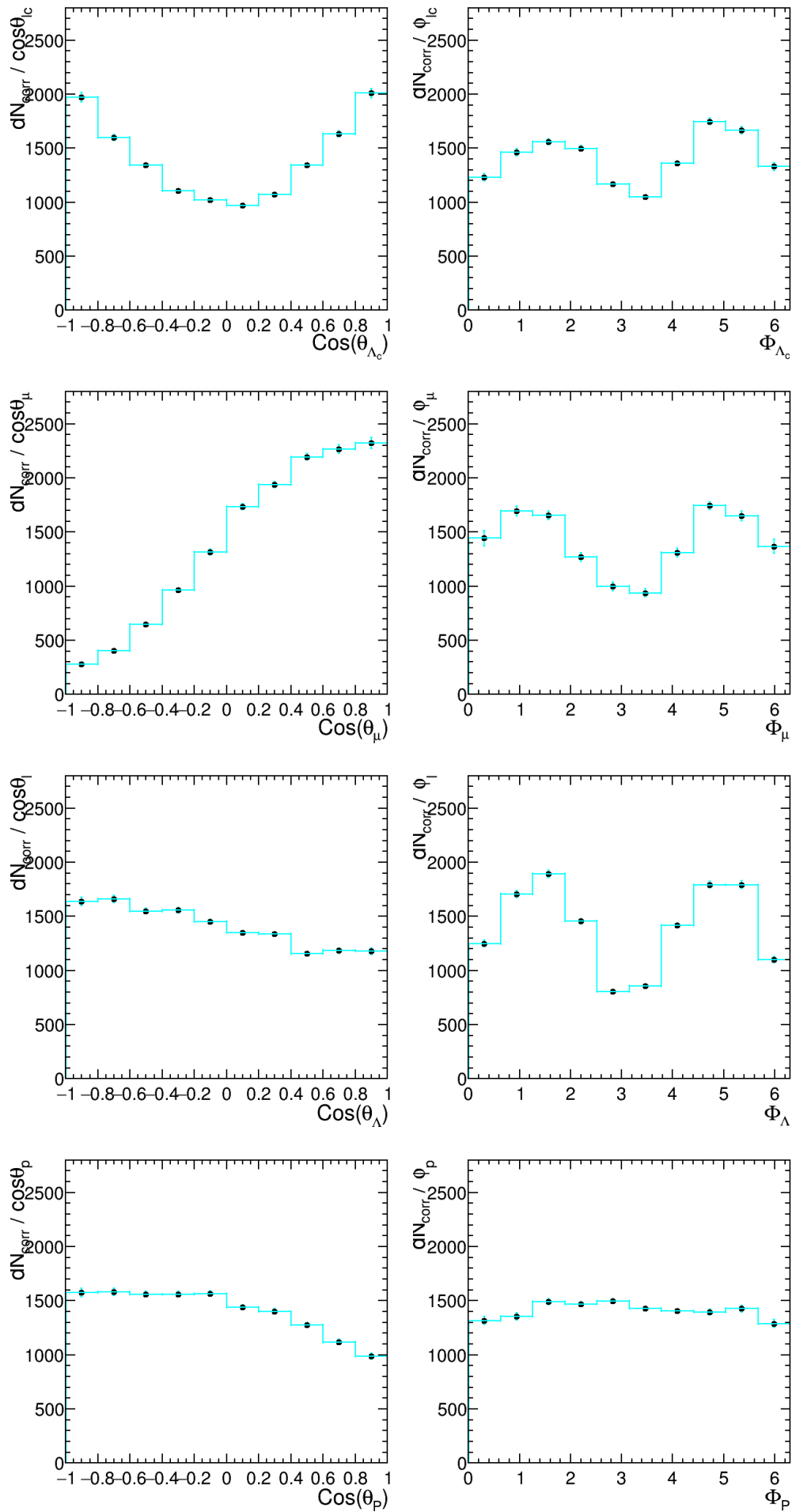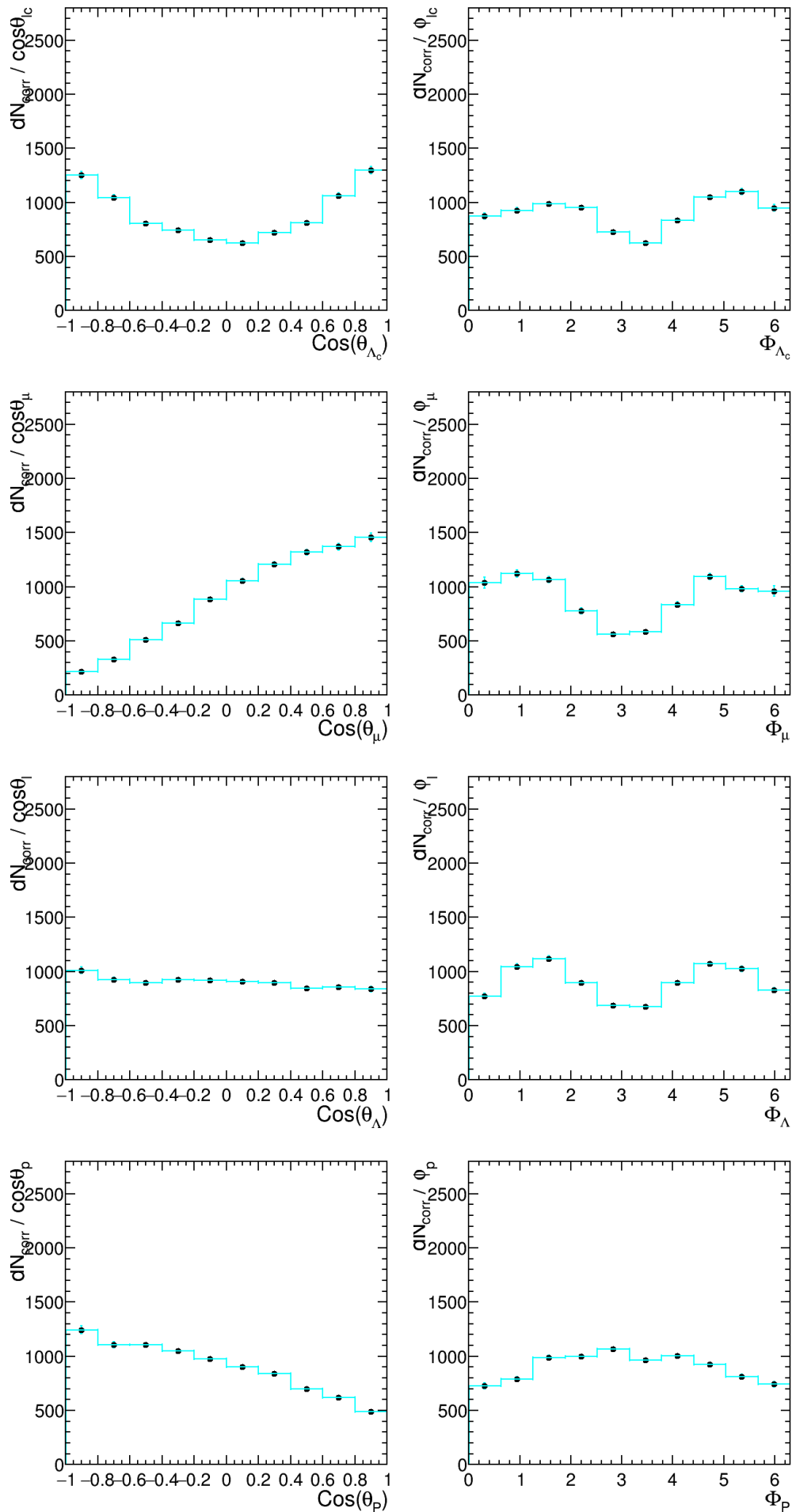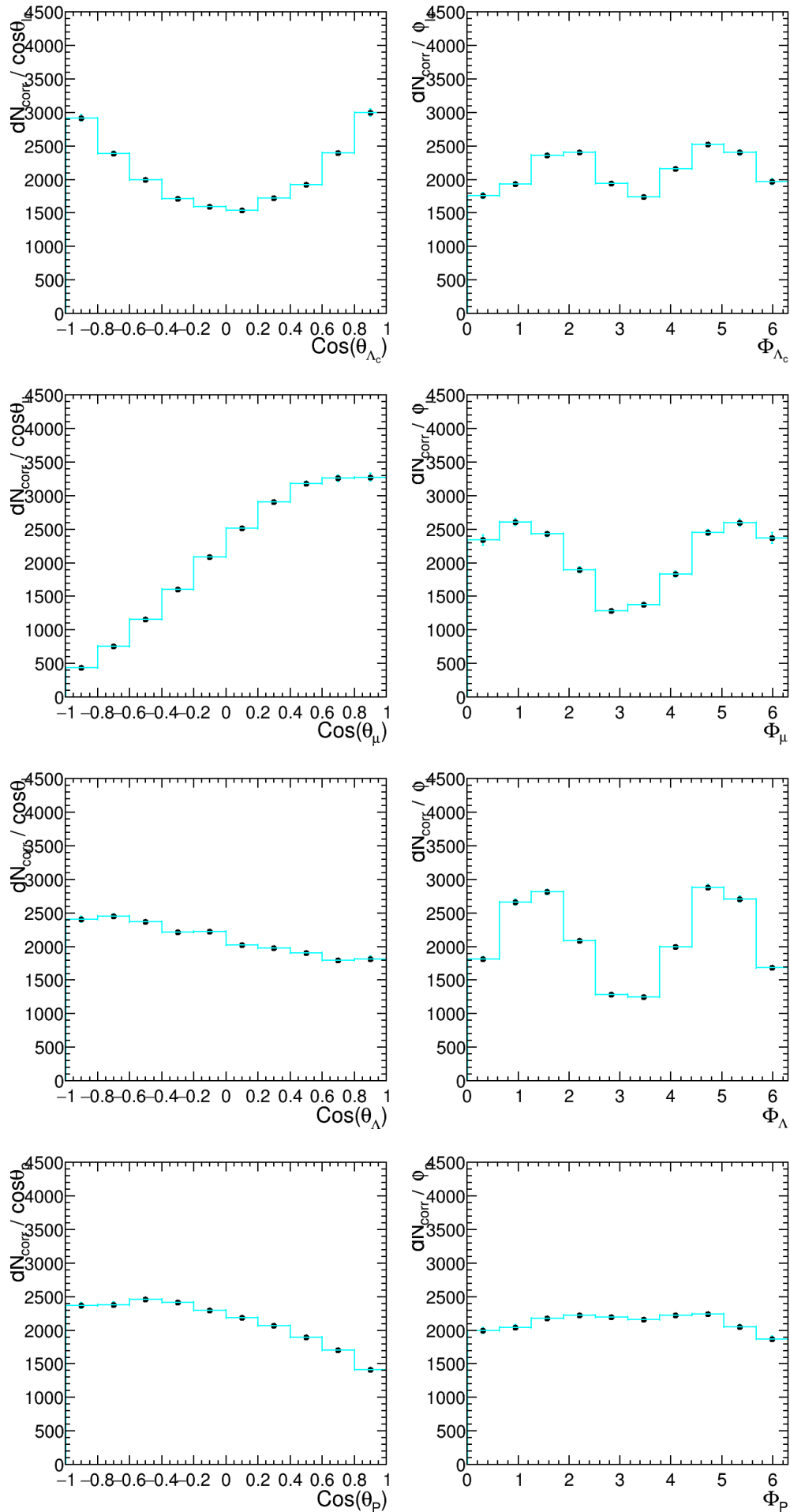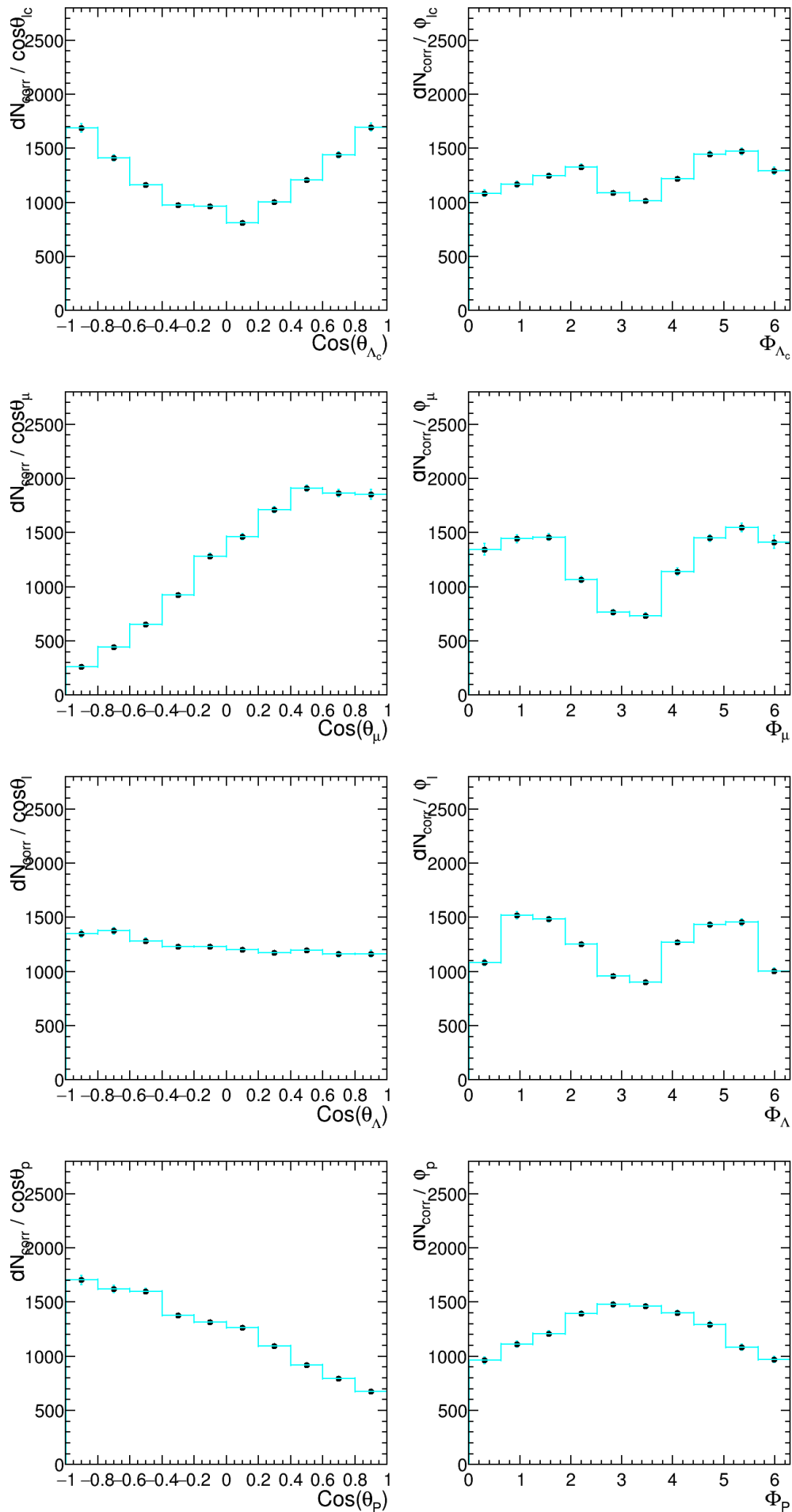
Appendix C

Correction of the Data by the Global Efficiency of the LHCb Detector

Here in this section we introduce another way for the correction of the data by the global efficiency of the LHCb detector. It is similar to the correction done by the unfolding however we restrict our selves to the correction given by the later.
We correct the efficiency bin by bin with the help of the MC. The general relation is given by:

$$\epsilon_j = \frac{N_{jR}^{MC}}{N_{jG}^{MC}} \tag{C.1}$$

Where ϵ_j is the efficiency of the bin j, N_{jR}^{MC} and N_{jG}^{MC} are the number of events reconstructed and generated respectively at the same bin j. Here, one can add another form of the N_{jG}^{MC}, the total number of the generated events is given by :$N_G^{MC} = N_{bins} \times N_{jG}^{MC}$. By substitution, the efficiency could be written as:

$$\epsilon_j = \frac{N_{jR}^{MC}}{N_{jG}^{MC}} = N_{jR}^{MC} \times \frac{N_{bins}}{N_G^{MC}} \tag{C.2}$$

and now correction and normalization of the real data spectra could be easily done using the following formula:

$$N_{kC}^{data} = \frac{N_k^{data}}{N_{kR}^{MC}/N_{kG}^{MC}} \times \sum_j \epsilon_j \tag{C.3}$$

where N_k^{data} and N_{kC}^{data} are the number of events before and after the correction by the global efficiency of the LHCb Detector.

Bibliography

[1] Julian Schwinger, "The Theory of Quantized Fields I", Phys. Rev. 82: 914-927, June 1951.

[2] Gerhart Luders, "On the Equivalence of Invariance under Time Reversal and under Particle-Antiparticle Conjugation for Relativistic Field Theories", Kongelige Danske Videnskabernes Selskab, Matematisk-Fysiske Meddelelser 28N5: 1–17,1954.

[3] Pauli, W.; Rosenfelf, L.; Weisskopf, V., "Niels Bohr and the Development of Physics". McGraw-Hill, LCCN 56040984, eds. (1955).

[4] Bell, J. S, " i.Time reversal in field theory, ii. Some functional methods in field theory",(1954), (Thesis), Birmingham University.

[5] O. W. Greenberg,"CPT Violation Implies Violation of Lorentz Invariance", Physical Review Letters 89 (23): 231602, arXiv:hep-ph/0201258. Bibcode:2002PhRvL..89w1602G. doi:10.1103/PhysRevLett.89.231602 .2002

[6] CPLEAR collaboration, "First direct observation of time-reversal non invariance in the neutral-kaon system", Phys. Lett. B, pages 43-51, 1998.

[7] E. Gabathuler and P. Pavlopoulos, "Strong and weak CP violation at LEAR", Proceedings of the Workshop on physics at LEAR with low energy cooled antiprotons (Erice, 1982), ed. U.Gastaldi and R. Klapish (Plenum, New York,1984) p.747.

[8] CPLEAR Collaboration,"Time reversal, CP and CPT violation studies in the CPLEAR experiment at CERN", Phys. Lett. B 444 (1998) 43.

[9] J. H. Christenson, J.W. Cronin, V. L. Fitch and R. Turlay,"Evidence for the 2π Decay of the K_2^0 Meson", Phys. Rev. Lett. 13 (1964)138.

[10] E. de Rafael, "Chiral Lagrangians and Kaon CP-Violation", `https://arxiv.org/abs/hep-ph/9502254arXiv:hep-ph/9502254[hep-ex]`.

[11] K.F. Smith, N. Crampin, J.M. Pendlebury, D.J. Richardson, D. Shiers, et al. "A Search for the Electric Dipole Moment of the Neutron",Phys.Lett., B234 :191–196, 1990.

[12] S.K. Lamoreaux and R. Golub, "Comment on New experimental limit for the electric dipole moment of the neutron", Phys.Rev., D61(hep-ph/9907282) :051301,2000.

[13] P.G. Harris, C.A. Baker, K. Green, P. Iaydjiev, S. Ivanov, et al., "New experimental limit on the electric dipole moment of the neutron", Phys.Rev.Lett., 82 :904–907, 1999.

[14] C.A. Baker, D.D. Doyle, P. Geltenbort, K. Green, M.G.D. van der Grinten, et al.,"An Improved experimental limit on the electric dipole moment of the neutron", Phys.Rev.Lett., 97(hep-ex/0602020) :131801, 2006.

[15] P.K KABIR, "What is not invariant under Time Reversal?", Phys. Rev. D 2, pages 540-542,1970.

[16] J. Belz, "Study of the decays $K_L^0 \rightarrow \pi^+\pi^-\gamma$ and $K_L^0 \rightarrow \pi^+\pi^-e^+e^-$ at KTeV",https://arxiv.org/abs/hep-ex/9903025arXiv:hep-ex/9903025v1.

[17] A.Alavi-Harati et al.,"Observation of CP Violation in $K_L \longrightarrow \pi^+\pi^-e^+e^-$ Decays", Phys. Rev. Lett. 84, 408(2000)

[18] L.M. Sehgal and M. Wanninger, CP violation in the Decay $K_L \rightarrow \pi^+\pi^-e^+e^-$", Phys. Rev.D46, 1035 (1992), D46, 5209(E).

[19] BABAR Collaboration, "Observation of Time-Reversal Violation in the B_0 Meson System",Phys. Rev. Lett. 109, 211801, (2012).

[20] J. Bernabeu, F. Martinez-Vidal, P. Villanueva-Perez, "Time Reversal Violation from the entangled $B_0 - \bar{B}_0$ system", JHEP 1208, 064 (2012).

[21] M. C. Banuls and J. Bernabeu, "CP, T and CPT versus temporal asymmetries for entangled states of the Bd-system", Phys. Lett. B 464, 117n(1999); Nucl. Phys. B 590, 19 (2000).

[22] L. Wolfenstein, "Direct test of time reversal invariance violation in B mesons",Int. Jour. Mod. Phys. 8, 501-511, (1999).

[23] J. Bernabeu,"Time reversal Violation for Entagled Neutral Mesons" J. Phys. Conf. Ser. 335, 012011 (2011).

[24] M.Jacob and G.C Wick, "On the General Theory of Collisions for Particles with Spin", Annals of Physics 821,774-779, 2000.

[25] LHCb collaboration, "LHCb Technical Proposal", CERN/LHCC 98-4 (1998).

[26] LHCb collaboration, "Heavy-Quark production, Advanced Series on Directions in High Energy Physics" 15 (1998) 609.

[27] E. Norrbin and T. Sjöstrand, "Production and Hadronization of Heavy Quarks", hep-ph/0005110 (2000).

[28] LHCb collaboration, "Some remarks on systematic effects of the trigger and Event Generator studies", (internal) LHCb 2003-157 (2003).

[29] LHCb Collaboration, "Absolute luminosity measurements with the LHCb detector at the LHC", LHCb-PAPER-2011-015.

[30] LHCb Collaboration, "Precision luminosity measurements at LHCb", LHCb-PAPER-2014-047.

[31] P. R. Barbosa Marinho et al., "LHCb VELO", CERN/LHCC 2001-011 (2001).

[32] LHCb Collaboration. "LHCb VELO TDR, Vertex Locator, Technical Design Report". (CERN-LHCC-2001-011), 2001

[33] LHCb Collaboration. "LHCb Magnet, Technical Design Report".(CERN-LHCC-2000-007), 2000.

[34] LHCb Collaboration. " Inner Tracker, Technical Design Report".(CERN-LHCC-2002-029), 2002.

[35] Antunes-Nobrega et al. "LHCb Trigger System, Technical Design Report.". CERN, Geneva, 2003.

[36] Vladimir V. Gligorov. "A Single Track HLT1 Trigger". Technical Report LHCb-PUB-2011-003. CERN-LHCb-PUB-2011-003.

[37] Roel Aaij and Johannes Albrecht. "Muon triggers in the High Level Trigger of LHCb". Technical Report LHCb-PUB-2011-017. CERN-LHCb-PUB-2011-017.

[38] M Williams, Vladimir V Gligorov, C Thomas, H Dijkstra, J Nardulli, and P. Spradlin. "The HLT2 Topological Lines", Technical Report LHCb-PUB-2011-002.CERN-LHCb-PUB-2011-002.

[39] G.Barrand et al., "GAUDI A software architecture and framework for building HEP data processing applications", Comput.Phys.Commun.140(12),45(2001)

[40] I. Belyacv, P. Charpentier, S. Easo, P. Mato, J. Palacios et al., "Simulation application for the LHCb experiment", eConf C0303241 (2003)TUMT003, arXiv:physics/0306035.

[41] LHCb Collaboration, "The Boole Project", http://lhcb-release-area.web.cern.ch/LHCb-release-area/DOC/boole/

[42] LHCb Collaboration, "The Moore Project", http://lhcb-release-area.web.cern.ch/LHCb-release-area/DOC/moore/

[43] LHCb Collaboration, "The Brunel Project", http://lhcb-release-area.web.cern.ch/LHCb-release-area/DOC/brunel/

[44] LHCb Collaboration, "The DaVinci Project", http://lhcb-release-area.web.cern.ch/LHCb-release-area/DOC/davinci/

[45] R. Hagedorn, "The Density Matrix" .CERN, April 1958.

[46] Sakurai, J, "Modern Quantum Mechanics" (2nd ed.), p. 181, ISBN 9780321503367.

[47] Z.J. Ajaltouni, and E. Conte, "Angular analysis of Λ_b^0 decays into Λ V(1^-):Applications to Time-Odd Observables and CP violation in Λ_b^0 decays "(I),2014. https://arxiv.org/abs/hep-ph/0409262arXiv:hep-ph/0409262v1 [hep-ex]

[48] J.D. Jackson, "Particle and Polarization Angular Distribution for two and Three-body decays",Les Houches,1965.

[49] Z. Ajaltouni, E. Conte, and O. Leitner, "Beauty Baryons at LHCb",(CERN-LHCb-2008-005), 2008.

[50] Marwa Jahjah, "Analyse du canal $\Lambda_b^0 \rightarrow J/\psi\Lambda$ et mesure de la polarisation du baryon Λ produit dans les collisions p-p at $\sqrt{s} = 7$ TeV avec le detecteur LHCb",Thesis, Universite Blaise Pascal, 2011.

[51] Z.J. Ajaltouni, E. Conte, and O. Leitner, "Λ_b^0 decays into Λ-vector", Phys.Lett.,B614(hep-ph/0412116) :165–173, 2005.

[52] J. Jackson, "Resonance decays In: High Energy Physics Les Houches lectures ", Gordon and Breach, 1966.

[53] Z.J. Ajaltouni, Elvio Di Salvo, and O. Leitner, "Testing Time-Reversal : Λ_b^0 Decays into Polarized Resonances", https://arxiv.org/abs/hep-ph/0702240.

[54] M.E. Rose, "Elementary Theory of Angular Momentum", Wiley, 1957.

[55] K.A. Olive et al., "Review of Particle Physics". Chin.Phys., C38 :090001, 2014.

[56] Kostelecký, V. A.; Russell, N. (2011), "Data tables for Lorentz and CPT violation". Reviews of Modern Physics 83 (1): 11–31.

[57] O. Leitner, Z.J. Ajaltouni, and E. Conte, "Testing fundamental symmetries with $\Lambda_b^0 \to \Lambda$-Vector decay". (hep-ph/0602043), 2006.

[58] C. Quigg , "Gauge Theories of the Strong, Weak and Electromagnetic Interactions", Front.Phys., (1983).

[59] Cheng, Hai-Yang, "Charm Baryon Production and Decays", Int.J.Mod.Phys. A, A24, 593-626, (2009).

[60] L. Wolfenstein, "The Search for Direct Evidence for Time Reversal Violation", Int.J.Mod.Phys., E,8 ,501–511, (1999).

[61] LHCb collaboration, "Measurements of the $\Lambda_b^0 \to J/\psi\Lambda$ decay amplitudes and the Λ_b^0 polarisation in pp collisions at $\sqrt{(s)} = 7$ TeV", LHCb-PAPER-2012-057.

[62] ALEPH collaboration, D. Buskulic et al., "Measurement of Λ_b^0 Polarization in Z^0 Decays", Phys. Lett. B365 (1996) 437.

[63] OPAL collaboration, G. Abbiendi et al., "Measurement of the Average Polarization of b-baryons in Hadronic Z^0 Decays", Phys. Lett. B444 (1998) 539.

[64] DELPHI collaboration, P. Abreu et al., "Λ_b^0 Polarization in Z^0 Decays at LEP", Phys.Lett. B474 (2000) 205.

[65] K. Lessnoff, "A Study of the LHCb Experiment's Sensitivity to CP Violation in Mixing and to Production Asymmetry in B_s Mesons, Using Semi-leptonic Decays," CERN-THESIS-2010-076 (2009).

[66] LHCb collaboration, Measurement of the Shape of the $\Lambda_b^0 \to \Lambda_c^+ \mu^- \bar{\nu}$ Differential Decay Rate",PRD96,112005, LHCb-PAPER-2017-016.

[67] M. Pervin, W. Roberts, and S. Capstick, "Baryon Spectra and Semileptonic Decay in a Constituent Quark Model", J.Phys.Conf.Ser. 69 (2007) 012040.

[68] A. Hoecker, P. Speckmayer, J. Stelzer, J. Therhaag, E. v. Toerne, and H. Voss. "TMVA : Toolkit for Multivariate Data Analysis". PoS,ACAT(physics/0703039).

[69] R. Brun and F. Rademakers, "ROOT - An Object Oriented Data Analysis Framework", Nucl.Inst. Meth. in Phys. Res. A 389, 81 (1997).

[70] Breiman L, Friedman J. H., Olshen R. A. and Stone C. J., "Classification and Regression Trees", Wadsworth International Group, Belmont, California, USA (1984)

[71] Schapire R. E. and Freund Y., "A Decision-Theoretic Generalization of on-Line Learning and an Application to Boosting", J. Comput. Syst. Sci. 55 (1997)

[72] M. Pivk and F. R. Le Diberder, "sPlot: a Statistical Tool to Unfold Data Distributions", Nucl.Inst. Meth. in Phys. Res. A555 (2005) 356,arXiv:physics/0402083

[73] M. Oregila. "A Study of the Reactions $\psi' \to \gamma\gamma\psi$", Thesis (1980),SLAC Stanford .

[74] http://lhcb-release-area.web.cern.ch/LHCb-release-area/DOC/moore/releases/v23r6/doxygen/db/d93/-evt-baryon-p-c-r-8cpp-source.html

[75] M. Pervin, W. Roberts and S. Capstick, "Semileptonic Decays of Heavy Lambda Baryons in a Quark Model," Phys. Rev. C 72, 035201 (2005).

[76] LHCb collaboration, "Measurement of $\sigma(\mathrm{pp} \to b\bar{b}\ \mathrm{X})$ at $\sqrt{(s)}$=7 TeV in the forward region", LHCb-PAPER-2010-002

[77] The RooUnfold package and documentation are available from http://hepunx.rl.ac.uk/ adye/software/unfold/RooUnfold.html

[78] K. Tackmann, A. Hoecker, "SVD-Based Unfolding: Implementation and Experience", 2011 (CERN, Geneva, January 2011),https://arxiv.org/abs/1112.2226

[79] A. Hoecker, V. Kartvelishvili, "SVD Approach to Data Unfolding",(1995). https://arxiv.org/abs/hep-ph/9509307

[80] Christos Hadjivasiliou, "Measurement of the form factor shape for the semileptonic decay $\Lambda_b^0 \to \Lambda_c^+ \mu^- \bar{\nu}_\mu$",Thesis, Syracuse University, 2015.

[81] The Roofit project. https://root.cern.ch/drupal/content/roofit.

[82] Z.J Ajaltouni, M. Kozeiha, R. Moustafa, "Λ_c^+ Quasi-two-body Decays : Angular Distributions,Polarization and Test of Time Reversal", LHCb-1NT-2015-032, Physics.